Spectral Evolution in Blazars
The Case of CTA 102

INAUGURAL-DISSERTATION
zur
Erlangung des Doktorgrades
der Mathematisch-Naturwissenschaftlichen Fakultät
Rheinischen Friedrich-Wilhelms-Universität Bonn

vorgelegt von
Christian M. Fromm
aus Bad Neustadt a. d. Saale, Deutschland

Bonn, November 2012

Angefertigt mit Genehmigung der Mathematisch-Naturwissenschaftlichen Fakultät der Rheinischen Friedrich-Wilhelms-Universität Bonn

1. Gutachter: Prof. Dr. Eduardo Ros Ibarra

2. Gutachter: Prof. Dr. Pavel Kroupa

Tag der Promotion: 22.01.2013

Erscheinungsjahr: 2013

“For the good of the country”

From Monty Python’s The meaning of Life

Abstract

Active Galactic Nuclei (AGN) are among the most powerful objects in the universe. In their centre they host a supermassive black hole (BH) with up to 10^{10} solar masses and an accretion disk is formed around them feeding the system. A fraction of the in-falling mater is ejected perpendicularly to the accretion disk forming the so-called jets. These relativistic flows are highly collimated and propagate up to kiloparsec distances from their central engine. The observed emission of AGN jets shows strong variability throughout the electro-magnetic spectrum which reflects variations in source intrinsic parameters such as the magnetic field and the rest-mass density. The variation in the emission of AGN jets can be best studied in their most powerful representatives, the blazars (AGN jets seen under a small viewing angle).

The blazar CTA 102 underwent a historic radio outburst in April 2006 which provides a perfect laboratory for studying the spectral evolution. CTA 102 has been a target of single-dish and VLBI observations for several years. In this work we use both kind of observations to study and model the spectral evolution during the flare. We use the dense sampling of the single-dish observations to trace the evolution of the flare in the turnover-frequency and turnover flux density plane and modelled the results with a modified shock-in-jet model, assuming a travelling shock recollimation shock interaction.

To test this hypothesis, we combine archival VLBI observations from the MOJAVE program (15 GHz) and Boston University Blazar Monitoring program (43 GHz) with our multi-frequency VLBI observations during the 2006 flare. The VLBI kinematic provides a unique view on the parsec-scale structure of CTA 102 over the last 15 years and reveals several stationary features. Our hypothesis of a shock-shock interaction as possible mechanism behind the 2006 is confirmed by a detailed spectral analysis of the multi-frequency VLBI observations.

We use 2D relativistic hydrodynamic simulations (RHD) to bridge the sparse time sampling of the observations and to further investigate the non-linear process of travelling shock recollimation shock interaction. From the simulations we compute the non-thermal emission taking adiabatic and radiative losses into account. The synthetic single dish spectra and radio maps can reproduce the observed structure in the VLBI maps and variation in the single dish spectra during the flare. In addition, we present observable predictions for the interaction between a travelling shock and a recollimation shock.

Zusammenfassung

Aktive Galaktische Kerne (engl. Active Galactic Nuclei, AGN) gehören zu den leuchtkräftigsten Quellen des Universums. In ihrem Zentrum beherbergen sie ein supermassives schwarzes Loch, das bis zu 10^{10} Sonnenmassen schwer sein kann. Um dieses schwarze Loch bildet sich eine Akkretionsscheibe, die es mit einfallender Materie füttert. Ein Teil der einfallenden Materie wird senkrecht zur Akkretionsscheibe ausgestoßen und bildet einen sogenannten Jet. Dieser gebündelte Materiestrom breitet sich über mehrere Tausende von Parsec aus und erreicht bis zu 99% der Lichtgeschwindigkeit. Die beobachtbare Strahlung dieser Jets weißt starke Variationen im gesamten elektromagnetischen Spektrum auf und spiegelt die Veränderungen in physikalischen Eigenschaften der Quelle, z. B. im Magnetfeld und in der Teilchendichte wieder. Die Fluktuationen in der Strahlung von AGN Jets können am besten in Blazaren, den energiereichsten Vertretern der AGNs, studiert werden.

Der Blazar CTA 102 zeigte seinen größten Helligkeitsausbruch im April 2006 und stellt ein grossartiges Versuchslabor für das Studium der zeitlichen Veränderung des Spektrums dar. CTA 102 ist einer der best beobachteten Blazare im Radiobereich, sowohl mit einzelnen Teleskopen als auch im Verbund von mehreren Teleskopen zur sogenannten Interferometrie mit langen Basislinien (engl. VLBI). In der vorliegenden Arbeit benutzen wir beide Beobachtungsdaten um die Veränderung des Spektrums zu analysieren und zu modellieren. Die grosse Anzahl von Beobachtungen der Quelle mit Einzelteleskopen ermöglicht die Veränderung der Strahlung zu verfolgen und sie mit einem modifizierten Shock-in-Jet Model zu modellieren. In diesem modifizierten Modell setzen wir eine Kollision zwischen einer relativistischen Schockwelle und einem stehenden Schock voraus.

Um unsere Annahme zu testen, werten wir zusätzliche VLBI Beobachtungen der Langzeitbeobachtungsprogramme MOJAVE bei 15 GHz und der Universität Boston bei 43 GHz aus und kombinieren diese mit VLBI Beobachtungen bei unterschiedlichen Frequenzen während des Helligkeitsausbruches. Die Auswertung der Langzeitmessungen liefert einen einzigartigen Einblick in die Struktur der Quelle und deren Entwicklung in den letzten 15 Jahren. Basierend auf diesen Daten können wir mehrere stehende Schocks innerhalb der Quelle identifizieren und die Auswertung der VLBI Beobachtungen bei mehreren Frequenzen bestätigt unsere Annahme der Kollision einer relativistischen Schockwelle und eines stehenden Schocks als mögliche Ursache für den Helligkeitsausbruch im April 2006.

Um die beobachtungsbedingten Zeitlücken zu überbrücken und um das nicht-lineare Verhalten während der Kollision zwischen der relativistischen Schockwelle und dem ste-

henden Schock weiter zu untersuchen verwenden wir 2D relativistische hydrodynamische Simulationen. Die Brechung der nicht-thermischen Strahlung aus den Ergebnisse der Simulationen erlaubt es uns diese mit den Beobachtungen zu vergleichen. In der Berechnung der Strahlung berücksichtigen wir sowohl adiabatische als auch Strahlungsverluste. Die berechneten Radiokarten und Spektren geben die charakteristischen Merkmale der VLBI Beobachtungen wieder und reproduzieren die beobachtete Änderung des Radiospektrums. Desweiteren können unsere Ergebnisse beobachtbare Prognosen für die Wechselwirkung zwischen relativistischen Schockwellen und stehenden Schocks liefern.

Mit der vorliegenden Arbeit wird ein weitere Beitrag zum besseren Verständnis der zeitlichen Veränderung des Spektrums von Blazaren geleistet.

Structure of this work

In this work, we investigate the spectral evolution in the blazar CTA 102 and present an research scheme, introducing the required observational and theoretical tools, which can be applied to other extragalactic jets:

- A brief introduction to the topic of Active Galactic Nuclei (AGN) and to the blazar CTA 102 is provided in the first Chapter.
- In Chapter 2 we introduce special relativistic hydrodynamics required to describe the jets together with the radiation physics needed to address the observed non-thermal emission.
- The analysis of the single-dish light curves of CTA 102, together with the required numerical routines for the application of a modified shock-in-jet model is presented in Chapter 3.
- The extraction of kinematic parameters from VLBI observations and the interpretation of gradients in the brightness temperature along jet in the frame work of the shock-in-jet model is shown in Chapter 4.
- Chapter 5 introduces non-standard analysis techniques for the core-shift and spectral analysis of multi-frequency VLBI observations. These techniques are used to extract values for the spatial and temporal evolution of the source intrinsic parameters such as the magnetic field, the relativistic particle density, and the magnetisation.
- In Chapter 6, we use relativistic hydrodynamic (RHD) simulations as a tool to farther investigate possible jet configurations and non-linear processes in the jets of AGNs. The connection to the observations is established by the calculation of the non-thermal emission in form of single dish spectra and synthetic radio maps. As an example, we use parameters extracted from the observations of CTA 102 and conduct source-tailored simulations and non-thermal emission calculations.
- In the last Chapter of this work, we provide a summary and present a detailed comparison between observations and numerical simulations.
- In the Appendices we present additional details of the data reduction and the developed routines for the error estimation of the source intrinsic parameters.

Contents

1 Introduction

This PhD is devoted to the study of active galactic nuclei by means of radio astronomical observations and numerical simulations. A general view of the observational techniques is shown in Burke & Graham-Smith (2009) and Thompson et al. (2007). A glimpse on the jet physics is provided in Krolik (1999), and on numerical simulations in Boettcher et al. (2012). In this introduction we will give just a flavour of the concepts to be used later in the description of the work, the interpretation of the results, and the discussion.

1.1 Active Galactic Nuclei

The light of normal galaxies is dominated by thermal emission of the embedded stars and the peak of the emission can be found between around 10^{14} Hz, which can be understood by the superposition of the Planck-spectrum of the individual stars.

In 1943 Carl Seyfert discovered a new type of galaxies with a bright central region and broad emission lines. In the 1960s observations at 158 MHz revealed several sources of strong radio emission. Since their optical counterparts were compact , they were labeled as quasi stellar radio sources (quasars). In 1963 Maarten Schmidt derived the redshift of the radio source 3C 273 and showed that this object is a powerful distant galaxy (Schmidt 1963). The point-like structure in the optical reveals that the emission is produced in the centre of the galaxy outshining the embedded stars. Therefore, these galaxies are referred as Active Galactic Nuclei (AGN).

AGNs count among the brightest objects in the universe ($L \sim 10^{47}$ erg/s) and their emission can vary on a time scale of days, which leads to a size estimate for the central region smaller than 3×10^{15} cm (1 light-day). Based on these estimates, the mechanism responsible for the production of the energy is of gravitational and not of thermo-nuclear nature[1]. Therefore, the current models of AGN consider a supermassive black hole (SMBH) in the centre of the galaxies surrounded by an accretion disk feeding the black hole (BH) with in falling material from the host galaxy. During the accretion process bi-polar, highly collimated relativistic outflow are formed, the so-called jets.

Besides their historical classification into Seyfert galaxies and quasars, AGNs are classified, based on their radio emission into radio-loud and radio-quiet quasars. An AGN is considered as radio-loud if the ratio between radio flux density measured at 5 GHz and optical flux at 4400 Å (6.8×10^{14} Hz) is larger than 10 (Kellermann et al. 1989).

A radio-loud quasar is called blazar (blazing quasi-stellar object) and represents the most powerful type of AGN. Seyfert galaxies are classified as radio-quiet AGNs, with a

[1] Nuclear fusion has an efficiency of 0.8%, whereas the accretion of matter can reach 29%.

sub-division based on the presence (type 1) or absence (type 2) of broad emission lines.

Additionally, there is a morphological classification, introduced by Fanaroff & Riley (1974) for radio-loud AGN into Fanaroff and Riley type I (FR I) and FR II sources. FRI sources show bight features in their centre and the radio flux decreases with distance, whereas FR II sources show bright radio lobes at the end of the jets.

The standard model of AGN assumes that observed properties and different subclasses of AGNs arise from the orientation of the object, i.e., the angle between the object and our line of sight (Antonucci 1993) (see Fig. 1.1).

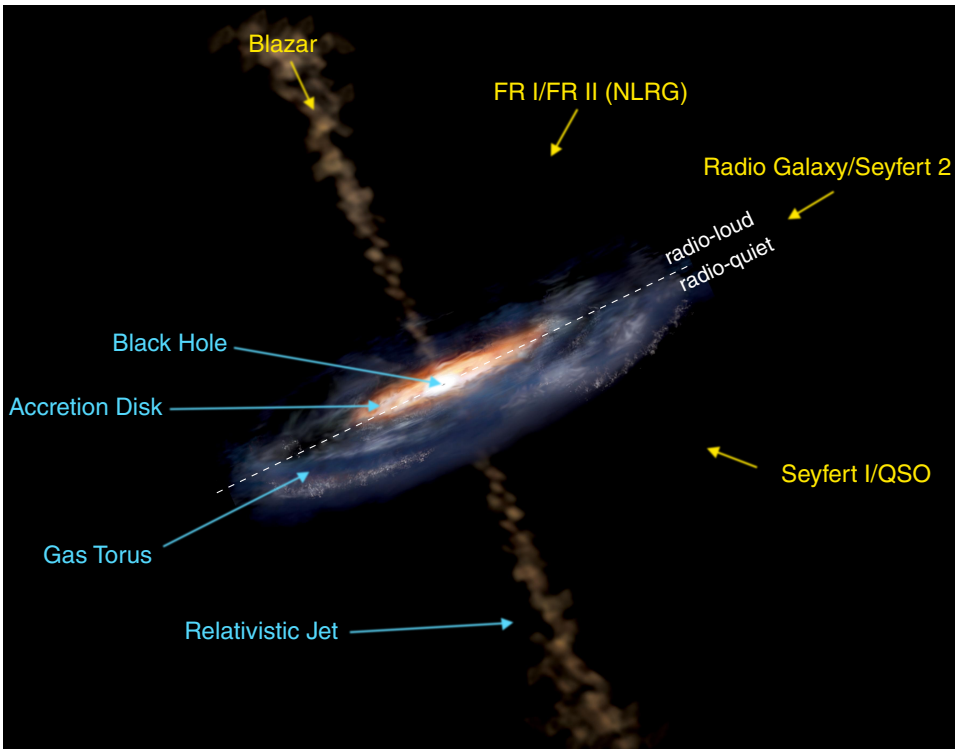

Figure 1.1: Illustration of the viewing angle dependent standard model of AGN. *Image produced by Aurore Simonnet, Sonoma State University.*

1.1.1 Formation and stability of jets

The process behind the formation of relativistic jets is still not well understood. It is generally believed that jets are launched by relativistic magneto-hydrodynamic (RMHD) processes . The origin of these magnetic fields could be i) in the accretion disk (Blandford & Payne 1982) or ii) in the ergosphere of the black hole (Blandford & Znajek 1977). 3D Numerical simulations of jet formation including general relativistic effects showed that faster jets are produced if the magnetic field is anchored in the ergosphere of a black hole as if the jet is launched for the accretion disk. The acceleration of the outflow depends also on the type of the BH, non-rotating (Schwarzschild BH) or rotating (Kerr BH), in the latter case, larger bulk Lorentz factors could be obtained (see Fig. 1.2). However, there

is still a discrepancy between the bulk Lorentz factors of the flow produced in GRMHD simulations and the observed ones (Meier et al. 2001).

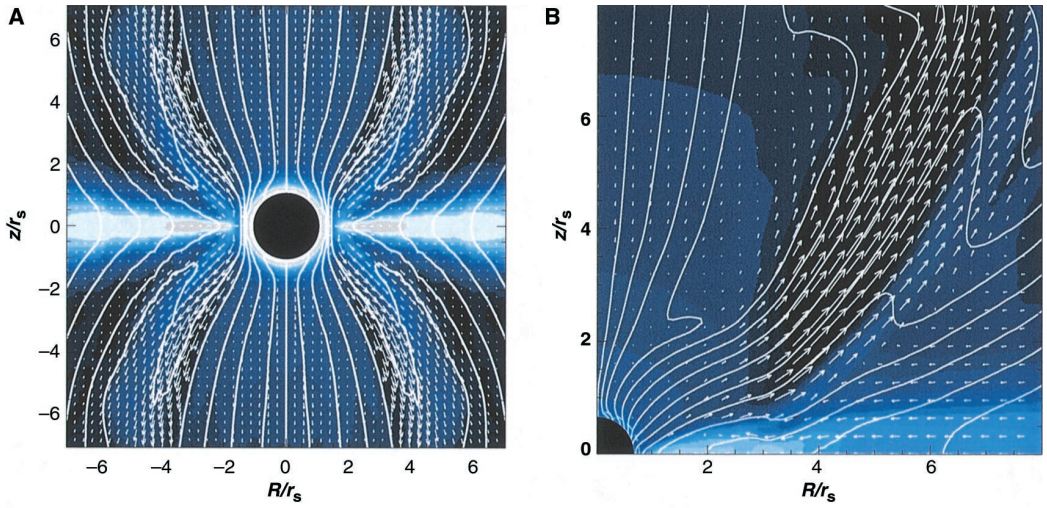

Figure 1.2: GRMHD simulation of jet launching. The color-scale corresponds to the rest-mass density, arrows velocity vectors and the white lines to the magnetic field. Panel A shows the formation of jet from a Schwarzschild BH with escape velocity of 0.4 c and panel B for a Kerr-BH ($j = 0.95$) where an escape velocity of 0.93 c is obtained for the jet. Taken from Meier et al. (2001).

Besides the issue of the launching of the jets, there is the question of their stability. The jets emerging from black holes are subject of several plasma instabilities such as current driven (CD) instability while the jet is magnetically dominated and Kelvin-Helmholtz (KH) instability if the jet is particle dominated. Both types of instabilities should lead to disruption and de-collimation of the jet (see review articles by, e.g., Hardee 2008; Perucho 2012). However, AGN jets are observed well collimated from parsec- to kilo parsec scales. There are several processes which could reduce the impact of the instabilities such as magnetic fields in the case of CD instability and tick shear layers or surrounding winds in case KH instability (Perucho 2012). The stabilising impact of a surrounding wind is presented in Fig. 1.3. The absence of a surround wind leads to the development of KH instability (top panel) and the presence of a wind clearly damps the development of KH instability (bottom panel).

1.1.2 Emission

The radiation observed from AGN is in general understood as non-thermal emission produced by relativistic charged particles. There are two main radiation processes, synchrotron and inverse Compton emission. The Synchrotron emission typically observed for AGNs in the frequency range of 10^5 Hz $< \nu < 10^{16}$ Hz is produced by charged particles accelerated in a magnetic field (see, e.g., Pacholczyk 1970). The total emitted radiation of a single electron is:

$$P_{\text{sync}} = \frac{4}{3}\sigma_T c \beta^2 \gamma^2 U_B, \tag{1.1}$$

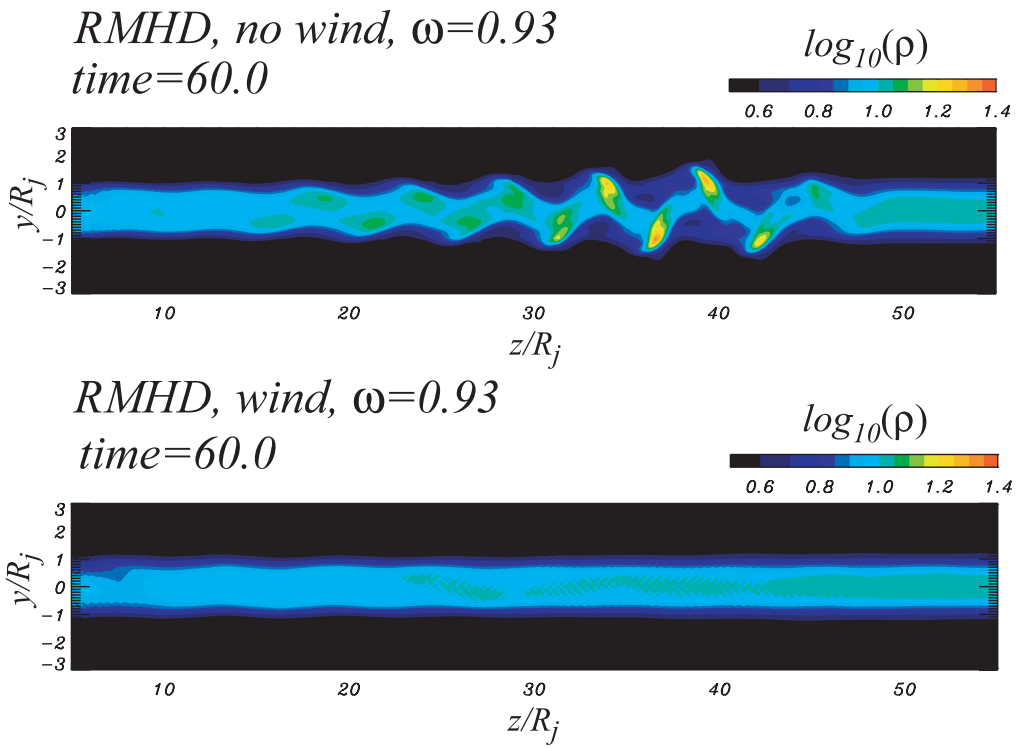

Figure 1.3: 2D distribution of the rest-mass density from an RMHD simulation without surrounding wind (top) and with surrounding wind (bottom). Taken from Hardee (2008).

where $\sigma_T = 8\pi r_e^2/3$ is the Thompson cross section, $r_e = e^2/(m_e c^2)$ is the classical electron radius and $U_B = B^2/8\pi$ is the magnetic field energy density. If proton synchrotron is considered, an increase in the Lorentz factor around 3×10^6 is required to produce the same power as for an electron due to the larger mass of the proton ($m_p = 1836 m_e$). More details about synchrotron radiation are presented in Sect. 2.2.

The high frequency emission ($10^{16}\,\mathrm{Hz} < \nu < 10^{26}$) is produced by inverse Compton scattering. In this process, the photon gains energy during the collision with a relativistic electron. During this collision, a low energy photon (radio photon) is up scattered to high energy photon (X- or γ-ray photon). The inverse Compton scattering can be divided into to two classes deepening on the origin of the seed photons. If the seed photons are produced by synchrotron radiation the process is referred as synchrotron-self Compton (SSC) or as external Compton (EC) if photon field is of external origin for instance from the broadline region or from the cosmic microwave background. The total power for inverse Compton scattering can be written as (see, e.g., Pacholczyk 1970):

$$P_{\mathrm{Comp}} = \frac{4}{3}\sigma_T c \beta^2 \gamma^2 U_{\mathrm{ph}}, \tag{1.2}$$

where U_{ph} is the energy density of the seed photon field.

1.2 The blazar CTA 102

1.2.1 Characteristics

We selected for our studies the blazar CTA 102[2](4C 11.69, B2230+114, J2232+1143). The source is located at a redshift of $z = 1.037$ (Hewitt & Burbidge 1989) and is classified as a highly polarized quasar (HPQ) with a linear optical polarization above 3% (Véron-Cetty & Véron 2003). Using a cosmology with $\Omega_m = 0.27$, $\Omega_\Lambda = 0.73$ and $H_0 = 71\,\mathrm{km\,s^{-1}\,Mpc^{-1}}$ together with $z = 1.037$, a luminosity distance of $D_L = 6942\,\mathrm{Mpc}$ is obtained for CTA 102. This results in a linear scale of $8.11\,\mathrm{pc\,mas^{-1}}$ or $26.45\,\mathrm{ly\,mas^{-1}}$ for CTA 102 (z=1.037). With these conventions, a proper motion of $1\,\mathrm{mas\,yr^{-1}}$ corresponds to an apparent speed of 52.9 c.

1.2.2 Observational history

The source was observed for the first time by Harris & Roberts (1960) and Kardashev (1964) reported on possible signals from an extraterrestrial civilization coming from CTA 102. Sholomitskii (1965) found the first variation in flux density for a radio source. Later observations identified CTA 102 as a quasar.

Since that time CTA 102 has been the target of numerous observations at different wavelengths. In addition to the variations in the radio flux density, CTA 102 also shows brightness variations in the optical band. Pica et al. (1988) reported a variation range of 1.14 mag around an average value of 17.66 mag in 14 years, and an increase of 1.04 mag within two days in 1978, which is so far the most significant outburst. CTA 102 has been monitored since 1986 within the cm-observations of the Metsähovi telescope. The strongest radio flare since the beginning of the monitoring took place around 1997, and a nearly simultaneous outburst in the optical R-band was observed with the Nordic Optical Telescope on La Palma (Tornikoski et al. 1999).

The source has been detected in the γ-ray regime by the telescopes *CGRO*/EGRET and *Fermi*/LAT with a luminosity, $L_\gamma = 5 \times 10^{47}$erg/s, defining CTA 102 as a γ-bright source (Nolan et al. 1993; Abdo et al. 2009). The spectral energy distribution (SED) of CTA 102 is presented in Fig. 1.4.

1.2.3 CTA 102 flux density monitoring

CTA 102 is one of the targets of several single dish monitoring programs. The source is observed since 1975 at 4.8 GHz, 8.0 GHz and 14.5 GHz within the long term monitoring program at the University of Michigan (Aller et al. 1981). At higher frequencies, 22 GHz, 37 GHz and partially 86 GHz, CTA 102 is monitored with the Metsähovi Radio Telescope (Terasranta et al. 1992). Within the F-GAMMA (Fermi-GST AGN Multifrequency Monitoring Alliance) program CTA 102 is observed on a monthly basis from 2 GHz to 140 GHz (Fuhrmann et al. 2007). The Sub-Millimetre Array (SMA) can observe the source at 230 GHz and 345 GHz, which presents the highest frequency monitor-

[2]CTA is the Caltech catalog of sources by Harris & Roberts (1960), as it is said in note to the table, the source was not previously catalogued (NPC) at the 3rd Cambridge catalog, and therefore took a CTA, being CT for Caltech and A for the first catalog published by this observatory.

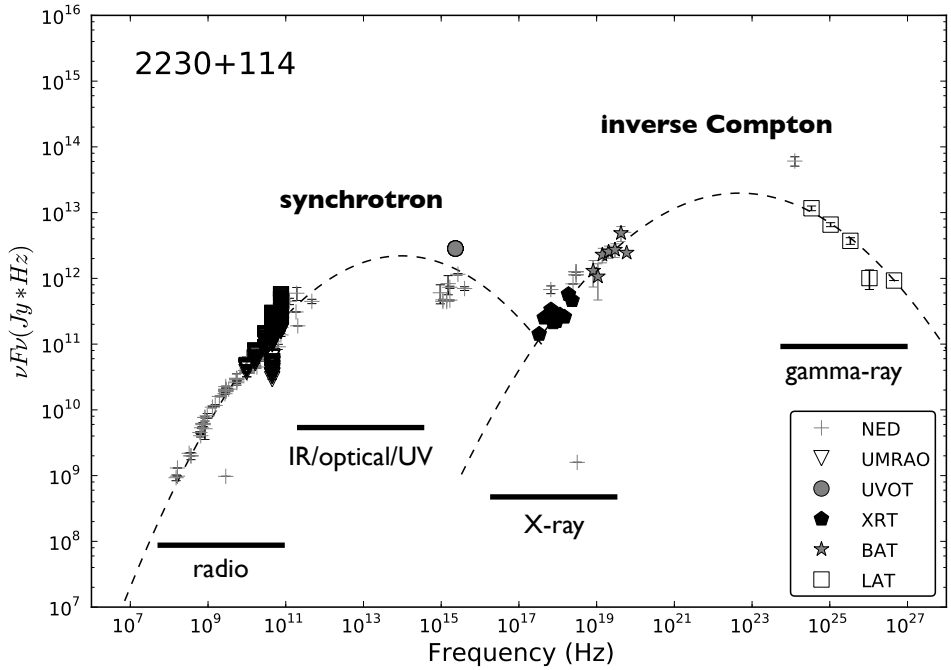

Figure 1.4: Spectral energy distribution (SED) for CTA 102 with indicated emission processes and frequency bands, taken from Chang (2010). The dashed lines correspond to a polynomial fit.

ing. These monitoring programs provide an excellent data set for the study of the flaring behaviour of AGNs (see Chapter 3).

1.2.4 CTA 102 radio structure from kiloparsec to parsec scales

In the 1980s, observations taken with the Multi-Element Radio Linked Interferometer Network (MERLIN) and Very Large Array (VLA) revealed the kpc-scale structure of CTA 102, which consists of a central core and two faint lobes (see Fig. 1.5) (Spencer et al. 1989) (see Fig. 1.5). The brighter lobe has a flux density of 170 mJy at a distance of 1.6 arcsec from the core at position angle (P. A.) of 143° (measured from north through east). The other lobe, with a flux density of 75 mJy, is located 1 arcsec from the center at P. A. −43°. The spectral indices, α, defined as $S \propto \nu^{+\alpha}$, between 2 GHz and 5 GHz of the lobes are −0.7 for the bright and −0.3 for the other one.

High-resolution VLBI observations at 1.4 GHz and 5 GHz resolved the central object into three components and a diffuse tail bending to the southeast. These observations provide and upper limit around 10 c (0.5 mas/yr) for the superluminal motion of the components (Bååth 1988; Wehrle & Cohen 1989). Several observations at different frequencies (for example at 326 MHz) confirmed the elongation of the source to the southeast (Altschuler et al. 1995).

The source was observed within the Radio Reference Frame Image Database five times at 8 GHz between 1994 and 1998 (Piner et al. 2007). The authors report apparent jet velocities from (−7 ± 14) c up to (24 ± 29) c (see Sect. 2.3 on the phenomenon of su-

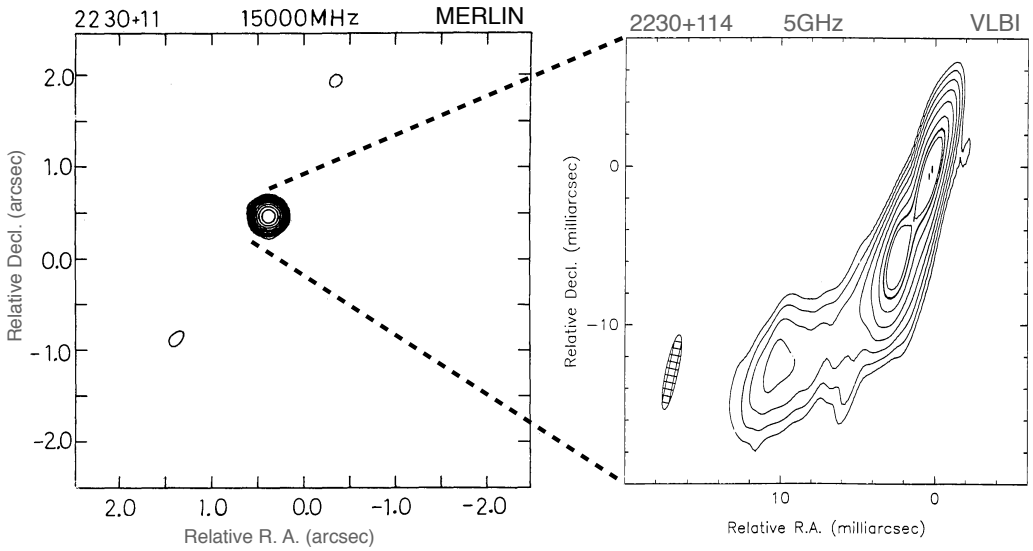

Figure 1.5: Radio images of CTA 102. The left panel shows the 15 GHz MERLIN observation and right panel the 5 GHz VLA observations of CTA 102. Taken from Spencer et al. (1989) and Wehrle & Cohen (1989).

perluminal motions). Higher quality images have been obtained within the 15 GHz VLBI observations within the VLBA 2 cm-Survey (e.g., Zensus et al. 2002) and its successor, the Monitoring of Jets in Active galactic nuclei with VLBA Experiments (MOJAVE) program [3] program (Lister et al. 2009a). Those results show an extended jet region towards the south-east spanning a distance up to 25 mas (de-projected 4.5 kpc using a viewing angle of 2.6° (Jorstad et al. 2005b)). This region contains several kinks and a kinematic analysis yields apparent speeds between (-3 ± 1) c and (19 ± 1) c. The negative apparent speed could be an projection effect in a highly curved jet, the blending of two unresolved components or the feature corresponds to pattern which is actually moving inwards (Lister et al. 2009b).

The structure and kinematics of the innermost jet region between March 1998 and April 2001 is revealed by the 43 GHz VLBA observations of CTA 102 within the Boston University monitoring program[4]. These observations show two stationary features, one close to the core ($r \approx 0.1 - 0.2$ mas) and the other further downstream at $r \approx 2$ mas. Furthermore, two newly ejected features ($t_{ej} = 1997.9 \pm 0.2$ and $t_{ej} = 1999.5 \pm 0.1$) which are separating from the core split into two components further downstream. The flux density associated to these moving features outshine the core for a short time in both total and polarized intensity (Jorstad et al. 2005b). The component ejected at $t_{ej} = 1997.9 \pm 0.2$ was connected to the 1997 flare in CTA 102 (Savolainen et al. 2002). Jorstad et al. (2005a) and Hovatta et al. (2009) computed Lorentz factors, Γ, of 17 and 15, respectively, and Doppler factors, δ, between 15 and 22 associated to this ejection.

The parsec-scale structure of CTA 102 as seen with the VLBA at different frequencies from 5 GHz to 86 GHz observed on the 19th of May 2005 is presented in Fig. 1.6

[3] http://www.physics.purdue.edu/MOJAVE
[4] http://www.bu.edu/blazars/research.html

(produced from the observations presented in this work). The observing frequency is indicated in the top left corner and the convolving beam size in the bottom right corner of each panel. The colour scale corresponds to the flux density in Jansky and the lowest contour is drawn at 5% of the off-source rms and increase in steps of 2.

1.2.5 Multi-frequency VLBI observations

During 2006 the MOJAVE program carried out 12 epochs of multi-frequency observations (8.1 GHz, 8.4 GHz, 12.8 GHz, and 15 GHz). These observations were used to i) address the opacity in the core region (Pushkarev et al. 2012), and ii) the Faraday rotation of the polarisation, i.e., the rotation of the electric field position angle (EVPA) (Hovatta et al. 2012).

Pushkarev et al. (2012) used the core-shift i.e., the correction for the frequency dependent position of the core, to estimate for the magnetic field at the core. For this analysis, the assumed that the jet is in equipartition ($k_r = 1$) and that the jet is of conical geometry. Given these assumptions, the magnetic field at the 15 GHz core is computed to be 0.05 G and is located 46.7 pc from the black hole.

The analysis of the multi-frequency EVPAs showed for CTA 102 at a distance of $r \sim 6$ mas a transversal gradient in the rotation measure. Such a gradient could be regarded as an indication for a dominant toroidal magnetic field (Hovatta et al. 2012).

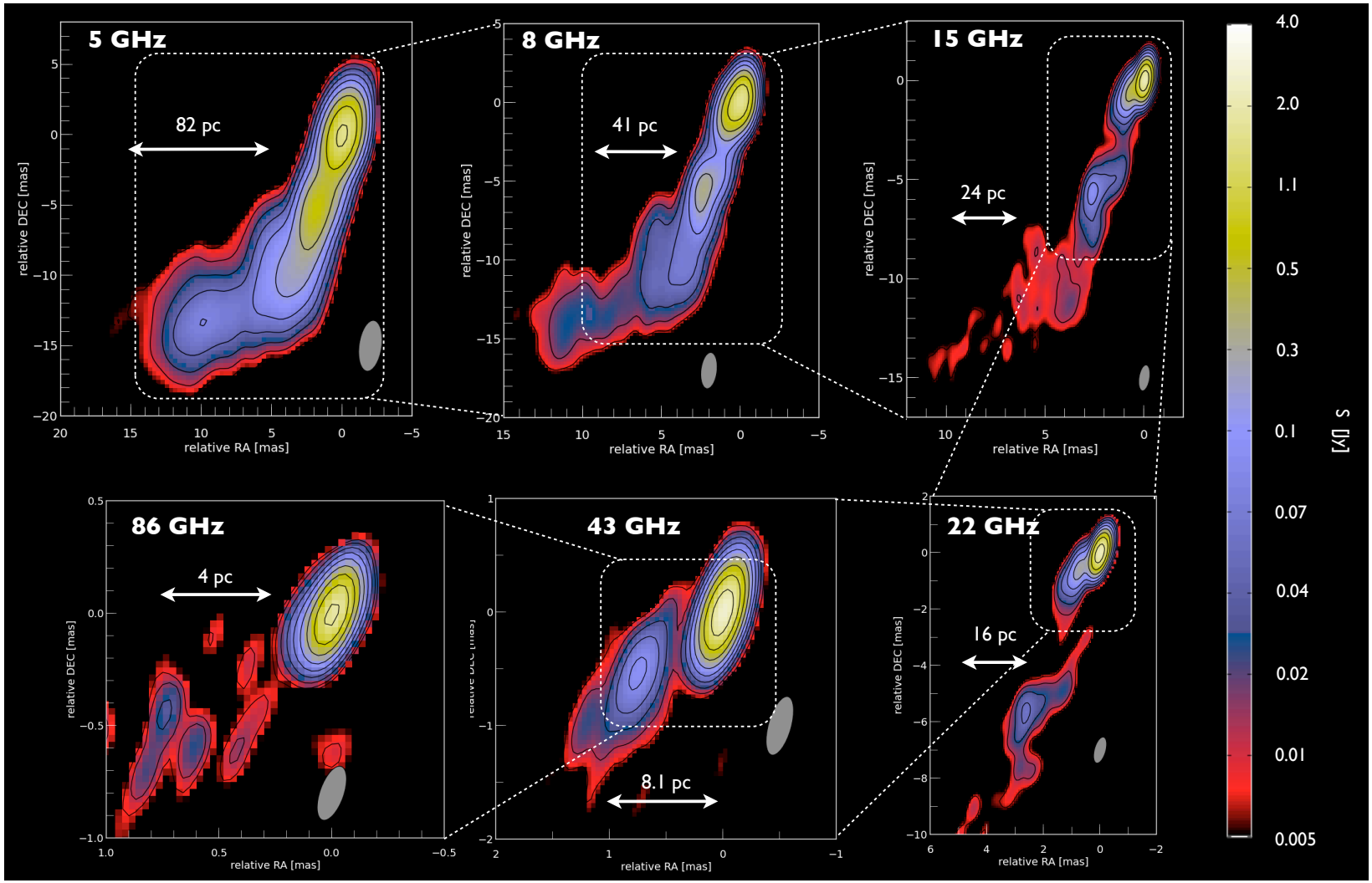

Figure 1.6: Multi-frequency VLBA images of CTA 102 for the May 2005 observations presented in this work. The observing frequency is plotted in the top left corner and the convolving beam size in the bottom right corner. The colour scale corresponds to the flux density in Jansky and the scale indicates the distance in parsec. The lowest contour is drawn at 5% of the off-source rms and additional contours increase in steps of 2.

2 Theory

This Chapter is partially published in Fromm et al. 2011, Fromm et al. 2012 and Fromm et al. in preparation

2.1 Relativistic Hydrodynamics

Since jets are collimated flows of relativistic particles, it is necessary to introduce the basic concepts of relativistic hydrodynamics. We will study the jet evolution far from the formation region. Thus, we use the equations of special-relativistic hydrodynamics. The two basic equations in special relativistic hydrodynamics are the conservation of mass and the energy-momentum. These two conservation laws can be written in the following form:

$$\partial_\mu (\rho u^\mu) = 0 \tag{2.1}$$

$$\partial_\mu (T^{\mu\nu}) = 0, \tag{2.2}$$

where $\mu, \nu = 0, 1, 2, 3$, ρ is the density, u the four velocity and $T^{\mu\nu}$ is energy-momentum tensor:

$$T^{\mu\nu} = \rho h u^\mu u^\nu + p g^{\mu\nu}, \tag{2.3}$$

with p the pressure, $g^{\mu\nu}$ the metric tensor (here Minkowski space-time) and $h = c^2 + \epsilon + p/\rho$ the specific enthalpy, where ϵ is the specific internal energy. The four-velocity can be written as $u^\mu = \Gamma(t, v^1, v^2, v^3)$ by introducing the Lorentz factor $\Gamma = 1/\sqrt{1 - u^i u_i / c^2}$. The set of equations is closed by the equation of state, i.e., the relation between pressure and density. Throughout this work we use an ideal equation of state:

$$p = (\hat{\gamma} - 1)\rho\epsilon, \tag{2.4}$$

where $\hat{\gamma}$ is the adiabatic index. Some additional parameters which can be helpful in describing the fluid properties are the sound speed, c_s and the Mach number, $M = u/c_s$. Notice that we use a Newtonian definition of the Mach number throughout this work. The relativistic sound speed is given by:

$$c_s = \sqrt{\frac{\hat{\gamma} p}{\rho h}} \tag{2.5}$$

To solve these equations numerically it is necessary to rewrite them in terms of conserved fluxes and recover the physical variables (p, ρ, and v) from conserved ones. For a more

detailed derivation of the RHD equations see, e.g., Martí & Müller (1999); Martí et al. (1997).

The conservation equations (Eq. 2.1 and 2.2) imply that the flux through a the cross-section of the jet is conserved. Thus, for a time independent flow these equations can be written for two arbitrary locations as:

$$\Gamma_0 \rho_0 v_0 R_0^2 = \Gamma_1 \rho_1 v_1 R_1^2 \tag{2.6}$$

$$\Gamma_0^2 h_0 v_0 R_0^2 = \Gamma_1^2 h_1 v_1 R_1^2, \tag{2.7}$$

where we assume a one-dimensional flow and the subscripts 0 and 1 correspond to two different locations along the jet. In the following, we present the application of the RHD equations to extragalactic jets, where we focus on two possible configurations: a) pressure-matched (conical) jets and b) over-pressured (non-conical) jets.

Throughout this work we do not include the magnetic field in the equations, i.e., we take a pure RHD approach, and, when needed, compute the magnetic field from the pressure, p, and assuming that the magnetic energy density is a fraction, ϵ_b of thermal energy density ($\epsilon_b = 1$ corresponds to equipartition between magnetic and thermal energy density):

$$B = \sqrt{\frac{8\pi p \epsilon_b}{\hat{\gamma} - 1}} \tag{2.8}$$

2.1.1 Pressure-matched Jets

The shape of the jet will be conical if there is a transversal pressure match with the ambient medium and if there is a gradient in the ambient pressure. The opening angle, φ, of such a freely expanding jet can be calculated from the Mach number, M_0, and the bulk Lorentz factor, Γ_0, at the jet nozzle (Begelman et al. 1984):

$$\varphi = \arctan\left(\frac{1}{\Gamma_0 M_0}\right) \tag{2.9}$$

In Fig. 2.1 we present the 2D distribution of the logarithm of rest mass density for a conical jet from a RHD simulation (axis are not drawn to scale). The strips at the boundary between jet and ambient medium are Kelvin-Helmholtz (K-H) instabilities, which are generated due to the velocity difference between the two fluids.

In a hot conical jet with constant opening angle, φ, the fluid speed, v, increases with distance from the jet nozzle and the density, ρ, and pressure, p, decrease with distance. This behavior can be seen in Fig.2.2 which shows the variation of the intrinsic parameters along the jet axis. The evolution of these parameters can be directly calculated from Eq. 2.6 and Eq. 2.7 if the conditions at the jet nozzle and $\hat{\gamma}$ are known (see, e.g., Hardee & Eilek 2011).

2.1.2 Over-pressured Jets

In contrast to a conical jet, there is no transversal pressure equilibrium in over-pressured jets. Therefore, the shape of the jet will not be conical and the evolution of the intrinsic parameters is not monotonously de- or increasing. Owing to the supersonic nature of the

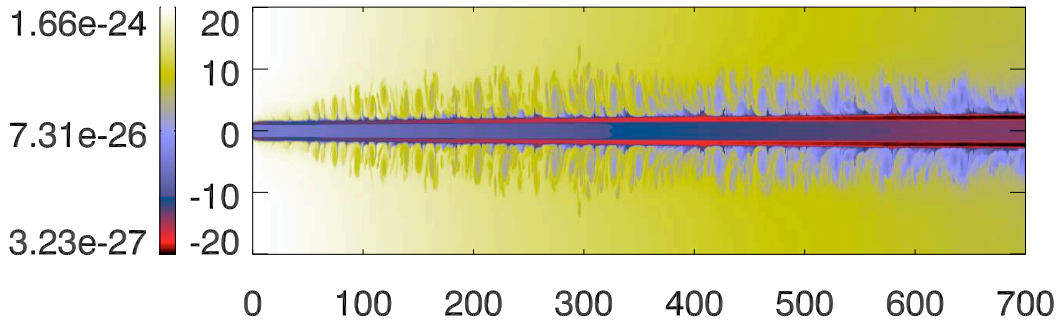

Figure 2.1: 2D distribution of the logarithm of the rest mass density from a RHD simulation of a conical jet.

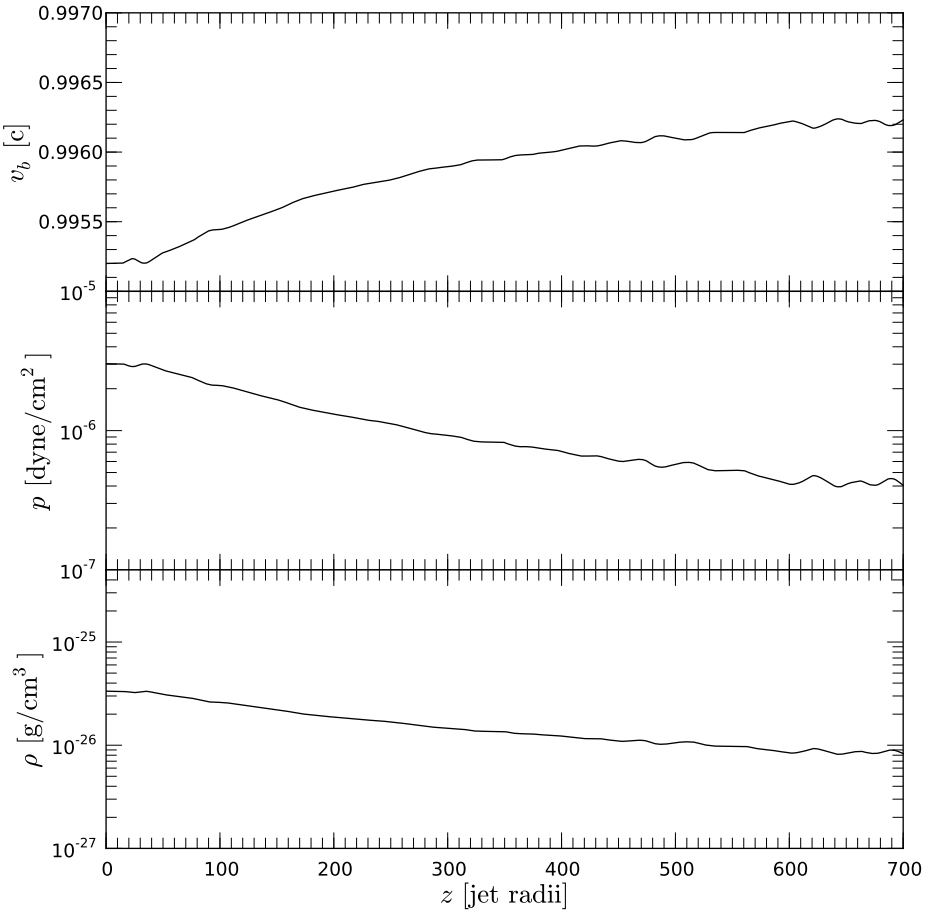

Figure 2.2: Variation of the intrinsic parameters along the jet axis for a conical jet. Top: evolution of velocity in terms of speed of light; Middle: evolution of pressure; Bottom: evolution of density

flow, recollimation or standing shocks will form along the jet.The formation of a standing shock can be described in the following way: The unbalance between the jet pressure

and the pressure of the ambient medium at the jet nozzle leads to an opening of the jet. Due to the conservation laws of hydrodynamics, this opening results in a decrease of the density, the pressure and the magnetic field intensity in the jet. The finite speed of the sound waves in the jet is responsible for an over-expansion followed by a recollimation of the jet that gives rise to the formation of a shock. During this collimation process the jet radius decreases and the shock leads to an increase of the pressure, density, and magnetic field intensity. Again, the finite speed of the sound waves is responsible for a over-collimation of the jet. This interplay between over-expansion and over-collimation leads to the picture of a pinching flow, i.e., a continuous change of the width along the jet axis, in contrast to conical jets. The intrinsic physical parameters (pressure, density, and magnetic field) along a pinching jet show a sequence of local maxima and minima (see, e.g., Daly & Marscher 1988; Falle 1991; Komissarov & Falle 1997; Perucho & Martí 2007; Nalewajko & Sikora 2009).

The equations 2.6 and 2.7 can not be directly used to derive the evolution of the intrinsic parameters. However, some properties of the recollimation shocks can be derived from analytical models. Daly & Marscher (1988) derived the position of the recollimation shock, $L_{\max}$, and the maximum jet width, $R_{\max}$ assuming a homogeneous ambient medium and ultra-relativistic equation of state, i.e., $\hat{\gamma} = 4/3$ (relativistic $e^- e^+$ plasma).

$$L_{\max} \sim 3.3\Gamma_0 R_0 d_k \tag{2.10}$$

$$R_{\max} \sim \left(1 + 1.9\left[\frac{1 - d_k^{-1/4}}{2d_k^{-1/4} - 1}\right]\right) R_0, \tag{2.11}$$

where Γ_0 and R_0 are the bulk Lorentz factor and the jet radius at the jet nozzle and $d_k = p_0/p_{\text{ext}}$ is the pressure ratio between the pressure in the jet and in the ambient medium at the same position. In the case of a homogeneous ambient medium the distance between the recollimation shocks is constant and the jump in the intrinsic values are equal. In this simplified model, each recollimation shock could be regarded as a new jet nozzle.

In a similar way to Daly & Marscher (1988), Komissarov & Falle (1997) derived the properties of a recollimation shock in an ambient medium with decreasing pressure $p_{\text{ext}} = aL^{-\eta}$, using an approximation for the pressure behind the recollimation shock that allows to solve the shock-jump conditions analytically. They derived the following relations for $L_{\max}$, $R_{\max}$, and, $L(R_{\max})$, the location of the maximum jet width and reconfinment angle φ_{conf}

$$L_{\max} = \left[\frac{\varphi\left(1 - \frac{\eta}{2}\right)}{A}\right]^{1/\left(1-\frac{\eta}{2}\right)} \left[1 + \frac{1}{\left(1 - \frac{\eta}{2}\right)} \chi^{1-\frac{\eta}{2}}\right]^{1/\left(1-\frac{\eta}{2}\right)} \tag{2.12}$$

$$L(R_{\max}) = \left(\frac{\varphi}{A}\right)^{1/\left(1-\frac{\eta}{2}\right)} \left(\frac{1 - \frac{\eta}{2}}{2 - \frac{\eta}{2}}\right)^{1/\left(1-\frac{\eta}{2}\right)} \left[1 + \frac{1}{1 - \frac{\eta}{2}} \chi^{1-\frac{\eta}{2}}\right]^{1/\left(1-\frac{\eta}{2}\right)} \tag{2.13}$$

$$R_{\max} = \left[\frac{1 - \frac{\eta}{2}}{2 + \frac{\eta}{2}}\right]^{\frac{4+\eta}{2+\eta}} \frac{R_0}{\chi} \tag{2.14}$$

$$\varphi_{\text{conf}} = \left(1 - \frac{\eta}{2}\right) \varphi \left[1 + \frac{1}{1 + \frac{\eta}{2}} \chi^{1-\frac{\eta}{2}}\right] \tag{2.15}$$

where $A = (a/K)^{1/2}$, with K defined as

$$K = \frac{\mu L u_j}{\pi \varphi^2 \Gamma_j}, \tag{2.16}$$

L being the total kinetic power of the jet. The parameter χ describes the influence of the initial jet radius at the jet nozzle, R_0, and is defined as:

$$\chi = \frac{R_0 A^{1/(1-\frac{\eta}{2})}}{\varphi^{(4+\eta)/(2-\eta)}} \tag{2.17}$$

Fig. 2.3 shows the influence of a gradient in the ambient medium on the shape of the jet and the formation of recollimation shocks. The top panel in Fig. 2.3 shows the distribution of the rest mass density in an ambient medium with decreasing pressure and the bottom panel in a homogeneous ambient medium. The plots show that in the case of a decreasing pressure in the ambient medium the number of recollimation shocks is smaller and their separation is increasing with distance. In addition, the length of the recollimation zone is increasing with distance if there is a gradient in the ambient medium.

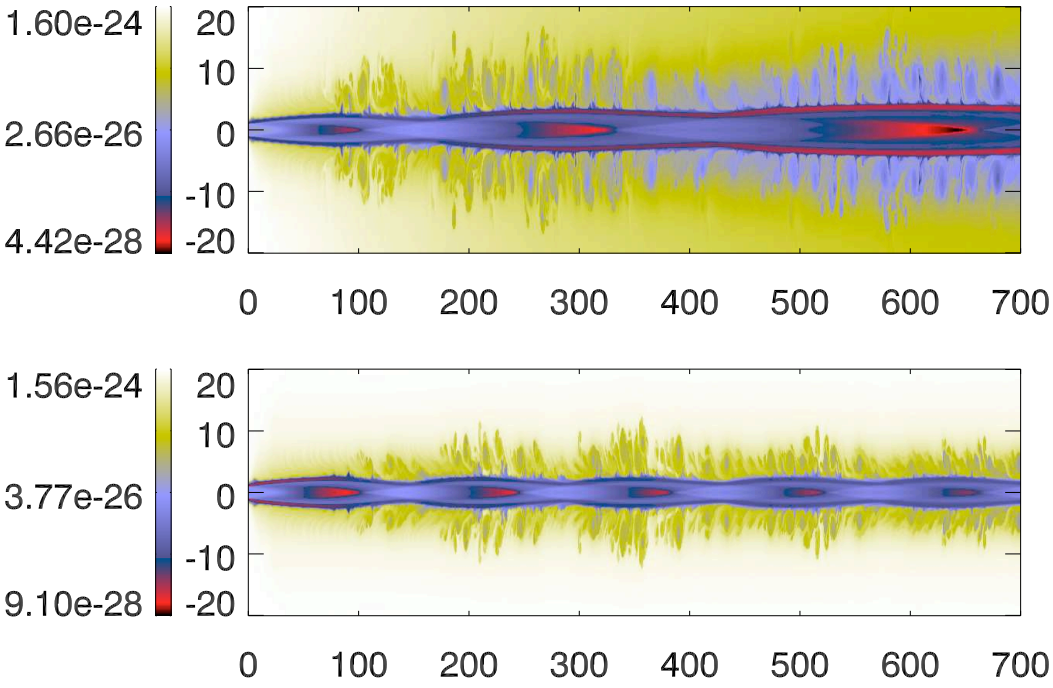

Figure 2.3: 2D distribution of the logarithm of the rest mass density from a RHD simulation of an over-pressured jet. Top: over-pressured jet in decreasing ambient medium; Bottom: over-pressured jet in constant ambient medium

The difference between both cases becomes more visible in the evolution of ρ, p, and v along the jet axis (see Fig. 2.4) The different panels in Fig. 2.4 show the evolution of the velocity (top), the pressure (middle) and rest-mass density (bottom), where the black solid line corresponds to the model with decreasing pressure and the blue solid line to the one with homogeneous ambient medium. As mentioned before, in the case of a

homogeneous ambient medium, the axial values at the location of the recollimation shock are comparable to the values at the jet nozzle. On the other hand, for the decreasing ambient medium, the increase of the intrinsic values at the position of the recollimation shock is decreasing with distance.

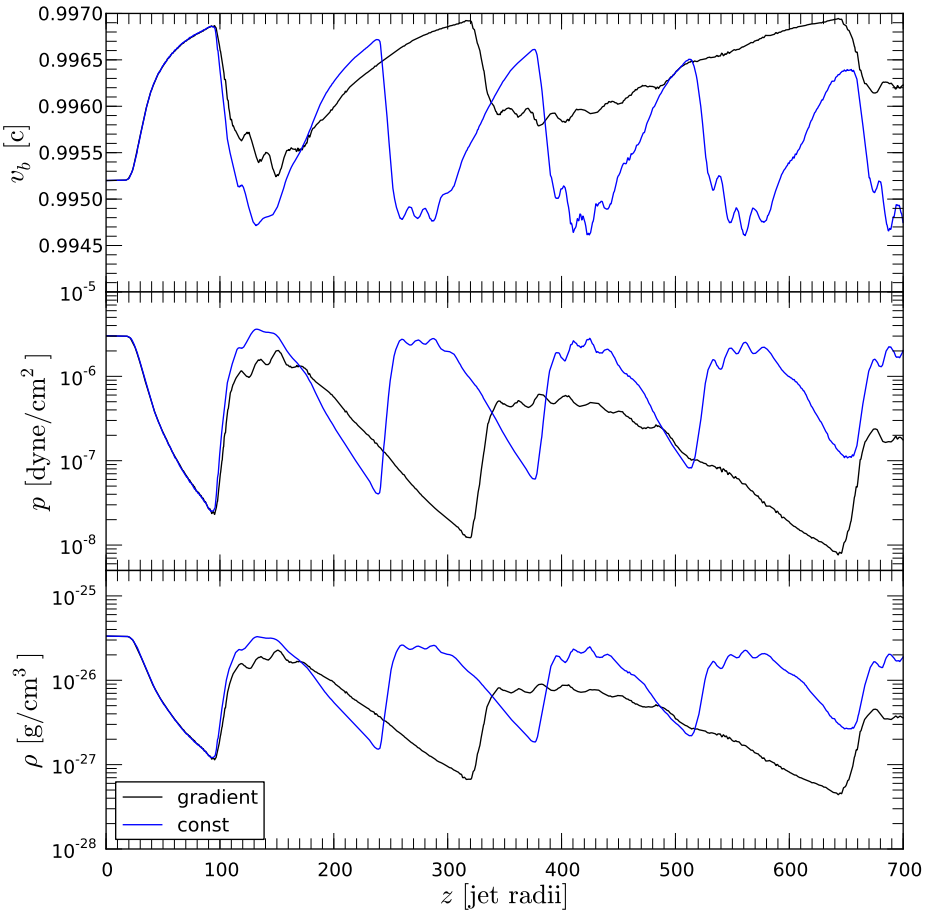

Figure 2.4: Variation of the intrinsic parameters along the jet axis for an over-pressured jet. The black lines correspond to a model with decreasing ambient medium and the red lines to a model with constant ambient medium. Top: evolution of velocity in terms of speed of light; Middle: evolution of pressure; Bottom: evolution of rest-mass density.

2.1.3 Kelvin-Helmholtz (K-H) Instability

Relativistic flows such as jets are affected by several kinds of fluid instabilities (see, e.g., Hardee et al. 1996; Perucho 2012) The most relevant instability in case of relativistic jets are K-H instability, which grow between two flows with non-vanishing relative velocity at the transition layer between the jet and the ambient medium. Fig. 2.5 shows an illustration of the generation of K-H instability.

The development of K-H instability can be explained by the Bernoulli effect. The relative difference in the velocities at the contact surface leads to a drop in the transversal

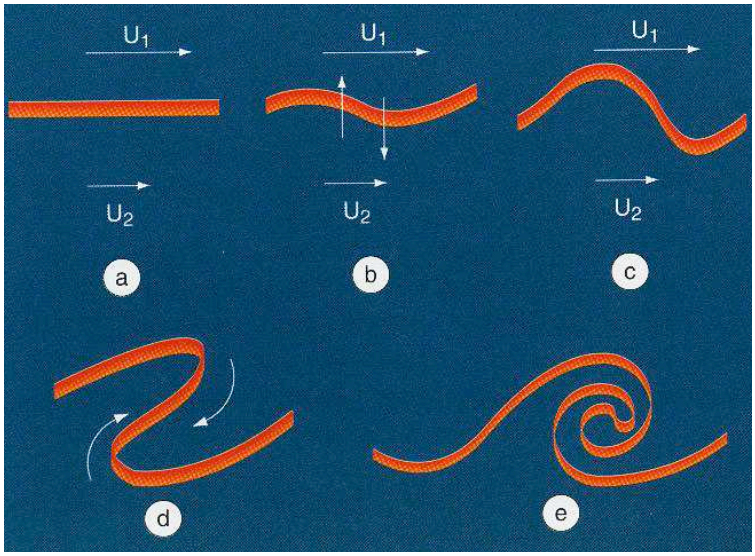

Figure 2.5: Illustration of the growth of K-H instabilities taken from Perucho (2005).

pressure forcing the fluid to increase its transversal velocity. Thus the fluid propagates into other medium, from the jet into ambient medium and viceversa (indicated by b and c in Fig. 2.5). The continuation of this effect leads to a displacement of the fluid and to the mass loading of the jet with material from the ambient medium (see d and e in Fig. 2.5). The mathematical treatment of the instability problem uses the classical perturbation theory, i.e., adding a perturbation term to the initial parameters (e.g. $p = p_0 + p_1$) (see, e.g., Hardee 2000). In general the pressure perturbation, p_1, in cylindrical geometry can be written in the form of $p_1 = \exp(i(kz \pm n\phi - \omega t))$ where k is the longitudinal wavenumber, n the azimuthal wave number, and ω the frequency. The different modes of K-H instabilities can thus be classified by their value of n and k. For example $n = 0$ corresponds to a pinching mode and $n = 1$ to a helical mode. Each mode, n, has a surface and multiple body modes (Perucho 2005).

2.2 Synchrotron Radiation

Here, we review the basic equations of synchrotron self absorption and present the relations needed for the performed spectral analysis (see e.g., Pacholczyk 1970; Marscher 1987; Lobanov 1998; Türler et al. 1999).

The emission, ϵ_ν, and absorption coefficients, κ_ν, of a power law distribution of relativistic electrons, $N(E) = KE^{-s}$, in the presence of a magnetic field, B, where K is the normalization coefficient of the distribution and s the spectral slope, can be written as (see Pacholczyk 1970, for details):

$$\epsilon_\nu = c_\epsilon(s) K (B \sin\varphi)^{(s+1)/2} \nu^{-(s-1)/2} \tag{2.18}$$

$$\kappa_\nu = c_\kappa(s) K (B \sin\varphi)^{(s+2)/2} \nu^{-(s+4)/2}, \tag{2.19}$$

where φ is the pitch angle and ν is the frequency. The constants $c_\epsilon(s)$ and $c_\kappa(s)$ are given by:

$$c_\epsilon(s) = \frac{\sqrt{3}e^3}{16\pi m_e c^2}\left(\frac{3e}{2\pi m_e^3 c^5}\right)^{\frac{s-1}{2}}\left(\frac{s+\frac{7}{3}}{s+1}\right)\hat{\Gamma}\left(\frac{3s-1}{12}\right)\hat{\Gamma}\left(\frac{3s+7}{12}\right) \tag{2.20}$$

$$c_\kappa(s) = \frac{\sqrt{3}\pi}{72}em_e^5c^{10}\left(\frac{3e}{2\pi m_e^3 c^5}\right)^{\frac{s+4}{2}}\left(\frac{s+10}{3}\right)\hat{\Gamma}\left(\frac{3s+2}{12}\right)\hat{\Gamma}\left(\frac{3s+10}{12}\right), \tag{2.21}$$

with e the electron charge, m_e the electron rest-mass, c the speed of light (all in cgs units) and $\hat{\Gamma}$ the complete Euler Gamma-function. For a random magnetic field, the constants above have to be averaged over the pitch angle, i.e., multiplied by $c_{\epsilon,b}$ and $c_{\kappa,b}$, respectively:

$$c_{\epsilon,b}(s) = \frac{\sqrt{\pi}}{2}\hat{\Gamma}\left(\frac{s+5}{4}\right)\left(\hat{\Gamma}\left(\frac{s+7}{4}\right)\right)^{-1} \tag{2.22}$$

$$c_{\kappa,b}(s) = \frac{\sqrt{\pi}}{2}\hat{\Gamma}\left(\frac{s+6}{4}\right)\left(\hat{\Gamma}\left(\frac{s+8}{4}\right)\right)^{-1}. \tag{2.23}$$

The specific intensity, I_ν, can be written as:

$$I_\nu = \frac{\epsilon_\nu}{\kappa_\nu}\left(1-e^{-\tau_\nu}\right), \tag{2.24}$$

where ϵ_ν and κ_ν are the emission and absorption coefficients and $\tau_\nu = \kappa_\nu x$ is the optical depth, with x the distance along the line of sight. Defining ν_1 as the frequency at which $\tau_\nu = 1$, Eq. 2.24 takes the following form (Pacholczyk 1970):

$$I_\nu = I_{\nu_1}\left(\frac{\nu}{\nu_1}\right)^{\alpha_t}\left[1-\exp\left(\frac{\nu}{\nu_1}\right)^{\alpha_0-\alpha_t}\right], \tag{2.25}$$

where α_t is the optically thick spectral index ($\alpha_t = 5/2$ for a homogenous source) and $\alpha_0 < 0$ is the optically thin spectral index. The optically thin spectral index is connected to the spectral slope, s, by the following relation:

$$\alpha_0 = -\frac{(s-1)}{2}. \tag{2.26}$$

Using the transformation from intensities to flux densities, Eq. 2.25 can be expressed in terms of the observed turnover flux density, S_m, and turnover frequency, ν_m (Türler et al. 1999).

$$S_\nu \approx S_m\left(\frac{\nu}{\nu_m}\right)^{\alpha_t}\frac{1-\exp\left(-\tau_m\left(\nu/\nu_m\right)^{\alpha_0-\alpha_t}\right)}{1-\exp\left(-\tau_m\right)}, \tag{2.27}$$

where $\tau_m \approx 3/2\left(\sqrt{1-\frac{8\alpha_0}{3\alpha_t}}-1\right)$ is the optical depth at the turnover. Depending on the value of ν/ν_m, Eq. 2.27 describes an optically thick ($\nu < \nu_m$) or optically thin ($\nu > \nu_m$) spectrum with their characteristic shapes $S_\nu \propto \nu^{5/2}$ and $S_\nu \propto \nu^{-(s-1)/2}$, respectively. In Fig. 2.6 we present an example of a synchrotron spectrum computed from Eq. 2.27.

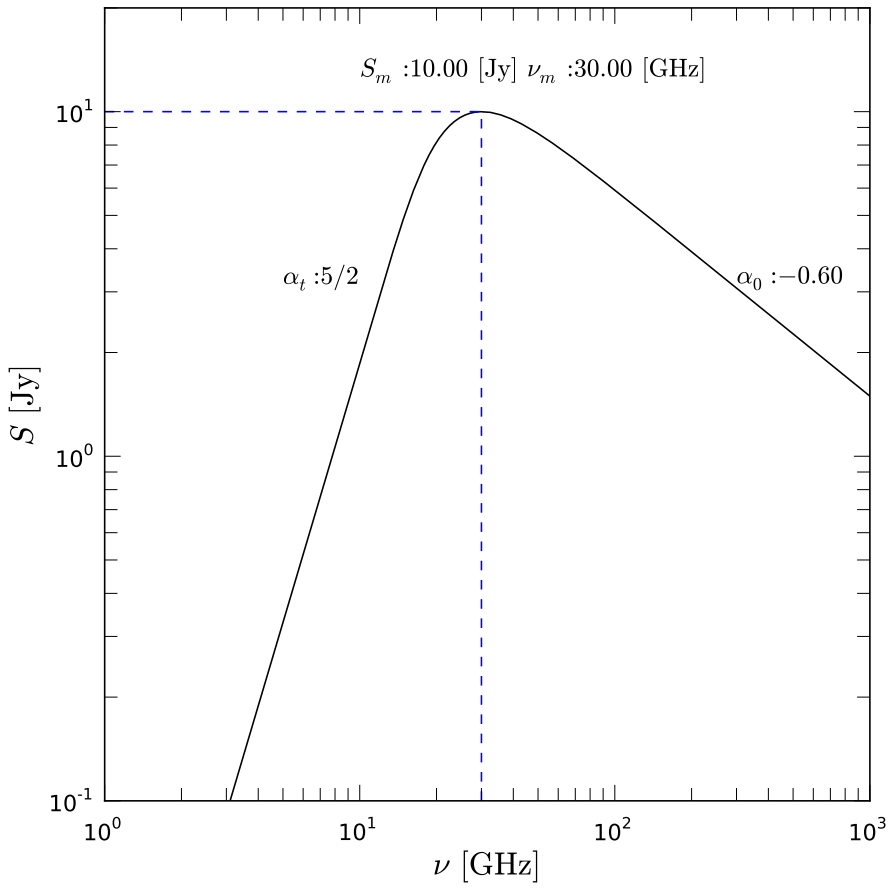

Figure 2.6: Synchrotron spectrum with a turnover position at $\nu_m = 30\,\mathrm{GHz}$ and $S_m = 10\,\mathrm{Jy}$ and an optically thin spectral index of $\alpha_0 = -0.6$

2.2.1 Magnetic field, B, and particle density, K

Once the turnover frequency, ν_m, and the turnover flux density, S_m, are obtained, we can derive estimates for the magnetic field, B, and the normalization coefficient, K, (see, e.g., Marscher 1987). Following Lind & Blandford (1985), the emission, ϵ_ν, and absorption, κ_ν, coefficient have to be corrected for relativistic and cosmological effects. In the following, primed variables correspond to the observers frame and the equations are derived for a random magnetic field (isotropic pitch angle, φ) with all parameters in cgs units:

$$\epsilon'_{\nu'} = \delta^2 \epsilon_{(\nu'(1+z)/\delta)} \tag{2.28}$$

$$\kappa'_{\nu'} = \delta^{-1} \kappa_{(\nu'(1+z)/\delta)} \tag{2.29}$$

with $\delta = \Gamma^{-1}(1 - \beta\cos\vartheta)^{-1}$ the Doppler factor and z the redshift. The optically thin flux, $S_{\nu',\mathrm{thin}} = \Omega\epsilon'_\nu R$, is given by:

$$S_{\nu',\mathrm{thin}} = \frac{\pi}{D_l^2} c_\epsilon(s) c_{\epsilon,b}(s) (1+z)^{-\frac{s-3}{2}} R^3 \delta^{\frac{s+5}{2}} K B^{\frac{s+1}{2}} \nu'^{-\frac{s-1}{2}}, \tag{2.30}$$

and the optical depth, τ_ν, is:

$$\tau'_{\nu'} = c_\kappa(s) c_{\kappa,b}(s) (1+z)^{-\frac{s-4}{2}} R\delta^{\frac{s+4}{2}} K B^{\frac{s+2}{2}} \nu'^{-\frac{s+4}{2}} \tag{2.31}$$

Using the obtained turnover values, the flux density, S'_ν, in Eq. 2.30 and the frequency, ν', in Eq. 2.31 can be replaced by the turnover flux density, S'_m, and the turnover frequency, ν'_m:

$$S'_m = \pi D_l^{-2} c_\epsilon(s) c_{\epsilon,b}(s) (1+z)^{-\frac{s-3}{2}} R^3 \delta^{\frac{s+5}{2}} K B^{\frac{s+1}{2}} \nu'^{-\frac{s-1}{2}}_m \tag{2.32}$$

$$\tau'_m = c_\kappa(s) c_{\kappa,b}(s) (1+z)^{-\frac{s-4}{2}} R\delta^{\frac{s+4}{2}} K B^{\frac{s+2}{2}} \nu'^{-\frac{s+4}{2}}_m \tag{2.33}$$

The equations above can be solved for the magnetic field, B, and the normalization coefficient, K:

$$B = \frac{\pi^2}{D_l^4} \left[\frac{c_\epsilon(s) c_{\epsilon,b}(s)}{c_\kappa(s) c_{\kappa,b}(s)}\right]^2 (1+z)^7 R^4 \delta \nu'^5_m S'^{-2}_m \tau'^2_m \tag{2.34}$$

$$K = \frac{D_l^{2s+4}}{(\pi)^{s+2}} \left[c_\epsilon(s) c_{\epsilon,b}(s)\right]^{-(s+2)} \left[c_\kappa(s) c_{\kappa,b}(s)\right]^{s+1} (1+z)^{-(3s+5)} R^{-(2s+5)} \delta^{-(s+3)} \tau'^{-(s+1)}_m S'^{s+2}_m \nu'^{-(2s+3)}_m. \tag{2.35}$$

Number of particles, N, relativistic energy density, U_e, and magnetization σ

The number of particles, N, and the relativistic energy density, U_e, can be calculated by integrating the distribution function $N(E) = KE^{-s}$ within the limits $E_1 = \gamma_{\min} m_e c^2$ and $E_2 = \gamma_{\max} m_e c^2$, where $\gamma_{\min,\max}$ are the lower and upper electron Lorentz factors:

$$N = \frac{K}{s-1} \left(m_e c^2\right)^{1-s} \gamma_{\min}^{1-s} \left[1 - \left(\frac{\gamma_{\max}}{\gamma_{\min}}\right)^{1-s}\right] \tag{2.36}$$

$$U_e = \begin{cases} \frac{K}{2-s} \left(m_e c^2\right)^{2-s} \gamma_{\max}^{2-s} \left[1 - \left(\frac{\gamma_{\min}}{\gamma_{\max}}\right)^{2-s}\right] & \text{if } 1 < s < 2 \\ K \ln\left(\frac{\gamma_{\max}}{\gamma_{\min}}\right) & \text{if } s = 2 \\ \frac{K}{s-2} \left(m_e c^2\right)^{2-s} \gamma_{\min}^{2-s} \left[1 - \left(\frac{\gamma_{\max}}{\gamma_{\min}}\right)^{2-s}\right] & \text{if } s > 2 \end{cases} \tag{2.37}$$

Together with the magnetic energy density $U_b = B^2/(8\pi)$ we can define the magnetization parameter

$$\sigma_{\mathrm{mag}} = \frac{U_b}{U_e}, \tag{2.38}$$

and can test whether the emitting region is in equipartition, $\sigma_{\mathrm{mag}} = 1$, or not.

Evolution of the electron Lorentz factor

Marscher (1987) pointed out that the energy limits, $E_{\rm min} = \gamma_{\rm min} m_e c^2$ and $E_{\rm max} = \gamma_{\rm min} m_e c^2$ are difficult to extract from observations and require a meaningful set of assumptions. Here we follow the suggestions of Marscher (1987) and present a first order approximation for the evolution of the lower, $\gamma_{\rm min}$, and upper, $\gamma_{\rm max}$ electron Lorentz factor. We consider two different jet geometries, i) a conical pressure matched jet ($d_k = p_0/p_a = 1$) and ii) an over-pressured jet ($d_k \neq 1$). We also assume that Compton losses can be neglected at parsec scale distances (Mimica et al. 2009) and we compute the evolution of the electron Lorentz factor assuming iii) only adiabatic losses and iv) synchrotron and adiabatic losses. In the following section we use an adiabatic index $\hat{\gamma} = 4/3$, which corresponds to a ultra-relativistic $e^- e^+$ plasma.

Since the expansion of the jet implies the adiabatic energy losses, the first step for both jet models includes the calculation of the jet profile.

Conical jet: In the case of a pressure matched jet, the profile will be of conical shape and it is characterized by its radius at the jet nozzle, R_0, and its opening angle φ. The opening angle, φ, can be obtained either from the measured bulk Lorentz factor $\varphi \sim 1/\Gamma$ (e.g., Konigl 1981), or from the transversal size of the jet (e.g., Pushkarev et al. 2009). The jet width at the nozzle, R_0, can be calculated in the following way:

$$R_0 = R_j - r_{j-0} \tan \varphi, \tag{2.39}$$

with R_j the jet width obtained at a position r_j, where the jet can be transversally resolved and r_{j-0} is the distance to the jet nozzle including the opacity shift correction (see Sect. 2.46). Finally the jet width for a conical geometry can be written as power law:

$$R(r) = R_0 \left(\frac{r}{r_0} \right)^{\epsilon}, \tag{2.40}$$

where $\epsilon = 1$ and r_0 is a normalization distance.

Overpressured jet: The initial over-pressure at the jet nozzle leads to the formation of recollimation shocks further downstream (e.g., Daly & Marscher 1988). Such stationary features can be detected and identified using VLBI observations. For the calculation of the jet width at the nozzle we use the approximation presented by Daly & Marscher (1988):

$$R_0 \sim \frac{r_{\rm max}}{3.3 \Gamma_0 d_k},$$

where $r_{\rm max}$ is the de-projected distance between the jet nozzle and the recollimation shock, Γ_0 is the bulk Lorentz factor of the fluid and $d_k = p_0/p_{\rm ext}$ is the overpressure. Here we use values obtained at the location of the standing shock which is justified by the fact that the conditions (pressure and density) at the position of the standing shock wave are roughly the same as those at the jet nozzle (a homogeneous ambient medium). If we assume a locally constant ambient medium, the distance between the jet nozzle and the location of maximal jet width is $r(R_{\rm max}) \sim 0.5 \cdot r_{\rm max}$ (Komissarov & Falle 1997). Together with R_0, we can now derive the jet opening index, ϵ, for $r < r(R_{\rm max})$. For $r > (R_{\rm max})$ the jet will

start to collimate and will reach a local minimum at the position of the standing shock. As in the case of the jet opening region we can, given the jet width at the position of the standing shock, compute ϵ for this region. If there are additional recollimation shocks with known distance from the previous shock and jet width, one can proceed as in the case of the first recollimation shock and define the jet geometry.

Adiabatic and synchrotron losses: In order to provide an estimate for the variation of the electron Lorentz factor γ along the jet, we have to solve the energy-loss equation, which includes both, radiative and adiabatic losses (see, e.g., Georganopoulos & Marscher 1998; Mimica et al. 2009)

$$\frac{d\gamma}{dr} = -\left(\frac{d\gamma}{dr}\right)_{\rm syn} - \left(\frac{d\gamma}{dr}\right)_{\rm adi}, \tag{2.41}$$

where γ corresponds to the electron Lorentz factor and r to the distance along the jet. The synchrotron and adiabatic losses are given by (Fromm et al., in prep.):

$$\left(\frac{d\gamma}{dr}\right)_{\rm syn} = \left(\frac{2}{3}\right)^2 \frac{e^4}{m_e^3 c^6}\gamma^2 B^2 \tag{2.42}$$

$$\left(\frac{d\gamma}{dr}\right)_{\rm adi} = \frac{\gamma}{3}\frac{d\ln\rho}{dz} \tag{2.43}$$

If we parametrize the magnetic field, $B = B_0(R/R_0)^{-b}$, and the jet geometry, $R = R_0(r/r_0)^{\epsilon}$, the energy loss equation can be simplified to:

$$\frac{d\gamma}{dr} = -\left(\frac{2}{3}\right)^2 \frac{e^4}{m_e^3 c^6}\gamma^2 B_0^2 \left(\frac{r}{r_0}\right)^{-2\epsilon b} - \frac{\gamma\epsilon}{r} \tag{2.44}$$

This differential equation has the following analytical solution (Fromm et al., in prep.):

$$\gamma(r) = \frac{\gamma_0\left(\epsilon + 2\epsilon b - 1\right) r_0^{\epsilon}}{-C\gamma_0 r r_0^{\epsilon} + r^{\epsilon}\left(\frac{r}{r_0}\right)^{2\epsilon b}\left(\epsilon + 2\epsilon b + C\gamma_0 r_0 - 1\right)}\left(\frac{r}{r_0}\right)^{2\epsilon b}, \tag{2.45}$$

where $C = \left(\frac{2}{3}\right)^2 (e^4)/(m_e^3 c^6) B_0^2$ and $\gamma_0 = \gamma\left(r_0\right)$ corresponds to the initial value.

As an example, we use the values tabulated in Table 2.1 and calculate the evolution of the electron Lorentz factors along the jet. In Fig. 2.7, we show the evolution of the electron Lorentz factor for an over-pressured (left panels) and conical jet (right panels). The x-axis are drawn in pc (bottom) and in mas (top). The panels show (from top to bottom) the evolution of the jet width with distance along the jet, the evolution of the magnetic field and the evolution of the electron Lorentz factor $\gamma_{\rm min,max}$. The red solid and dashed lines in the bottom panels correspond to the variation of the electron Lorentz factor taking synchrotron and adiabatic losses into account and the black solid and dashed lines show the evolution of the electron Lorentz factor assuming only adiabatic losses.

For both jet models, the evolution of the upper electron Lorentz factor, $\gamma_{\rm max}$, decreases fast if the synchrotron losses are taken into account. The adiabatic losses are the dominant

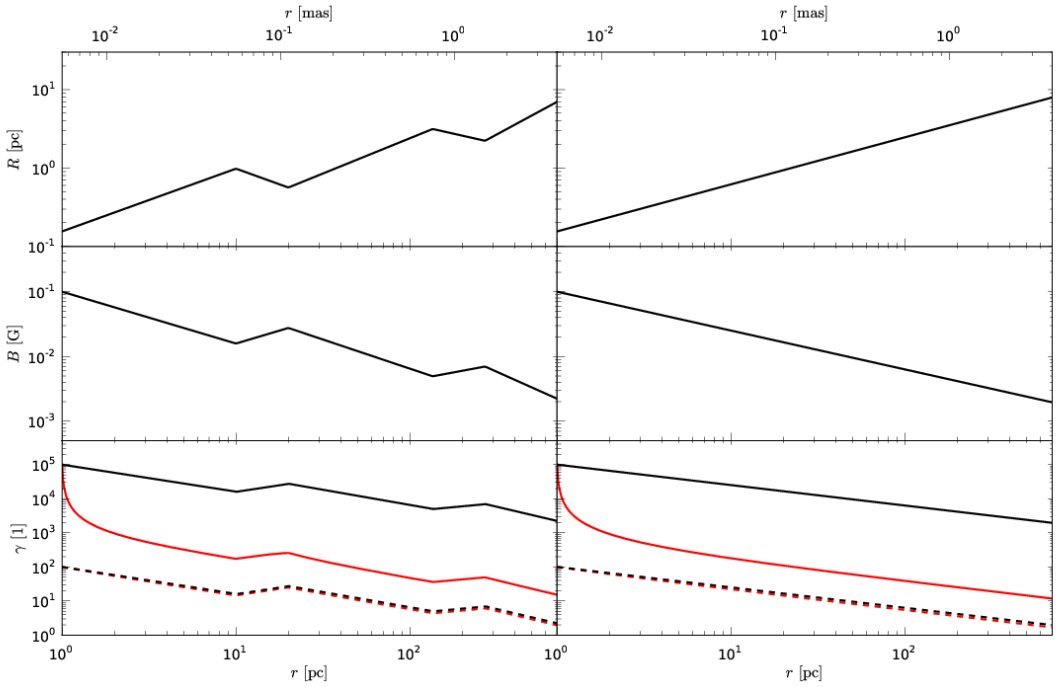

Figure 2.7: Evolution of source intrinsic parameters for an over-pressured jet, $d_k \neq 1$, (left panels) and for a conical jet, $d_k = 1$, (right panels). The upper panels show the variation of the jet width, R, in pc along the jet, the middle panels the evolution of the magnetic field, B, in G, and the bottom panels show the variation of the maximum and minimum electron Lorentz factors, $\gamma_{\mathrm{min,max}}$. The solid and dashed red lines correspond to a model where we take both, synchrotron and adiabatic losses into account. In order to demonstrate the influence of radiative losses we computed additionally the evolution of the electron Lorentz factor only for adiabatic losses (solid and dashed lines in bottom panels).

energy loss mechanism for $r > 3$ pc, which can be deduced from the similar slopes of the solid black and red lines. However, the evolution of the lower electron Lorentz factor, γ_{min}, is hardly affected by synchrotron losses.

The calculations show that in the case of an over-pressured jet, the magnetic field intensity increases at the position of the recollimation shocks (in the plot at $r \sim 20$ pc and $r \sim 270$ pc), and at the same position the electron Lorentz factor increases. This increase of the Lorentz factor corresponds to the local increase of the particle density, i.e., adiabatic compression (see, e.g., Mimica et al. 2009). Farther downstream, the jet expands and the magnetic field and the Lorentz factors decrease again. At the second recollimation shock, there is again a local increase in both, magnetic field and electron Lorentz factor. This behavior is also visible if we assume only adiabatic losses.

In contrast to the over-pressured jet, the evolution of the magnetic field and the elec-

tron Lorentz factor are continuously decreasing in the case of a conical jet (see right panels in Fig. 2.7).

Table 2.1: Parameters used in the calculation of $\gamma_{\rm min}$ and $\gamma_{\rm max}$ presented in Fig. 2.7

Parameter	Symbol	Value	Source
normalization of B-field	B_0	0.1 G	VLBI†
exponent B-Field evolution	b	1.0	VLBI†
normalization distance	r_0	1.0 pc	VLBI†
viewing angle	ϑ	2.6°	VLBI‡
Bulk Lorentz factor	Γ_0	13	VLBI‡
pressure matched jet	d_k	3	VLBI*
jet opening index	ϵ	0.6, 0.8,−0.5,1.2	VLBI†
electron Lorentz factor	$\gamma_{\rm min,max}$	100, $1 \cdot 10^5$	Theory*

‡ taken from Chapter 4
† taken from Chapter 5
* taken from Jorstad et al. (2005b)
* taken from Mimica et al. (2009)

2.2.2 Opacity Variations

Assuming that the position of the observed VLBI core coincides with the ($\tau = 1$)-surface, Marcaide & Shapiro (1983) and Lobanov (1998) used Eq. 2.31 to derive the frequency-dependent position of the core, the so-called core-shift. This core-shift is illustrated in Fig. 2.46 and shows the variation of the distance between the core and an optically thin jet region, whose position is assumed to be frequency independent.

Assuming, a conical jet geometry, i.e., $R \propto r$, a decreasing magnetic field, $B = B_1 r^{-b}$ and a decreasing particle density, $K = K_1 r^{-k}$, where the constants B_1 and K_1 correspond to the magnetic field and electron normalization coefficient at 1 pc, Eq. 2.31 results in:

$$r \propto \nu^{-1/k_r}, \tag{2.46}$$

where $k_r = [2k + 2b\,(3 - 2\alpha_0) - 2] \,/\, (5 - 2\alpha_0)$ and α_0 is the optically thin spectral index.

Measurements of the core-shift can yield estimates of several physical parameters such as the magnetic field and the distance to the central engine (Lobanov 1998; Hirotani 2005; O'Sullivan & Gabuzda 2009; Pushkarev et al. 2012). The core shift measure, $\Omega_{r\nu}$ between two frequencies is defined as:

$$\Omega_{r\nu} = 4.85 \cdot 10^{-9} \frac{\Delta r_{\nu_1,\nu_2} D_L \nu_1^{1/k_r} \nu_2^{1/k_r}}{(1+z)^2 \left(\nu_2^{1/k_r} - \nu_1^{1/k_r}\right)} \,[\mathrm{pc \cdot GHz}], \tag{2.47}$$

with $\Delta r_{\nu_1,\nu_2}$ being the core shift between the frequencies ν_1 and ν_2, in mas, and D_l the luminosity distance, in pc. Following Hirotani (2005) and replacing the jet opening angle φ and the viewing angle ϑ by the more directly measurable apparent speed $\beta_{\rm app}$, the magnetic field at 1 pc is given by:

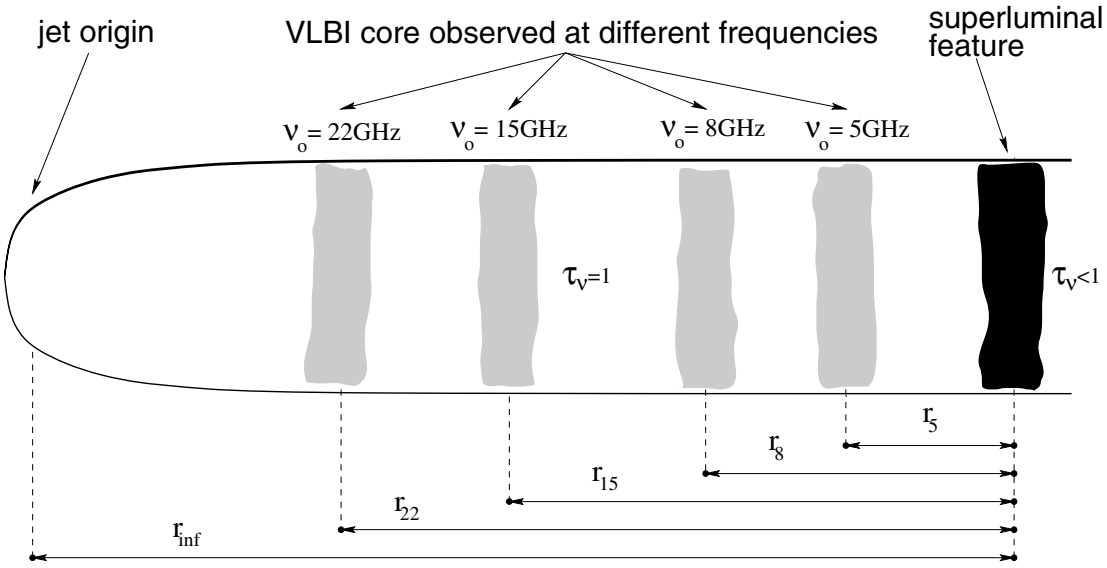

Figure 2.8: Illustration of the frequency dependence of the core position. Taken from Kovalev et al. (2008).

$$B_1 \approx \frac{2\pi m_e^2 c^4}{e^3}\left[\frac{e^2}{m_e c^2}\left(\frac{\Omega_{r\nu}}{r_1\left(1+\beta_{\rm app}^2\right)^{1/2}}\right)^{k_r}\right]^{\frac{5-2\alpha_0}{7-2\alpha_0}} \cdot \left[\pi C\left(\alpha_0\right)\frac{r_1 m_e c^2}{e^2}\right. \\ \left.\frac{-2\alpha_0}{\gamma_{\rm min}^{2\alpha_0+1}} K\left(\gamma,\alpha_0\right)\left(1+\beta_{\rm app}\right)^{\frac{-(1+2\alpha_0)}{4}}(1+z)^{\alpha_0-\frac{3}{2}}\right]^{\frac{-2}{7-2\alpha_0}} \text{[G]}, \tag{2.48}$$

where $C\left(\alpha_0\right)$ and $K\left(\gamma,\alpha_0\right)$ are defined as:

$$C\left(\alpha_0\right) = \frac{3^{1-\alpha_0}}{8}\sqrt{\pi}\hat{\Gamma}\left(\frac{7-2\alpha_0}{4}\right)\hat{\Gamma}\left(\frac{5-6\alpha_0}{12}\right)\hat{\Gamma}\left(\frac{25-6\alpha_0}{12}\right) \\ \hat{\Gamma}\left(\frac{9-2\alpha_0}{4}\right) \tag{2.49}$$

$$K\left(\gamma,\alpha_0\right) = \frac{2\alpha_0+1}{2\alpha_0}\frac{\left[\left(\gamma_{\rm max}/\gamma_{\rm min}\right)^{2\alpha}-1\right]}{\left[\left(\gamma_{\rm max}/\gamma_{\rm min}\right)^{2\alpha+1}-1\right]} \tag{2.50}$$

The distance to the central engine can be calculated by inserting the value for B_1 (Eq. 2.48) into Eq. 2.31 and solving for $r_{\rm core}$:

$$r_{\rm core}(\nu) \approx \Omega_{r\nu}\left(1+\beta_{\rm app}^2\right)^{1/2}\nu^{-1/k_r}\,\text{[pc]} \tag{2.51}$$

The equations above can be simplified if we assume a conical jet, $b = 1$, $k = 2$, equipartition between the magnetic energy density and the kinetic energy density and a spectral index of $\alpha_0 = -0.5$ (which leads to $k_r = 1$, see definition of k_r):

$$B_1 \approx 0.042\Omega_{r\nu}^{3/4}(1+z)^{1/2}\frac{\left(1+\beta_{\rm app}^2\right)^{3/8}}{\beta_{\rm app}^{1/2}}\,[\rm G], \tag{2.52}$$

$$r_{\rm core}(\nu) \approx \Omega_{r\nu}\left(1+\beta_{\rm app}^2\right)^{1/2}\nu^{-1}\,[\rm pc]. \tag{2.53}$$

The particle density N_1 is given by:

$$N_1 = \frac{K(\gamma,\alpha_0)}{8\pi m_e c^2}\gamma_{\rm min}^{-1}B_1^2. \tag{2.54}$$

If we assume $k_r = 1$, $\alpha_0 = -0.5$ and a ratio of 10^3 between the upper and lower electron Lorentz factors, the equation above can be written as:

$$N_1 = 0.47\cdot 10^6\gamma_{\rm min}^{-1}B_1^2. \tag{2.55}$$

If we assume that the jet is in equipartition and has a conical geometry, we can calculate the magnetic field using Eqs. 2.48 - 2.53. In addition, we can derive an estimate for the magnetic field at the core, $B_{\rm core} = B_1 r_{\rm core}^{-1}$ and the relativistic particle density $N_{\rm core} = N_1 r_{\rm core}^{-2}$. These relations are only valid for a conical jet with a dominating toroidal magnetic field. In general the radial evolution of the magnetic field in the jet is given by $B \propto r^{-\epsilon b}$, where ϵ is the jet opening index ($R \propto r^{\epsilon}$) and b parametrizes the evolution of the magnetic field ($B \propto R^{-b}$). For a jet in equipartition the particle density has to decrease as $N \propto R^{-2b}$ or, in terms of distance along the jet $N \propto r^{-2b\epsilon}$ Assuming a conical jet $\epsilon = 1$ and a toroidal magnetic field ($b = 1$) the given relations are obtained.

2.2.3 Shock-in-Jet Model

In the last two Sections we only considered the steady-state conditions of a jet. However, to study the flaring process we need to describe the propagation of a shock wave within the unperturbed flow. The shock-in-jet model of Marscher & Gear (1985) describes the evolution of a traveling shock wave in a steady state jet. During the passage of the shock through a steady jet, the relativistic particles are swept up at the shock front and gain energy while crossing it. In this model, the flaring flux density is assumed to be produced by the accelerated particles within a small layer of width x behind the shock front. The width of this layer is assumed to depend on the dominant cooling process and can be approximated by $x \propto t_{\rm cool}$, where $t_{\rm cool}$ is the typical cooling time.

Evolutionary stages

Compton losses: If the photon energy density, $u_{\rm ph}$, is higher than the magnetic energy density, $u_{\rm b} = B^2/(8\pi)$, the inverse Compton scattering is the dominant energy loss mechanism during the first stage of the flare. The width of the layer behind the shock front during this Compton stage, x_1, is computed to be:

$$x_1 \propto B^{1/2}\nu^{-1/2}\delta^{1/2}u_{\rm ph}^{-1}. \tag{2.56}$$

An approximation of the photon energy density, $u_{\rm ph}$, can be obtained by integrating the emission coefficient, ϵ_ν, over the optically thin regime ($\nu_m < \nu < \nu_{\rm max}$)[1], which leads to:

$$u_{\rm ph} \propto K \left(B^{3s+7} R^{s+5} \right)^{1/8}. \tag{2.57}$$

The final expression for the width of the layer behind the shock front during the Compton stage can be written as:

$$x_1 \propto R^{-(s+5)/8} K^{-1} B^{-3(s+1)/8} \delta^{1/2} \nu^{-1/2} \tag{2.58}$$

Synchrotron losses: Synchrotron losses become more important at the point where the photon energy density, $u_{\rm ph}$, is comparable to the magnetic energy density, $u_{\rm b}$. The width of the layer x_2 in the synchrotron stage can be computed by replacing $u_{\rm ph}$ in Eq. 2.56 with $u_{\rm b} = B^2/(8\pi)$ and is given by:

$$x_2 \propto B^{-3/2} \delta^{1/2} \nu^{-1/2}. \tag{2.59}$$

Adiabatic losses: Radiative losses become less important in the last stage of the shock evolution. During this final stage the losses are dominated by the expansion of the source and the width of the layer, x_3, is consistent with the radius of the jet:

$$x_3 \propto R. \tag{2.60}$$

The evolution of the turnover frequencies $\nu_{m,i}$ and turnover flux densities $S_{m,i}$, where i indicates the different energy loss stages (1=Compton, 2=synchrotron and 3=adiabatic loss stage), can be derived by replacing the expressions for R in Eq. 2.32 and Eq. 2.33 with the expression for x_i, assuming that the enhanced emission is produced within this layer of size, x_i, and dropping the coefficients $c_{\kappa/\epsilon}$:

$$\begin{aligned}
\nu_{m,1} &\propto (1+z)^{-(s+4)/(s+5)} R^{-1/4} B^{1/4} \delta^{(s+3)/(s+5)} && (2.61)\\
S_{m,1} &\propto (1+z)^{(2s+15)/(2s+10)} D_L^{-2} R^{11/8} B^{1/8} \delta^{(3s+10)/(s+5)} && (2.62)\\
\nu_{m,2} &\propto (1+z)^{-(s+4)/(s+5)} \left[K^2 B^{s-1} \delta^{s+3} \right]^{1/(s+5)} && (2.63)\\
S_{m,2} &\propto (1+z)^{(2s+15)/(2s+10)} D_L^{-2} R^2 \left[K^5 B^{2s-5} \delta^{3s+10} \right]^{1/(s+5)} && (2.64)\\
\nu_{m,3} &\propto (1+z)^{-1} \left[RKB^{(s+2)/2} \delta^{(s+2)/2} \right]^{2/(s+4)} && (2.65)\\
S_{m,3} &\propto (1+z) D_L^{-2} \left[R^{2s+13} K^5 B^{2s+3} \delta^{3s+7} \right]^{1/(s+4)} && (2.66)
\end{aligned}$$

Marscher (1990) and Lobanov & Zensus (1999) assumed that the evolution of K, B and δ could be written as a power-law with the jet radius R (notice that in a conical jet the distance along the jet r is linearly proportional to the jet radius R, $r \propto R$, so the proportionality is preserved):

$$K \propto R^{-k} \quad B \propto R^{-b} \quad \delta \propto R^{-d}. \tag{2.67}$$

[1] Marscher & Gear (1985) included only first order Compton scattering

In this case, a relation between the turnover flux density and the turnover frequency can be found:

$$\nu_{m,i} \propto (1+z)^{p_i} R^{n_i} \tag{2.68}$$
$$S_{m,i} \propto D_L^{-2} (1+z)^{q_i} R^{f_i}, \tag{2.69}$$

which leads to:

$$S_{m,i} \propto D_L^{-2} \, (1+z)^{(q_i n_i - p_i f_i)/n_i} \, \nu_{m,i}^{\epsilon_i}, \tag{2.70}$$

where $\epsilon_i = f_i/n_i$. The exponents f_i, n_i, p_i and q_i include the dependence with the physical quantities B, $N(E)$, K, and D and are defined:

$$n_1 = -(b+1)/4 - d(s+3)/(s+5) \tag{2.71}$$
$$n_2 = -[2k + b(s-1) + d(s+3)]/(s+5) \tag{2.72}$$
$$n_3 = -[2(k-1) + (b+d)(s+2)]/(s+4) \tag{2.73}$$
$$f_1 = (11-b)/8 - d(3s+10)/(s+5) \tag{2.74}$$
$$f_2 = 2 - [5k + b(2s-5) + d(3s+10)]/(s+5) \tag{2.75}$$
$$f_3 = [2s + 13 - 5k - b(2s+3) - d(3s+7)]/(s+4) \tag{2.76}$$
$$p_1 = -(s+4)/(s+5) \tag{2.77}$$
$$p_2 = -(s+4)/(s+5) \tag{2.78}$$
$$p_3 = -1 \tag{2.79}$$
$$q_1 = (2s+15)/(2s+10) \tag{2.80}$$
$$q_2 = (2s+15)/(2s+10) \tag{2.81}$$
$$q_3 = 1. \tag{2.82}$$

The typical evolution of a flare in the turnover frequency – turnover flux density ($\nu_m - S_m$) plane can be obtained by inspecting the R-dependence of the turnover frequency, ν_m, and the turnover flux density, S_m. For a typical set of parameters: b=1, $s = 2.5$, $k = 3$ (assuming an adiabatic flow, $k = 2(s+2)/3$, and $d = 0.02$ corresponding to a nearly constant velocity for a fixed viewing angle, these parameters lead to a set of exponents n_i and f_i, which are summarized in Table 2.2.

Table 2.2: Values of the indices used in the generalized spectrum expression of Eq. 2.70, n_i and f_i for $b = 1$, $s = 2.5$, $k = 3$, and $d = 0.02$

stage	n_i	f_i	ϵ
Compton	−0.52	1.2	−2.3
Synchrotron	−1.01	−0.06	0.06
Adiabatic	−1.32	−0.82	0.62

During the first stage, in which Compton losses are dominant, the turnover frequency decreases with radius while the turnover flux density increases. In the second stage, in which synchrotron losses are the dominating energy loss mechanism, the turnover frequency continues to decrease while the turnover flux density remains constant. Both the

turnover frequency and turnover flux density decrease in the final, adiabatic stage. Figure 3.1 shows the evolution of a flare using the shock-in-jet model with the parameters presented in Table 2.2.

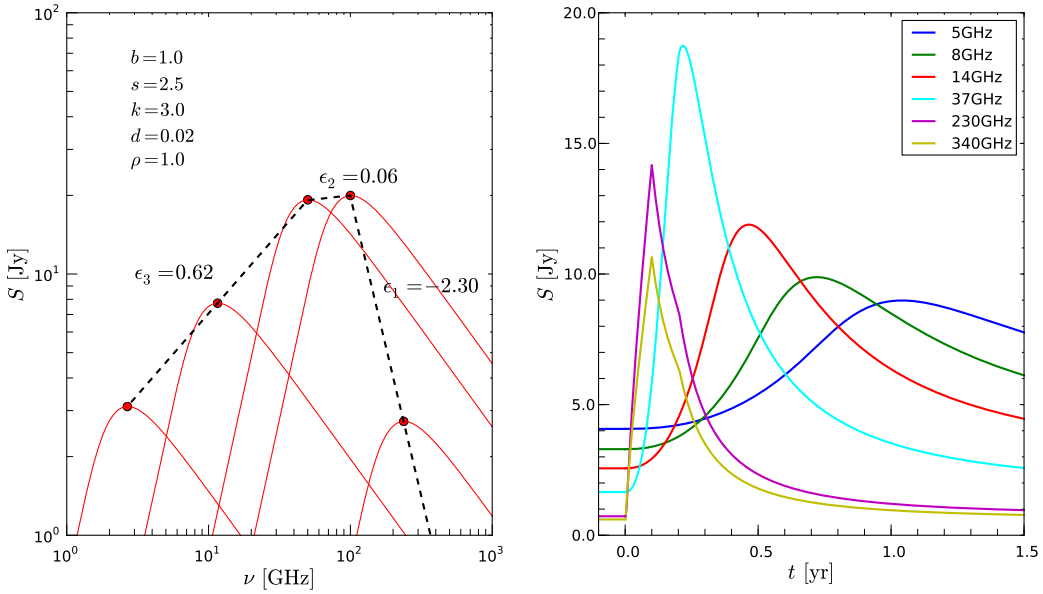

Figure 2.9: Spectral Evolution of a flare computed from the shock-in-jet model with the parameters presented in Table 2.2. Left: The dashed black line corresponds to the evolution of the turnover frequency and turnover flux density during the flare. The slope of the different stages is indicated in the plot and the red lines show some example spectra during the evolution. Right: Single dish light curves calculated from the spectral evolution for different frequencies. The zero time is set to the onset of the flare and the flux densities for $t < 0$ correspond to the flux density of the quiescent spectrum.

Generalization of the shock-in-jet model

Türler et al. (2000) expanded the shock-in-jet model to non-conical jets, e.g., the distance along the jet, r, is no longer a linearly proportional to the jet radius, R. This modification is expressed by $R \propto r^{\rho}$ with $(-1 < \rho < 1)$, which represents a collimating ($\rho < 0$) or expanding ($\rho > 0$) jet. An important implication of allowing non-conical jets ($\rho \neq 1$) in the shock-in-jet model is the r-dependence of the evolution of the spectral parameters (b, k and d). Therefore the evolution of B, K and δ along the jet is given by:

$$K \propto r^{-\rho k}, \quad B \propto r^{-\rho b}, \quad \delta \propto r^{-\rho d}. \tag{2.83}$$

Besides the modification of the jet geometry, Türler et al. (2000) parametrized the temporal evolution of the turnover frequency, ν_m, and the turnover flux density, S_m, using the equations of superluminal motion[2]

$$t = \frac{r}{v_{\mathrm{obs}}}, \tag{2.84}$$

[2]The time used here was that in the observers frame.

where $v_{obs} = (\beta_{app} c)/((1+z)\sin\vartheta)$. Using the definition of the apparent speed, $\beta_{app} = (\beta \sin\vartheta)/(1-\beta\cos\vartheta)$, the bulk Lorentz factor, Γ, and the Doppler factor, δ, the equation above results in

$$t = \frac{1+z}{\beta c \delta \Gamma} L. \tag{2.85}$$

Assuming that $\beta \sim 1$ and $\vartheta \sim 1/\Gamma \ll 1$, it can be shown that $\Gamma \propto \delta$ (Taylor expanding $\cos 1/\Gamma$ in the definition of δ). Including the non-conical jet geometry ($R \propto L^r$) the equation above can be written as

$$t \propto (1+z)\delta^{-2} R^{1/\rho} \propto (1+z) R^{\zeta}, \tag{2.86}$$

where $\zeta = (2d\rho + 1)/\rho$. By replacing R in Eqs. 2.68 and 2.69 by Eq. 2.86, the temporal evolution of the turnover frequency and turnover flux density is:

$$\nu_m \propto (1+z)^{(p_i\zeta - n_i)/\zeta} \cdot t^{n_i/\zeta} \tag{2.87}$$

$$S_m \propto D_L^{-2} (1+z)^{(q_i\zeta - f_i)/\zeta} \cdot t^{f_i/\zeta}. \tag{2.88}$$

The equations above can be further simplified by replacing $D_L \propto (1+z)$, which leads to:

$$S_m \propto (1+z)^{[(q_i-2)\zeta - f_i]/\zeta} \cdot t^{f_i/\zeta}. \tag{2.89}$$

Modification of the Compton stage

The determination of the distance that the relativistic particles travel behind the shock front before losing most of their energy is a crucial parameter in shock-in-jet models. Björnsson & Aslaksen (2000) presented a different derivation of this distance than previous works, including the possibility of multiple Compton scattering (in the Thompson regime) during the first rising phase of the flare. In the case of first order Compton scattering, the slope of the Compton stage would be less steep as predicted by Marscher & Gear (1985). Therefore, the existence of a synchrotron stage is no longer needed. The evolution of the turnover-flux density and the turnover frequency with distance (or time) is given, within the model of Björnsson & Aslaksen (2000), by:

$$\nu_m \propto R^{-[4(s+2)+3b(s+4)]/[3(s+12)]} \tag{2.90}$$

$$S_m \propto R^{-[4(s-13)+6b(s+2)]/[3(s+12)]}, \tag{2.91}$$

assuming no changes in the Doppler factor and constant velocity of the shocked particles. Using the same set of parameters as in Table 2.2 gives $n_1 = -0.9$ and $f_1 = 0.3$, resulting in a less steep slope $\epsilon_1 = f_1/n_1 = -0.3$ in the $\nu_m - S_m$-plane which is flatter than in Marscher & Gear (1985) case.

Evolution of the brightness temperature T_b

The equations presented so far require the knowledge of the evolution of the turnover frequency and turnover flux density to model the flare and to obtain the evolution of the source intrinsic parameters. Therefore, multi-frequency single dish or multi-frequency

VLBI observations are needed. However, for most of the sources, simultaneous multi-frequency VLBI observations are not available. In order to apply the model and obtain the relevant information to single frequency VLBI observations one can rewrite the equations presented in this chapter in terms of the brightness temperature, which is defined as:

$$T_{\rm b} = 1.22 \times 10^{12} S_\nu R^{-2} \nu^{-2} (1+z)\,[{\rm K}] \tag{2.92}$$

where S_ν is the flux density in Jy, R is the width of the jet in mas and ν is the observing frequency in GHz. Some physical conditions, such as the evolution of the magnetic field in the source can be derived from the brightness temperature (e.g., Kadler et al. 2004; Schinzel et al. 2012). The optically thin flux density is given by Eq. 2.32 and the size of the emission region depends on the main depends on the main energy loss mechanism, namely Compton (1), synchrotron (2) and adiabatic losses (3) see Eq. 2.58–2.60. Inserting the equations above into Eq. 2.32 leads to:

$$S_{\nu,1} \propto R^{-(s-11)/8} \delta^{(s+4)/2} B^{(s+1)/8} \nu^{-s/2} \tag{2.93}$$
$$S_{\nu,2} \propto R^2 \delta^{(s+4)/2} K B^{(s-2)/2} \nu^{-s/2} \tag{2.94}$$
$$S_{\nu,3} \propto R^3 \delta^{(s+3)/2} K B^{(s+1)/2} \nu^{-(s-1)/2}. \tag{2.95}$$

If we assume that the magnetic field, B, the normalization coefficient of the relativistic electron distribution, K, and the Doppler factor, δ, follow a power law with the jet radius:

$$B \propto R^{-b} \quad K \propto R^{-k} \quad \delta \propto R^{-d}, \tag{2.96}$$

Eqs. 2.93 - 2.95 can be written in terms of the jet radius:

$$S_{\nu,i} \propto R^{p_i} \nu^{q_i}, \tag{2.97}$$

where the exponent p_i includes the dependencies on B, K and δ and the exponent q_i includes the dependence on the frequency. For the different stages, they are defined as:

$$p_1 = -(s-11)/8 - b(s+1)/8 - d(s+4)/2 \tag{2.98}$$
$$p_2 = 2 - b(s-2)/2 - d(s+4)/2 - k \tag{2.99}$$
$$p_3 = 3 - b(s+1)/2 - d(s+3)/2 - k \tag{2.100}$$
$$q_1 = -s/2 \tag{2.101}$$
$$q_2 = -s/2 \tag{2.102}$$
$$q_3 = -(s-1)/2. \tag{2.103}$$

In order to generalize these equations to non-conical jets, the distance along the jet, r, is no longer directly proportional to the jet radius R. This modification is expressed by $R \propto r^\rho$ where $-1 < \rho < 1$. Finally, we can write the evolution of the brightness temperature as:

$$T_{\rm b} \propto r^{\epsilon_i} \nu^{q_i - 2}, \tag{2.104}$$

where the exponent ϵ_i is given, for the different stages, by:

$$\epsilon_1 = \rho\,[-(s+5)/8 - b(s+1)/8 - d(s+4)/2] \tag{2.105}$$
$$\epsilon_2 = \rho\,[-b(s-2)/2 - d(s+4)/2 - k] \tag{2.106}$$
$$\epsilon_3 = \rho\,[1 - b(s+1)/2 - d(s+3)/2 - k]\,. \tag{2.107}$$

The equations above can be further simplified (i. e., dropping the k dependence in the equations above) if we assume adiabatic expansion $k = k_{\rm ad} = 2(s+2)/3$ and equipartition between the magnetic energy density, $\mathcal{E}_{\rm mag} \propto B^2$, and the kinetic energy density, $\mathcal{E}_{\rm kin} \propto K$, which leads to $b = b_{\rm eq} = (s+2)/3$:

$$\epsilon_1^{\rm ad,eq} = \rho\left[-(s^2+5s+12)/16 - d(s+4)/2\right] \tag{2.108}$$

$$\epsilon_2^{\rm ad,eq} = \rho\left[-(s^2+4s+8)/6 - d(s+4)/2\right] \tag{2.109}$$

$$\epsilon_3^{\rm ad,eq} = \rho\left[-(s^2+7s+4)/6 - d(s+3)/2\right]. \tag{2.110}$$

These relations can be used to derive the parameter range for exponents ρ, s, k, b and d using the observed evolution of the brightness temperature at a given frequency.

2.3 Superluminal motion and the relativistic beam of radiation

Some of the observed and traced features at the parsec scale of jets show exhibit an speed which is larger than the speed of light. This apparent superluminal motion can be explained by intrinsic velocities close to the speed of light and a projection of the 3D geometry into the sky plane by a small angle to the line of sight (Rees 1967).

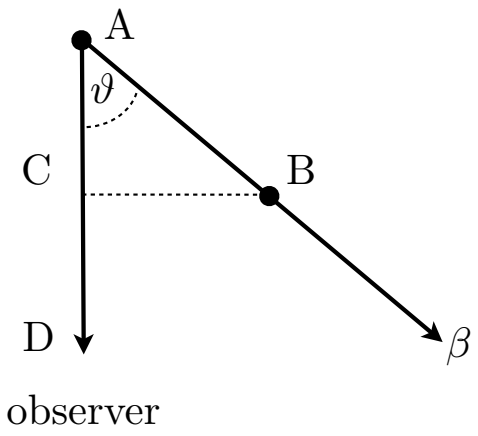

Figure 2.10: Illustration of for the de-projection of superluminal motion

Assuming a source of relativistic motion located in the sky which has a viewing angle, ϑ, to an observers. Lets assume a blob of plasma moves at a velocity $\beta = v/c$ and emits a photon at the location A at $t = t_0$ and at the location B at $t = t_1$ (see Fig. 2.10). The distance the blob has travelled in the source frame AB is given by $\beta c \Delta t_e$, where $\Delta t_e = t_1 - t_0$. Within the time interval Δt_e the blob has travelled the distance AC=$\beta c \Delta t_e \cos\vartheta$ in the observers frame and the photon emitted in A have travelled the distance AD=$c\Delta t_e$. The distance between the two photons emitted in A and B is equal to the distance CD=$c\Delta t_e(1-\beta\cos\vartheta)$ and their time difference in the observers frame is $\Delta t_o = {\rm CD}/c = \Delta t_e(1-\beta\cos\vartheta)$.

In the observes frame the distance between the two locations of the blob is CB=$\beta c \Delta t_e \sin\vartheta$ from which the apparent velocity $\beta_{\rm app}$ follows:

$$\beta_{\rm app} = \frac{\beta \sin\vartheta}{1 - \beta\cos\vartheta} \tag{2.111}$$

The maximum apparent speed is obtained if the features are travelling at the critical angle, the angle that maximizes the speed of the feature. The critical viewing angle, $\vartheta_{\rm crit}$ can be derived by calculating the derivative of the apparent speed with respect to ϑ for any given β. This leads to the result that the maximum apparent speed is obtained if $\cos\vartheta_{\rm crit} = \beta = \left[\beta_{\rm app}^2/(1+\beta_{\rm app}^2)\right]^{1/2}$. For jets seen at this critical angle, the Doppler factor is:

$$\delta_{\rm crit} = \sqrt{1+\beta_{\rm app}^2}. \tag{2.112}$$

From Eq. 2.112 follows that the existence of relativistic motions (apparent speeds) give rise to large Doppler factors. Relativistic aberration leads to a forward boosting of the emission of an electron into a cone with half-opening angle similar to the inverse of the bulk Lorentz factor. Therefore, the flux density increases by a factor δ^2. Additionally, the frequency is Doppler shifted which results into a final boosting of the flux density (see, e.g., Marscher 2006):

$$S_\nu \propto \delta^{2-\alpha}\nu^{+\alpha} \quad \text{steady state} \tag{2.113}$$

$$S_\nu \propto \delta^{3-\alpha}\nu^{+\alpha} \quad \text{moving feature} \tag{2.114}$$

3 Light Curve Analysis

This Chapter is partially published in Fromm et al. 2011, A&A 531, A95

In this Chapter we use the multi-frequency single dish observations of CTA 102 to study the flaring behavior of the source. For our analysis we focused on the radio flare around April 2006 and used observations spanning from 4.8 GHz to 340 GHz (see Fig. 3.1). The observations have been carried out by the Radio Observatory of the University of Michigan (UMRAO), the Metsähovi Radio Observatory, and the Submillimeter Array (SMA). The average sampling time intervals and flux density uncertainties are presented in Table 3.1.

Figure 3.1 shows the total flux densities measured by the telescopes at different frequencies. The most prominent feature in the light curve is the major flare around 2006.2, best seen at 37 GHz. This feature is accompanied by smaller flares in 2005.2, 2007.6, 2008.5, and 2009.4. The light curves show the typical evolution of a flare: the flaring phenomenon usually starts at high frequencies and propagates to lower frequencies with a certain time delay of the peak, but there are also flares that develop simultaneously over a wide frequency range (see Fig. 3.2). The flare around 2005.0 appears nearly si-

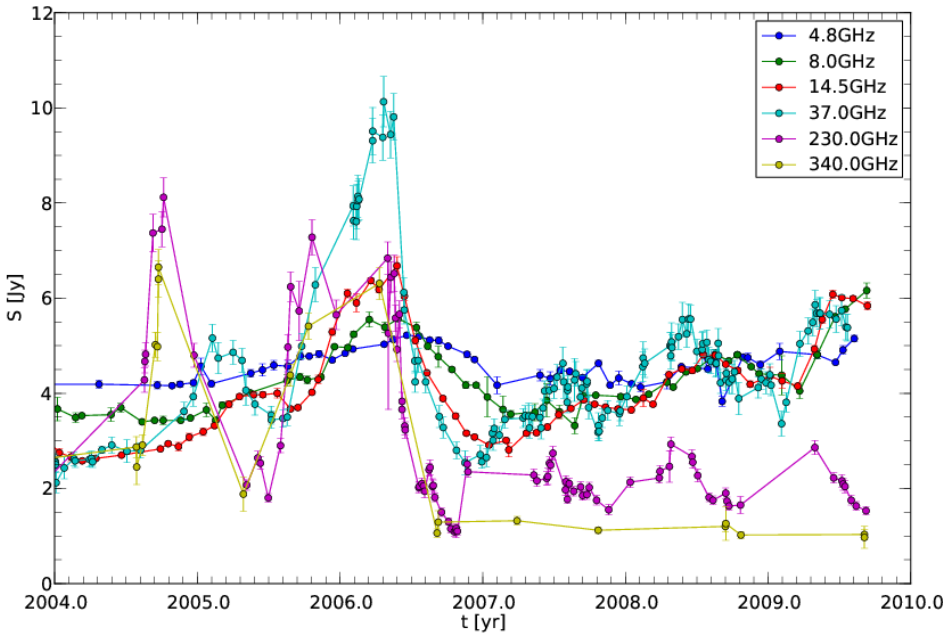

Figure 3.1: Radio−mm light curves for CTA 102, centered around the 2006 radio flare.

Table 3.1: Average time sampling and average flux density uncertainties for the used light curves

ν [GHz]	Observatory	$\langle t_{\mathrm{obs}} \rangle$ [days]	$\langle \Delta S_{\mathrm{obs}} \rangle$ [Jy]
4.8	UMRAO	46	0.09
8.0	UMRAO	38	0.07
14.5	UMRAO	32	0.07
37	Metsähovi	16	0.24
230	SMA	27	0.18
340	SMA	132	0.25

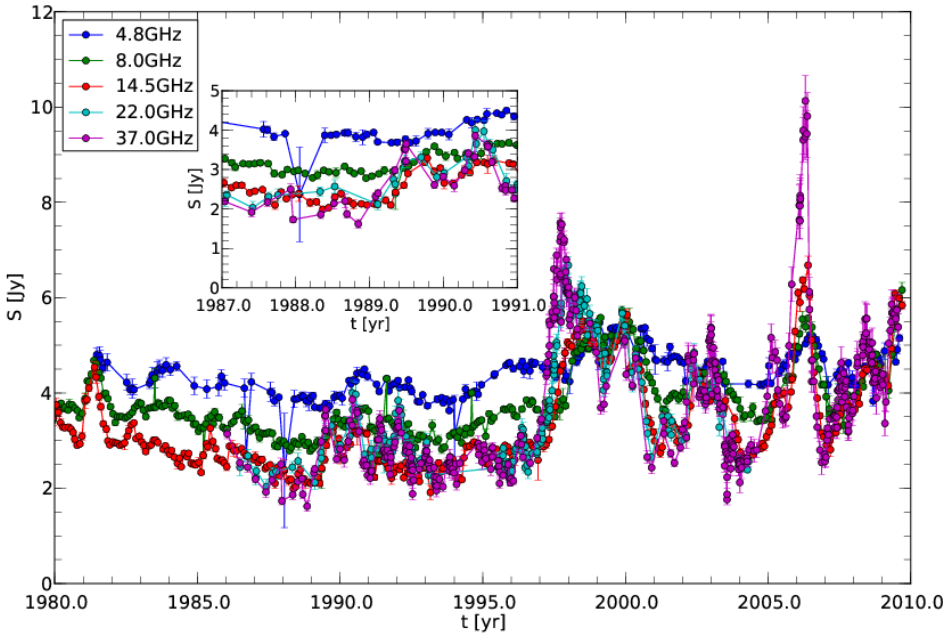

Figure 3.2: Archival low frequency light curves for CTA 102. See insert plot for the absolute quiescent state.

multaneously at the highest frequencies (230 GHz and 340 GHz) and delayed at 37 GHz and 14.5 GHz, whereas it seems that the lowest frequencies (4.8 GHz and 8 GHz) are not affected by this event.

The main flare shows the typical evolution: it is clearly visible at all frequencies with increasing time delays towards lower frequencies. Due to the poor time sampling of the 340 GHz observations, the rise and the time shift at this frequency are not easy to determine. The remarkable double peak structure of the 230 GHz measurements is an interesting feature and will be discussed later. After the flare, the flux decreases at all frequencies, with a steeper descent at higher frequencies.

3.1 Time sampling and interpolation

To perform a spectral analysis of the light curves, simultaneous data points are needed. This was achieved by performing a linear interpolation between the flux density values

from the observations. The choice of an adequate time sampling, Δt, depends on the time interval of the observations and the significance of the frequency for the determination of the peak frequency, i.e., the frequency where the spectral shape changes from optically thick to optically thin. If a too short time interval is chosen, most of the data points would be interpolated ones. On the opposite situation, if a too long time interval is chosen, most of the light curves would be smoothed. Moreover, in this case, the data are sampled inhomogeneously at the different frequency, so a compromise is required. The influence of a certain frequency on the calculation of ν_m can be estimated from the light curve (see Fig. 3.1). The turnover frequency is usually between the frequencies of the highest and second highest flux density at a certain epoch. In the case studied here, the dominating frequencies are 37 GHz and 230 GHz. From this distribution it could be concluded that an appropriate time sampling should not be significantly shorter than the observational time interval used for these frequencies. A time sampling of $\Delta t = 0.05$ yr was selected for the interpolation, corresponding approximately to the observation cadence of the 37 GHz-light curve.

The correct handling of the uncertainties in the interpolated flux densities requires knowledge of a mathematical relation describing the light curves. Since this approach is out of the scope of this work, we assigned the maximum uncertainty of the two closest observed flux densities to the interpolated flux density. For our analysis we focused on the time interval between 2005.6 and 2006.8. The interpolation of the poorly sampled 340 GHz light curve after 2006.2 could induce artificially flat spectra. We took this fact into consideration by excluding the interpolated 340 GHz flux densities from the spectral analysis for $2006.2 < t < 2006.8$.

3.2 Spectral analysis

We fitted a synchrotron self absorbed spectrum (see Eq. 2.27) to the interpolated light curves to obtain the turnover flux density, ν_m, the turnover flux density, S_m, and the optically thin spectral index, α_0.

The observed spectra may in general be thought as the superposition of the emission from the steady state and perturbed (shocked) jet. We re-constructed this quiescent spectrum from archival data and we identified the quiet state with the minimum flux density of the low frequency light curves (4.8 GHz - 37 GHz) around $t = 1989.0$ (see Fig. 3.2 and Table 3.2). The flux densities were fitted by a power law $S(\nu) = c_q \nu^{\alpha_0}$ and we obtained $c = (7.43 \pm 0.65)$ Jy/GHz and $\alpha_0 = -0.45 \pm 0.04$.

Table 3.2: Frequencies and flux density values for the quiescent spectrum

ν [GHz]	S [Jy]	Observatory
4.8	3.68±0.05	UMRAO
8.0	2.95±0.06	UMRAO
14.5	2.10±0.06	UMRAO
22	2.12±0.14	Metsähovi
37	1.62±0.11	Metsähovi

For the spectral analysis, we removed the contribution of the quiescent spectrum from

the interpolated data points and applied Eq. 2.30. The uncertainties of the remaining flaring spectrum were calculated using the errors of the interpolated data points and the obtained uncertainties of the quiescent spectrum. During the fitting process we allowed both spectral indices, α_t and α_0 to vary. Figure 3.3 shows the result of a spectral fitting at a selected epoch applied to interpolated light curve data.

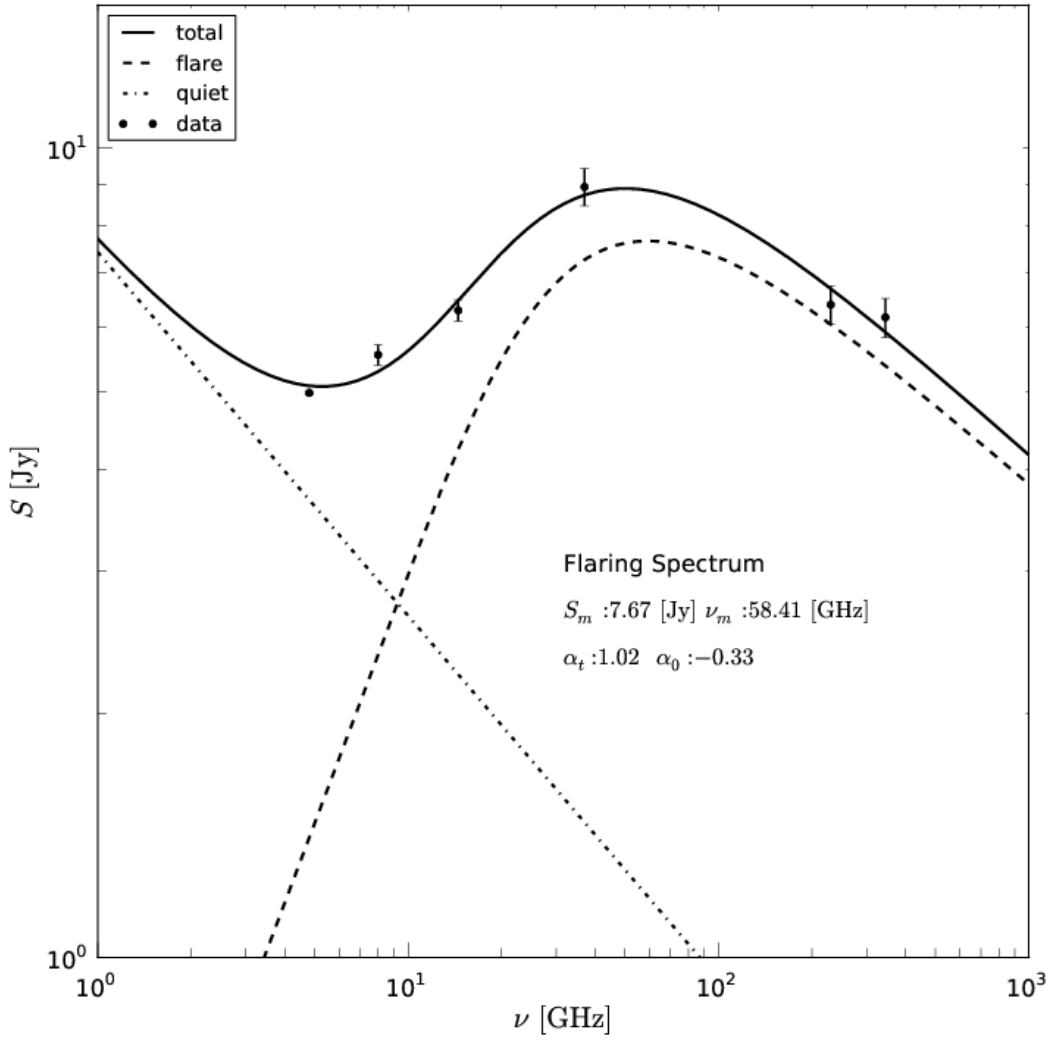

Figure 3.3: Result of the spectral fitting to the 2006.20 data. The dashed-dotted line corresponds to the quiescent spectrum, the dashed line to the flaring spectrum, and the solid black line to the total spectrum. The values presented indicate the spectral turnover of the flaring spectrum.

3.3 Error analysis of the spectra

Due to the non-linear nature of Eq. 2.30 we applied a Monte-Carlo simulation to the observed/interpolated flux densities in order to derive estimates for the uncertainties of the

Table 3.3: Spectral parameters (expected values) and corresponding uncertainties from the Monte-Carlo simulation

t [yr]	ν_m [GHz]	S_m [Jy]	α_t	α_0
2005.60	222±99	3.3±0.3	0.33±0.14	−0.27±0.50
2005.65	163±27	5.9±0.5	0.56±0.11	−1.80±0.57
2005.70	135±25	5.7±0.8	0.59±0.15	−0.90±0.50
2005.75	119±19	6.5±1.1	0.70±-0.16	−0.78±0.42
2005.80	109±12	8.4±1.0	0.78±0.14	−1.02±0.28
2005.85	96±12	7.7±1.0	0.82±0.16	−0.72±0.25
2005.90	88±14	6.7±0.9	0.81±0.16	−0.42±0.28
2005.95	73±14	6.1±0.5	1.0±0.3	−0.22±0.15
2006.00	62±12	6.2±0.5	1.2±0.3	−0.20±0.11
2006.05	56±11	6.5±0.6	1.3±0.4	−0.19±0.11
2006.10	63±12	6.5±0.6	1.1±0.3	−0.20±0.13
2006.15	60±9	7.2±0.6	1.0±0.3	−0.28±0.13
2006.20	57±7	7.9±0.6	1.1±0.2	−0.33±0.12
2006.25	56±7	8.5±0.8	0.93±0.22	−0.47±0.20
2006.30	56±7	8.4±0.7	0.94±0.21	−0.43±0.19
2006.35	53±7	8.4±0.7	0.97±0.24	−0.45±0.20
2006.40	41±5	7.2±0.6	1.0±0.3	−0.49±0.13
2006.45	27±6	4.5±0.3	1.1±0.5	−0.35±0.13
2006.50	25±7	3.8±0.4	0.89±0.56	−0.40±0.18
2006.55	25±7	3.4±0.3	0.37±0.38	−0.66±0.32
2006.60	25±10	2.9±0.4	0.28±0.35	−0.61±0.35
2006.65	25±9	2.6±0.4	0.24±0.19	−0.47±0.34
2006.70	21±11	2.3±0.4	0.26±0.13	−0.59±0.34
2006.75	17±7	2.0±0.3	0.22±0.18	−0.63±0.33
2006.80	16±8	1.8±0.3	0.24±0.11	−0.75±0.43

fitting parameters (S_m, ν_m, α_t, and α_0). Random values for each simulated spectrum were drawn from a Gaussian distribution with a mean, μ, equal to the observed flux density, $S(\nu)$, and a variance, σ, equal to the observed flux density error, $\Delta S(\nu)$. In order to achieve a good statistical ensemble, up to 1000 spectra were simulated per interpolated spectrum. Each of these simulated spectra were fitted with a synchrotron spectrum (see Eq. 2.30). As the expected value and uncertainty of a spectral parameter we take the mean and standard deviation of its simulated probability density distribution, respectively. The derived spectral parameters and their uncertainties are presented in Table 3.3.

3.4 Results

The spectral evolution of the 2006 radio flare in CTA 102 is presented in the turnover frequency - turnover flux density ($\nu_m - S_m$) plane, shown in Fig. 3.4. Figures 3.5 and 3.6 display the time evolution of the spectral parameters ($\nu_m, S_m, \alpha_0,$ and α_t).

In the next paragraphs, we summarized the evolution of the event in the turnover

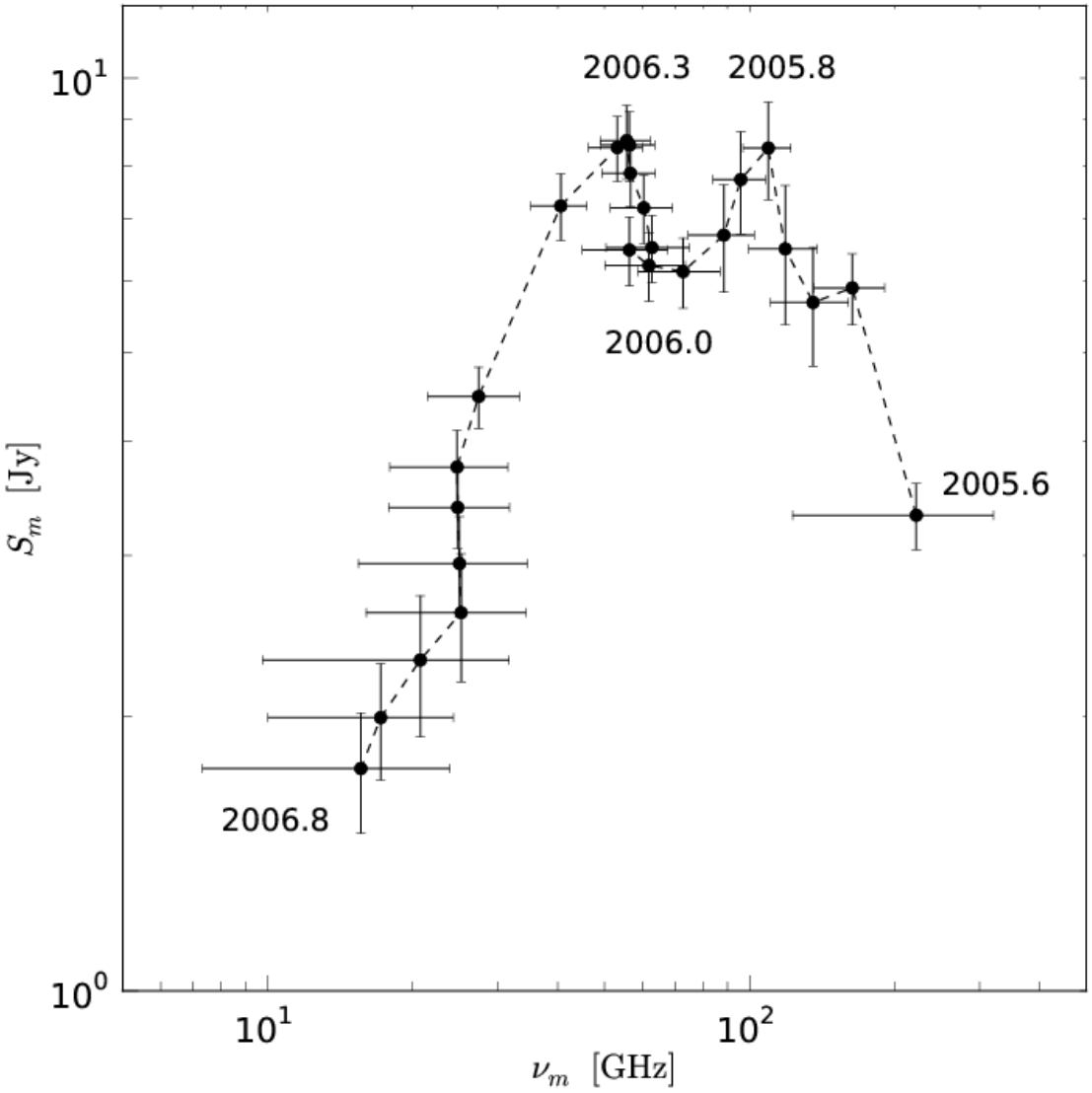

Figure 3.4: The 2006 radio flare in the turnover frequency - turnover flux density plane. The time labels indicate the time evolution and the temporal position of local and global extrema in the spectral evolution. The error bars are computed from a Monte Carlo simulation (see text for details).

frequency — turnover flux density plane and compared it with the standard shock-in-jet model (Marscher & Gear 1985) and later modifications to it (Björnsson & Aslaksen 2000). This information is also summarized in Table 3.4.

The flare started around 2005.6 with a high turnover frequency ($\nu_m \sim 200\,\mathrm{GHz}$) and a low turnover flux density ($S_m \sim 3\,\mathrm{Jy}$). During the first 0.2 yr, the turnover flux density, S_m, increased, reaching $S_m \sim 8.4\,\mathrm{Jy}$, while the turnover frequency decreased to $\nu_m \sim 110\,\mathrm{GHz}$. The slope of the optically thick part of the spectrum, represented by α_t, steepened (0.33 to 0.78), while the optically thin spectral index, α_0, steepened during the first 0.05 yr and flattened (-1.8 to -1.02) afterwards. The large uncertainties of the op-

tically thin spectral index, α_0, are due to the lack of data points beyond 340 GHz. The exponential relation between the turnover flux density, S_m and the turnover frequency, ν_m, ($S_m \propto \nu_m^{\epsilon_i}$, see Sect. 2.2.3), led to a value of $\epsilon = -1.21 \pm 0.22$.

As mentioned in Chapter 2.2.3, the dominant loss mechanism during the first stage of flare (increasing turnover flux density while the turnover frequency was decreasing) was Compton scattering. Marscher & Gear (1985) predicted a value of $\epsilon = -5/2$, whereas Björnsson & Aslaksen (2000) derived $\epsilon = -0.43$ using a modified expression for the shock width (both assumed $s = 2.4$ and $b = 1$). The obtained value of $\epsilon = -1.21 \pm 0.22$ was in between these two values, but it is impossible to reproduce using the approach of Björnsson & Aslaksen (2000).

During the time interval between 2005.8 and 2006.0, involving 0.2 yr, the turnover flux density and turnover frequency decreased to $S_m \sim 6.2$ Jy and to $\nu_m \sim 62$ GHz, respectively. The slope in the $\nu_m - S_m$-plane changed to $\epsilon = 0.77 \pm 0.11$. The average optically thick spectral index reached a value $\alpha_t \sim 0.82 \pm 0.17$ while the optically thin spectral index, α_0, continued rising to -0.22. This behavior of the turnover values fits well in the adiabatic stage in the shock-in-jet model. For this stage Marscher & Gear (1985) derived an exponent $\epsilon = 0.69$ (assuming $s = 3$), which is well within our value.

However, the increase of the turnover flux density starting in 2006.0, which reached a peak value of $S_m \sim 8.5$ Jy in 2006.3, cannot be explained within the frame of the shock-in-jet model. Its behavior, though, resembles that expected from a Compton stage ($\epsilon = -0.99 \pm 0.46$). The spectral indices during this stage were roughly constant, $\alpha_t = 1.33 \pm 0.27$ and $\alpha_0 = -0.26 \pm 0.13$.

After 2006.3, the turnover flux density and turnover frequency decreased. This last phase could be understood as an adiabatic stage and the power law fit in the $\nu_m - S_m$-plane led to an $\epsilon = 1.24 \pm 0.10$. The optically thin spectral index was nearly constant, $\alpha_0 = -0.46 \pm 0.21$ while the evolution of the optically thick spectral index, α_t, could be divided into two parts: $\alpha_t = 0.96 \pm 0.28$ until 2006.5 and $\alpha_t = 0.26 \pm 0.18$ after.

Our results show no evidence for a synchrotron stage, characterized by a nearly constant turnover flux density, S_m, while the turnover frequency, ν_m, is decreasing ($\epsilon = -0.05$ for $s = 2.4$ and $b = 1$, Marscher & Gear 1985).

The first hump in the evolution of the flare in the $\nu_m - S_m$-plane ($2005.6 < t < 2006.0$) fulfills, despite no evidence for a synchrotron stage, the phenomenological requirements of the shock-in-jet model of Marscher & Gear (1985). However, the evolution after 2006.0 did not follow the predicted evolution. The turnover flux density and the turnover frequency should continue decreasing. But their behavior mimicked the evolution of a Compton stage ($2006.0 < t < 2006.3$) and the one of an adiabatic stage ($2006.3 < t < 2006.8$). Considering these points, we decided to model the evolution of the 2006 flare in CTA 102 according to the standard shock-in-jet model (Marscher & Gear 1985) including a second Compton and adiabatic stage. This decision is evaluated in Sect. 5.6.

3.5 Modeling the 2006 radio flare

In this section we present the results of applying the shock-in-jet model and the fitting technique to the observed spectral evolution of the 2006 radio flare in CTA 102.

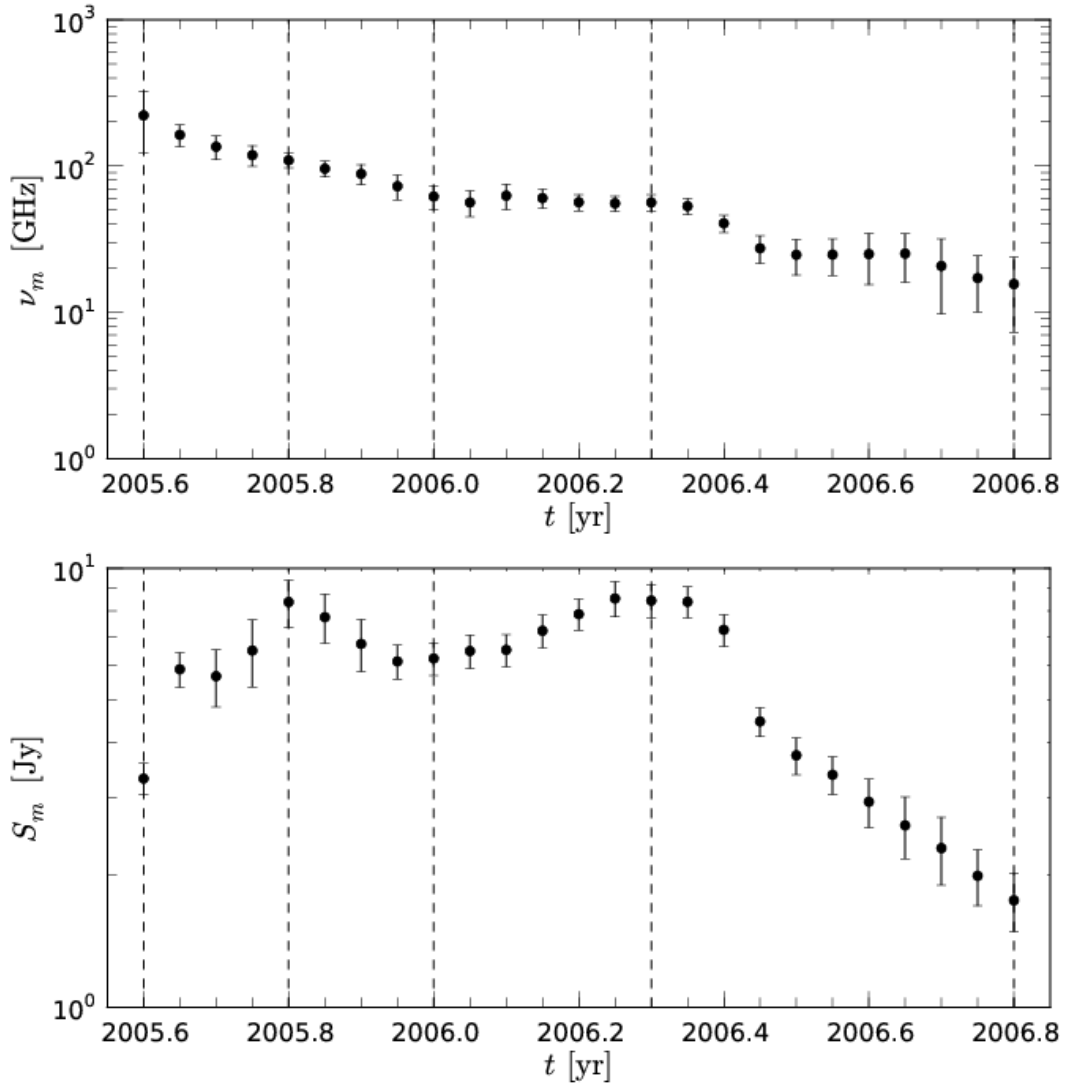

Figure 3.5: Temporal evolution of the 2006 radio flare: top turnover frequency and bottom turnover flux density. The dashed vertical lines correspond to the time labels in Figure 3.4 and indicate the extrema in the evolution.

Table 3.4: Different stages of the spectral evolution and their characteristics

time	stage	model	ϵ ($S_m \propto \nu_m^\epsilon$)	$\langle\alpha_t\rangle$	$\langle\alpha_0\rangle$
2005.6 – 2005.8	C	C1	−1.21±0.22	0.33 – 0.78[a]	−1.80 – −1.02[a]
2005.8 – 2006.0	A	A1	0.77±0.11	0.82±0.17	−1.02 – −0.21[a]
2006.0 – 2006.3	C	C2	−0.99±0.46	1.03±0.27	−0.26±0.13
2006.3 – 2006.8	A	A2	1.24±0.10	0.96±0.29[b], 0.26±0.18[c]	−0.46±0.21

[a] rising, [b] until 2006.4, [c] after 2006.45

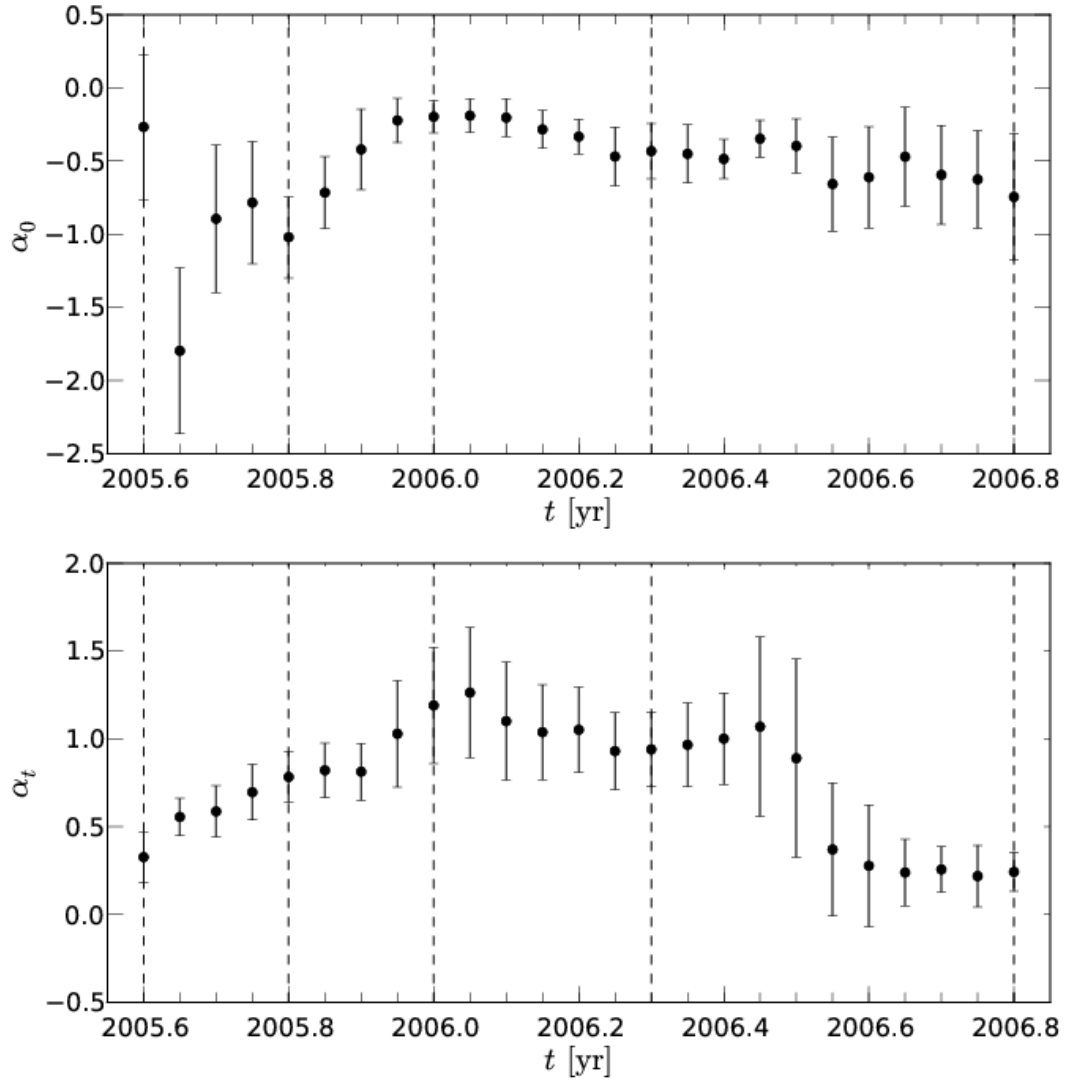

Figure 3.6: The temporal evolution of the optically thin (α_0, top) and thick (α_t, bottom) spectral indices for 2006 radio flare. The dashed vertical lines corresponds to the time labels in Figure 3.4 and indicate the extrema in the evolution.

3.5.1 Fitting technique

We used a multi-dimensional χ^2-optimization for deriving a set of parameters that fit the spectral evolution of the different stages. Our approach consists on fitting the temporal evolution of the spectral turnover values, ν_m and S_m using Eqs. 2.87 and 2.89 and the definition of the spectral exponents (see Eqs. 2.71-2.82). The proportionalities in Eqs. 2.87 and 2.89 can be removed by introducing the constants $c_{\nu_{m,i}}$ and $c_{S_{m,i}}$, which reflect logarithmic shifts of the turnover frequency and flux density and depend on the intrinsic properties of the source and flare, having no further importance for our study. From the observed values, $\nu_{m,i}^{obs,j}$ and $S_{m,i}^{obs,j}$ (i indicating the radiation loss stage, and j indicating the position among the total number of points in the stage, q, so that $j = 1 \cdots q$), the proportionality

constants can be derived as:

$$c_{\nu_{m,i}} = \nu_{m,i}^{obs,j} \cdot t_{obs,j}^{-n_i/\zeta}, \tag{3.1}$$

$$c_{S_{m,i}} = S_{m,i}^{obs,j} \cdot t_{obs,j}^{-f_i/\zeta}, \tag{3.2}$$

where $t_{obs,j}$ is the time in the observers frame. Using these definitions, the constant for the spectral evolution in the $\nu_m - S_m$ plane (see Eq. 2.70) yields:

$$c_{(\nu_m - S_m),i} = S_{m,i}^{obs,j} \cdot \left(\nu_{m,i}^{obs,j}\right)^{-f_i/n_i} \cdot t_{obs,j}. \tag{3.3}$$

From Eqs. 2.71-2.82, 2.87, and 2.89, we see that there are 5 parameters (b, s, k, d, and ρ) that describe the whole spectral evolution, although they have different values at each stage. Starting from basic physical principles, we used boundaries for the different parameters to avoid unphysical results. These boundaries are listed in Table 3.5.

Table 3.5: Range for spectral parameters allowed to vary in the fits to the observed spectrum for all stages.

b	s	k	d	ρ
1 to 2[a]	2 to 4	1 to 6	−2 to 2	-1 to 1

[a] if $\rho > 0$

The negative values for parameter d stand for the possibility for an increase in the Doppler factor, δ, with radius. Regarding ρ, negative values correspond to collimation, i.e., a decrease of the jet radius, and positive values correspond to an expansion process.

On top of the listed limitations, the evolution of the optically thin spectral index, α_0, can be used to provide estimates of the parameter $s = 1 - 2\alpha_0$. Marscher & Gear (1985) used a lower limit of $s = 2$ to keep the shock non-radiative. A flatter spectral slope, e.g., $s < 2$, would increase the amount of high energy electrons, which will dominate the energy density and the pressure in shock. Since these particles suffer radiative cooling, their energy losses would affect the dynamics leading to a radiative shock.

As mentioned before, allowing non-conical jet expansion ($\rho \neq 1$) also affects the boundaries for the spectral parameters k and d presented in Table 3.5, which depend on the value of ρ in the non-conical case. Note that this should be taken into account in order to properly interpret the evolution of the physical parameters with distance to the core.

We developed a least-square algorithm to fit the three different radiation loss stages (Compton, synchrotron, or adiabatic, or combinations of them) to the observed evolution using one single set of parameters. During the optimization of χ^2 all observed data points were used for calculating the constants $c_{\nu_{m,i}}$ and $c_{S_{m,i}}$, which allows for an improved χ^2. This technique allowed us to test and analyze different possible scenarios (b, s, k, d, and ρ).

3.5.2 Spectral evolution before 2006.0

The spectral evolution until 2006.0 followed approximately the standard evolution described by the shock-in-jet model. However, we have not found evidence for a plateau

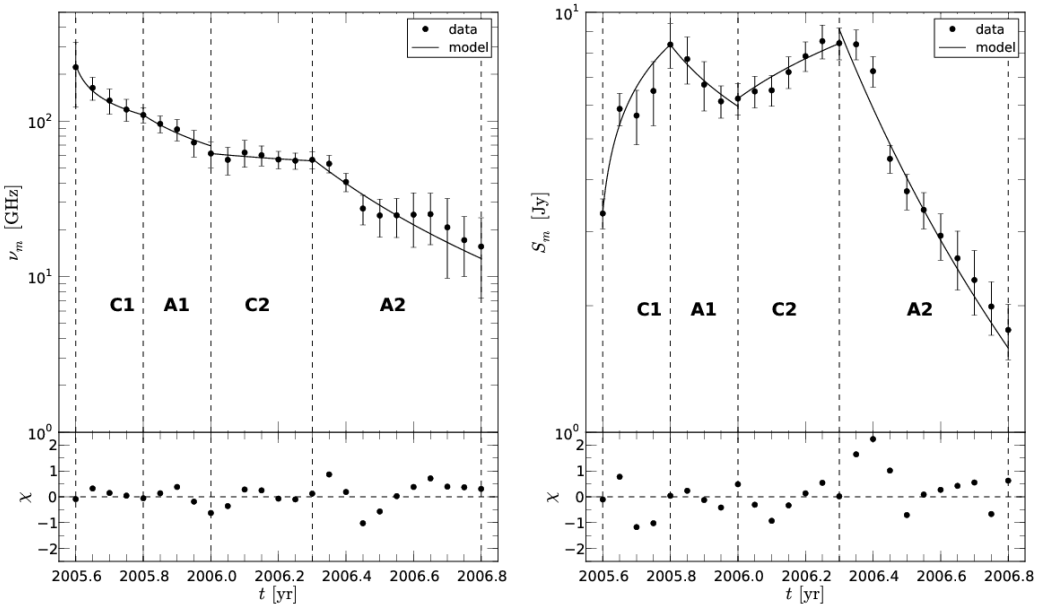

Figure 3.7: Temporal spectral evolution of the 2006 radio flare in CTA 102 left: turnover frequency; right: turnover flux density. The lower panels show the residuum for the fits $\chi = (x_{\mathrm{obs}} - x_{\mathrm{model}})\,/\Delta x$. The dashed black lines correspond to the time labels in Figure 3.4 and indicate the extrema in the evolution.

Table 3.6: Best fit values for spectral evolution modeling of the 2006 radio flare in CTA 102, parameters b, d, s, k, ρ and t.

	2005.60−2005.95	2005.95−2006.30	2006.30−2006.80
	C1A1	C2	A2
b	$1.0^{+0.08}_{a}$	$1.35^{+0.65}_{-0.35}$	1.7±0.2
d	0.2±0.02	−0.1±0.03	$-0.2^{+0.08}_{-0.05}$
s	2.1	2.0	2.4
k	2.7±0.14	not fitted	4.7±0.4
ρ	0.60±0.03	0.35±0.02	0.90±0.07
t	0.02±0.01	not fitted	

[a] value hits lower boundary

phase of turnover flux density, S_m, neither after the first Compton stage nor after the second Compton-like stage. Therefore, we excluded the synchrotron stage from our modeling using a direct transition from the Compton to the adiabatic one. The result of this modeling is presented in Table 3.6 as model C1A1.

3.5.3 Spectral evolution between 2006.0 and 2006.3

The second peak in the $S_m - \nu_m$ plane shows a similar behavior to a Compton stage, as stated above. Therefore, we applied the equations of the Compton stage to the spectral evolution between 2006.0 and 2006.3. Since the Compton stage can be explained within a 4-dimensional parameter space (note that it does not depend on parameter k, Eqs. 2.71 – 2.82), we selected carefully a physically meaningful combination of parameters.

Boundaries for the slope of the relativistic electron distribution, s, can be derived by using the evolution of the optically thin spectral index of the emission ($s = 1 - 2\alpha_0$) between 2006.0 and 2006.3. This evolution is shown in Fig. 3.6. We obtained values of $s_{\rm min} = 1.4$ and $s_{\rm max} = 2$ from the optically thin spectral indeces $\alpha_0 = -0.20$ and $\alpha_0 = -0.47$, respectively.

3.5.4 Spectral evolution after 2006.3

The spectral evolution after 2006.3 shows the typical behavior of an adiabatic loss stage. Again, we used the evolution of the optically thin spectral index, α_0, shown in Fig. 3.6,to derive limits for the parameter s. The obtained values are $s_{\rm min} = 1.6$ and $s_{\rm max} = 2.5$. This stage could be divided into two substages (before and after 2006.45) but the limited time sampling (with only three data points in the first part) forced us to perform the spectral fitting to the whole adiabatic stage.

3.5.5 Final model and error analysis

Table 3.6 lists the best fits and errors of the different stages. In the first column, we show the values for C1A1. Since we have not found evidence for a synchrotron stage, we assumed a direct transition between a Compton and an adiabatic stage.

A study of the uncertainties of the spectral parameters as in Lampton et al. (1976) is not suitable due to the small number of data points and the strong mathematical interdependence of the parameters. This yields to mathematically correct, but non-physical solutions. For the same reason, we did not perform an analysis of the large 5 or 6-dimensional parameter space. To provide first-order error estimates we followed this approach: The set of parameters derived minimizes the χ^2-distribution in the parameter space, so we investigated the stability of this point in the parameter space. This error analysis is based on the variation of the χ^2 for a given parameter sweep within the listed boundaries (Table 3.5), while keeping the others fixed. The final values for the uncertainties were obtained by calculating the 68% probability values, assuming a normal distribution for the values of the parameters. Note that the χ^2 distribution is not always symmetric around the minimum value, and this leads to lower and upper limits for the error estimates. Fig. 3.7 shows the result of our spectral modeling.

3.6 Modeled spectra and light curves

With the derived parameters and their error estimates we calculated the evolution of flaring spectrum and compared it to the observed flux density values at any given epoch. For each time step during the flaring activity the turnover frequency and the turnover flux density can be thus calculated. The optically thin spectral index follows from the assigned spectral slope, s. The calculation of the optically thick spectral index, α_t, can be performed following the approach of Türler et al. (2000), setting $\alpha_t \sim f_3/n_3$ (see Eqs. 2.76 and 2.73). This leads to a set of four spectral parameters ($S_m, \nu_m, \alpha_0, \alpha_t$) from which the shape of the flaring spectrum can be derived by using Eq.2.30. By incorporating the quiescent spectrum, the total spectrum can be computed. From the uncertainties of the parameters (b, s, k, d, and ρ) and the quiescent spectrum, the lower and upper boundaries for the modeled spectra can be obtained. Fig. 3.8 shows the modeled spectrum for the 2006.2 observations as an example. The calculation of the optically thick spectral index, using $\alpha_t \sim f_3/n_3$ led to values which reproduce well high frequency part of the spectrum but not the low frequency one (see Fig.3.8). The discrepancy in the optically thick part of the spectrum was probably caused by the quiescent contribution, which is known to vary slightly over time (see variations in the flux density for $t < 1995$ Figure 3.2).

Once the spectra are calculated, it is straightforward to obtain the modeled light curves at a given frequency. The comparison between the modeled and the observed 37 GHz light curve is presented in Fig. 3.9. Although similar plots can be obtained for other frequencies, it is meaningful to select a frequency at which the observed emission is mainly generated by the interaction of the traveling shock with the underlying flow. Moreover, the dense sampling of the 37 GHz observations provided a more complete picture of the evolution of the flaring event. Taking this consideration into account, we picked the 37 GHz light curve as the best possible comparison. The observed data points fall well within the range of modeled light curve. At the beginning of the flare, the 37 GHz flux density was still in its quiet state and therefore the main uncertainty for this time is due to the uncertainties in the quiescent spectrum. The error band presented here corresponds only to the flaring state, which was the dominant contribution to the 37 GHz flux density after 2005.60, leading to broader error bands from this epoch and on.

3.6.1 Rejected solutions

As already mentioned, the solutions for the spectral fitting were embedded in a 4- or 5-dimensional parameter space. Some of those can be highly degenerate given the small number of data points. When fitting the spectral evolution, a deep study of the parameter space was performed, including all possible combinations of the parameters, (i.e., variation of single, pairs and triplets of parameters) and simultaneously fitted stages, (one-, two- and three-stage fits). Within this study we found families of solutions with χ^2 values similar to the presented final set of parameters, but with unphysical values. After a sanity check, those fits were discarded. The meaningful set of solutions is presented in Table 3.6 and discussed in Sect. 5.6.

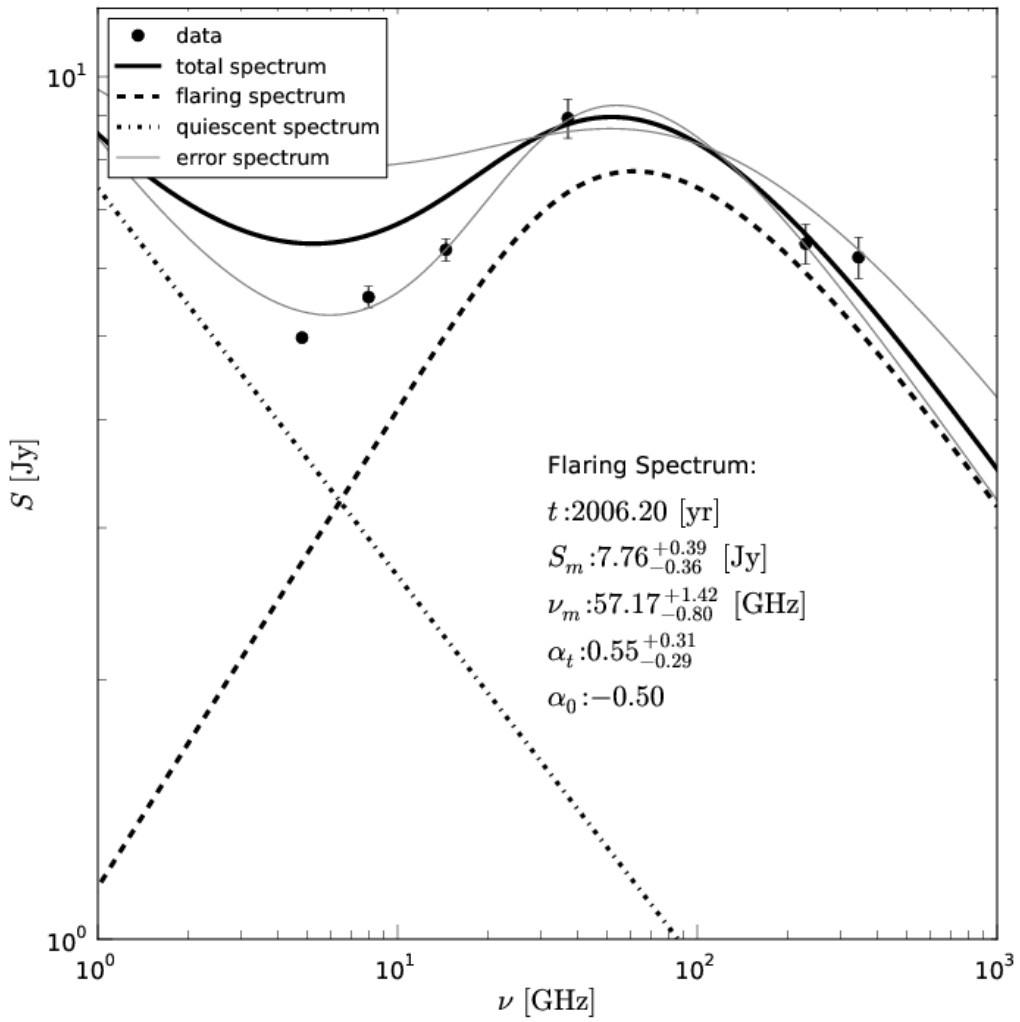

Figure 3.8: Modeled spectrum for the 2006.20 observations.The dashed-dotted line corresponds to the quiescent spectrum, the dashed line to the flaring spectrum, and the solid black line to the total spectrum. The gray lines indicate the uncertainties in the calculation of the spectrum (for more details see Sect. 3.6.

The geometrical model

Stevens et al. (1996) found a similar double hump in the $\nu_m - S_m$ plane for 3C 345. They assumed that this behavior could be due to changes of the viewing angle, expressed in a variation of the Doppler factor, δ, along the jet. Therefore we used as an alternative to the previous modeling of the second hump in the $\nu_m - S_m$ plane, a purely geometrical approach. Such an approach could easily explain the variation in the observed turnover flux density $\left(S'_m \propto \delta^{3-\alpha_0} S_m\right)$ while the observed turnover frequency kept a nearly constant value $(\nu'_m \propto \delta \nu_m)$. It was assumed that the deviation from the standard shock-in-jet model around 2005.95 was caused by changes in the evolution of the Doppler factor $\delta = \Gamma^{-1}(1 - \beta \cos\vartheta)^{-1}$ during the final adiabatic loss stage. The remaining parameters were taken from the best fit to the evolution until 2006.0 (first column in Table 3.6, model

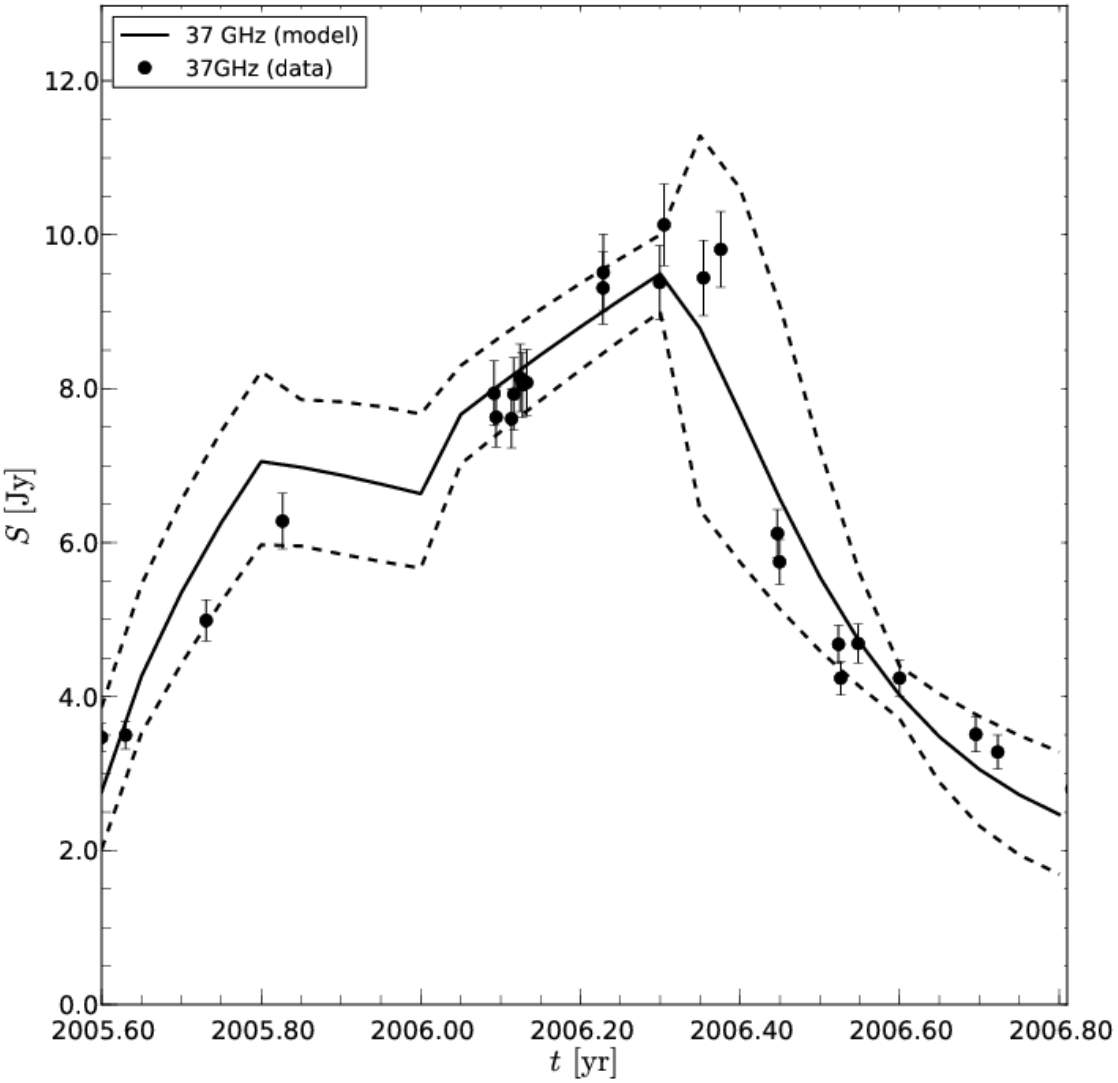

Figure 3.9: Modeled and observed 37 GHz light curve. The black solid line corresponds to the calculated model and the dashed lines indicate the uncertainties in the calculation of the modeled light curve (for more details see text).

C1A1) and only the parameter d was allowed to vary.

The result of our calculations for the different models is presented in Fig. 3.10 and Table 3.7. The figure shows the fits separating the different stages observed after 2006.0 (Figs. 3.4 and 3.5). We recall that these stages are the increase of the flux density between 2006.0 and 2006.3 and the decrease in flux density and frequency from 2006.3 until 2006.8.

A simple change in the evolution of the Doppler factor, expressed by the exponent d, $\left(\delta \propto R^{-d(t)}\right)$, can not explain the observed temporal evolution of the turnover frequency and turnover flux density.

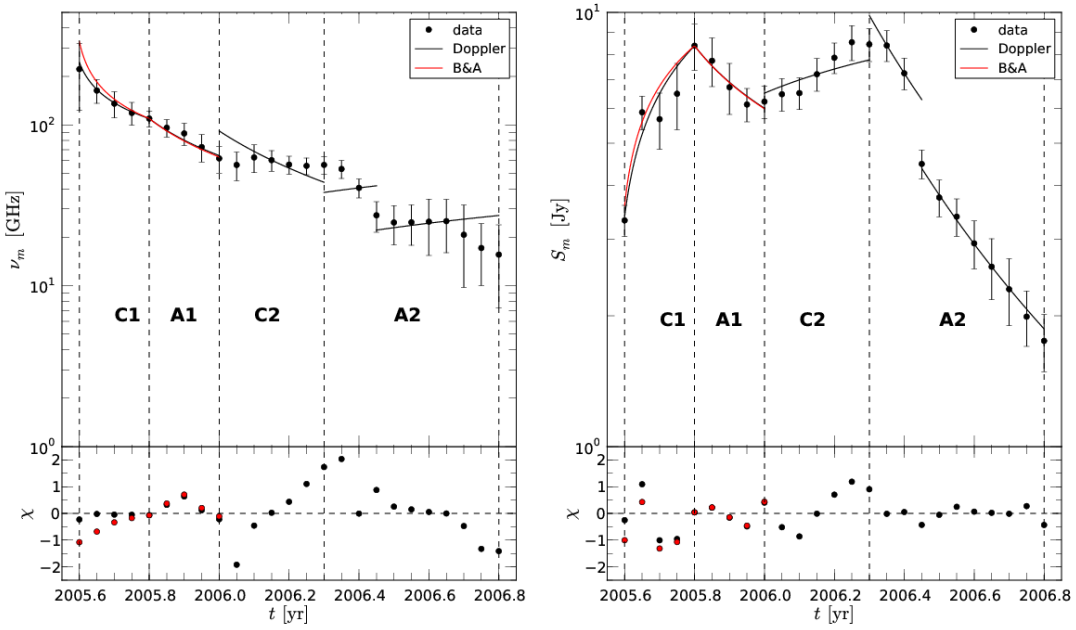

Figure 3.10: The temporal evolution of the 2006 radio flare in CTA 102 modeled with varying Doppler factor (black solid line) for $t > 2006.0$ and with the modifications of Björnsson & Aslaksen (2000) for the first two stages (red solid line). Both models fail to describe the 2006 flare (compare to Fig. 3.7).; left: turnover frequency; right: turnover flux density. The lower panels show the residuum for the fits $\chi = (x_{\rm obs} - x_{\rm model})/\Delta x$. The dashed black lines correspond to the time labels in Figure 3.4 and indicate the extrema in the evolution.

Table 3.7: Results of the geometrical model for parameter d.

time	type	d
2006.0–2006.8	3-stage	−0.04
2006.0–2006.5	2-stage	−0.30
2006.5–2006.8	2-stage	−1.24
2006.0–2006.3	1-stage	−0.41
2006.3–2006.5	1-stage	−1.33
2006.5–2006.8	1-stage	−1.27

Applying the modified Compton stage

As mentioned in Sect. 2.2.3, Björnsson & Aslaksen (2000) reviewed Marscher & Gear (1985) assumption for the Compton stage and modified the equations for the evolution of the turnover frequency, ν_m, and the turnover flux density, S_m. We applied this model to the first two stages of the 2006 flare in CTA 102 (Model C1A1), using the expression as in Sect. 2.2.3 for the time evolution (Eq. 2.85) and $d = 0$. The result of the modeling is shown in Fig. 3.11, Fig.3.10 and Table 3.8.

The result of the fitting shows that the approach of Björnsson & Aslaksen (2000) cannot explain the steep rise of the turnover flux density with decreasing turnover frequency

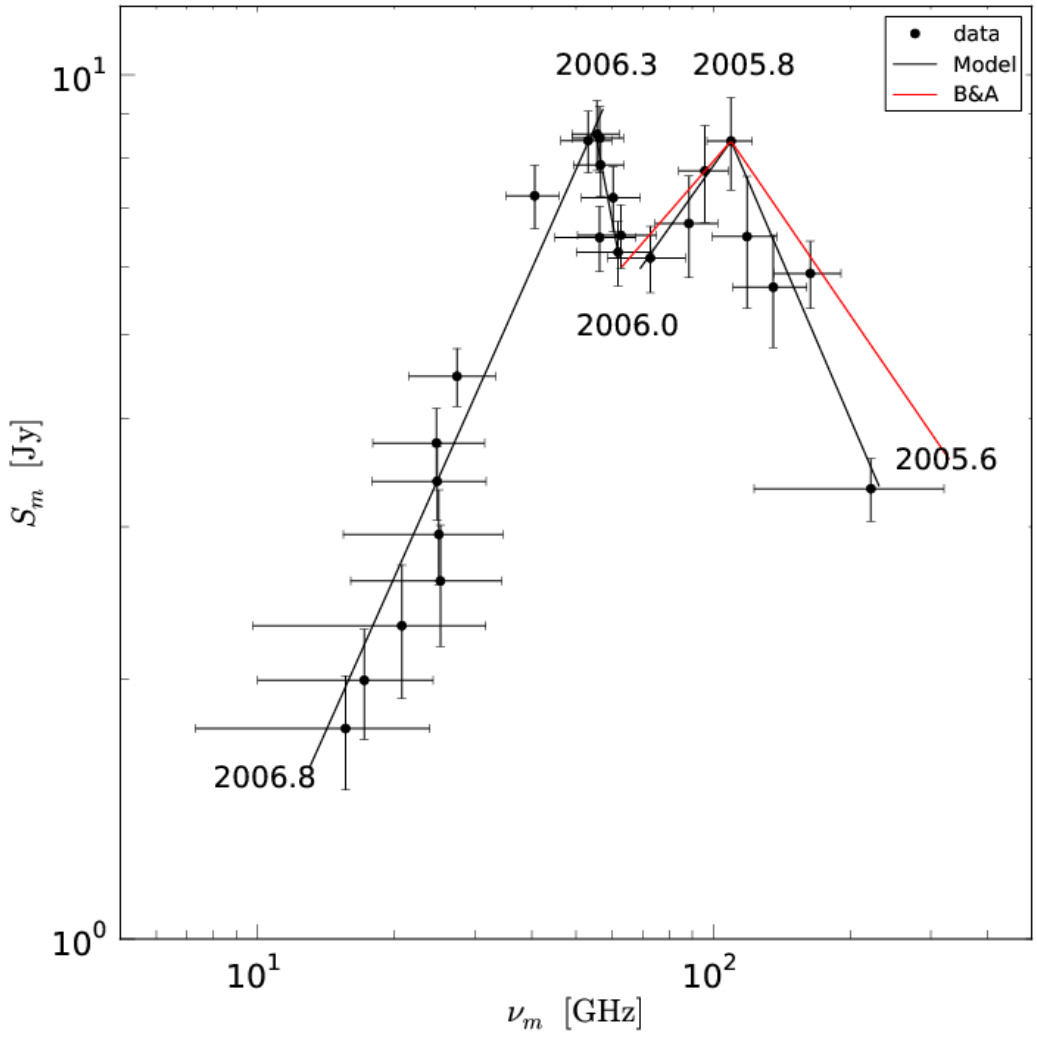

Figure 3.11: The 2006 radio flare in the turnover frequency - turnover flux density plane. The time labels indicate the time evolution and the temporal position of local and global extrema in the spectral evolution. The black line corresponds to the final model presented in Table3.6 (based on Marscher & Gear 1985) and the red one to Table 3.8 (based on Björnsson & Aslaksen 2000).

Table 3.8: Spectral parameters for C1A1 using Björnsson & Aslaksen (2000)

b	s	k	d	ρ	t
1.0	1.6	2.9	0	0.6	0.02

in the first stage of the flare (see solid red line in Fig. 3.11). Following the authors, this could be an indication that inverse Compton scattering is not the dominant energy loss mechanism during the rising stage (Björnsson & Aslaksen 2000). This aspect will be discussed in Sect. 5.6.

3.7 Discussion

Our analysis of the strong radio flare observed in CTA 102 around 2006 shows that its behavior until epoch 2006.0, i.e., the first hump in the $\nu_m - S_m$ plane, can be well modeled by a Compton and adiabatic stage within the standard shock-in-jet model (Marscher & Gear 1985) (see Sect. 3.5.2). We found no evidence of a synchrotron stage between the Compton and the adiabatic stages during the first part of the evolution. This behavior was similar to the one found in another prominent blazar 3C 345 (Lobanov & Zensus 1999), where a bright jet component also appeared to proceed from the Compton stage to the adiabatic stage, with the synchrotron stage ruled out by combination of the observed spectral and kinematic evolution of this component. The flare in CTA 102 shows a second hump in the $\nu_m - S_m$ plane (see Fig.3.11) after 2006.0, that cannot be explained within this model. The evolution between 2006.0 and 2006.3 seems to follow the predicted evolution of a Compton stage, i.e., increasing turnover flux density and decreasing the turnover frequency. Based on this apparent behavior we applied the equations of the Compton stage to this second hump (see Sect. 3.5.3). After epoch 2006.3, the evolution shows a decrease in both turnover values, which can be interpreted as an adiabatic stage. Thus, we used the appropriate equations for this stage to fit the data points (see Sect. 3.5.4). This approach led to a set of exponents which describe the evolution of the magnetic field, B, the Doppler factor, D, the spectral slope of the electron distribution, s, the normalization coefficient of the relativistic electron distribution, K, and the jet radius, R. The results of our modeling are summarized in Fig. 3.7. Our hypothesis is that this behavior can be interpreted in terms of the interaction between a traveling shock and a standing shock wave in an over-pressured jet. A pure geometrical model failed to explain the observed behavior (see Sect. 3.6.1). We also tried to fit the evolution of the flare using the modification of the shock-in-jet model by Björnsson & Aslaksen (2000), but this also failed. However, the failure of this model, which takes into account multiple Compton scattering, could have further implications in our understanding of flaring events in AGN jets, as discussed at the end of this section.

The formation of standing shocks (recollimation shocks) is presented in Sect. 2.1.2. Figure 3.12 illustrates the basic configuration of an over-pressured jet and present the characteristic regions i) the expansion region, i.e., continuous increase of the jet radius, ii) the collimation region, i.e., decrease of the jet radius and formation of the recollimation shock, and iii) the re-expansion region. In such a scenario, enhancements of emission can be produced by the interaction between traveling and standing (recollimation) shocks (Gomez et al. 1997). In the following, the evolution of the travelling shock in these regions is described and our results are put in context.

3.7.1 The expansion region

A relativistic shock propagating through this region accelerates particles at the shock front. These particles travel behind the shock and suffer different energy loss mechanisms, depending on their energy. The resulting evolution of the turnover frequency and turnover flux density is explained by the shock-in-jet model (Marscher & Gear 1985) under certain assumptions.

The parameters derived for the time between 2005.6 and 2006.0 can be associated

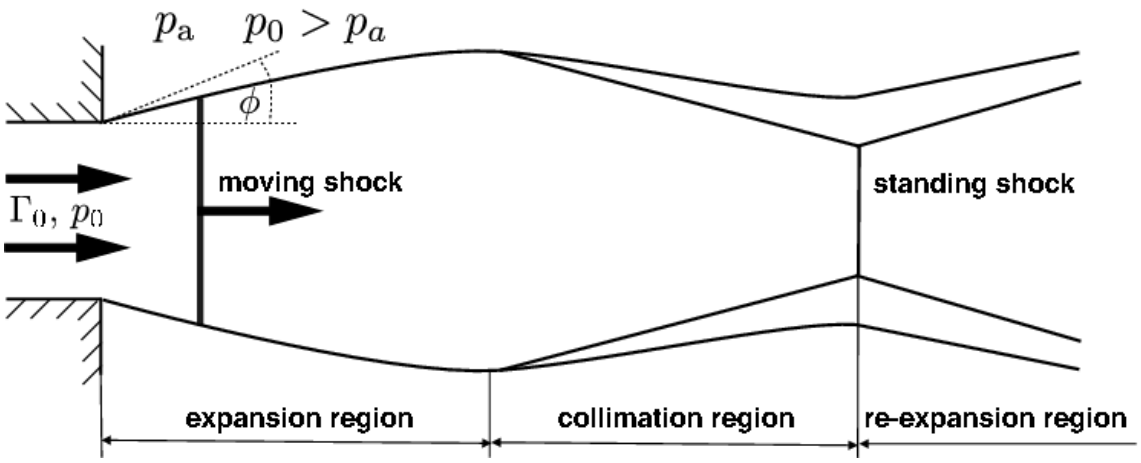

Figure 3.12: Sketch of an over-pressured jet with indicated characteristic regions, with Γ_0 being the bulk Lorentz factor at the jet nozzle, p_0 the pressure at the jet nozzle and p_a the pressure in the ambient medium (adopted from Daly & Marscher 1988).

with this region, including a Compton and an adiabatic stage. The expansion of the jet is parametrized by $\rho = 0.60$, which differs from the value expected for a conical jet $\rho = 1$. The non-conical behavior could be due to acceleration of the flow (Marscher 1980). This acceleration should be expressed by $-\rho \cdot d > 0$ ($D \propto L^{-rd}$). However, from our results, this value is negative $-\rho \cdot d = -0.12$, but very small, i.e., compatible with no changes in the Doppler factor. Thus, we cannot confirm this point.

For the evolution of the magnetic field with distance we derive a value of $b = 1.0$, indicating that the magnetic field could be basically toroidal in this region. The injected spectral slope for the relativistic electron distribution $s = 2.1$ leads to an optically thin spectral index $\alpha_0 = -0.55$. A decrease in the density can be deduced from $-\rho \cdot k = -1.6$, which corresponds to the evolution of the normalization coefficient of the relativistic electron distribution, K.

The parameter $t_{\rm off}$ corresponds to the time difference between the onset of the Compton stage and the first detection of the flare. From the value of $t_{\rm off} = 0.02$ yr together with independently obtained values for the viewing angle, $\vartheta = 2.6°$, and the apparent speed of the VLBI component ejected by the 2006 flare, $\beta_{\rm app} = 17\,c$ (Jorstad et al. 2005a; Fromm et al. 2010), we calculated the displacement between the onset and the detection of the flare to be $\Delta r = 3.5$ pc.

3.7.2 The collimation region

After the recollimation region, at the position of the hypothetical standing shock, the local increase in density, pressure and magnetic field should generate an increase in the emission. The interaction between a travelling and a standing shock would further enhance the emission (Gomez et al. 1997). Furthermore, the standing shock would be dragged downstream by the traveling shock and re-established after a certain time at its initial position (Gomez et al. 1997; Mimica et al. 2009). We compare here our results with this scenario.

Since the evolution of the turnover frequency and turnover flux density between 2006.0

and 2006.3 showed Compton-stage-like behavior, i.e., decreasing turnover frequency and increasing flux density, we used the equations of the Compton stage to derive the possible evolution of the physical parameters (model C2). In this region a slower rate of jet expansion is found ($\rho = 0.35$). During this stage, the Doppler factor seems to be constant with distance, $-\rho \cdot d = 0.035$. In the context of the hypothetical shock-shock interaction, acceleration of the flow close to the axis is expected down to the discontinuity of the stading shock, where sudden deceleration would occur (see, e.g., Perucho & Martí 2007). Thus, it is difficult to assess whether the Doppler factor should increase or decrease in the whole region.

The magnetic field intensity decreases with an exponent $b = 1.35$, implying that the geometry of the magnetic field has changed, with contributions of non-toroidal components, but showing no hints of magnetic field enhancement. The parameter s, giving the spectral slope of the relativistic electron distribution changes to $s = 2$, which gives an optically thin spectral index $\alpha_0 = -0.5$.

The set of parameters derived for this time interval do not reflect the expected physical conditions of a traveling−standing shock interaction, other than a slight flattening of the spectral slope (from possible refreshment of particles). Nevertheless, the shock-shock scenario could hardly be reproduced by a one-dimensional model. Numerical simulations should be performed in order to study this hypothesis in detail. Another possibility is that the reason for the second peak is attached to the injection of a second shock from the basis of the jet. This is not observed, though.

3.7.3 The re-expansion region

After the re-collimation process, the jet re-expands, i.e., the jet radius increases again. In principle, the position of the re-collimation shock can be regarded as a "new" nozzle from which the fluid emerges. Therefore, when the shock front reaches this region, the expected evolution is, again, that predicted by the shock-in-jet model.

The evolution between 2006.3 and 2006.8 is identified within our hypothesis with the re-expansion region. Thus, the equations for an adiabatic loss stage were applied to the evolution turnover frequency and turnover flux density.

The opening of the jet is clearly apparent at this stage $r = 0.90$. This opening should produce a decrease in density, which translated into smaller values of the parameter $-\rho \cdot k$, $\left(K \propto r^{-\rho\, k}\right)$. From the fits, we derive $-\rho \cdot k = -4.2$, confirming a decay in the density. The magnetic field falls with $b = 1.7$, which shows again that the geometry of the field changes from a purely toroidal to a mixed structure with the distance. The values for $-\rho \cdot d = 0.18$ reveal an acceleration of the flow, which can naturally arise during the expansion of the jet. The spectral slope of $s = 2.4$ translates into an optically thin spectral index of $\alpha_0 = -0.7$.

3.7.4 Spectral slopes and optically thin spectral indices

The variation of the fitted optically thin spectral index, $\alpha_{0,\mathrm{f}}$, (see upper panel in Fig. 3.6) is an indication of the aging of the relativistic electron distribution due to the different energy loss mechanisms during the evolution of the flare. The model presented by Marscher & Gear (1985) did not include such an aging of the relativistic electron distribution. Despite

this restriction, we could model the qualitative behavior of the evolution via the different values obtained for parameter s in the different fitted stages: For the expansion region we obtained $\alpha_{0,\mathrm{m}} = -0.55$, a slightly flatter spectral index for the collimation region $\alpha_{0,\mathrm{m}} = -0.50$ and a steeper value for the re-expansion $\alpha_{0,\mathrm{m}} = -0.7$.

3.7.5 The influence of the interpolation and the quiescent spectrum

We applied several interpolation steps together with different quiescent spectral parameters to the analysis of the light curves in order to test their influence on the study of the evolution of the peak parameters in the turnover frequency−turnover flux density ($\nu_m - S_m$) plane. All the tests showed a second hump in the $\nu_m - S_m$ plane. From the tests, the positional shifts (in time of appearance, turnover frequency and turnover flux density) of the second hump were calculated: The hump appeared at $t = 2006.30 \pm 0.05$ yr at a turnover frequency $\nu_m = 56^{+5}_{-3}$ GHz and turnover flux density $S_m = 8.5^{+0.1}_{-0.9}$ Jy.

These tests proved that the increase of the turnover frequency and turnover flux density around 2006.3 is not an artifact generated by the interpolation and/or the choice of the quiescent spectrum.

3.7.6 Adiabatic versus non-adiabatic shock

Björnsson & Aslaksen (2000) suggested that the steep slopes in the rising region of the ν_m-S_m- plane, which is generally identified as the Compton stage in the shock-in-jet model, could not be due to Compton radiation, but to other processes such as isotropization of the electron distribution or even to the non-adiabatic nature of the shock.

The slope we obtained for this time-interval in the ν_m-S_m plane is too steep to be reproduced by the model presented in Björnsson & Aslaksen (2000) (see Sect. 3.6.1). Thus, the non-adiabatic nature of the first stages of evolution of shocks in extragalactic jets remains an open issue on the basis of our limited data set.

3.8 Summary

In this Chapter we presented the analysis of the 2006 flare in CTA 102 in the cm − mm regime. The obtained evolution could be well described, up to a certain point ($t < 2006.0$), with the standard shock-in-jet model (Marscher & Gear 1985). In order to model the further evolution of the flare we proposed a second Compton-like stage and a second adiabatic stage. We derived the evolution of the physical parameters of the jet and the flare and we performed a parameter space analysis to obtain the uncertainties of the values obtained. From the obtained parameters, together with their uncertainties, the theoretical light curves and spectra were computed. The result was shown to be in fair agreement with the observations.

However, the shock-in-jet model is not able to reproduce the second peak of the double-hump structure found in the evolution of the peak flux - peak frequency plane in a consistent way within our hypothesis of a shock-shock interaction.

In order to confirm or reject our hypothesis of the existence of a standing shock close to the jet nozzle and a travelling shock wave connected to the 2006 flare we have to

analyse Very Long Baseline Interferometer (VLBI) observations of the source. These observations have the unique capability to resolve the parsec-scale structure of the source and allow to image the innermost regions of the jet. In the next Chapter we perform a full kinematic analysis of CTA 102 using multi-epoch and multi-frequency VLBI observations.

4 VLBI kinematic analysis

This Chapter is partially published in Fromm et al. 2012, A&A, accepted

In Chapter 3 we analyzed the single-dish observations of the flare in CTA 102 and interpreted the double hump structure in the $\nu_m - S_m$-plane as the interaction between a traveling shock wave and recollimation shock. To prove the hypothesis of a shock-shock interaction we studied the kinematical evolution on the parsec scale. Since single-dish observations cannot resolve the jet structure, we used several high-resolution multi-frequency VLBA observations with a frequency range between 5 GHz and 86 GHz during the flaring time to study the kinematical variations. We combined our observations with the results of the 15 GHz MOJAVE observations and additionally analyzed the available 43 GHz VLBA observations of CTA 102 within the Boston Blazar Monitoring program. This extended data set allowed us to study the morphological evolution of the source over nearly two decades (early 1995 until late 2011).

4.1 VLBA observations and data analysis

4.1.1 Multi-frequency VLBA observations

We analyzed eight multifrequency VLBA observations with a frequency range between 2 GHz and 86 GHz centered around the 2006 radio flare. This coverage allowed us to study the flaring process during its different stages; the rise in the flux density from the quiescent stage, the flare, and the decay of the flare. The source was observed with all ten antennas of the VLBA, where CTA 102 was the main target within the experiment BR122. In the other observations CTA 102 was used as a D-term calibrator (see Table 4.1). In Table 4.2 we present the characteristic image parameters for the multifrequency VLBA observations. Out of the six 86 GHz observations only the May 2005 run has a high enough dynamic range to allow us to detect the extended structure of the source. Therefore, we cannot provide any kinematic results for images at this frequency.

4.1.2 Additional 15 GHz and 43 GHz VLBA observations from survey programs

The 15 GHz VLBA observations were taken from the MOJAVE archive (Lister et al. 2009b) and combined with our 15 GHz observations. We analyzed 36 epochs starting from June 1995 until October 2010 ($\langle \Delta t \rangle$ = 157 days).

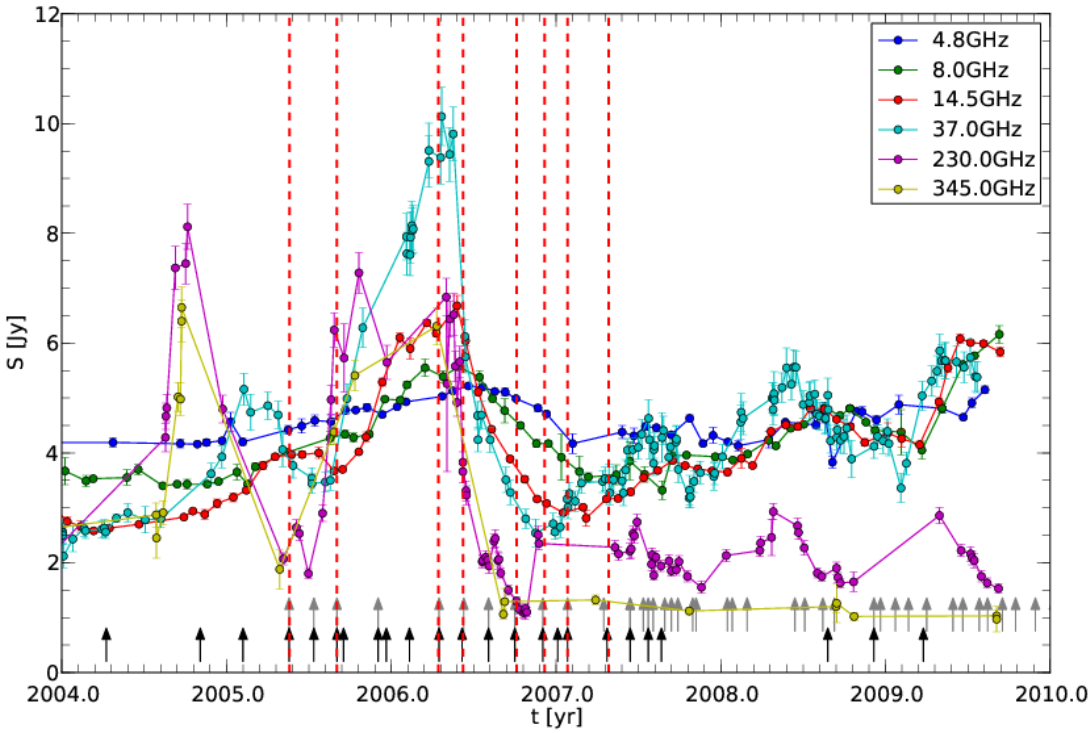

Figure 4.1: cm-mm single-dish light curves for CTA 102, covering the 2006 radio flare. The red dashed lines correspond to the epochs of multi-frequency VLBI observations presented in this work, the black arrows to the 15 GHz and the grey arrows to the 43 GHz VLBA observations.

Table 4.1: Used VLBI observations and frequency range

VLBA-ID	Date [yyyy-mm-dd]	Radio bands [a]	Notes
BS157A	2005-05-19	CXUKQW	HN receiver warm
BS157C	2005-09-01	CXUKQW	–
BR122A	2006-04-14	SCXUKQ	BR receiver warm
BR122B	2006-06-08	SCXUKQ	HN 3 hours lost
BW086B	2006-10-02	CXUKQW	BR focus problems
BW086C	2006-12-04	CXUKQW	–
BW086D	2007-01-26	CXUKQW	–
BW086E	2007-04-26	CXUKQW	SC weather problems

[a] S=2 GHz, C=5 GHz, X=8 GHz, U=15 GHz, K=22 GHz,Q=43 GHz,W=86 GHz

The 43 GHz VLBA observations were partially taken from the Boston blazar monitoring program database[2]. The source was on average observed every 58 days between May 2005 and January 2011, which led to a total number of 46 epochs.
In Figure 4.1 we present the temporal correspondence between the cm-mm light curves and the VLBA observations of CTA 102.

Table 4.2: Image parameters of the multi-frequency VLBA observations (see Table 4.1)

Frequency [GHz]	Epoch [yyyy-mm-dd]	RMS[a] [mJy/beam]	S_{peak} [Jy/beam]	S_{total} [Jy]	Θ_{maj} [mas]	Θ_{min} [mas]	P.A. [deg]
5.0	2005-05-19	0.21	1.61	4.05	3.65	1.62	−8.0
8.3	2005-05-19	0.25	1.68	3.91	2.32	1.02	−6.7
15.3	2005-05-19	0.26	2.22	3.71	1.33	0.55	−8.8
22.2	2005-05-19	0.55	2.33	3.21	0.95	0.40	−15.4
43.1	2005-05-19	0.60	2.63	3.16	0.53	0.20	−15.9
86.2	2005-05-19	2.76	1.94	2.34	0.25	0.11	−19.3
5.0	2005-09-01	0.32	1.73	4.13	3.36	1.57	−3.7
8.3	2005-09-01	0.39	1.48	3.23	1.98	0.94	1.4
15.3	2005-09-01	0.31	1.96	3.37	1.21	0.52	−6.1
22.2	2005-09-01	0.51	1.67	2.49	0.78	0.34	−7.4
43.1	2005-09-01	0.58	3.48	4.18	0.45	0.18	−12.3
2.3	2006-04-14	0.51	2.34	4.66	8.60	3.91	−7.7
5.0	2006-04-14	0.18	2.05	4.48	3.90	1.45	−11.2
8.4	2006-04-14	0.31	2.94	4.91	2.74	0.97	−13.2
15.4	2006-04-14	0.26	4.88	6.32	1.46	0.51	−14.1
22.2	2006-04-14	0.43	5.85	6.84	1.04	0.34	−16.6
43.2	2006-04-14	0.75	6.43	7.35	0.65	0.15	−15.8
2.3	2006-06-08	0.29	2.30	5.47	7.75	3.54	−2.4
5.0	2006-06-08	0.17	2.04	4.40	3.52	1.52	−6.7
8.4	2006-06-08	0.22	2.78	4.71	2.11	0.95	−1.1
15.4	2006-06-08	0.25	4.13	5.37	1.26	0.51	−8.7
22.2	2006-06-08	0.42	3.83	4.76	0.76	0.33	−6.2
43.2	2006-06-08	0.43	3.62	4.74	0.39	0.18	−5.0
5.0	2006-10-02	0.22	2.04	4.44	3.51	1.69	−9.5
8.3	2006-10-02	0.59	1.72	3.45	2.16	1.11	−4.9
15.3	2006-10-02	0.23	1.96	2.94	1.35	0.60	−14.7
22.2	2006-10-02	0.46	1.49	2.20	0.76	0.37	−7.5
43.1	2006-10-02	0.73	1.89	2.78	0.43	0.19	−10.6
5.0	2006-12-04	0.25	1.84	4.16	3.65	1.75	−9.7
8.3	2006-12-04	0.23	1.48	3.32	2.11	1.17	−4.0
15.3	2006-12-04	0.20	1.26	2.23	1.21	0.61	−10.7
22.2	2006-12-04	0.39	1.08	1.81	0.96	0.55	9.9
43.1	2006-12-04	0.51	1.76	2.40	0.45	0.21	−14.4
5.0	2007-01-26	0.72	1.43	3.32	3.36	1.71	−1.6
8.3	2007-01-26	0.26	1.12	2.55	2.06	1.11	−0.8
15.3	2007-01-26	0.22	1.13	1.99	1.20	0.58	−10.4
22.2	2007-01-26	0.39	1.22	1.94	0.72	0.39	−7.7
43.1	2007-01-26	0.66	2.61	3.31	0.38	0.19	−9.9
5.0	2007-04-26	0.24	1.39	3.59	3.46	1.81	−6.8
8.3	2007-04-26	0.28	1.16	2.99	2.10	1.14	−1.2
15.3	2007-04-26	0.20	1.55	2.50	1.23	0.57	−9.4
22.2	2007-04-26	0.34	1.58	2.24	0.88	0.39	−13.0
43.1	2007-04-26	0.54	2.54	3.04	0.44	0.20	−14.7

[a] RMS values are determined in a region of the final map without significant emission

4.1.3 Data reduction

We used National Radio Astronomy Observatory's (NRAO) Astronomical Image Processing System (AIPS) for calibrating the data. We performed an amplitude calibration and applied a correction to the atmospheric opacity for the high-frequency data ($\nu > 15$ GHz). The parallactic angle correction was taken into account before we calibrated the phases using the pulscal signal and a final fringe fit. The time- and frequency-averaged data were imported to DIFMAP (Shepherd 1997), where we used the CLEAN algorithm combined with phase and amplitude self-calibration and MODELFIT algorithms for imaging and model fitting, respectively (see Sect. 4.1.4).

The uncertainties on the obtained fluxes were estimated by comparing the total VLBA flux densities with the values measured by the University of Michigan Radio Astronomy Observatory (UMRAO) program (see Chapter 3. For the 5 GHz and 8 GHz VLBA observations we calculated a flux density difference between 10% and 15%, where the difference was between 5% and 10% for the 15 GHz ones. The estimates for frequencies above 15 GHz were more difficult to derive since the observations could be easily effected by variations in the wet component of the troposphere, but a conservative estimate led to an uncertainty value of 10% of the UMRAO flux density (Savolainen et al. 2008).

4.1.4 Model fitting

To parametrize the jet and trace the evolution of local flux density peaks along the jet, we fitted 2D circular Gaussian components to the fully calibrated visibilities using the MODELFIT algorithm in DIFMAP. These components were characterized by their flux density, $S_{\rm mod}$, position $r_{\rm mod}$, position angle (P.A.), $\theta_{\rm mod}$ (measured from north through east) and full width half maximum (FWHM), i.e., the deconvolved size of the components. We modeled the data at each frequency separately to avoid biasing effects. Since the number of fitted Gaussians was initially not limited, we added only a new component at a given frequency if this resulted in a significant decrease in the χ^2 value. This approach led to a minimum number of Gaussians that can be regarded as a reliable representation of the source. As mentioned in Lister et al. (2009b) the fitted components do not necessary correspond to physical features in the jet and may reflect a mathematical requirement to properly describe the complex structure of the source. To minimize the above-mentioned effect of a fitted Gaussian having a purely mathematical nature, we applied the following criterion: A fitted feature at a given frequency should be traceable at least within five consecutive epochs, and its evolution in position and flux density should be smooth without any strong jumps. If a component satisfies this principle we may interpret it as a region of locally enhanced emission generated by perturbations (shocks or instabilities) in the underlying jet flow.
the following we identify the most northern component at each frequency as the core, e.g., the foot point of the jet and compute the position of the additional components relative to the core. The uncertainties of the fitted components were typically around 5% on the total intensities(Lister & Homan 2005). In this paper we follow the suggestion of Lister et al. (2009b) that the uncertainties of the fitted components are around 10% of the component size convolved with the beam size. A more detailed determination of the component uncertainties is beyond the scope of this thesis.

4.2 Results

Here we present the results of modeling the source at different frequencies. Following the criteria presented by Lister et al. (2009b), we derive the kinematical parameters, e.g., the apparent speed, $\beta_{\rm app}$, only for those that are identified in five consecutive epochs or more, and we regard a component as stationary if the angular speed obtained is consistent with $\mu = 0$ within the observational accuracy. All analyzed epochs and modeled components at a given frequency are presented in the Appendix A.

4.2.1 Cross-frequency component identification

With multifrequency VLBI observations we can study the same physical region of a jet at different angular resolutions. In addition to the increase in the angular resolution with increasing frequency, there is the physical effect of the self-absorption of the emission. The shape of spectrum of the observed radiation, assuming that the detected emission is mainly generated by an ensemble of relativistic electrons, can be characterized by its spectral turnover, e.g., the frequency and flux density at the peak (ν_m and S_m). If the observing frequency is lower than the turnover frequency, ν_m, the emission will be self-absorbed (optically thick), in contrast, if the observing frequency is higher than the turnover frequency, the emission will be optically thin. This transition between optically thick and optically thin emission occurs in general in the core region.These two effects are reflected in the modeling of the source by splitting the core region into several features with increasing frequency.

For labeling the fitted components we use capital letters for the same physical regions and the numbers increase with decreasing core distance. The first criterion for the cross-frequency identification of fitted Gaussians is based on their position. Since we have not aligned the maps, e.g., corrected for the opacity shift, there is a slight shift in the position of these components. (The analysis of the opacity shift will be presented in Chapter 5) However, if a fitted component at a given frequency parametrizes a physical region in the jet, the observed angular speed obtained for this feature should be consistent with the angular speed derived from its counterpart at the other frequencies. Based on these two criteria we can clearly identify components across the different frequencies involved in this study. From our modeling we could cross-identify (in frequency and time) four different regions, labeled from A to D (see Figs. 4.2 and 4.3). The influence of the increased resolution on frequency is clearly visible by the amount of detail on the jet structure, which is most obvious on the kink around 4 mas away from the core (compare 5 GHz and 15 GHz image in Fig. 4.2). The combined effect of increased resolution and the transition from optically thick and optically thin emission can be seen in Fig. 4.3.

4.2.2 Calculation of kinematic parameters

The motions for the fitted components in CTA 102 can be divided into three different categories: i) stationary, ii) non-accelearting and iii) accelerating. To derive the kinematics of the source, we fit polynomials to the observed x- and y-positions of the fitted components. We follow the procedure presented in e.g., Lister et al. (2009b) and Schinzel et al. (2012), using first- and second-order polynomials if the components was detected in more than

ten epochs. (The latter can only be applied to the long-term monitoring of the source at 15 GHz and 43 GHz):

$$x(t) = \mu_x \left(t - t_{\mathrm{x},0}\right) + \frac{\dot{\mu_x}}{2} \left(t - t_{\mathrm{mid}}\right)^2 \tag{4.1}$$

$$y(t) = \mu_y \left(t - t_{\mathrm{y},0}\right) + \frac{\dot{\mu_y}}{2} \left(t - t_{\mathrm{mid}}\right)^2, \tag{4.2}$$

where $t_{\mathrm{mid}} = (t_{\mathrm{min}} + t_{\mathrm{max}})/2$, $t_{\mathrm{x},0} = t_{\mathrm{mid}} - x(t_{\mathrm{mid}})/\mu_x$ and $t_{\mathrm{y},0} = t_{\mathrm{mid}} - y(t_{\mathrm{mid}})/\mu_y$ are the component ejection times. Owing to the bent structure of CTA 102, the ejection cannot be computed from a simple back extrapolation if the trajectory is not clearly radial outwards. We only use the results of the second-order polynomial fit, if there is a significant decrease in the χ^2 value as compared to the linear fit. Using the average angular speed $\langle\mu\rangle$ obtained, we compute the kinematic parameters, e.g., apparent speed, β_{app}, and the Doppler factor, δ. The apparent speed of the components, β_{app}, is derived from the angular speed, μ:

$$\beta_{\mathrm{app}} = \frac{\langle\mu\rangle\, D_{\mathrm{L}}}{1+z}, \tag{4.3}$$

where D_{L} is the luminosity distance and z the redshift.

The Doppler factor is defined as $\delta = \Gamma^{-1}(1 - \beta\cos\vartheta)^{-1}$, where $\Gamma = (1-\beta^2)^{-1/2}$ is the bulk Lorentz factor and $\beta = v/c$. Since the β and ϑ are not measurable directly from the observations, two approaches have been used in the recent past to estimate the the Doppler factor, δ:
i) The first one assumes that the observed features are traveling at the critical angle, the angle that maximizes the speed of the feature (see Chapter 2.3). ii) We can also use causality arguments and estimate δ from the variability of the flux density and the size of the component (see, e.g., Jorstad et al. 2005b), to get a 'variability' Doppler factor

$$\delta_{\mathrm{var}} = \frac{d_{\mathrm{eff}} D_{\mathrm{L}}}{c\Delta t_{\mathrm{var}}(1+z)}, \tag{4.4}$$

with $d_{\mathrm{eff}} = 1.8 \times \mathrm{FWHM}$, the effective size of the component and $\Delta t_{\mathrm{var}} = dt/\ln(S1/S2)$, where $S1$ and $S2$ are the maximum and minimum of the component flux density and dt the time difference between these two flux density values. The variability Doppler factor and the apparent speed can be used to calculate estimates for the bulk Lorentz factor, Γ, and the viewing angle, ϑ, according to

$$\Gamma_{\mathrm{var}} = \frac{\beta_{\mathrm{app}}^2 + \delta_{\mathrm{var}} + 1}{2\delta_{\mathrm{var}}} \tag{4.5}$$

$$\vartheta_{\mathrm{var}} = \arctan\frac{2\beta_{\mathrm{app}}}{\beta_{\mathrm{app}}^2 + \delta_{\mathrm{var}}^2 - 1}. \tag{4.6}$$

The limited resolution at low frequencies means we cannot resolve some of the components that leads to blending effects between two or more features. Under these circumstances the values obtained for the apparent speed, β_{app} are too low and the calculated values for the viewing angle, ϑ are too high. The kinematic parameters for the fitted components are presented in Sects. 4.2.8 and 4.2.7. Since we observe CTA 102 at 2 GHz only for two epochs, April 2006 and June 2006, we neither derived kinematic parameters nor present model fitting results in the Appendix A.

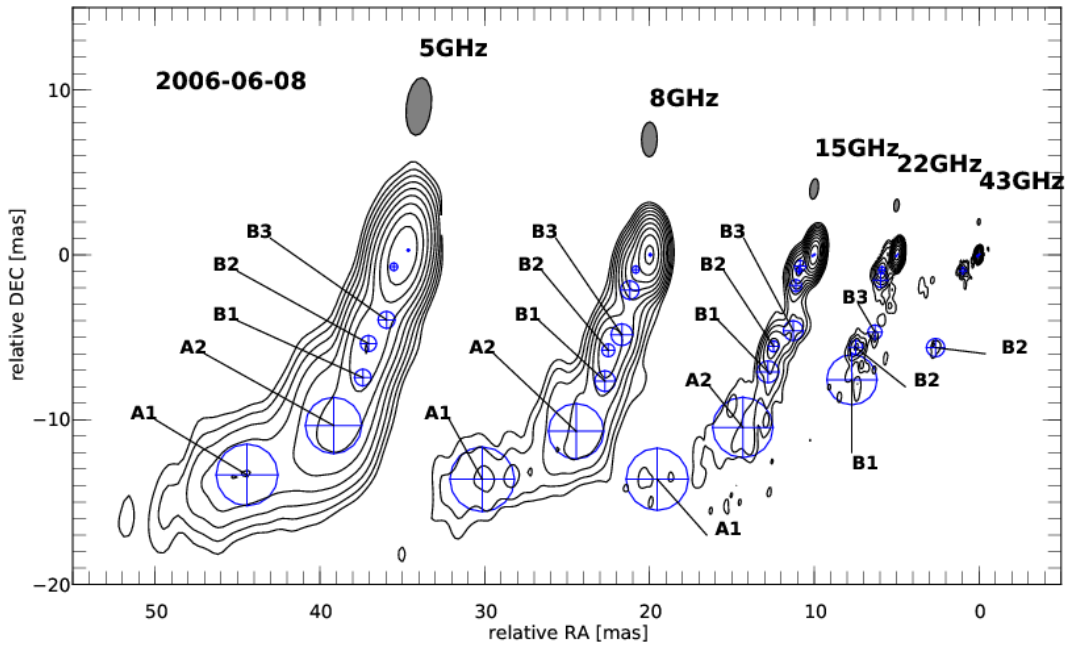

Figure 4.2: Uniform weighted VLBA CLEAN images with fitted circular Gaussian components at different frequencies for the July 2006 observation of CTA102. The lowest contour is plotted at 10× the off-source rms at 43 GHz and increases in steps of 2. The observing frequency and the restoring beam size are plotted above each map. For the labeling we use capital letters for the same physical region in the jet and the numbers increase with inverse distance from the core. For a more detailed picture of the core region see Fig. 4.3

4.2.3 Jet region A

The region labeled as A spreads from $r \sim 10$ mas to $r \sim 18$ mas. This region could be parametrized with two Gaussian components, labeled as A1 and A2, which we traced and cross-identified within our 5 GHz, 8 GHz, and 15 GHz observations (see Fig. 4.2). From our multifrequency observations we derived an angular speed for A1 between (0.15 ± 0.09) mas/yr at 5 GHz and (0.29 ± 0.16) mas/yr at 8 GHz. With the long-term monitoring of CTA 102 at 15 GHz, the angular speed we obtained is (0.18 ± 0.03) mas/yr.

The fit of the trajectory of A1 by a second-order polynomial led to $\chi^2_{\rm red} = 5.08$, which is no significant increase as compared to a first-order polynomial ($\chi^2_{\rm red} = 5.14$), from which we conclude that there is no detectable acceleration for this component. Based on the 15 GHz observations we derived an apparent speed, $\beta_{\rm app} = (9.4 \pm 1.9)c$ (for additional kinematic parameters see Table 4.3).The angular speed for the second feature in this region, A2, spans from (0.11 ± 0.06) mas/yr to (0.21 ± 0.045) mas/yr. We could not detect any clear indication of deceleration or acceleration of this feature from the long-term monitoring at 15 GHz and the calculated apparent speeds cover a range between $(6 \pm 3)\,c$ and $(11 \pm 2)\,c$.

For the presentation of the component trajectories we selected 15 GHz as the representative frequency. In Fig. 4.4 we show the temporal separation of A1 and A2 from the

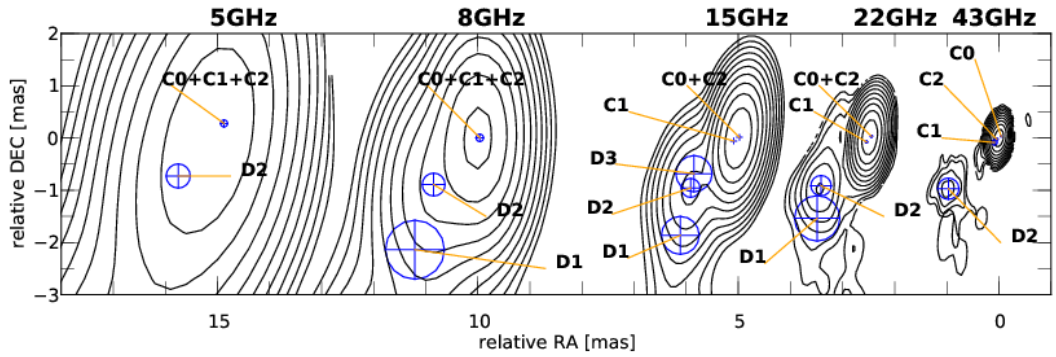

Figure 4.3: Zoom into the core region for the images presented in Fig.4.2. Notice the splitting of the C-components with increasing frequency. For map details see Fig.4.2.

core and the vector motion fits are presented in Fig. 4.5, where the lefthand panel shows the position of the components in the sky and the righthand side a zoom of the individual regions with overplotted trajectory in the contour plot. The components are plotted relative to the core position and the contour map corresponds to the 2006 June observations CTA 102. The lowest contour level is drawn at ten times the off-source rms (1 mJy and increase with a factor of 2). The apparent inward motion of A1 (see Fig. 4.4) is partly due to the nonradial, nearly transversal motion of this feature and in contrast, component A2 is mainly moving radially outwards (see inlets in Fig. 4.5).

Based on the derived angular speeds, μ, we could, within the accuracy and limitation of our time sampling in the multifrequency observations, identifiy A1 and A2 across our observations.

4.2.4 Jet region B

We parametrized the region further upstream the jet, between 4 mas and 8 mas with three circular Gaussian components. One of these features, labeled as B2, could be identified throughout our entire multifrequency data set (5 GHz to 43 GHz). All three components, B1, B2, and B3, show very low pattern speeds. In the following we discuss the properties of those components separately and in detail.

The angular speed for B1 is on average comparable to $\mu = 0$. However, we found from the 15 GHz observations an angular speed of $\mu = 0.016 \pm 0.005$ that corresponds to an apparent speed $\beta_{\rm app} = (0.85 \pm 0.25)c$. Furthermore, the second-order polynomial fit of the y-component of the B1 trajectory leads to a significant reduction of the χ^2 value compared to a linear fit, from $\chi^2_{\rm red} = 2.0$ to $\chi^2_{\rm red} = 1.0$. The value obtained for acceleration $\dot{\mu_y} = (0.01 \pm 0.002)\,{\rm mas/yr^2}$

Similar behavior to B1 is found for B2. The angular speed takes values between 0.05 ± 0.04 mas/yr and 0.015 ± 0.003 mas/yr, and the corresponding apparent speeds span $0.77 \pm 0.14\,c$ to $3 \pm 2\,c$. From the long-term monitoring programs at 15 GHz and 43 GHz we compute angular velocities around 0.015 mas/yr and subluminal apparent speeds $\beta_{\rm app} \sim 0.77\,c$. Based on the high-resolution 43 GHz observations, we could identify B2 within our observational limitations as quasi-stationary with a slight radial inward motion (see

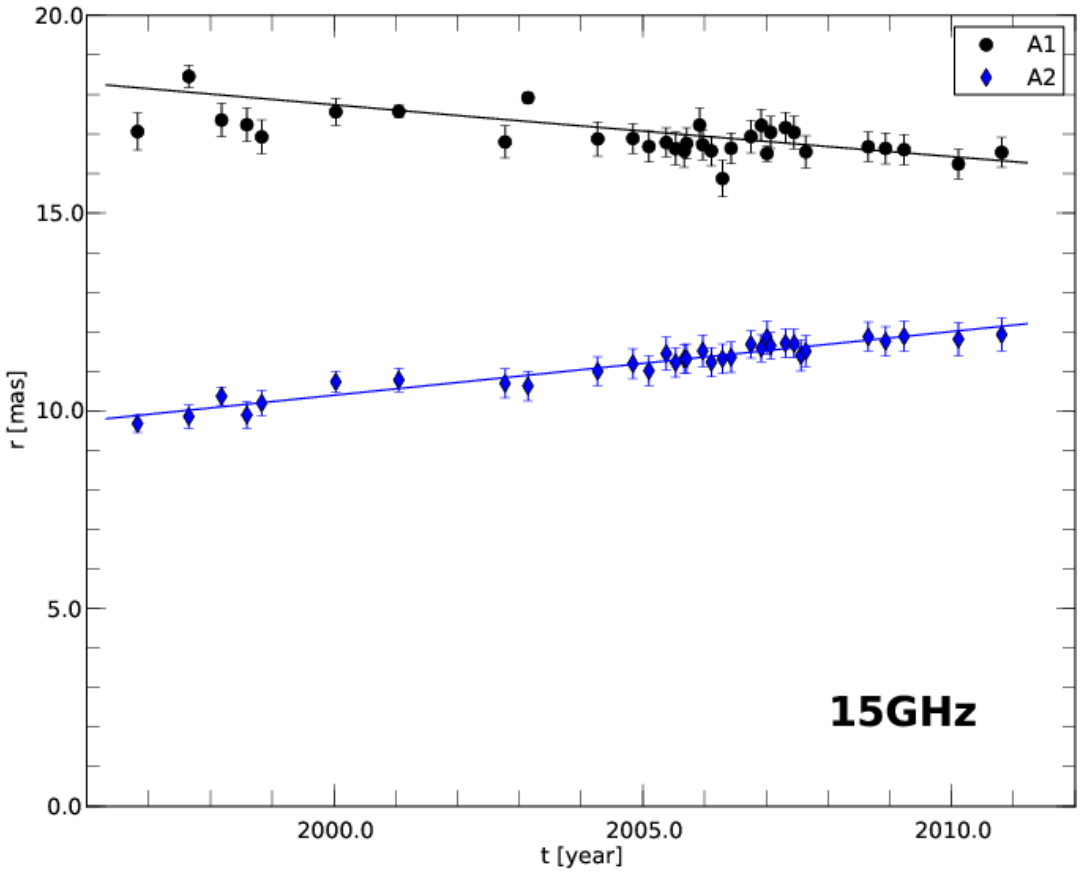

Figure 4.4: Temporal separation from the core for the components A1 and A2 at 15 GHz taken as representative frequency for the evolution of the cross-identified components within this region. The solid lines correspond to a first order polynomial fit to the x- and y-position separately.

inlet in Fig. 4.7).

The innermost component of this triplet is B3. Similar to the features farther downstream in region B, it is characterized by a small angular speed, where the scatter in μ obtained from the multifrequency campaign is larger due to the limited time span but is, within the uncertainties comparable to the derived angular speed from the 15 GHz observation. From these observation we calculated an angular speed of $\mu = (0.027 \pm 0.006)$ mas/yr and an apparent speed of $\beta_{\mathrm{app}} = (1.4 \pm 0.3)\,c$. The trajectory of B3 shows a nonradial outward motion with slow pattern speed.

As mentioned before, we used the 15 GHz modelfit results of the fitted components in region B as representative of the kinematics within this area. The evolution of the separation from the core for all components in region B is plotted in Fig. 4.6.The vector motion of the components B1, B2, and B3 is presented in Fig. 4.7.

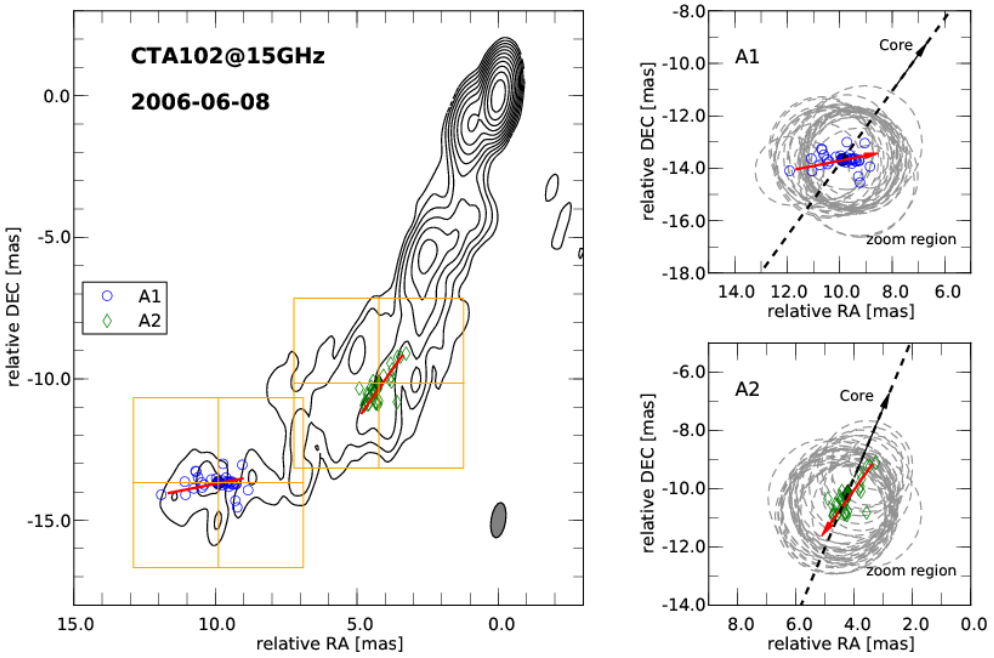

Figure 4.5: Vector motion fits and position of the fitted component in the sky. Left: 15 GHz CLEAN VLBI map of the June 2006 observations of CTA 102. The lowest contour level is drawn at 10× the off-source rms and the contours increase with steps of 2. The observational beam is plotted at the bottom right corner. The blue open symbols indicate the position of the components labeled as A1 and A2. The filled symbol correspond to the component position at the middle time, t_0, and the red solid line to the trajectory of the feature. The orange squares show the zoom region. Right: Zoom region for the individual components. The dashed gray circle are the components size (FWHM) and the dashed black line and black arrow correspond the direction to the core drawn from the position of the component at t_0. The red solid line illustrates the trajectory of the component and the direction of the component is indicated by the arrow.

4.2.5 Jet region D

The third region of the jet spans 1 mas to 3 mas away from the core and we parametrized this area with 2 to 3 Gaussians, labeled as D1, D2, and D3. At these distances from the core, the mentioned effects of increasing resolution with frequency lead to splitting fitted Gaussians into additional components. Therefore, it is difficult to distinguish and clearly cross-identify them.

The outermost component D1 is located around 3 mas from the core and is detected at 8 GHz, 15 GHz, and 22 GHz. We found from the long-term monitoring of CTA 102 at 15 GHz indications of an acceleration in the y direction. This acceleration is clearly visible in the y-direction of the 15 GHz representative of D1 for $t > 2005$. Since our time sampling at 8 GHz and 22 GHz spans $2005.4 < t < 2007.5$, the calculated values for the angular speed cannot be directly compared to the ones obtained at 15 GHz. Therefore, we could not clearly cross-identify this feature. The angular and apparent speeds obtained at

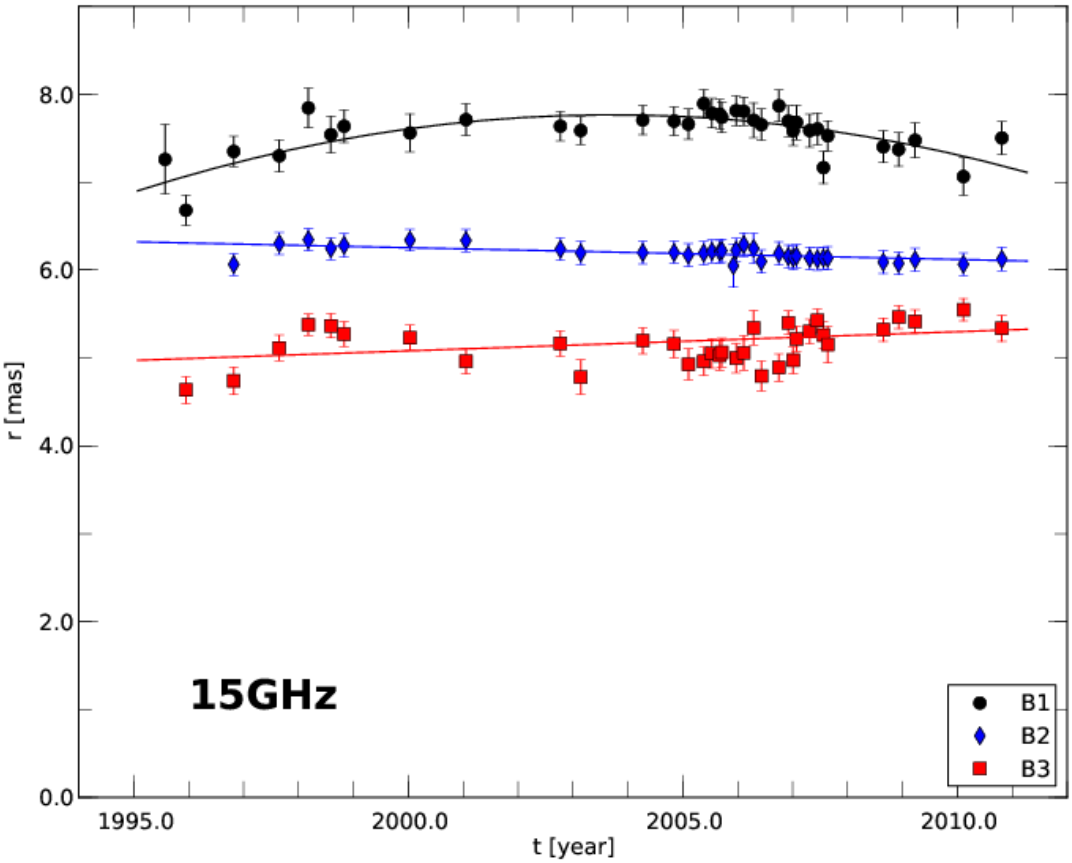

Figure 4.6: Temporal separation from the core for the components B1, B2, and B3 at 15 GHz taken as representative frequency for the evolution of the cross-identified components within this region. The solid lines correspond to polynomial fits to the x- and y-position separately.

15 GHz are (0.1 ± 0.02) mas/yr and $(5.7 \pm 1.2)\,c$. The component is moving on a highly nonradial trajectory outwards, nearly transversal to the main jet direction (see inlet in Fig. 4.9).

The feature labeled as D2 is detected throughout our entire multifrequency set. As in the case of D1 we found indications of an accelerating motion in both, the x and y-component of D2 from the 15 GHz and 43 GHz observations. As mentioned before, owing to the acceleration connected to this component and the limited time sampling at 5 GHz, 8 GHz, and 22 GHz the angular speeds obtained from those observations do not necessarily correspond to the ones derived from the 15 GHz and 43 GHz, but their positions are comparable within the uncertainties. We calculated an angular speed $\mu = (0.016 \pm 0.001)$ mas/yr, which corresponds to an apparent speed of $\beta_{\mathrm{app}} = (8.3 \pm 0.6)\,c$ using the long-term monitoring data at 15 GHz and 43 GHz. The trajectory of D2 is compared to the main jet direction at t_0 within the uncertainties in good agreement with a radial outward motion (see inlet in Fig. 4.9).

At 15 GHz we detect one additional feature in this jet region, labeled as D3, which we

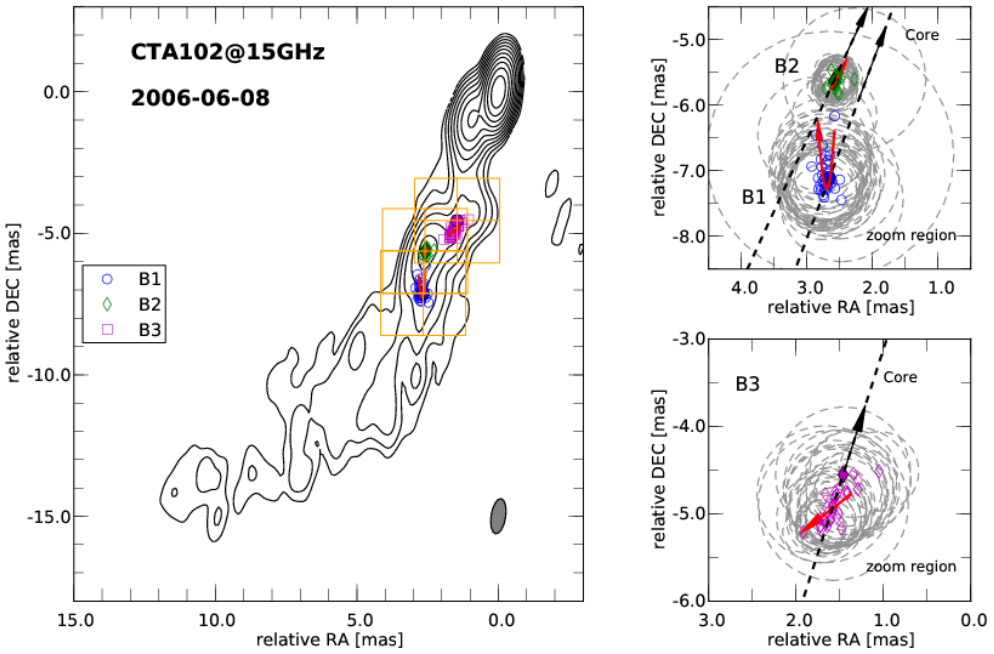

Figure 4.7: Same as Fig. 4.5 for components B1, B2, and B3.

could not distinguish at the other frequencies (see Appendix for all fitted components). The component D3 could be interpreted by blending effects in the core between two features that could be resolved at higher frequencies, especially 43 GHz (see following section).

In Fig. 4.8 we show the temporal separation from the core for D1, and D2 at 15 GHz and in Fig. 4.9 we present the vector motion fits of these components as crossidentified.

4.2.6 Jet region C

The cross-identification of the fitted features at distances $r < 1$ mas from the core is a difficult task due to both the aforementioned splitting of the components and the ejection of new components, which may be associated with flares. These new components can be partially resolved at the highest frequencies but not at lower frequencies. In general such a component will appear delayed at lower frequencies after it has clearly separated from the core and can be resolved at a given frequency. Therefore, we concentrate for the core region of CTA 102 on the results of the fitting using the 43 GHz observations. We use six circular Gaussians, including the core, for the parameterization of the core region. Two out of these six components are within our multifrequency observations, labeled as C1 and C2.

C1 is ejected from the core around 2005.3 with an apparent speed of $\beta_{\rm app} = (11.6 \pm 3.0)\,c$ ($\mu = (0.22 \pm 0.06)$ mas/yr). The y-component of the C1 trajectory shows indication of an nonlinear motion but there was not a significant increase in the $\chi^2_{\rm red}$ to use a second-order polynomial fit. Within the uncertainties of our observations we classify the motion

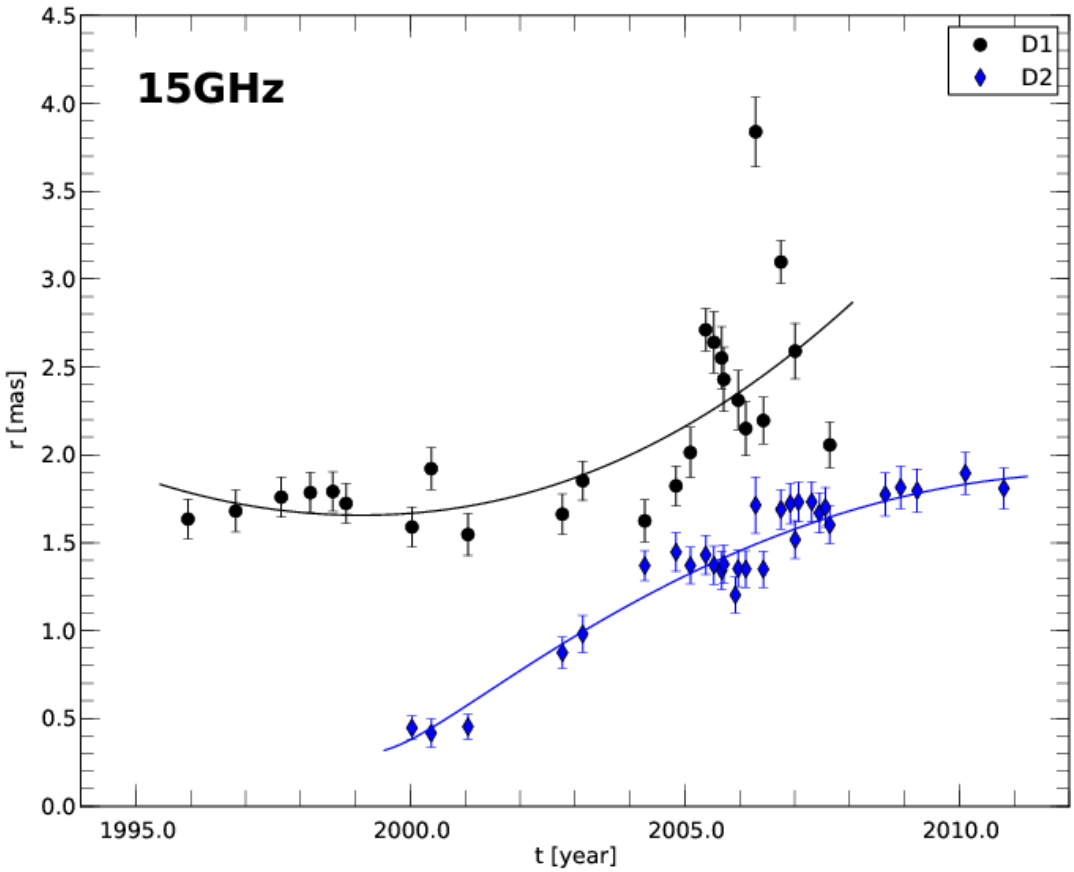

Figure 4.8: Temporal separation from the core for the components D1 and D2 at 15 GHz taken as representative frequency for the evolution of the cross-identified components within this region. The solid lines correspond to a first order polynomial fit to the x- and y-position separately.

of C1 as radially outwards.

The second component is ejected from the core in $t_{\mathrm{ej}} = (2005.9 \pm 0.4)$ yr with a comparable angular speed to C1 $\mu = (0.25 \pm 0.04$ mas/yr corresponds to an apparent speed of $\beta_{\mathrm{app}} = (13.0 \pm 2.1)\,c$. This feature is most probably connected to the strong radio outburst in CTA 102 in April 2006 and is moving radially outwards (see Sect. 5.6).

The two additional features, C3 and C4, show a clear nonlinear trajectory. In the case of C3, the component moves away from the core until a distance of 0.15 mas and keeps this position until the last of our observations. A second-order polynomial fit reduced the χ^2_{red} from 5.0 to 2.3, and the apparent speed obtained is $\beta_{\mathrm{app}} = (3.8 \pm 0.6)$ c, which is three times smaller than the apparent speeds obtained for C1 and C2. Owing to the highly curved trajectory of the component, we could not compute an estimate for the ejection time. The first part of the trajectory could be classified as radially outward. However, farther downstream the component is moving nonradially inwards.

The position of C4 remains constant at $r \sim 0.1$ mas from the core until 2009.6 and increases later. The reduced χ^2 value decreased from a value of 5.5 to 2.2 by using a

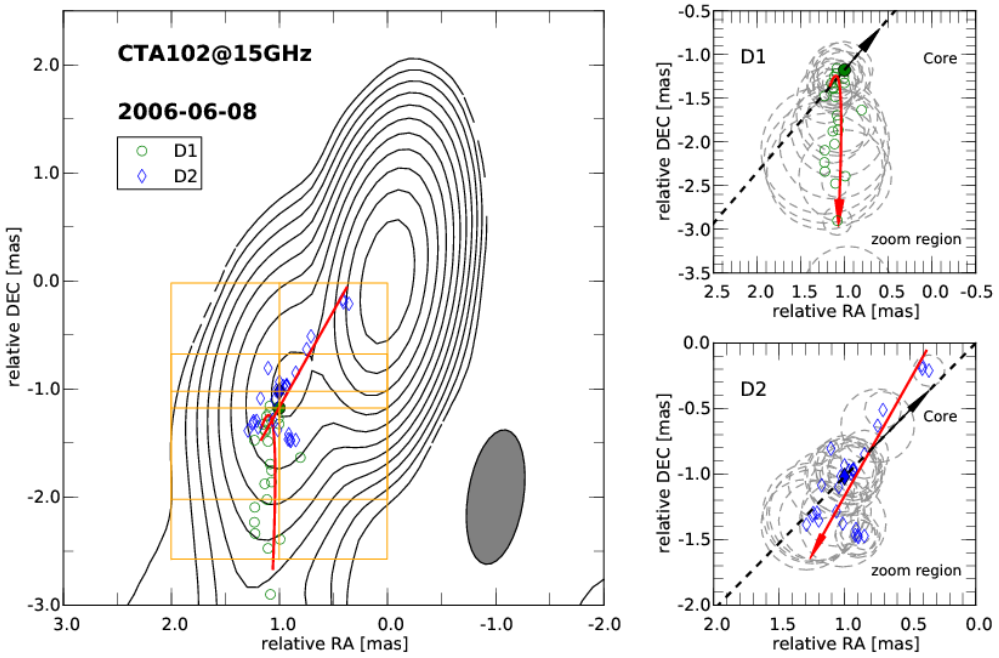

Figure 4.9: Same as Fig. 4.5 for components D1, and D2.

second-order polynomial instead of a first-order one. This fit leads to an apparent speed of $\beta_{\rm app} = (9.1 \pm 0.5)\,c$. As in the case of C3, we could not derive an estimate for the time where the radial separation from the core is consistent with zero ($r(t_{\rm ej}) = 0$), i. e., the ejection time. The trajectory of C3 shows clear indications of a nonradial motion.

In Fig. 4.11 we plot the radial separation from core for all components in the core region and in Fig. 4.10 we present the vector motion fits. All fitted components in this region have the common behavior of having a nearly constant separation from the core during their early detection (See inlets in Fig. 4.10).

4.2.7 Summary of cross-identification

Here we summarize the results of the previous sections on the cross-identification of fitted components. We could clearly identify seven features throughout our entire data set. As mentioned before identification of components in the core region is a difficult task due to resolution, self-absorption effects and continuous ejection of new features. However from the 43 GHz observations we could detect four new features, were two of them where ejected during our multifrequency observations and one of them could be connected to the 2006 radio flare (see Sect. 5.6). In Table 4.3 we present the average kinematic parameters of those components.

Only four components show a clear radial outward motion, best seen in C1 and C2. These components are detected in the core region, where the jet is straight and does not show strong bends. On the other hand, the nonradial motion of the majority of the cross-identified components may reflect the highly curved nature of CTA 102. The inward mo-

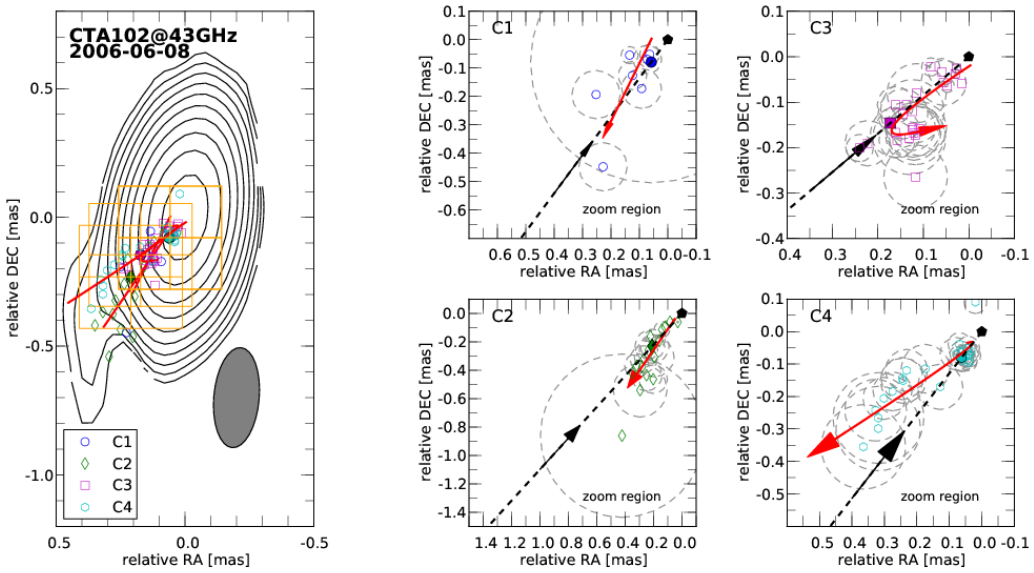

Figure 4.10: Same as Fig. 4.5 for components C1, C2, C3, and C4. Notice, that the core is indicated here by the black pentagon marker

tion of B2 could be the effect of its low pattern speed and the uncertainties in the position of the component. In Fig. 4.12 we show a vector motion map for all identified components. In case of the critical angle assumption the apparent speed corresponds also the lower limit of the Doppler factor.

The detected acceleration in C3 and C4 could reflect either an acceleration of the fluid or the blending effect between a stationary feature close to core at $r \sim 0.1$ mas. However, we could not detect indications of any acceleration in C1 and C2, which are located at a similar distance from core. Furthermore, Jorstad et al. (2005b) find in their analysis of earlier 43 GHz VLBI observations a stationary feature (labeled as A1 in Jorstad et al. (2005b)) at 0.1 mas from the core. If we assume that there is such a feature, we could split the components C3 and C4 into a stationary and traveling feature and compute the kinematic parameters for the moving ones. Such a procedure leads to an angular speed of $\mu = (0.20 \pm 0.05)$ mas/yr ($\beta_{\rm app} = (10 \pm 2)\,c$) for C3 and $\mu = (0.30 \pm 0.02)$ mas/yr ($\beta_{\rm app} = (15 \pm 1)\,c$) for C4. The values obtained are, within the uncertainties, in good agreement with the ones for C1 and C2, which favors the blending between a stationary and traveling components as a possible explanation for the trajectories of C3 and C4.

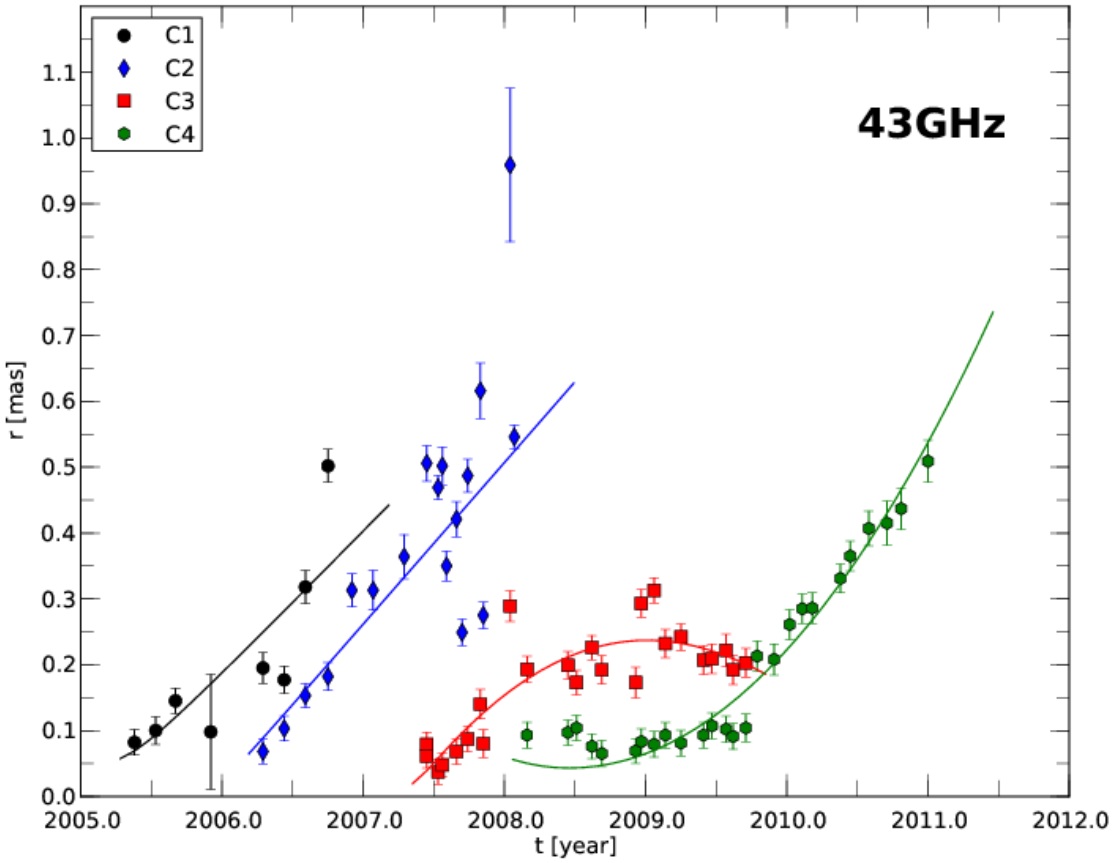

Figure 4.11: Temporal separation from the core for the components C1, C2, C3, and C4 at 43 GHz taken as representative frequency for the evolution of the cross-identified components within this region. The solid lines correspond to a first order polynomial fit to the x- and y-position separately.

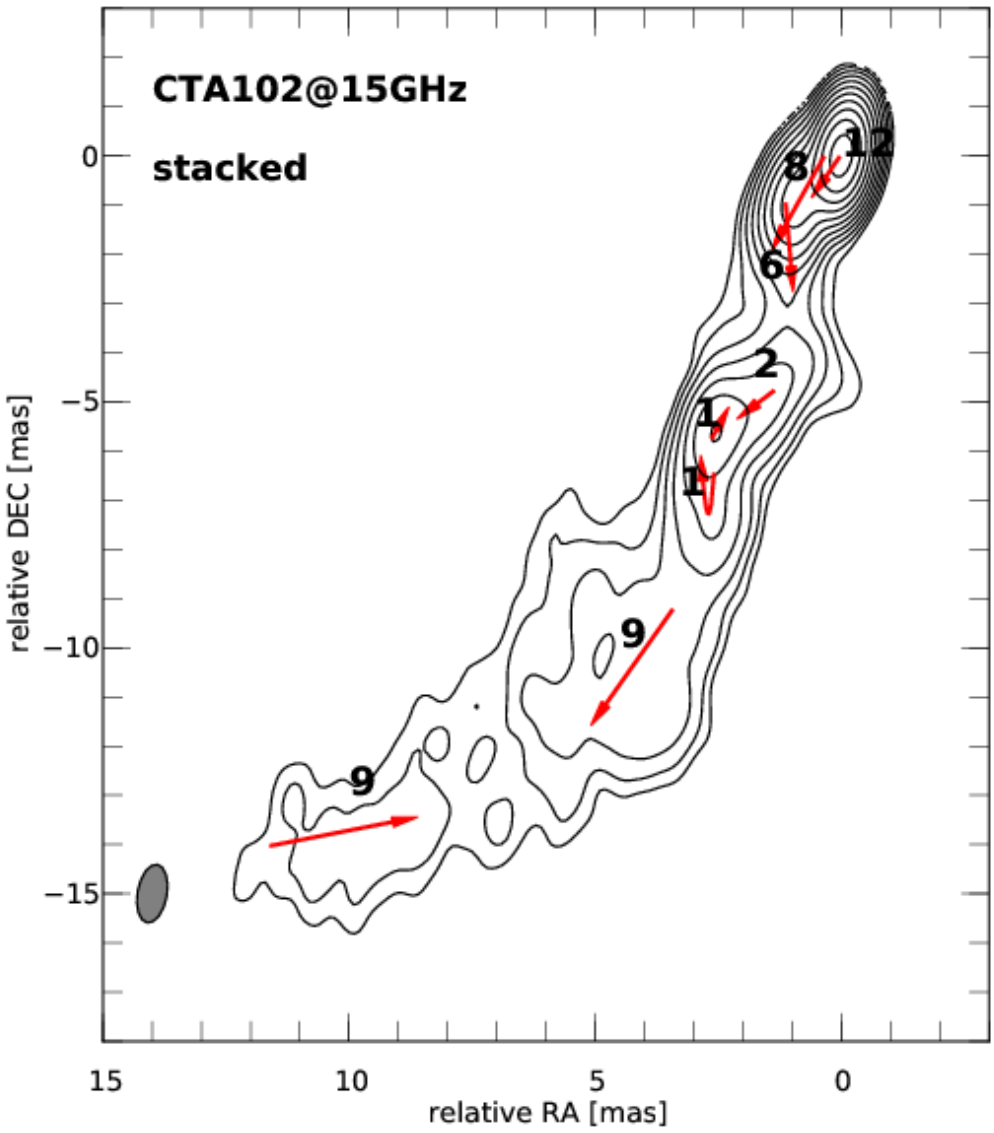

Figure 4.12: Vector motion map for CTA 102. The contour maps corresponds to the stacked 15 GHz observation of CTA 102 and the arrows indicate the trajectories of each cross-identified component. The lowest contour level is drawn at 5× the average off-source rms (4 mJy) and the contours increase with steps of 2. The numbers above are the apparent speed of the component as multiples of the light speed. Notice, that in case of the critical angle assumption the apparent speed corresponds also the lower limit of the Doppler factor.

Table 4.3: Results of the kinematic analysis for the cross-identified components

Comp	$< \mu >$ [mas/yr]	$\beta_{\rm app}$ [c]	$\delta_{\rm crit}$ [1]	$\vartheta_{\rm crit}$ [°]	$t_{\rm ej}$ [yr]	$< r >$ [mas]	$t_{\rm min}$ [yr]	$t_{\rm max}$ [yr]	acceleration	classification
A1	0.18±0.03	9.4±1.9	9	6	−−	17.0±0.5	1996.8	2010.8	no	no-radial inward
A2	0.17±0.01	8.7±0.5	9	7	1945±6	11.2±0.2	1996.8	2010.8	no	radial outward
B1	0.016±0.005	0.85±0.25	1	–	−−	7.6±0.3	1995.6	2010.8	yes	no-radial outward
B2	0.015±0.003	0.77±0.14	1	–	−−	6.2±0.1	1996.8	2010.8	no	radial inward
B3	0.027±0.006	1.41±0.32	2	–	−−	5.1±0.2	1995.9	2010.8	no	non-radial outward
D1	0.10±0.02	5.7±1.2	6	10	−−	2.1±0.4	1995.9	2007.6	yes	non-radial outward
D2	0.16±0.01	8.3±0.6	8	7	1997.1±0.4	1.6±0.4	2000.0	2011.0	yes	radial outward
C1	0.22±0.06	11.6±3.0	12	5	2005.1±0.2	0.2±0.1	2005.4	2006.8	no	radial outward
C2	0.25±0.04	13.0±2.1	13	4	2005.9±0.2	0.4±0.2	2006.3	2008.0	no	radial outward
C3	0.07±0.01	3.8±0.6	4	15	−−	0.2±0.1	2007.5	2009.7	yes	non-radial outward
C4	0.17±0.01	9.1±0.5	9	6	−−	0.2±0.1	2008.2	2011.0	yes	non-radial outward

4.2.8 Variation of the apparent speed and Doppler factor

The results of the kinematic analysis of the cross-identified components show that the apparent speed increases between 0.2 mas $< r <$ 1.0 mas (region C in Fig. 4.3) from $\beta_{\rm app} = 4$ to $\beta_{\rm app} = 13$. Farther downstream the values decrease from $\beta_{\rm app} = 8$ to $\beta_{\rm app} = 1$ between regions D (1.0 mas $< r <$ 5.0 mas) and B (5.0 mas $< r <$ 8.0 mas). This fall is related with the very low pattern motion of the components in the latter. In the extended jet region A ($r >$ 8.0 mas), the apparent speed increases again and reaches a constant value (within uncertainties). Figure 4.13 shows the apparent speed for all cross-identified components versus its average position, taken as a representation of its location. The apparent speed, $\beta_{\rm app}$, and the Doppler factor, $\delta_{\rm crit}$, assuming the components are traveling at the critical angle, $\vartheta_{\rm crit}$, are presented in Table 4.3.

The degeneracy of the apparent speed and Doppler factor on the intrinsic speed, β, and the viewing angle, ϑ, does not allow any direct conclusion on the variation in the fluid speed. This degeneracy can be broken if we obtain additional information on the Doppler factor from the variability of the flux densities. One of the requirements for applying this second method in calculating of the Doppler factor is that the flux densities should have an exponential behavior for several time segments (Jorstad et al. 2005b). The components C2 and D1 fulfill this requirement (see Fig. 4.14), and we computed their variability Doppler factor, $\delta_{\rm var}$ and the corresponding viewing angle, $\vartheta_{\rm var}$. The results of these calculations are presented in Table 4.4. The variability Doppler factor decreases from $\delta_{\rm var} = 17 \pm 3$ at $\langle r \rangle \sim 0.4$ mas (C2) to $\delta_{\rm var} = 8 \pm 2$ at $\langle r \rangle \sim 2.1$ mas (D1). The viewing angle, $\vartheta_{\rm var}$ is smaller than the critical angle for both components (see Tables 4.3 and 4.4). We can then conclude that the fluid decelerates between (0.4 $< r <$ 2.1) mas. However, there is also a change in the viewing angle, ϑ.

Table 4.4: Used parameters for the calculation of the variability Doppler factor and viewing angle for components C2 and D1

component	$d_{\rm eff}$ [mas]	$\Delta t_{\rm var}$ [yr]	$\delta_{\rm var}$	$\vartheta_{\rm var}$
C2 (2006.3<t<2007.9)	0.16 ± 0.02	0.33 ± 0.06	17 ± 3	3.2 ± 0.2
D1(1998.6<t<2003.1)	0.77 ± 0.05	3.3 ± 0.8	8 ± 2	6.8 ± 0.5

4.2.9 Variation of the brightness temperature, $T_{\rm b}$

We approximated the evolution of the brightness temperature by a power-law ($T_{\rm b} \propto r^a$) and applied the formalism and equations presented in Sect. 2.2.3 in order to extract the variation of the physical parameters along the jet.

Following the convention of regions defined above, from A to D, we derived a decrease in the brightness temperature between 0.1 mas and 1 mas (region C). Region D, 1 mas to 4 mas, shows a decrease in the Doppler factor (Fig. 4.13) and a further steepening of the brightness temperature gradient as compared to region C. In region B (4 mas to 7 mas) the brightness temperature values increases and farther downstream ($r >$ 7 mas), the brightness temperature decreases again (see Fig. 4.15). We applied power-law fits to

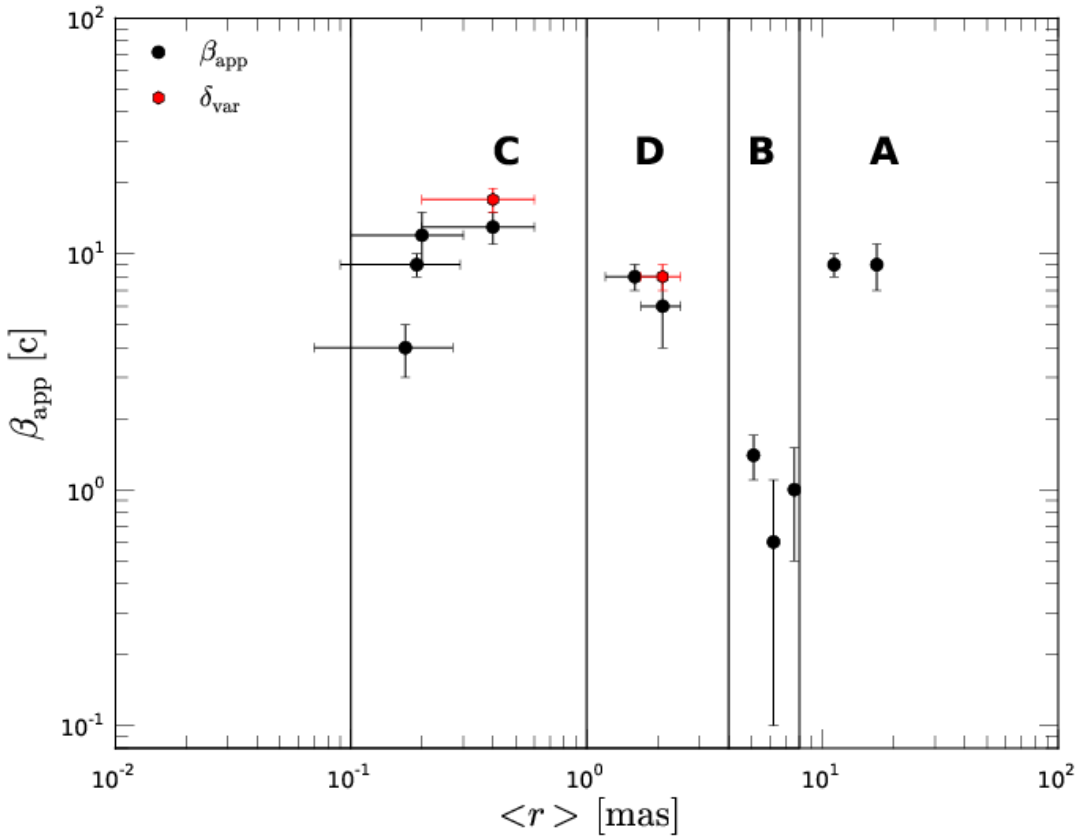

Figure 4.13: Variation of the apparent speed, β_{app} along the jet. The two red points correspond to the variability Doppler factors, δ_{var}, computed for components C2 and D1.

the brightness temperature evolution as a function of the core distance to the different regions. The results are presented in Table 4.5 and are discussed in the following. The study of the transversal jet size within the analysis of the jet ridge line allowed us to constrain the estimates for the exponent ρ, thereby parametrizing the jet width (see Chapter 5). The values obtained for the parameter ρ (jet opening index) are presented in Table 4.6.

Table 4.5: Results of the power law indices from the brightness temperature as a function of the distance to the jet basis $T_b \propto r^a$.

region	C	D	B	A
a	-1.9 ± 0.2	-4.8 ± 0.3	2.0 ± 0.6	-2.7 ± 0.2

Table 4.6: Estimates for the exponent ρ, defining the jet geometry $R \propto r^\rho$ (see Chapter 5).

region	C	D	B	A
ρ	0.8 ± 0.1	0.8 ± 0.1	-1.0 ± 0.1	1.3 ± 0.2

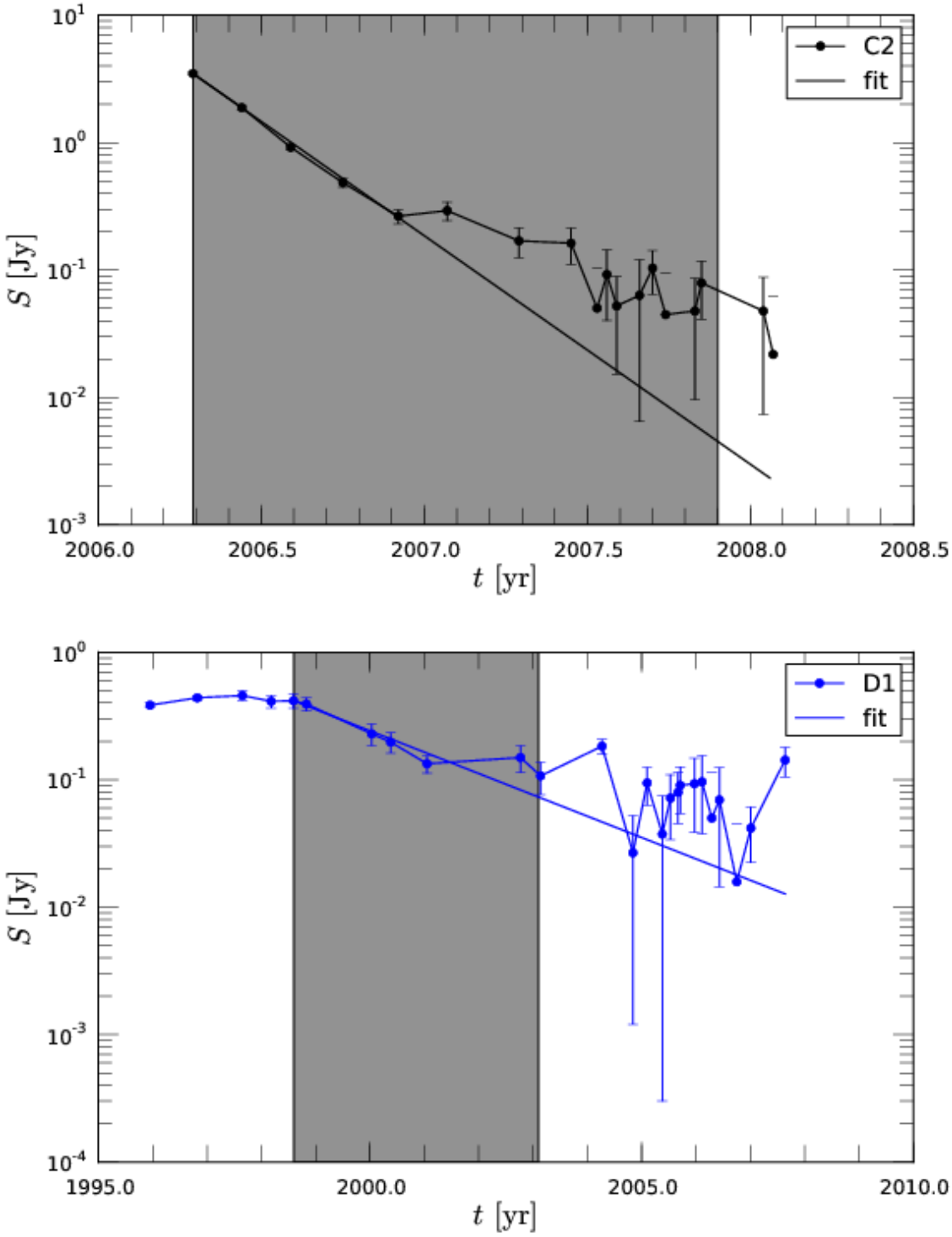

Figure 4.14: Variation of the flux densities for the components C2 (left panel) and D1 (right panel). The grey shaded ares indicate the time range used for the calculation of the variability Doppler factor and the solid line correspond to an exponential fit to the flux densities.

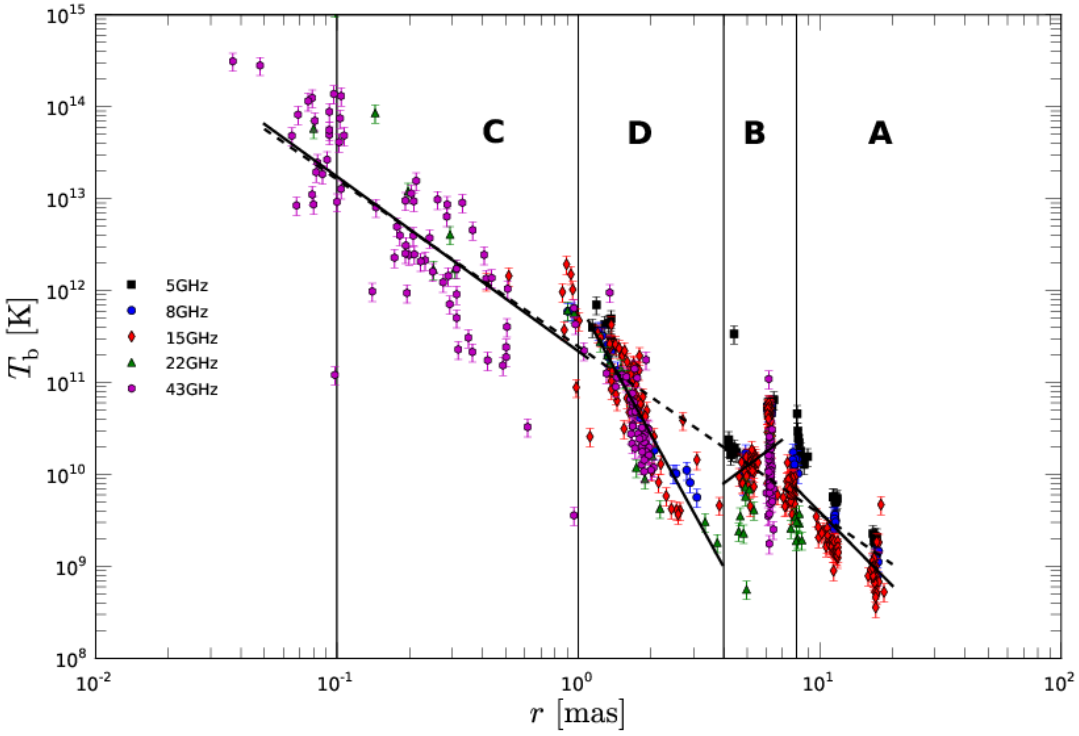

Figure 4.15: Variation of the brightness temperature, T_b with distance along the jet for all available epochs and cross-identified components (presented in Tables A.6 and A.7). Notice that the nearly vertical variation within 6 mas $< r <$ 8 mas in region B reflect the temporal variation in the size of the fitted Gaussians. The solid lines corresponds to power law fits $T_b \propto r^a$ to the individual regions and the dashed line to a power law fit to the entire range 0.1 mas $< r <$ 20 mas which leads to an exponent $a = -1.8$ (see text).

We discuss the results in the following terms: i) the jet is in equipartition (magnetic energy density is equal to the kinetic energy density of the relativistic particles), ii) the magnetic field is toroidal ($b = 1$), and iii) the magnetic field is poloidal ($b = 2$). In the three cases we consider adiabatic expansion and compression. We thus assumed that, at distances $r >$ 0.1 mas (deprojected 18 pc) Compton and synchrotron losses can be neglected as the dominant energy-loss mechanism (Mimica et al. 2009). The energy losses that the jet undergoes imply a decrease in the intensity of the magnetic field and in the Lorentz factors of the electrons. This makes it difficult for synchrotron radiation to dominate the losses far from the jet nozzle (Mimica et al. 2009). Therefore, we considered only adiabatic losses within adequate boundaries for the parameters s, b, k, and d in our analysis.

Region C (0.1 mas $< r <$ 1.0 mas)

The variation in the brightness temperature in the region B (0.1 mas $< r <$ 1.0 mas) could be best studied at 43 GHz. At this frequency we achieved the required resolution to resolve the jet, and the long-term monitoring provides us a large number of data points that

increased the statistical significance. The power-law fit gave an exponent of $a = -1.9 \pm 0.2$ (Table 4.5). In Fig. 4.16, the different panels, labeled 1 to 3, show the range of possible parameters for the three different jet configurations proposed (indicated at the top of each panel). The panels show the variation in the exponent that determines the evolution of the Doppler factor, $\delta \propto R^{-d}$ or in terms of distance along the jet $\delta \propto r^{-\rho d}$ using $R \propto r^{\rho}$ in terms of the exponents ρ and s.

We find that for all three magnetic field configurations, the Doppler factor should increase with distance ($d < 0$). Among the three cases studied, the slowest increase corresponds to the toroidal magnetic field ($b = 1$), and it is faster for the other field configurations, with a higher value of abs(d). The increase in the Doppler factor could be due to an increase in the fluid speed and/or a decrease in the viewing angle. The increase in $\beta_{\rm app}$, together with the increasing δ, suggests an acceleration of the fluid. However, our kinematic analysis of the cross-identified components did not allow us to extract any indication of fluid acceleration (see Fig. 4.11 and Table 4.3).

Region D (1 mas $< r <$ 4 mas)

The power law fitted to the evolution of the brightness temperature ($T_b \propto r^a$) in this region yields a value of $a = -4.8 \pm 0.3$. The results of the parameter space study in this case are shown in panels 4−6 in Fig. 4.16. The three different configurations, using the value obtained for ρ (see Table 4.6), lead to two clearly different results: On the one hand, if the magnetic field is purely toroidal, the Doppler factor had a decreasing exponent throughout the entire parameter space. On the other hand, an equipartition magnetic field and a purely poloidal magnetic filed permitted a decreasing or increasing Doppler factor, depending on the spectral slope. Based on the kinematics obtained, we found a slightly decreasing Doppler factor derived for components C2 and D1, which is compatible with the toroidal configuration (see panel 5 in Fig. 4.16), but due to the lack of data within this region we could not rule out any other possibility.

Region B (4 mas $< r <$ 7 mas)

In contrast to the regions C, D, and A, the brightness temperature increased with distance in this region. This behavior led to a positive value for the exponent a ($T_b \propto r^a$). We derived an exponent $a = 2.0 \pm 0.6$ and at the same distance from the core, we found a change from an expanding jet $\rho > 0$ to a collimating jet $\rho < 0$ (see Table 4.6). We calculated the possible values for the parameter d for a collimating jet $\rho < 0$, and the results are presented in panels 7-9 in Fig. 4.16. In the case of a collimating jet, a positive value of d corresponds to an increase in the Doppler factor, and the opposite is also true ($\delta \propto R^{-d}$ & $R \propto r^{\rho} \rightarrow \delta \propto r^{-\rho d}$). The parameter space study showed that the Doppler factor decreased for all jet configurations within the limits obtained for jet expansion rate, ρ. The major difference between the model is that the computed values for d are rather extreme $0.6 < d < 1.6$ for nontoroidal magnetic field configurations. Assuming that the magnetic field is toroidal $\left(B \propto r^{-1}\right)$ in region D, we favor the continuation of the magnetic field configurations.

Region A ($r > 7$ mas)

At distances over $r > 7$ mas, the brightness temperature decreased again with an average exponent of $a = -2.7 \pm 0.2$. Taking into account that the expansion index of the jet in this region is $\rho = 1.3 \pm 0.2$ (see Table 4.6), we obtained the possible values for the evolution in the Doppler factor (see panels 10 – 12 in Fig. 4.16). All the studied jet configurations imply an increase in the Doppler factor and the different models only differ in terms of the resulting exponent d. As in the case of region C, the slowest increase of the Doppler factors was obtained for $b = 1$. Considering that the field geometry cannot change from toroidal to poloidal, a continuation of a toroidal magnetic field configuration is the most plausible one (see panel 11 in Fig. 4.13).

4.3 Discussion

In the region close to the core ($r < 4$ mas), we detect several traveling features, most visible at 43 GHz (Figs. 4.10 and 4.11). These features can be interpreted as traveling shock waves, which can be generated by differential injection pressure at the jet nozzle (e.g., Perucho et al. 2008). Shock waves travel downstream, compressing the medium ahead of the shock front and re-accelerating particles. The increase in radiation induced by the shock is observed and can be traced along the jet, until it fades due to losses and to the limited dynamical range of the observations. In contrast to the expected flux density evolution of a traveling shock, we observe that C1, C3, and C4 show some local increase in their flux densities while they propagate downstream around $r \simeq 0.1 - 0.2$ mas. This could be explained in terms of the interaction of this shock with a standing recollimation shock (e.g., Gomez et al. 1997; Mimica et al. 2009), or by an increase in the Doppler boosting of the component if it travels along a helical jet, at the positions where it is closer to the line of sight (e.g., Hardee 2000; Aloy et al. 2003). Recollimation shocks may appear if the jet and the ambient medium are not in pressure equilibrium at the nozzle. Our observations do not allow us to resolve any change in the jet direction at this position, and neither the Doppler factor (Sect. 4.2.8 and Fig. 4.13) nor the brightness temperature (Sect. 2.2.3 and Fig. 4.15) analysis permit us to obtain any clear results from this region, but we did find some independent evidence that favors the presence of a standing shock at this position (see Chapter 3 and 5).

4.3.1 The physical parameters along the jet

The Doppler factor δ

In the previous sections, we have seen that Doppler factor should increase in region C (0.1 mas $< r <$ 1 mas), according to the shock-in-jet model applied to the observed evolution of the brightness temperature. Since our sampling at 43 GHz is not dense enough we could not calculate variability Doppler factors to test this conclusion.

The variability Doppler factor, $\delta_{\rm var}$, computed between regions C and D shows a decrease with distance (see Fig. 4.13 and Sect. 4.2.8). At the same time, the apparent speed decreases and the viewing angle, $\vartheta_{\rm var}$, is smaller than the critical viewing angle, $\vartheta_{\rm crit}$. This implies that the fluid decelerates within this region. This deceleration of the fluid is in

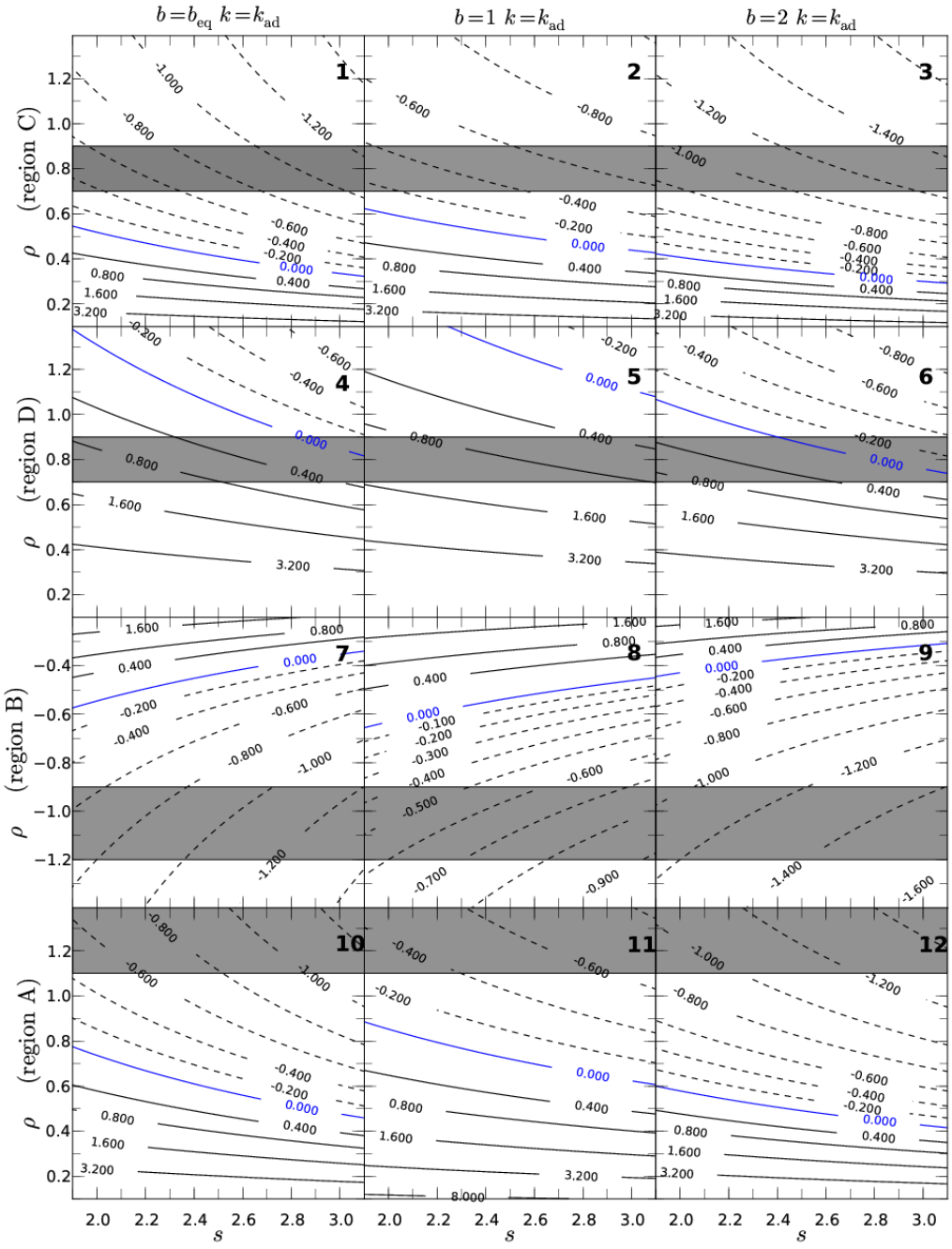

Figure 4.16: Parameter space for the evolution of the Doppler factor index d as a function of the jet expansion index ρ and the spectral slope s for the different region A - D for three different jet configurations, The first column assumes a an adiabatic jet ($k = k_{ad} = 2(s+2)/3$) and equipartition between the magnetic energy density and the kinetic energy of the relativistic particles, represented by $b = b_{eq} = (s+2)/3$. The second and third column show the evolution of d for an adiabatic jet ($k = k_{ad}$) and decreasing magnetic field $b = 1$ or $b = 2$, respectively. The panels show the allowed range for the exponent d ($\delta \propto r^{-\rho d}$) and the grey shaded area the range for the parameter ρ ($R \propto r^{\rho}$). Please notice the different scales for parameter ρ in region B. For more details see text.

good agreement with the calculated behavior of the Doppler factor based on the gradient in the brightness temperature, T_b (see panel 4−6 in Fig. 4.16).

For region B (4 mas $< r <$ 8 mas) we could not derive Doppler factors owing to the lack of traveling components. Our calculations suggest a decrease in the Doppler factor with respect to region D, which is independent of the geometry of the magnetic field. This deceleration coincides with a region of collimation of the jet ($\rho < 0$). Farther downstream, the jet expands again and, based on the evolution of the brightness temperature within this region, we derived an increase in δ. The obtained evolution of the Doppler factor can be interpreted within the framework of an overpressured jet, where the fluid accelerates in the regions where the jet expands ($\rho > 0$) and decelerates, on average, in the regions where the jet reconfines ($\rho < 0$).

The brightness temperature T_b

The brightness temperature (see Sect. 2.2.3 and Fig. 4.16) decreases between 0.1 mas $<$ $r <$ 1 mas (region C), and the decreasing trend continues until $r \simeq$ 4 mas (region D). However, there are hints of a change in this trend around $r \simeq$ 1 mas, i.e., between regions C and D. Between $r \simeq$ 4 mas and $r \simeq$ 8 mas (region B), the brightness temperature increases, and decreases thereafter.

From the evolution of the brightness temperature in region C (0.1 mas $< r <$ 1 mas, see Sect. 2.2.3 and Fig. 4.16), we derive that the Doppler factor should be increasing. The value of the exponent of δ as a function of distance depends on the configuration of the magnetic field, and it increases with b, where $1 < b < 2$. The lowest range for the increase in the Doppler factor $-0.8 < d < -0.2$ is obtained for a toroidal magnetic field ($b = 1$), as seen in panel 2 in Fig. 4.16.

In region D (1 mas $< r <$ 4 mas) the decrease in the Doppler factor could be related to a recollimation and deceleration process, ending up in the stationary component at $r \simeq$ 2 mas. (Jorstad et al. (2005b) report a standing component at the same distance.) There is an indication of a slight decrease in the growth of the jet radius with distance that could be related to the onset of the recollimation process (see Chapter 5). The highest values for d, implying a steeper decrease in the Doppler factor ($\delta \propto R^{-d}$), are obtained in the case of a toroidal field and equipartition. Among these two cases, the latter implies a flatter spectral distribution, a situation that will be sstudied in Chapter 5. The fall in the brightness temperature could be due to the deceleration of the flow in a possible shocked region and to it's not being compensated for by the expected increase in flux density at those shocks.

Between $r \simeq$ 4 mas and $r \simeq$ 8 mas, i.e., region B, the brightness temperature increases and the jet radius decreases with distance (Paper III, in preparation, see Fig. 4.16). According to our calculations, the Doppler factor should decrease. Thus, the increase in the brightness temperature could also be explained in terms of a new process of recollimation of the jet flow, which would generate the standing components visible in the region. It is difficult to relate the evolution of the Doppler factor with distance to the results shown in Fig. 4.16 owing to the lack of data and the large error in the determination of the exponent for the evolution of jet radius, ρ. For larger distances from the core the Doppler factor increases, and the brightness temperature increases again. Within this same interpretation, region A would represent a new expansion region.

4.3.2 Helical versus over-pressured jet

The viewing angles calculated for the components C2 and D1 increase with distance from the core, which indicates a bend in the jet away from our line of sight. Since the viewing angles are smaller than the critical angles and the apparent speeds decrease, we know that the plasma also decelerates. The observed drop in the brightness temperature within region D, as compared to region C, is a direct consequence of the decreasing Doppler factor due to a deviation of the jet away from our line of sight, together with the deceleration of the plasma. On the one hand, the stationary behavior of components at $r \sim 1.5$ mas could indicate the presence of a recollimation shock at this position. Such recollimation shocks are expected to form in overpressured jets, and the flow should decelerate when crossing them. On the other hand, the increasing viewing angle between regions C and D could indicate the growth of helical instabilities triggered by pressure asymmetries within the jet.

These instabilities lead to the formation of a helical pattern with regions of higher pressure, and hence enhanced emission as compared to the rest of the jet flow. Depending on the jet properties, we would expect to see the higher pressure region tracing helical patterns at higher frequencies and the straighter flow at lower frequencies (Perucho et al. 2012). The observed morphology of CTA 102 at different frequencies confirms this aspect to the extent that the resolution at each frequency permits. In the case of a strongly over pressured jet, the subsequent expansions and collimations would dominate over the linear amplitudes of growing instabilities and we would expect a straight flow. The observed changes in the viewing angle imply that the jet is not largely over pressured with respect to its surroundings. The stability of such a flow and extensions of the regions of enhanced emission depend on the jet properties and the interaction/competition between the pinching and helical modes (see, e.g., Perucho et al. 2004a,b).

At $r > 4$ mas from the core, the source is dominated by three apparently stationary components at all the observing frequencies that allow detection. These components also show nearly constant size and flux density during the observed period. If the components are related to physical regions, this behavior can also be explained either by recollimation shocks in a pinching jet, by changes in the viewing angle in a helical jet or a combination of both. The scenario of an overpressured jet is supported by two facts. 1) There are clear hints of jet expansion and subsequent recollimation in the innermost regions (see Chapter 5), which is naturally explained in terms of overpressure, and 2) the position of stationary components at in region B show that the separation between them is growing with distance along the jet. We find a separation of ~ 1.0 mas between B3 and B2, and ~ 1.5 mas between B2 and B1. This increase could be naturally caused by a decrease in the ambient pressure: If the ambient medium is homogeneous, the standing shocks appear at equidistant positions and show similar properties, e.g., the jump in pressure and density at each shock, whereas if the density in the ambient decreases with distance, the shocks appear at increasing separations, while pressure jumps become smaller.

Although the increase in size and the decrease in flux density with distance of the stationary components is expected in the frame of an expanding jet, this is not an exclusive feature of pinching jets, but can also happen in a helical jet. The jet does not show any apparent kink between $r = 4$ mas and $r \simeq 12$ mas, but components B1, B2, and B3 are slightly misaligned (see Fig. 4.7), which leaves room for short-wavelength kinks in

the jet in this region, with the changes in the jet direction occurring in the short projected distances between components in regions B and A. The increase in the separation between components with distance to the core could then be explained in this frame if the kinks were associated to a helical instability in an expanding jet (e.g., Hardee & Hughes 2003; Hardee et al. 2005). The Doppler factor seems to grow from region B to region A (see Fig. 4.13). However, the lack of components (notice, that Fig. 4.13 is logarithmic) does not allow us to discard local changes on this trend, i.e., changes in scales of 1 mas.

It is thus possible to relate, at least partially, the changes in the Doppler factor between $r = 0.1$ mas and $r = 4$ mas (regions C and D) with changes in the viewing angle, but it is not so easy to interpret standing components along the jet within the same frame. From the visible changes in the jet direction in the radio maps, it seems that the core and the region including components B1, B2, and B3 would be viewed at short angles than the region between D1 and D2 ($2\,\mathrm{mas} < r < 4\,\mathrm{mas}$) and the region beyond B3 ($r > 8$ mas). These changes could be due to a helical pattern in the jet with observed wavelength $\lambda_{\rm obs} \simeq 5$ mas. The misalignment among components B3, B2, and B1 could be explained by a small wavelength pattern ($\lambda_{\rm obs} \simeq 1$ mas) developing on top of the longer one ($\lambda_{\rm obs} \simeq 5$ mas). A study of the variations in the ridgeline of the jet with time, such as those performed in Perucho et al. (2012), could shed some light on possible helical patterns propagating along the jet and on their relation with the reported components.

4.3.3 The connection to the 2006 radio flare

As mentioned in Sect. 5.4.1 we detect several newly ejected features within the core region (see Figs. 4.10 and 4.11). Furthermore, we proposed that the feature at a distance of $r \sim 0.1$ mas from the core is stationary. In Chapter 3 we suggested the interaction between a traveling and a stationary recollimation shock as a possible process behind the 2006 radio flare and the double hump structure in the turnover frequency−turnover flux density plane at radio frequencies in CTA 102. In the top panel of Fig. 4.17 we show the trajectories of the components C1, C2, C3, and C4. The bottom panel shows the flux density evolution of C1, C2, C3, C4, and core, together with single-dish light curves at 37 GHz and 230 GHz, and the evolution of the flux density of the innermost components of CTA 102.

If we assume that there is a standing shock at a distance of $r \sim 0.1$ mas from the core, and if we associate the ejected components with traveling shock waves, there will be shock-shock interaction at a given time. This crossing time, $t_{\rm cross}$, is indicated in Fig. 4.17. The derived ejection time for C2, $t_{\rm ej} = 2005.9 \pm 0.2$ fits nicely to the first peak in the 230 GHz light curve and to the peak in the core flux density (see bottom panel in Fig. 4.17). The value obtained for the crossing time between C2 and the proposed standing shock, $t_{\rm cross,C2} \sim 2006.3$ is in good agreement with the peak in the 37 GHz and the second peak in 230 GHz single-dish light curve.

The ejection time for the components C3 and C4 are difficult to obtain owing to their highly non-radial trajectory. To calculate the ejection times of these components (assuming a blending between a traveling and standing shock at $r \sim 0.1$ mas), we could split the trajectory into moving and standing parts. Since this separation could lead to a strong variation in the calculated ejection time depending on the position of the separation, we only indicate the crossing time for C3 and C4 in Fig.4.17. However, the calculated crossing times $t_{\rm cross,C3} \sim 2007.7$ and $t_{\rm cross,C4} \sim 2009.3$ correspond to local peaks in the 37 GHz

single dish light curves (see dashed lines in Fig. 4.17).

The peak in the 37 GHz single-dish light curve around 2008.6 is not connected to the ejection of a new component and seems to be connected to C4. However, this region could be highly affected by blending and/or misidentification of the components. Furthermore, if we assume that there is a standing feature at $r \sim 0.1$ mas, the observed flux density behavior could reflect the highly nonlinear interaction of a the shock-shock interaction: The strong traveling shock wave associated with C2 drags the standing feature downstream. After a given time this standing shock wave is re-established at its initial position (traveling inward). During this time a new traveling shock wave is ejected from the core and collides with the inward traveling standing shock wave. This proposed scenario could not be tested within our observations due to the limited resolution within this region and sparse time sampling, and it would require high-resolution relativistic hydrodynamic simulations.

As mentioned before, standing features arise naturally in overpressured jets. Therefore, based on the results presented above, the overpressured jet model is slightly favored, at least in the core region, as a possible jet configuration.

4.4 Summary

Here we present the kinematic analysis of the multifrequency VLBA observations of the blazar CTA 102 for eight observing epochs during its 2006 radio flare. We combined our data with the long-term monitoring at 15 GHz and at 43 GHz provided by the MOJAVE and the Boston Blazar Monitoring survey, respectively. The modeling of the source at different frequencies with several Gaussian features shows that the source consists of several apparently stationary components at 4 mas $< r <$ 8 mas and a mixture of stationary and traveling ones both in the core region and extended regions of the jet. Throughout our entire data set, we could clearly cross-identify seven components and several newly ejected components in the core region.

Based on the observed evolution of the cross-identified component trajectories and on the brightness temperature gradients obtained, we divided the jet into four different regions. The gradients in these regions were used to estimate the possible jet configuration, e.g., orientation of the magnetic field. For our modeling we calculated the gradients for the evolution of the brightness temperature according to a generalization of the shock-in-jet model, which allows for nonconical geometry (Türler et al. 2000). We applied three different configurations for the magnetic field, $b = 1$, $b = b_{\rm eq} = (s + 2)/3$, and $b = 2$ ($B \propto R^{-b}$), to the observed T_b gradients and derived the evolution of the Doppler factor index d ($\delta \propto R^{-d}$) as a function of the spectral slope, s, and the jet geometry. The result of this parameter-space study shows that i) in region C there is an increase in the Doppler factor that is independent of the magnetic field configuration, ii) the obtained decrease in δ between region C and D favors a jet with a magnetic field toroidal magnetic field and/or in equipartition, iii) the decrease in the Doppler factor in this region is due to a deceleration of the fluid and a change in the viewing angle, iv) for the recollimation region B ($\rho < 0$) the Doppler factor decreases for all magnetic field geometries studied and the smallest decrease is obtained for a toroidal field, and v) farther downstream the Doppler factor rises again, with the steepnes of the acceleration depending on the geometry of the

magnetic field.

The very detailed study of the core region at 43 GHz revealed four newly ejected traveling components and one possible stationary feature at $r \sim 0.1$mas from the core. We could connect one of the components labeled as C2 with the April 2006 radio via a linear back-interpolation of its observed trajectory. This feature was ejected around 2005.9 from the core with an apparent speed of $(13 \pm 2)\,c$. The ejection time of C2 fits nicely to the first peak in the 230 GHz single dish light curve and the crossing time computed for the interaction between C2, and the stationary feature corresponds to the second peak at 230 GHz and to the observed global maximum in the 37 GHz single-dish light curve.

The results were interpreted within the framework of a) an overpressured jet, b) a helical jet, and c) a combination of both. Within these models the obtained evolution in the Doppler factors and brightness temperature are caused by a) an acceleration or deceleration of the plasma generated by collimation and expansion of the jet, i.e., the pressure mismatch between the jet and the ambient medium, by b) a variation in the viewing angle and the connected Doppler boosting or deboosting and by c) nonaxial recollimation shocks that create a transversal pressure gradient and lead to a bend in the jet. Based on the analysis of the kinematics and the brightness temperature the third option was favored.

To summarize, our results on the component trajectories and the brightness temperature evolution suggest a shock-shock interaction in an overpressured jet as the driving mechanism behind the 2006 radio flare (see Chapter 3).

For a detailed modelling of the 2006 flare and the connected shock-shock interaction, we need absolute values for the magnetic field, the particle density, the relativistic energy density and an estimate of the magnetization. Therefore, we need to perform a core-shift and spectral analysis on the multi-frequency VLBI observations to obtain the steady-state values and there variation during the flare.

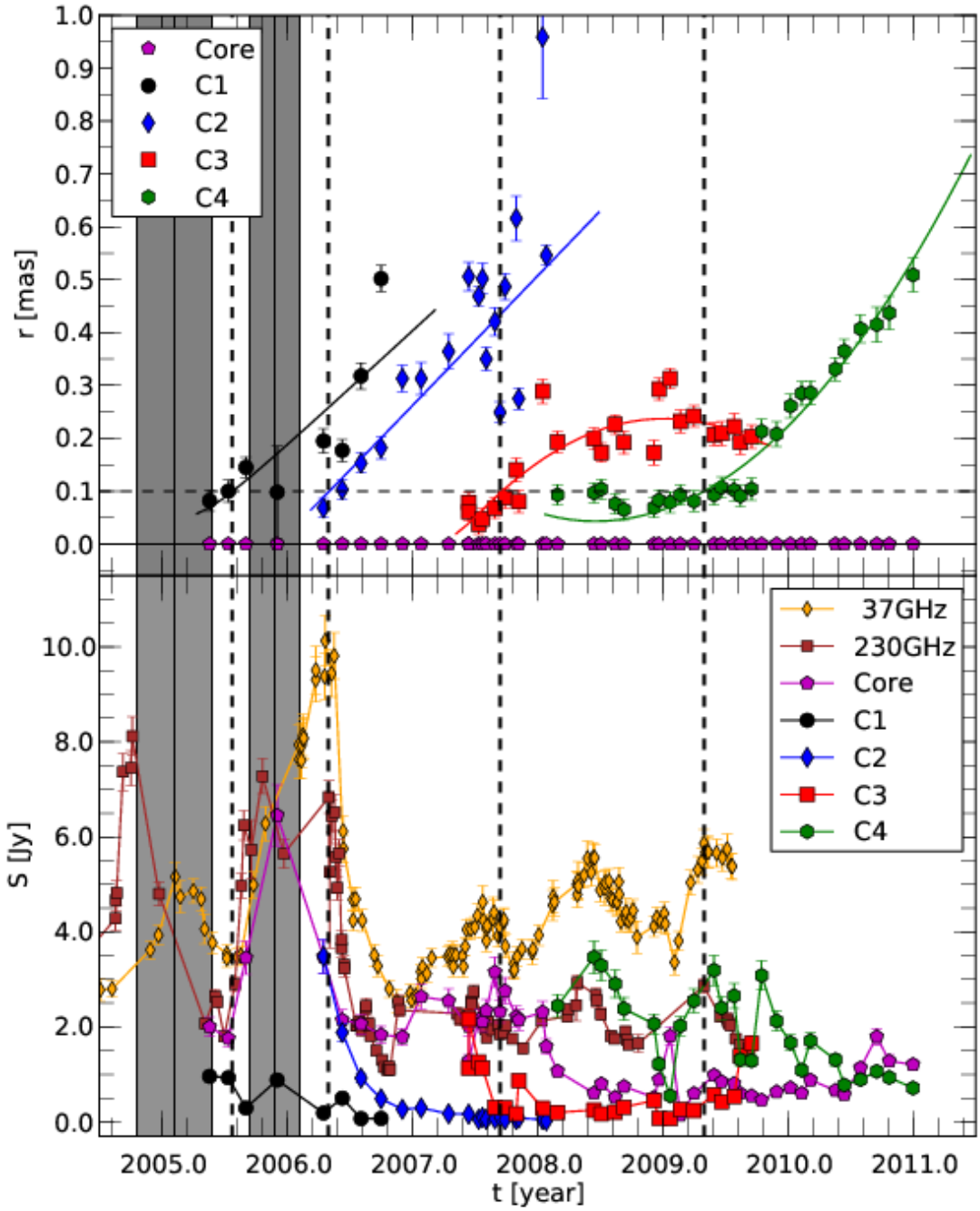

Figure 4.17: Evolution of the component separation from the core and the flux density for the innermost components of CTA 102. Top: Separation from the core and fitted trajectories for C1, C2, C3 and C4. The grey shaded ares correspond to the ejection epochs for C1 and C2 and the dashed line to the crossing of a possible stationary feature at $r \sim 0.1$, mas away from the core (dashed horizontal line). Bottom: Flux density evolution of the components including the core and single-dish flux density measurements at 37 GHz and 230 GHz. For details see text.

5 Core-shift and spectral analysis

This Chapter is partially published in Fromm et al. in preparation

In Chapter 3 we suggested, based on single-dish observations that the interaction between a propagating and a standing shock could be the driving mechanism behind the strong flare and derived the evolution of physical parameters according to a slightly modified shock-in-jet model. The kinematic analysis of the source during the flare and its long-term evolution has been studied in Chapter 4. This study revealed one apparently stationary component at $r \sim 0.1$mas from the core and we could connect the 2006 radio flare to the ejection of a new component $T_{\rm ej} = 2005.9 \pm 0.2$. Based on the gradients in the evolution of the brightness temperature we tested several jet configurations and derived estimates for the variation of the Doppler factor along the jet. The existence of a clearly bent structure together with quasi stationary feature could be explained by both an pinching jet (over-pressured jet) or a helical jet (bent jet), where the existence of standing features slightly favors the over-pressured jet scenario.
The analysis of the 2006 radio flare is finalized after the analysis of the single dish light curves and the kinematic analysis by the core-shift and spectral analysis. The large coverage of outburst by our multi-frequency VLBI observations between May 2005 and April 2007 allows to examine the changes in the physical properties of the source under these extreme circumstances.

5.1 Data analysis

For our analysis we used eight VLBI observations spanning from May 2005 until April 2007. The coverage of the 2006 radio flare in CTA 102 by our VLBI observations is presented in Fig. 4.1, where we show the temporal correspondence between the cm-mm light curves and the VLBA observations of CTA 102. The red dashed lines correspond to the epochs of multi-frequency VLBA observations. More details about calibration, imaging and model fitting of these VLBI images are presented in Sect. 4.1.3.

Following the convention used in Chapter 4, the structure of the jet in CTA 102 can be studied by dividing it into four regions labeled as A ($r > 8$ mas), B (4 mas $< r <$ 8 mas), D (2 mas $< r <$ 4 mas) and C ($r <$ 2 mas). Throughout our data set we could clearly cross-identify seven features within regions A, B, and D. The analysis of the long-term monitoring of the source at 43 GHz revealed four additional features in region C (see Chapter 5.4.1).

Figure 4.2 shows the VLBI observation of CTA 102 in June 2006 together with the cross-identified circular Gaussian components. A more detailed view into region C is

provided in Fig. 4.3. All images of the source at different frequencies together with the fitted components are presented in the Appendix A. Table 5.1 presents a list of typical (average) image parameters for the CTA 102 observations at different frequencies.

Table 5.1: Averaged image parameters for the CTA 102 observations

ν [GHz]	Θ_{maj} [mas]	Θ_{min} [mas]	P.A. [deg]	pixel size [mas]
2	8.17	3.73	−5	0.70
5	3.65	1.52	−8	0.30
8	2.32	0.97	−7	0.20
15	1.33	0.52	−9	0.10
22	0.95	0.33	−13	0.07
43	0.45	0.18	−11	0.04
86	0.25	0.11	−19	0.03

5.1.1 Image Alignment

During the calibration process of VLBI observations the absolute position of the source is lost due to the use of closure phases. However, a proper alignment of the different frequency images is a basic requirement for a reliable core-shift and spectral analysis. The ideal technique to restore the initial position of the source would be based on phase-referencing observations. Such experiments require a compact object in the neighborhood of the source. In most of the cases this object would be not within the primary antenna beam of the interferometer, and this requires a switching between the main source and the calibrator (e.g., Ros 2005). Our observations were not designed in phase-referencing mode, so that another approach is necessary.

A common procedure to correct for the frequency dependent position of the source and especially the core, is based on the assumption that the position of an optically thin region ($S \propto \nu^{\alpha_0}$) does not depend on the observing frequency. There are two different approaches for the registration of multi-frequency VLBI observations; one based on cross-identification of fitted Gaussian functions to the visibilities (denoted as components) and another based on 2D cross-correlation of the optically thin emission regions. The advantage of the 2D approach is that the whole optically thin emission region is taken into account for the alignment, whereas the one based on fitted components takes only a single region into account. Nevertheless, if the source does not exhibit an extended jet region the approach based on fitted features would be a better choice (Kovalev et al. 2008; Croke & Gabuzda 2008).

In this thesis we used a hybrid approach (2D cross-correlation and fitted components) depending on the amount of extended structure and on the resulting spectral index maps. We followed the work of Croke & Gabuzda (2008) and adjusted their technique to our needs. For the alignment based on cross-identified components we used the feature labeled as B2 for frequencies $\nu < 22$ GHz and component D2 for higher frequencies. Both features could be cross-identified throughout our entire data-set (see Fig. 4.2).

2D cross-correlation of VLBI maps

The image parameters of a VLBI map, e.g., map size (ms), pixel size (ps) and convolving beam size (bs), increase with decreasing frequency (to optimize them with the resolution in each case). Before we perform the cross-correlation of the VLBI images we select a set of common image parameters. The best results for the cross correlation of two VLBI images with frequencies, ν_1 and ν_2, where $\nu_1 > \nu_2$, are achieved by using the map size and beam size of the low frequency image, $ms(\nu_2)$ and $bs(\nu_2)$, and half of the pixel size of the high frequency image $ps(\nu_1)$. These settings guarantee that no structure information is lost during the alignment process. After both images are convolved with the common beam and the selected pixel size, the optically thick core region is masked in both maps. During the cross-correlation process one of the images is shifted in Δx and Δy direction and the cross-correlation coefficient (see Eq. 5.1) at each shift position $(\Delta x, \Delta y)$ is calculated. The cross-correlation coefficient $cc_{\Delta x,\Delta y}$, between the two maps is defined as (assuming that only the second map is shifted):

$$cc = \frac{\sum_{i=1}^{n}\sum_{j=1}^{m}\left(S_{\nu_1}^{i,j} - \overline{S}_{\nu_1}\right)\left(S_{\nu_2}^{\Delta x\cdot i,\Delta y\cdot j} - \overline{S}_{\nu_2}\right)}{\left[\sum_{i=1}^{n}\sum_{j=1}^{m}\left(S_{\nu_1}^{i,j} - \overline{S}_{\nu_1}\right)^2 \sum_{i=1}^{n}\sum_{j=1}^{m}\left(S_{\nu_2}^{\Delta x\cdot i,\Delta y\cdot j} - \overline{S}_{\nu_2}\right)^2\right]^{\frac{1}{2}}}, \tag{5.1}$$

where i, j, n and m are the lower and upper boundaries for the indices of the different images, $S_{\nu_1}^{i,j}$ is the flux density of the non-shifted image at the position (i, j) and $S_{\nu_2}^{\Delta x\cdot i,\Delta y\cdot j}$ is the flux density of the shifted map by Δx and Δy. Finally, $\overline{S}_{\nu_{1,2}}$ is the average flux density in the images. The result of this 2D-position variation is the distribution of cross-correlation coefficients within the shift area. The best shift position, which is equal to the correction of the opacity shift, corresponds to the maximum cross-correlation coefficient. The finite width of the pixel size leads to discrete values for the best shift position in steps of the used pixel size. This dependence on the selected pixel size can be overcome by fitting a 2D elliptical Gaussian to the cross-correlation distribution achieved. A 2D elliptical Gaussian distribution can be written in the following form

$$g(x, y) = Ae^{-\left(a(x-x_0)^2+2b(x-x_0)(y-y_0)+c(y-y_0)^2\right)}, \tag{5.2}$$

where the coefficients a, b, c are defined by:

$$a = \frac{\cos^2\Theta}{2\sigma_x^2} + \frac{\sin^2\Theta}{2\sigma_y^2}, \tag{5.3}$$

$$b = -\frac{\sin 2\Theta}{4\sigma_x^2} + \frac{\sin 2\Theta}{4\sigma_y^2}, \tag{5.4}$$

$$c = \frac{\sin^2\Theta}{2\sigma_x^2} + \frac{\cos^2\Theta}{2\sigma_y^2}, \tag{5.5}$$

with Θ the rotation angle, x_0 and y_0 the mean values, and σ_x and σ_y the standard deviations. The fitted parameters x_0 and y_0 can be regarded as the best shift position.
If the distribution of the cross-correlation coefficient is smooth and symmetric around the mean values, the distribution of the cross correlation coefficient could be described as a Gaussian distribution and the mean values are the best choice for the correction of the

core shift. Otherwise, the position of the highest cross correlation coefficient is a suitable choice.
The distribution of the spectral index, α, computed from two adjacent frequencies is highly sensitive to positional changes:

$$\alpha = \frac{\log\left(S\left(\nu_1\right)/S\left(\nu_2\right)\right)}{\log\left(\nu_1/\nu_2\right)} \tag{5.6}$$

In this way, a visual check on α for both alignment methods allows us to diagnose their performance. In principle, the distribution of the spectral index, α, should be uniform across the jet with a decrease towards the extended structure and a slight transversal gradient. We computed several spectral index maps using the 2D cross-correlation approach and component approach in order to investigate the difference between both methods. These results are presented in the following for the alignment of two low frequency and two high frequency VLBI images.

Low frequency alignment

For the alignment of the 8 GHz and 5 GHz maps of the May 2005 observations, we used a pixel size of 0.04 mas and beam size of 3.65×1.52 mas and a P.A. of $-8°$ for the 2D cross-correlation and for the component based approach we used the feature labeled as B2 (see contour plots in Fig. 4.2). Figure 5.1 presents the distribution of the cross correlation coefficient between the 8 GHz and the 5 GHz image. The best shift position was found at $\Delta x = 0.38$ mas and $\Delta y = -0.28$ mas. From the component-based approach we obtained an image shift of $\Delta x = 0.47$ mas and $\Delta y = -0.34$ mas.

Figure 5.3 illustrates this case. The distribution of the spectral index shows in both cases an optically thick core region ($\alpha > 0$) and an optically thin jet region ($\alpha < 0$), with the transition at a distance of $r \approx 2.7$ mas away from the core. The evolution of the spectral index along the jet axis is similar for both approaches with minor variations (see inlet A in Fig. 5.3). However, there are major differences in the transversal distribution of the spectral index (inlet B in Fig. 5.3). The modelfit based approach has a strong transversal gradient in the spectral index (blue line in inlet B), which is smoothed out by the 2D cross-correlation technique (red line in inlet B).

High frequency alignment

We used the 22 GHz and 43 GHz VLBA observations in May 2005 epoch to study the alignment of high frequency maps. The 2D cross-correlation technique resulted in a correction of $\Delta x = 0.04$ mas and $\Delta y = 0.01$ mas ,using a pixel size of 0.01 mas, beam size of 0.95×0.33 mas, and a P.A. of $-13°$ (see Fig. 5.2 for the distribution of the cross-correlation coefficient). Fixing component D2 (see Fig. 4.3), we calculated a value of $\Delta x = 0.03$ mas and $\Delta y = 0.01$ mas for the correction of the opacity shift. Since the distribution of the cross-correlation coefficient is not well described by a 2D-Gaussian, we selected the position of the highest cross-correlation coefficient as the best shift position (see Fig. 5.2).

The computed spectral index maps between 22 GHz and 43 GHz are presented in Fig. 5.4. The distribution of the spectral indices in the optically thick core region ($r < 0.3$ mas)

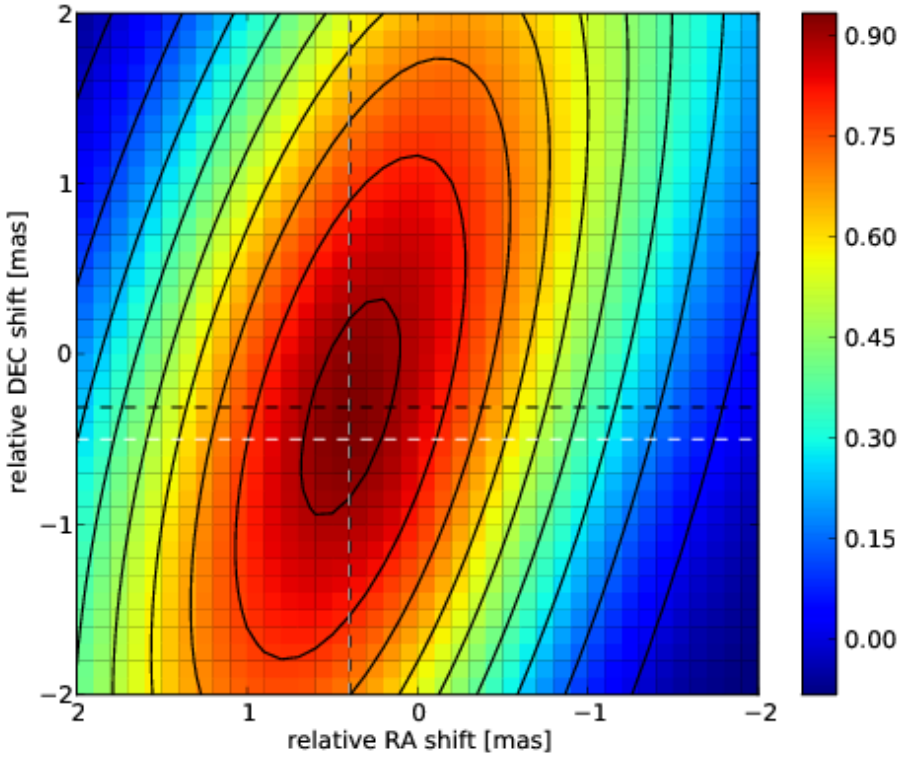

Figure 5.1: Distribution of the cross-correlation coefficient for the alignment of the 8 GHz and 5 GHz VLBA maps. The white dashed lines corresponds to the maximum cross-correlation coefficient in the color-map and the dashed black line for the peak position of the fitted 2D Gaussian.

follows the same decreasing trend as in the low-frequency case (see inlet A in Fig. 5.4). The distributions are slightly rotated by roughly 15°. The two different techniques, 2D cross-correlation and component-based alignment lead to nearly identical spectral index maps.

5.1.2 Spectral Analysis

For the extraction of the spectral parameters, turnover frequency, ν_m, turnover flux density, S_m, and optically thin spectral index, α_0 we need at least three VLBI observations at different frequencies. In general, there are two approaches for the extraction of the spectral parameters, one based on the flux densities in each pixel (Lobanov 1998) and the other one on the fitted components (Lobanov & Zensus 1999; Savolainen et al. 2008). The advantage of the pixel-based approach is that it provides a continuous evolution of the spectral values along the jet as long as the individual spectrum is homogenous. If the spectrum is not homogenous because there are several components within a region of the size of the convolving beam, or the turnover frequency, ν_m, is out of our frequency range, we can no longer obtain the turnover values. Nevertheless, the spectral index, α ($S_\nu \propto \nu^\alpha$)

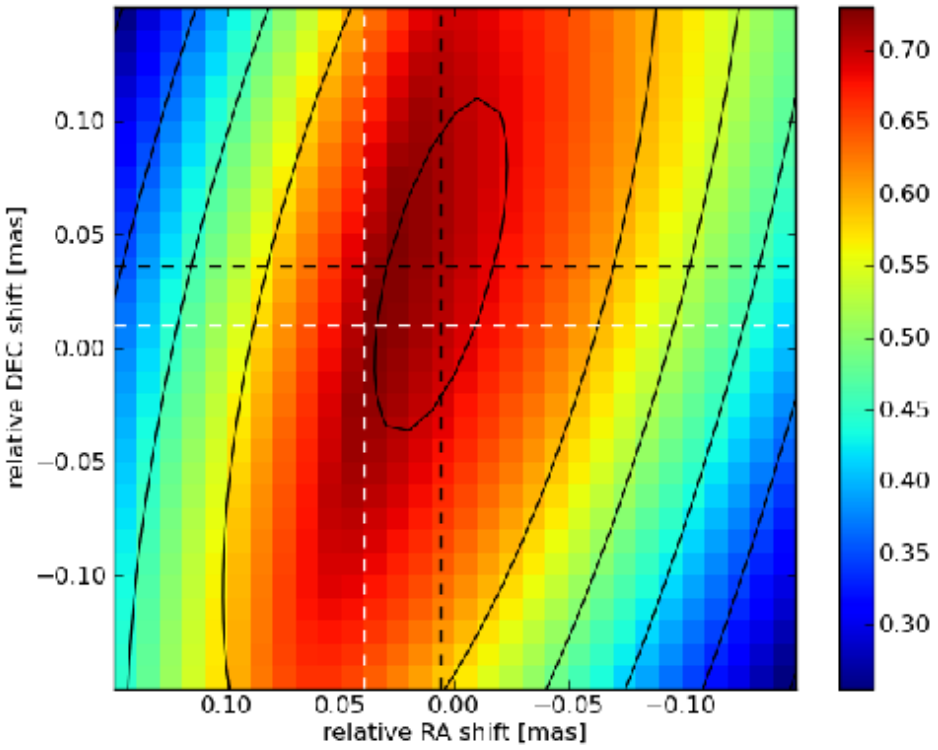

Figure 5.2: Distribution of the cross-correlation coefficient for the alignment of the 43 GHz and 22 GHz VLBI map. The white dashed lines corresponds to the maximum cross-correlation coefficient in the color-map and the dashed black line for the peak position of the fitted 2D Gaussian.

can still de derived.

As mentioned in section 5.1.1, the convolving beam and pixel size of the maps are decreasing with increasing frequency (see Table 5.1). An appropriate selection of the common beam and pixel size for all the maps involved in the analysis is needed to avoid the generation of image artifacts (small beam size) or the loss of sensitivity (too large pixel size). There are two possible techniques that can be used to avoid these difficulties. The first one uses the beam size of the lowest frequency map and pixel size of the highest frequency map. The second one is an adaptive method, where the beam and pixel size are selected depending on the distance to the core, i.e., the closer to the core, the smaller the beam and the pixel size. Using the latter implies that the lower frequency maps have to be excluded from the spectral analysis closer to the core region to avoid image artifacts.

After one of the aforementioned methods is selected and the opacity shift is corrected in the maps relative to a reference one (Sect. 5.1.1), the pixel-to-pixel spectral analysis can be performed. The procedure is the following: i) The aligned images are all convolved with a common beam and pixel size and are stacked on top of each other into a so-called “datacube”. ii) The dimensions of this cube are the map dimensions

in the $x-$ and $y-$direction and the number of involved frequencies in the $z-$direction. Due to the already performed image alignment (see previous section), each pixel at a given frequency $[j(\nu_u), i(\nu_u), k(\nu_u)]$ corresponds to its counterpart at the other frequencies $\left[j(\nu_p), i(\nu_p), k(\nu_p)\right]$, where $j(\nu_{u/p}), i(\nu_{u/p})$ are the array indices of each VLBA map in $x-$ and $y-$direction and $k(\nu_{u/p})$ is the $z-$layer in the "datacube". iii) For each position (x,y) a frequency vector $\boldsymbol{\nu_{x,y}} = [\nu_0 \cdots \nu_n]$ and a flux density vector $\boldsymbol{S_{\nu,x,y}} = [S_{\nu,0} \cdots S_{\nu,n}]$ vector can be extracted, with n the total number of maps included in the spectral analysis.

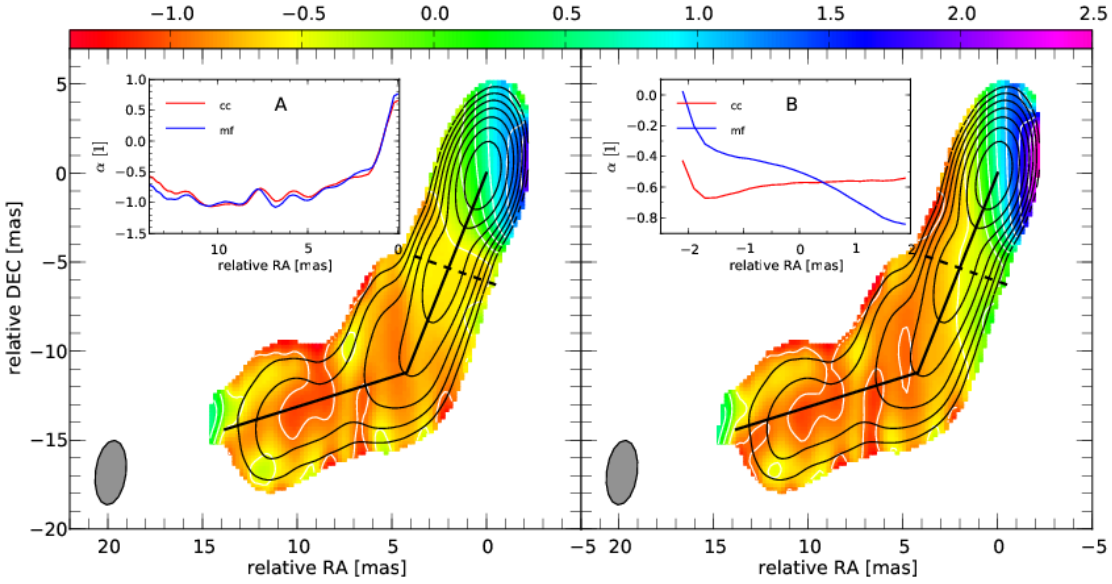

Figure 5.3: 5 GHz-8 GHz spectral index maps for the May 2005 observations of CTA 102. Left panel shows the spectral index map produced by the 2D cross-correlation and right panel the one by using the component based approach. The contours are drawn for the 8 GHz observations. The inlets show the distribution of the spectral index along the jet axis, black solid line, (inlet A) and transversal to the jet axis, dashed black line, (inlet B). See text for more details.

By fitting the approximation of the synchrotron-self absorbed spectrum to $\boldsymbol{\nu_{x,y}}$ and $\boldsymbol{S_{\nu,x,y}}$, the turnover frequency, $\nu_{m,x,y}$, the turnover flux density $S_{m,x,y}$, and the optically thin spectral index, $\alpha_{0,x,y}$, can be obtained, while fixing $\alpha_{t,x,y} = 5/2$ (assuming homogeneous synchrotron emission). Extending this technique to the overall source structure results in a 2D-distribution of the turnover values for each multi-frequency epoch.

We estimated the uncertainties on the derived spectral parameters including the uncertainties of the measured parameters and the sensitivity of the computing method to the shifts between images, as described in Appendix C. In short, first we assumed that the uncertainties in the flux density vary between 5% and 15%. We included this frequency-dependent flux density uncertainty in our error analysis and, additionally, we incorporated the flux density errors for each pixel, based on the image SNR at each of them. To estimate the influence of the uncertainties of the opacity shifts we assumed that the uncertainties of the obtained shift positions are within the used pixel size. Therefore, we randomly shifted each map within the allowed position, extracted the spectral parameters and calculated

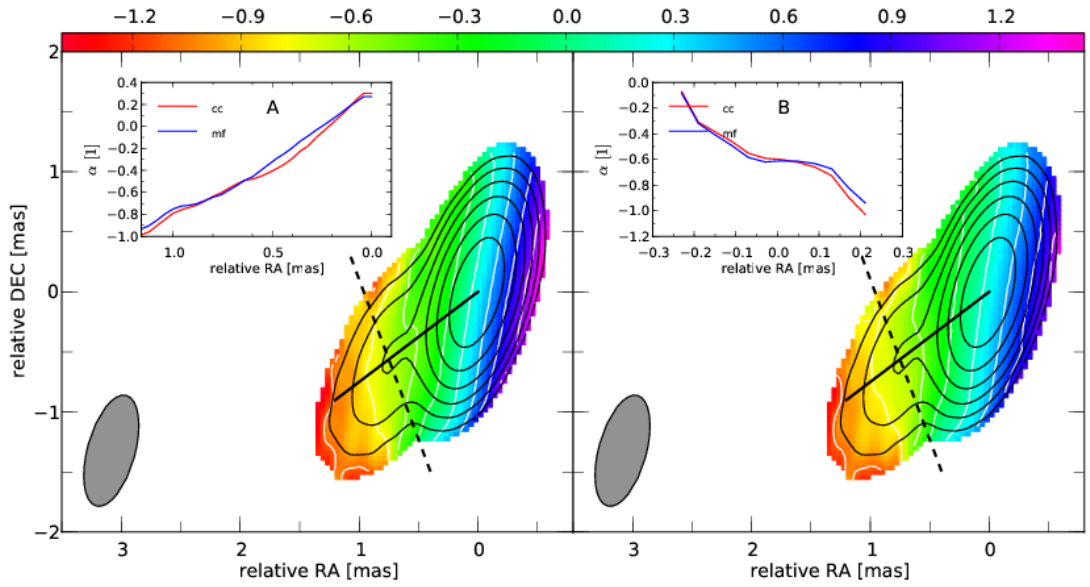

Figure 5.4: 22 GHz-43 GHz spectral index maps for the May 2005 observations of CTA 102. Left panel shows the spectral index map produced by the 2D cross-correlation and right panel the one by using the component based approach. The contours are drawn for the 43 GHz observations. The inlets show the distribution of the spectral index along the jet axis, black solid line, (inlet A) and transversal to the jet axis, dashed black line, (inlet B). See text for more details.

the scatter of the obtained values. This was done by performing a Monte Carlo simulation for which we used up to 10^4 random shifts for each epoch to derive the uncertainties for the spectral parameters. We rejected turnover values which are not well constrained within our data set, i.e., spectra for which we obtained turnover frequencies, ν_m, lower than 75% percent of the minimum frequency in the data set. This procedure provides the most reliable turnover values and are incorporated in presented evolution of the spectral parameters.

5.2 Core-shift analysis

We used the technique presented in section5.1.1 to align the VLBI observations of CTA 102. Due to the difference in the image parameters, especially in the convolving beam size, we used only adjacent frequency maps in the alignment. The shift values obtained relatively to the initial position are presented in table 5.3.

There are two different shift directions towards the north-east (positive $x-$ and $y-$ directions) for frequencies larger than 22 GHz (see panel A in figure 5.5) and towards the south-east direction for lower frequencies (relative to the highest frequency involved in the analysis, see panels B, C, and D in figure 5.5). An exception of this observed behavior appears in the April 2006 epoch, possibly due to the large flux density outburst during this time.

We derived the core-shift vector from the correction of the opacity shift (see table 5.3) and the position of the VLBI core (see Chapter 4.1.4 for more details on the model fitting of the source). Figure 5.5 shows the variation of the core-shift vector for the different frequency pairs with time. The solid circles indicate the distance from the reference core in mas, the dashed lines are drawn in intervals of 30° and the different colors of the arrow correspond to the different observational epochs.

The variation of the 43 GHz − 22 GHz core-shift vector around 0.01 mas reflects the uncertainties in the alignment method used (see panel A in Fig. 5.5). The 22 GHz − 15 GHz and 8 GHz − 5 GHz shift-vectors are mainly oriented in south-east direction (see panel B and D in Fig. 5.5) whereas the 15 GHz − 8 GHz ones show some variation in the north-east to south-east direction. This variation in the direction of the core-shift vector for this frequency pair may reflect the slightly different orientation of the radio jet axis between 15 GHz and 8 GHz. For the other frequency pairs, the difference in the jet axis is not as pronounced as for the 15 GHz − 8 GHz pair (see contour plots in figure4.2).

In order to derive the parameter k_r (see Eq. 2.46), we used the highest frequency during each observation as a reference frequency and computed the relative radial core-shift. Since CTA 102 has a curved structure, clearly visible in Fig. 4.2, we would have underestimated the core-shift by using only the one-dimensional radial distance between two VLBA cores. Therefore, we calculated the core-shift along a curved trajectory given by the x- and y-position of the image alignment. Table 5.4 presents the calculated core-shift values relative to the highest frequency during each observation epoch.

Since we measure the core shift relative to a reference frequency, $\nu_{\rm ref}$, equation 2.46 can be re-written in the following form (O'Sullivan & Gabuzda 2009):

$$r_{\rm core} = A\left(\nu^{-1/k_r} - \nu_{\rm ref}^{-1/k_r}\right). \tag{5.7}$$

Applying equation 5.7 to the core-shifts, the core-shift between frequencies can be obtained. The results are listed in table 5.2. The weighted average of the different k_r and A values obtained is $k_r = 0.8 \pm 0.1$ and $A = 3.4 \pm 1.6$. All values are compatible with $k_r \sim 1$ but for the October 2006 and April 2007 observations.

Table 5.2: Results of the core-shift analysis

Epoch [yyyy-mm-dd]	$\nu_{\rm ref}$ [GHz]	k_r [1]	A [1]
2005-05-19	86	0.9±0.1	3.3±0.7
2005-09-01	43	0.8±0.4	3.7±4.4
2006-04-14	43	0.8±0.1	2.9±0.6
2006-06-08	43	1.2±0.3	1.0±0.3
2006-10-02	43	0.7±0.1	3.2±1.4
2006-12-02	43	0.8±0.1	5.2±1.5
2007-01-26	43	0.8±0.2	3.4±1.6
2007-04-26	43	0.6±0.1	3.9±2.0

Table 5.3: Correction for the opacity shifts obtained by 2D cross correlation between adjacent frequencies

Epoch	(86 − 43) GHz		(43 − 22) GHz		(22 − 15) GHz		(15 − 8) GHz		(8 − 5) GHz		(5 − 2) GHz	
	x	y	x	y	x	y	x	y	x	y	x	y
[yyyy-mm-dd]	[mas]	[mas]	[mas]	[mas]	[mas]	[mas]	[mas]	[mas]	[mas]	[mas]	[mas]	[mas]
2005-05-19	0.02	0.02	0.04	0.01	0.04	−0.04	0.12	−0.12	0.38	−0.28	–	–
2009-09-01	–	–	0.01	−0.02	0.06	−0.11	0.10	0.02	0.32	−0.52	–	–
2006-04-16	–	–	0.02	−0.03	0.03	−0.01	0.09	−0.09	0.24	−0.52	0.80	−2.25
2006-06-08	–	–	0.01	0.02	0.01	−0.01	0.03	−0.05	0.12	−0.32	0.80	−2.54
2006-10-02	–	–	0.03	−0.03	0.05	−0.02	0.03	−0.03	0.26	−0.45	–	–
2006-12-04	–	–	0.08	−0.05	0.06	−0.04	0.06	−0.09	0.35	−0.52	–	–
2007-01-26	–	–	0.03	0.00	0.10	−0.05	0.04	−0.03	0.30	−0.50	–	–
2007-04-26	–	–	0.01	−0.02	0.03	−0.02	0.09	−0.06	0.48	−0.64	–	–

Table 5.4: Core shift values relative to reference frequency (second column) for different epochs

Epoch	ν_{ref}	43 GHz		22 GHz		15 GHz		8 GHz		5 GHz		2 GHz	
		r	PA	r	PA	r	PA	r	PA	r	PA	r	PA
[yyyy-mm-dd]	[GHz]	[mas]	[°]	[mas]	[°]	[mas]	[°]	[mas]	[°]	[mas]	[°]	[mas]	[°]
2005-05-19	86	0.03±0.01	85	0.10±0.02	50	0.20±0.05	−13	0.31±0.1	16	0.57±0.14	−1	–	–
2009-09-01	43	–	–	0.02±0.02	−177	0.14±0.05	−74	0.24±0.08	−58	0.37±0.14	−65	–	–
2006-04-16	43	–	–	0.02±0.02	−118	0.06±0.05	−60	0.17±0.08	−46	0.45±0.14	−66	1.1±0.3	−47
2006-06-08	43	–	–	0.03±0.02	35	0.08±0.05	12	0.18±0.20	−31	0.33±0.30	−38	0.5±0.4	0
2006-10-02	43	–	–	0.02±0.02	109	0.06±0.05	−18	0.14±0.08	−11	0.28±0.14	−49	–	–
2006-12-04	43	–	–	0.04±0.03	3	0.13±0.05	−25	0.29±0.08	−42	0.59±0.14	−52	–	–
2007-01-26	43	–	–	0.03±0.02	81	0.11±0.05	5	0.23±0.08	6	0.40±0.14	−41	–	–
2007-04-26	43	–	–	0.01±0.02	133	0.05±0.05	−50	0.12±0.08	−21	0.25±0.14	−24	–	–

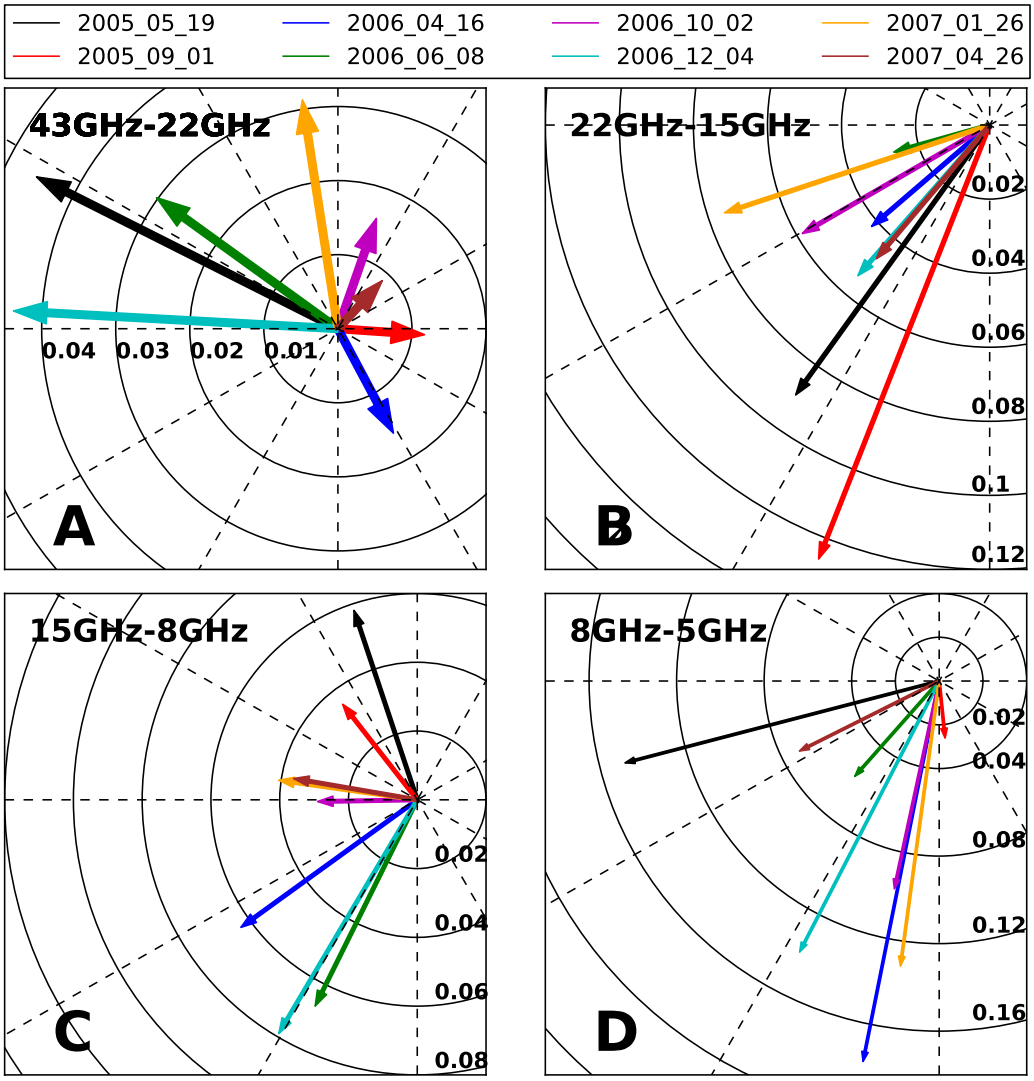

Figure 5.5: Variation of the core-shift vector with time for different frequency pairs. The solid circles correspond to the radial distance from the reference core and the dashed lines are drawn in intervals of 30°. The color of the arrow indicated the different observational epochs. (See text for more details).

Assuming that the jet is in equipartition and has a conical geometry, which is a valid assumption for region C as seen from the value obtained for k_r and figure 5.9, the magnetic field can be obtained using equations 2.48 - 2.53. In general, the radial evolution of the magnetic field in the jet is given by $B \propto r^{-\epsilon b}$, where ϵ is the jet opening index ($R \propto r^{\epsilon}$) and b parametrizes the evolution of the magnetic field ($B \propto R^{-b}$). For a jet in equipartition the particle density has to decrease as $N \propto R^{-2b}$ or, in terms of distance along the jet $N \propto r^{-2b\epsilon}$. Assuming a conical jet (i.e., $\epsilon = 1$) and a toroidal magnetic field ($b = 1$), an estimate can be derived for the magnetic field, $B_{\rm core} = B_1 r_{\rm core}^{-1}$, and the relativistic particle density at the core, $N_{\rm core} = N_1 r_{\rm core}^{-2}$. For the calculation of the magnetic field we used the shifts obtained between 22 GHz and 15 GHz because we obtained a small variation in the core-

Table 5.5: Physical parameters from the core-shift analysis between 43 GHz and 22 GHz using $k_r = 1$ and $\alpha_0 = -0.5$.

Epoch [yyyy-mm-dd]	k_r [1]	α_0 [1]	Δr [mas]	$\Omega_{r\nu}$ [pc GHz]	B_1 [G]	N_1 [10^3cm^{-3}]	$r_{\rm core}$ [pc]	$B_{\rm core}$ [G]	$N_{\rm core}$ [cm^{-3}]
2005-05-19	1.0	−0.5	0.05	17.6	0.98	4.5	10.0	0.09	42
2005-09-01	1.0	−0.5	0.01	4.6	0.36	0.6	2.7	0.13	81
2006-04-14	1.0	−0.5	0.02	6.1	0.44	0.9	3.6	0.12	70
2006-06-08	1.0	−0.5	0.03	11.5	0.71	2.4	6.8	0.10	51
2006-10-02	1.0	−0.5	0.02	6.1	0.44	0.9	3.6	0.12	70
2006-12-02	1.0	−0.5	0.04	16.8	0.95	4.2	10.0	0.10	42
2007-01-26	1.0	−0.5	0.03	11.9	0.73	2.5	7.0	0.10	51
2007-04-26	1.0	−0.5	0.01	3.8	0.31	0.5	2.3	0.14	89

shift orientation for this frequency pair. We used an apparent speed, $\beta_{\rm app} = (12 \pm 3)\,c$, derived from the components C1 and C2 (see Chapter 5.4.1). These components were ejected during the time of our observations and are the ones that best reflect the velocities in the core region.

Table 5.5 presents values for the magnetic field and the particle density computed from the core shift results using $k_r = 1$ and $\alpha_0 = -0.5$. For these calculations we assume a fixed ratio of $\gamma_{\rm max}/\gamma_{\rm min} = 10^3$ and lower electron Lorentz factor $\gamma_{\rm min} = 100$.

Figure 5.6 shows the evolution of $B_{\rm core}$ and $N_{\rm core}$, we obtained nearly constant values for $B_{\rm core} \sim 10^{-1}$ G. The particle density at the core varies between $N_{\rm core} = 40{\rm cm}^{-3}$ and $N_{\rm core} = 90\,{\rm cm}^{-3}$. If we allow for a variation of the k_r both, the magnetic field and the particle density at the core decrease with k_r.

5.3 Transversal jet structure and jet ridge line

n the modeling presented in the previous section a conical jet geometry was assumed. In order to test this assumption we studied the transversal jet structure of CTA 102. Therefore, we derived the jet ridge line, i.e., the line connecting the local flux density peaks along the jet, and fitted a Gaussian to the flux density profiles perpendicular to the jet ridge-line (see, e.g., Pushkarev et al. 2009). Since we were interested in the average jet width and ridge line, we used stacked VLBA images, which include all the observations at a given frequency, here from 2003 until 2011. The advantage of using stacked images is that the values obtained for the width and the ridge line are less affected by individual calibration uncertainties. Each map was convolved with its individual common beam, and thus, we used the average beam for each frequency (see Table 5.1).

Figure 5.7 shows a 15 GHz stacked VLBI image of CTA 102 over-plotted with the obtained jet ridge-line. We corrected the starting point of the jet ridge line at each frequency for the opacity shift using the average image shift obtained as explained in Section 5.2. The results are presented in Fig. 5.8.

After applying the opacity correction to the ridge lines derived at different frequencies, we obtained a good spatial agreement between them (see Fig. 5.8). The jet ridge line at low frequencies $\nu < 8$ GHz shows an oscillating pattern with an observed wavelength $\lambda_{\rm obs,1} \sim 20$ mas. Within the first 13 mas away from the core, the ridge line is oriented

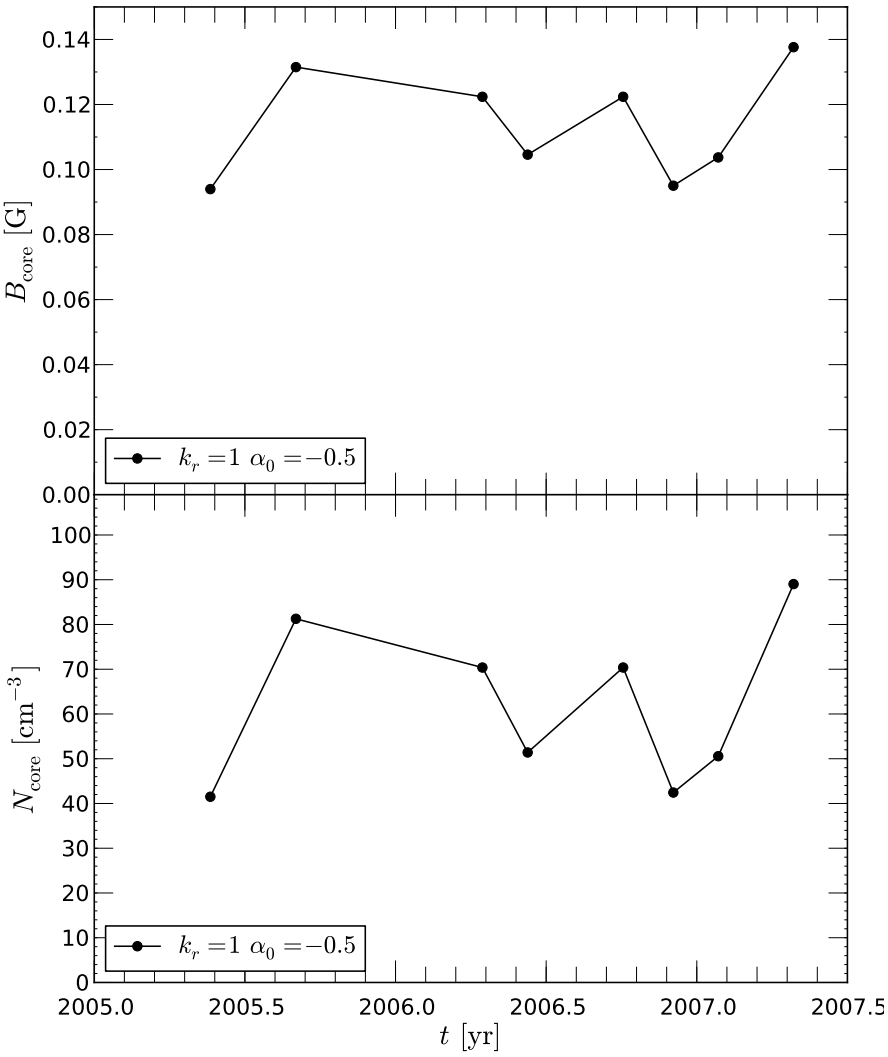

Figure 5.6: Physical parameters derived from the core shift analysis assuming $k_r = 1$ and $\alpha_0 = -0.5$. Top panel: Evolution of the core magnetic field, $B_{\rm core}$. Bottom panel: Evolution of the relativistic particle density at the core, $N_{\rm core}$.

along an observed angle of −65°. At higher frequencies, a second oscillating pattern developing on top of the first one is observed, as reported in Perucho et al. (2012) for the case of the jet in the quasar S5 0836+710. This second pattern is best visible at 15 GHz and 22 GHz and has an observed wavelength, $\lambda_{\rm obs,2} \sim 5$ mas. There are also indications for an additional pattern with $\lambda_{\rm obs,3} < 1$ mas visible at the highest frequencies, 43 GHz and 86 GHz. A full analysis on the jet ridge lines as described in Perucho et al. (2012) could lead to additional parameters of the three dimensional helical patterns, which maybe connected to fluid instabilities, but this is beyond the scope of this work.

Figure 5.9 shows the variation of the de-convolved jet width, $w = \sqrt{d^2 - b_\phi^2}$, with distance, where d is the FWHM of the fitted Gaussian and b_ϕ is the size of the beam transversal to the jet ridge line along the jet. As we did for the jet ridge line, we corrected

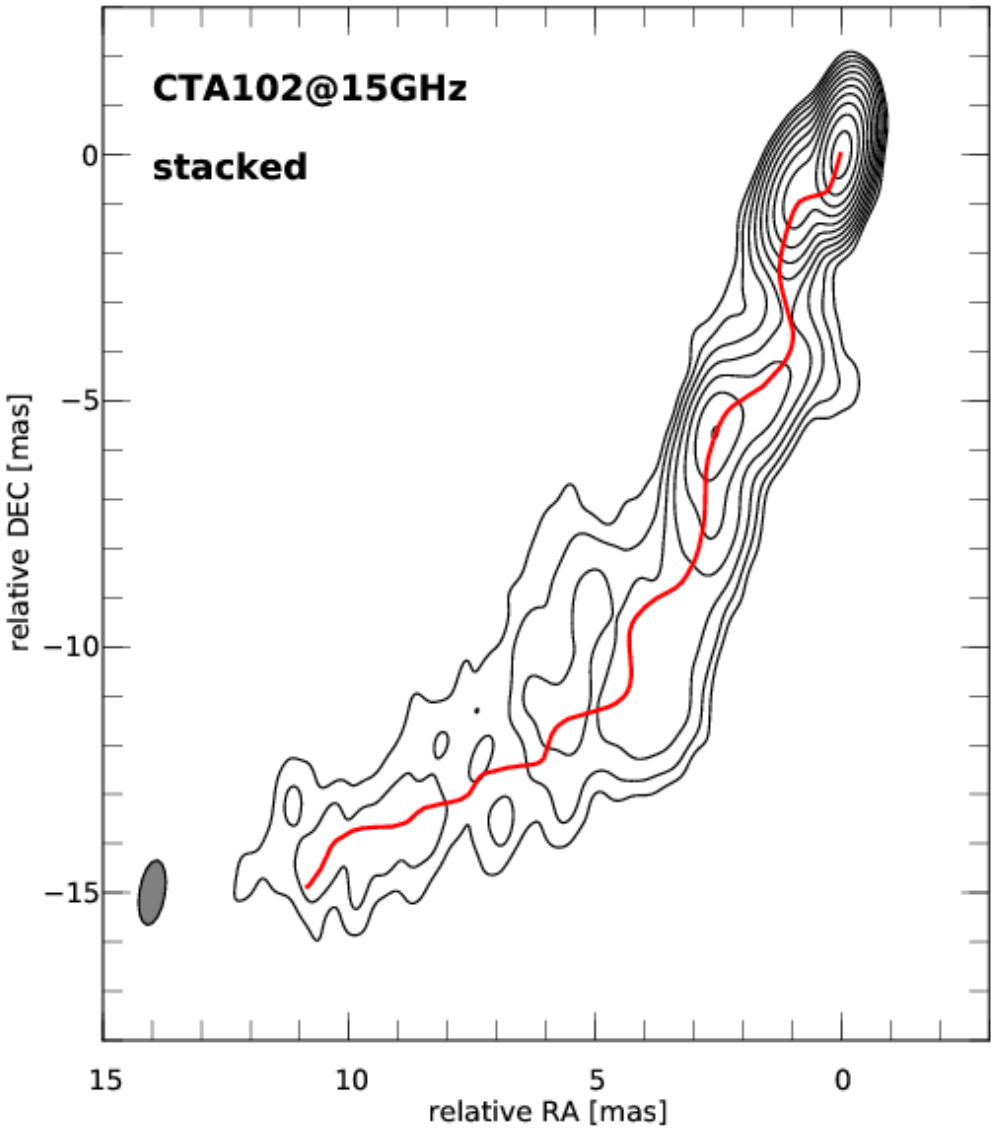

Figure 5.7: Stacked 15 GHz contour map of CTA 102 obtained from observations between 2005 and 2007 convolved with a common beam size of 1.33 mas × 0.52 mas and a P. A. of −9° with over-plotted jet ridge line. The lowest contour level is drawn at 5× the average off-source rms (4 mJy) and the contours increase with steps of 2.

the starting position using the average core-shift value, $r = 3.4 \cdot \nu^{-1.25}$. The constant horizontal points for each frequency reflect the resolution limit where we can not resolve the transversal structure of the jet. However, as soon as the transversal jet structure can be resolved, the width of the jet increases. The position of the first observed rise of the jet width increases with decreasing frequency and is in good agreement with the position found at neighboring frequencies, which certifies the validity of the measure. Tracing this point back to the highest frequency available in our data set (86 GHz) leads to a distance of 0.1 mas from the jet nozzle and to a jet width of 0.05 mas, which corresponds to one half of the convolving beam size transversal to the jet ridge line. The jet width is varying,

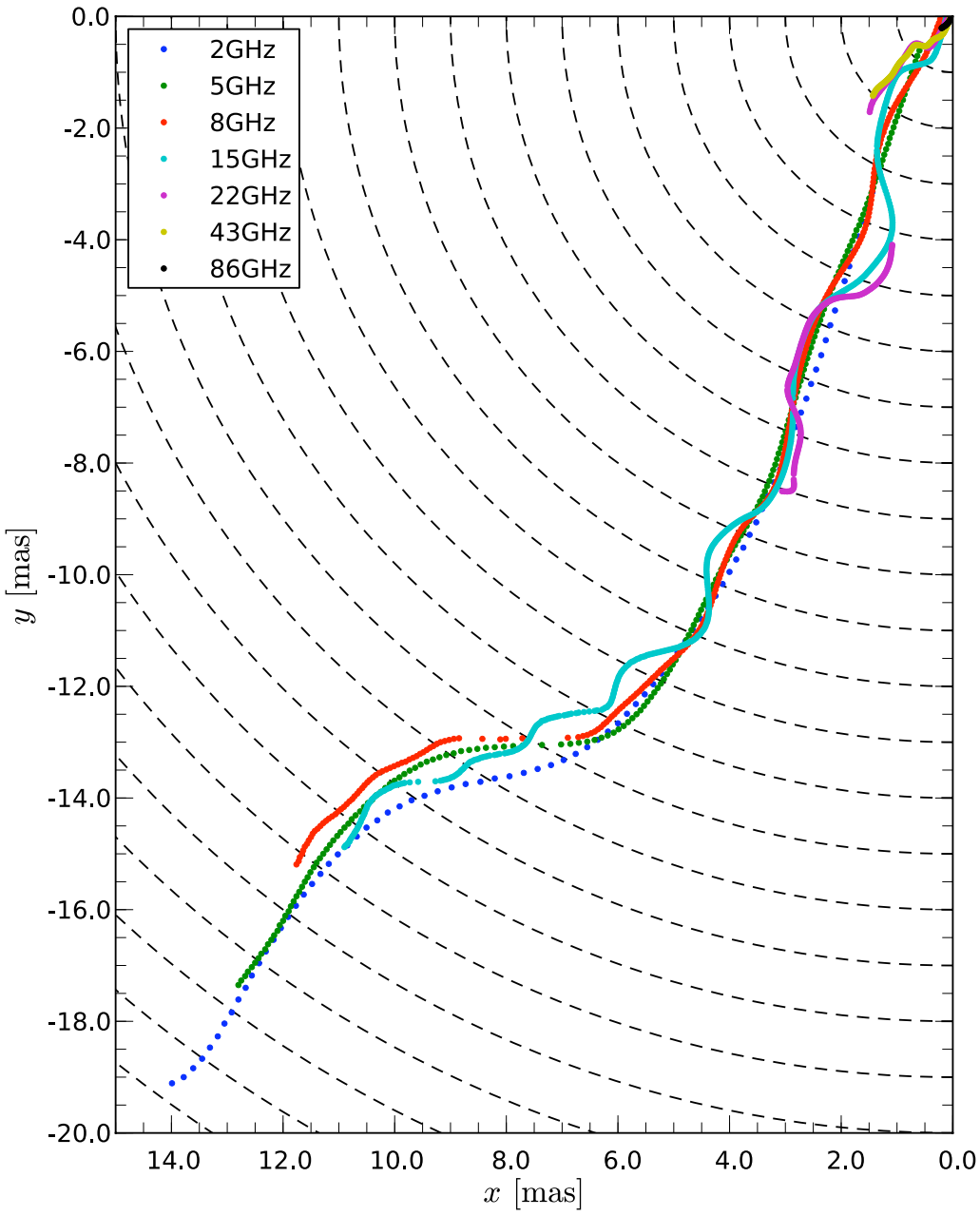

Figure 5.8: Opacity corrected jet ridge line for CTA 102 obtained from stacked VLBA images at different frequencies. The dashed lines correspond to the radial distance and are plotted every 1 mas.

with several indications for collimation and recollimation along the jet. This behavior is best visible at 15 GHz. For this frequency our analysis reveals three local maxima of the jet width at a core distance along the ridge line of $r = 1.2$ mas, $r = 5.4$ mas and $r = 13.3$ mas. At the higher frequencies $\nu = 22$ GHz and $\nu = 43$ GHz we also find indications of recollimation of the jet at the same positions.

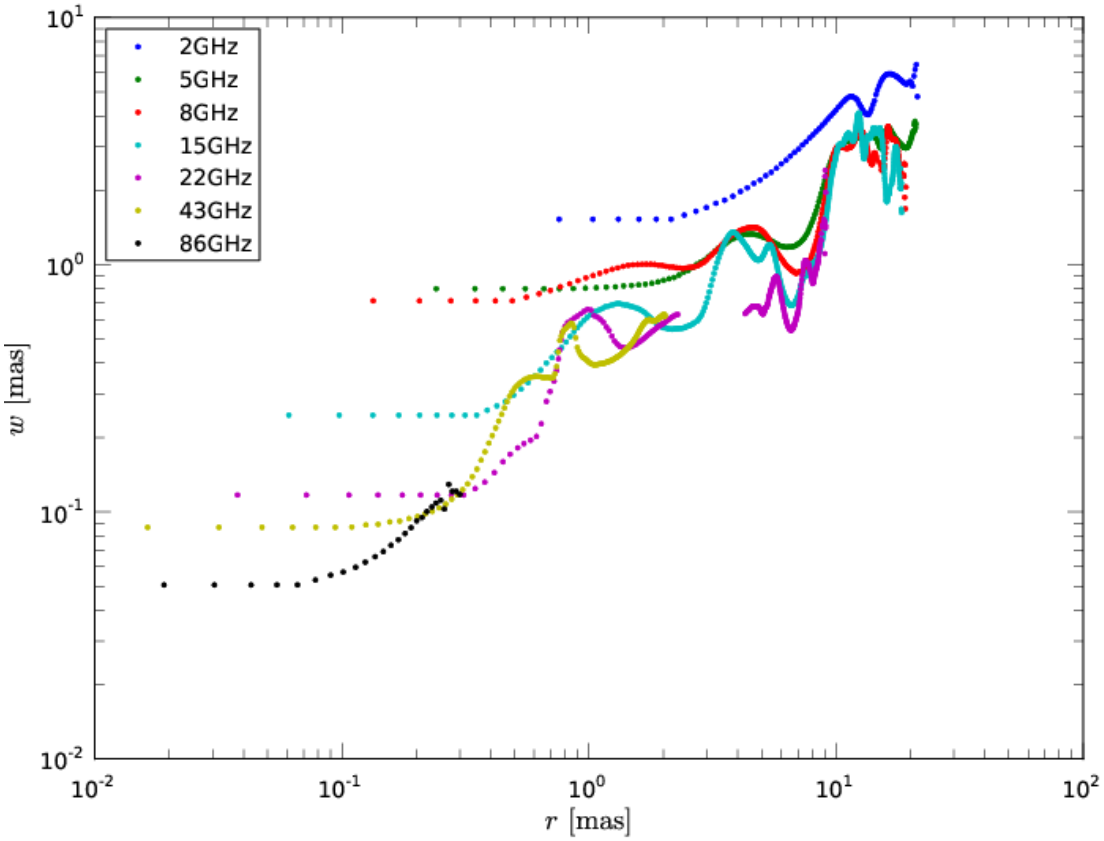

Figure 5.9: opacity corrected jet width of CTA 102 obtained from stacked VLBA images at different frequencies.

The jet width can be parametrized as a power law, $R \propto r^{\epsilon}$ with ϵ as the jet opening index. In Chapter 4 we divided the jet into four different regions, labeled as C ($r < 1$mas), D (1mas $< r <$ 5mas), B (5mas $< r <$ 8mas), and A ($r >$ 8mas) to facilitate the analysis. The jet opening index obtained for each of these regions is presented in Table 5.6. A single power law fit applied to the jet width gives $\epsilon = 0.6 \pm 0.1$ for the four regions.

Table 5.6: Estimates for the exponent ρ, defining the jet geometry, $R \propto r^{\rho}$.

region	C	D	B	A
ρ	0.8 ± 0.1^a	0.8 ± 0.1^b	-1.0 ± 0.1	1.3 ± 0.2

[a] fitted together with region D, otherwise $\rho = 1.2$
[b] fitted together with region C, otherwise $\rho = 0.4$

The results of the jet width analysis show that CTA 102 embeds a pinching jet width, i.e., it consists of regions where the jet cross-section is opening or closing. At $r < 1$ mas the jet shows a nearly conical geometry $\epsilon = 0.8 \pm 0.1$. Farther downstream ($r > 4$ mas) the jet geometry differs significantly from conical.

5.4 Spectral analysis

Here we present the result of the spectral analysis for the different jet regions as introduced in Chapter 4. We show the spectral parameters along the jet ridge-line and averaged values transversal to it, which reflect possible transversal gradients in the spectral parameters across the jet. The 2D distribution of the spectral parameters can be found in Appendix C.

Since the spectral turnover is outside our frequency range for regions B and A, we applied a power law $S_\nu \propto \nu^\alpha$ to the measured flux densities. The uncertainties on the spectral parameters were calculated using a Monte-Carlo simulation taking into account the uncertainties of the image alignment and the flux densities of the individual pixels. Since the uv-coverage is changing with frequency we only used those uv-radii covered throughout the selected frequency range. Table 5.7 gives the average uv-ranges for the different frequencies, and in Appendix B we present the influence of the uneven uv-coverage on the derived spectral parameters.

Table 5.7: UV ranges for different frequencies

ν	$r_{uv,\mathrm{min}}$	$r_{uv,\mathrm{max}}$
[G]	Mλ	Mλ
2	1	66
5	3	144
8	5	250
15	9	450
22	14	640
43	27	1240
86	66	1760

5.4.1 Region C ($r < 1$ mas)

The core region is characterized by an inverted spectrum (increasing flux density with increasing frequency) throughout our data set. Therefore, we applied a power law fit to obtain the 2D distribution of the spectral index α. The region could be best studied using the high frequency VLBI maps ($\nu > 8$ GHz), a common beam size of 0.95×0.33 mas with a P.A. of $-13°$, which corresponds to the average beam of the 22 GHz observations, and a pixel size of 0.03 mas. These image settings allowed us to extract the spectral index without generating image artifacts in the low frequency maps or losing structural information in the high frequency maps.

The spectral index along the jet axis is presented in Fig. 5.10, where we used the 43 GHz core of each observation as the origin of coordinates. Within $r < 0.3$ mas from the core, the spectral index is positive ($\alpha > 0$), which corresponds to an inverted spectrum and farther downstream α decreases with distance. There is a variation of α with distance and time. The latter is best visible between May 2005 and October 2006, when the slope of the the spectral index along the jet changes from -1.6 (May 2005) to -1.1 (June 2006) and back to -1.3 (October 2006). This could be an indication for the injection of relativistic

particles and the connected energy losses during the propagation of a relativistic shock wave.

Since our frequency coverage for the May 2005 observations spans from 5 GHz to 86 GHz, estimates on the values at the spectral turnover could be derived. For this epoch, we only present axial turnover values, since we could hardly resolve the transversal structure of the source with the selected beam size. Figure 5.11 shows the spatial evolution of the turnover frequency, ν_m, the turnover flux density, S_m, and the optically thin spectral index, α_0 along the jet ridge line. The optically thin spectral index decreases from -0.1 at $r = 0.15$ mas to -0.45 at $r = 0.5$ mas. At the same distance the turnover frequency changes from $\nu_m = 30$ GHz to $\nu_m = 15$ GHz at $r = 0.5$ mas. A drop in the turnover flux density, S_m, occurs at $r = 0.2$ mas from $S_m = 2.3$ Jy to $S_m = 1.2$ Jy.

In the turnover frequency–turnover flux density plane, the spatial evolution shows a constant turnover flux density $S_m = 2.3$ Jy for $r < 0.15$ mas, while the turnover frequency decreases (see fig. 5.12). For $r > 0.15$ mas both, the turnover frequency and the turnover flux density decline. This monotonic decrease in the turnover position is in agreement with the expected behaviour, when the (adiabatic) expansion losses are the dominant energy loss mechanism (Marscher & Gear 1985). The constant turnover flux density measured across the region at $r < 0.1$ mas could be due to the smearing of the flux density caused by the convolution.

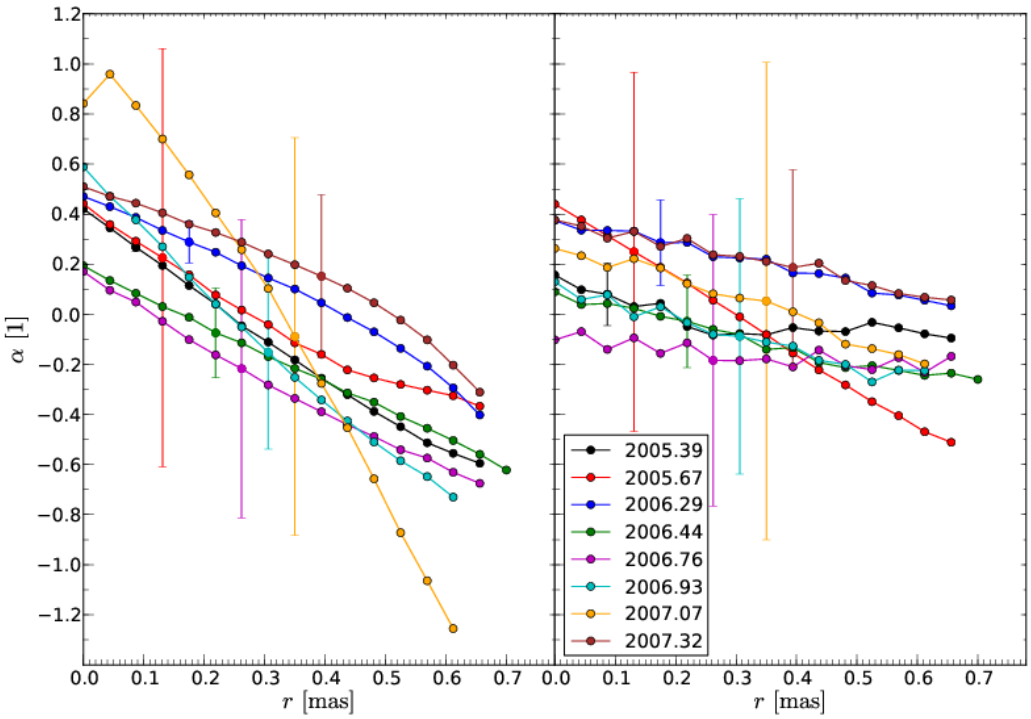

Figure 5.10: Evolution of the spectral index, α ($S_\nu \propto \nu^\alpha$) for region C ($r < 1$ mas), where we used a beam size of 0.95×0.33 mas with a P.A. of $-13°$. For reasons of readability we plot only one representative uncertainty for each epoch. Left: along the jet ridge line. Right: average values transversal to the jet ridge line.

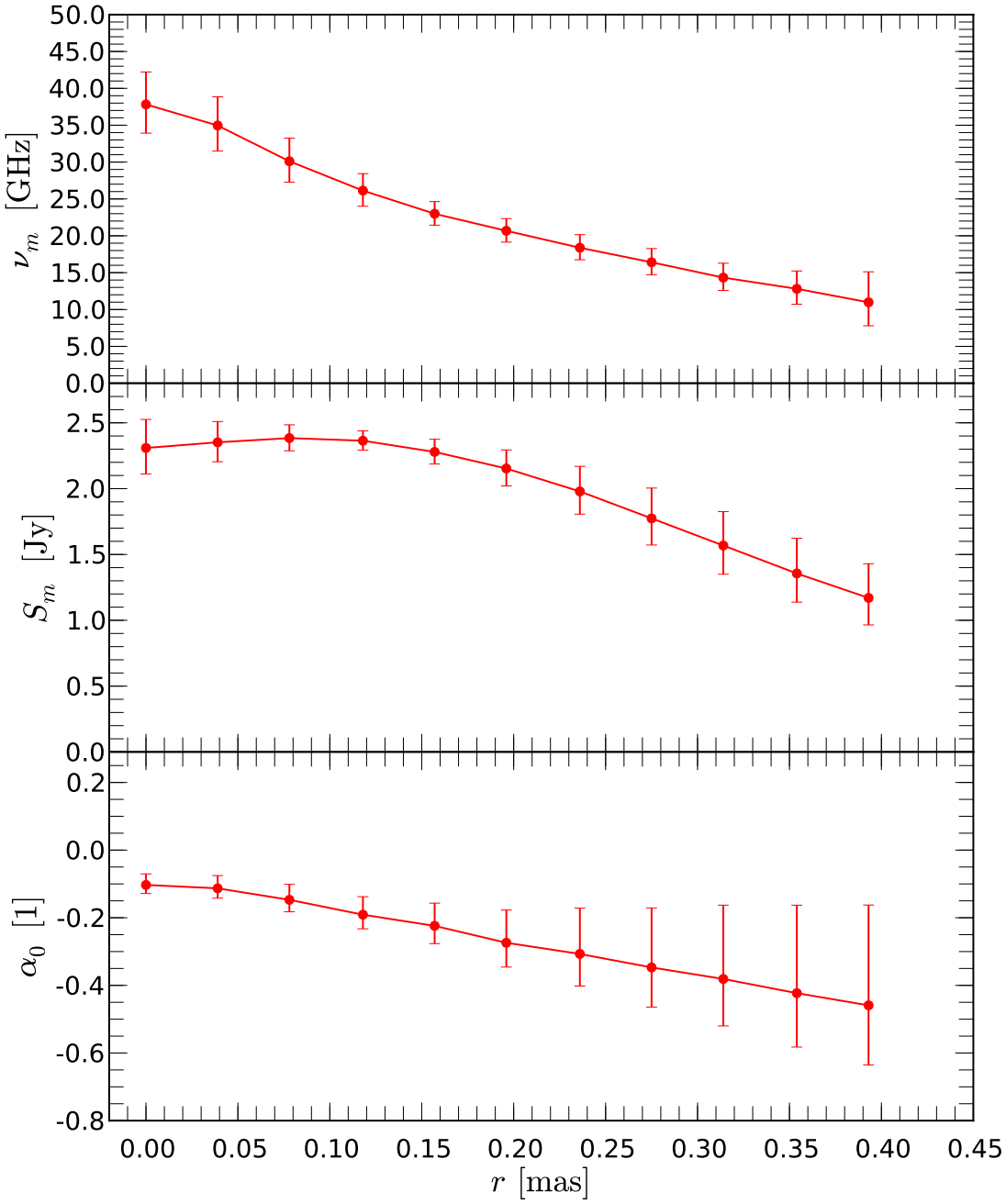

Figure 5.11: Spatial evolution of the turnover values along the jet ridge line for the May 2005 observation (2005.39). We used beam size of 0.95×0.33 mas and a pixel size of 0.01 mas. The error estimates were derived by means of a Monte Carlo simulation (see text for more details). Top panel: Turnover frequency, ν_m; middle panel: turnover flux density, S_m; bottom panel: optically thin spectral index, α_0

5.4.2 **Region D** (1 mas $< r <$ 4 mas)

For the spectral analysis of region D we used a beam size of 1.33×0.52 mas and a pixel size of 0.04 mas and included the 5 GHz and 8 GHz VLBI maps into the analysis. Due to this extended frequency range we could derive the turnover values by applying equation 2.27. We rejected turnover frequencies below 5 GHz and optically thin spectral indices, $\alpha_0 > -0.2$. These criteria provide the most reliable and physically meaningful values from our data. The values obtained for the turnover frequency in this region are between 5.0 GHz and 10.0 GHz. The axial turnover frequencies exhibit a curved distribution, where the value of the peak and its position vary in time (see the left panel in fig. 5.13). This curvature could be an artifact of the convolution. However, the transver-

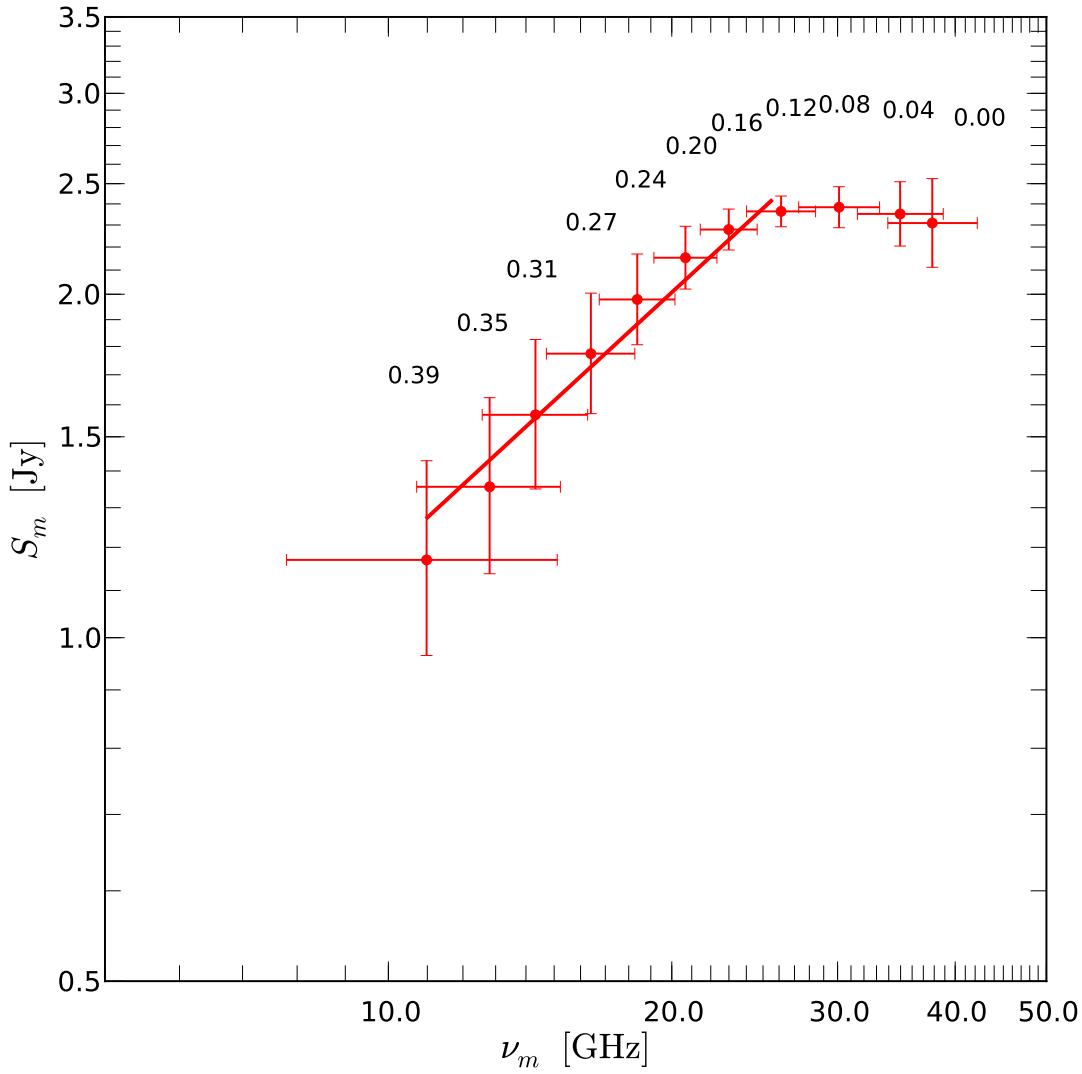

Figure 5.12: Turnover frequency–turnover flux density plane for region C for the May 2005 observations. The number correspond to the distance to jet nozzle in mas.

sally averaged values show a monotonic decrease in the turnover frequency (see the right panel in fig. 5.13).

The evolution of the turnover flux density, S_m, shows a clear decreasing trend with time and a slight shift in the position of the flux density maxima with distance from the core (see Fig. 5.14). The optically thin spectral index shows an increasing trend with distance from $\alpha_0 \sim -1.0$ to $\alpha_0 \sim -0.5$, but the large uncertainties in the optically thin spectral index do not allow to detect a clear temporal variation (see Fig. 5.15).

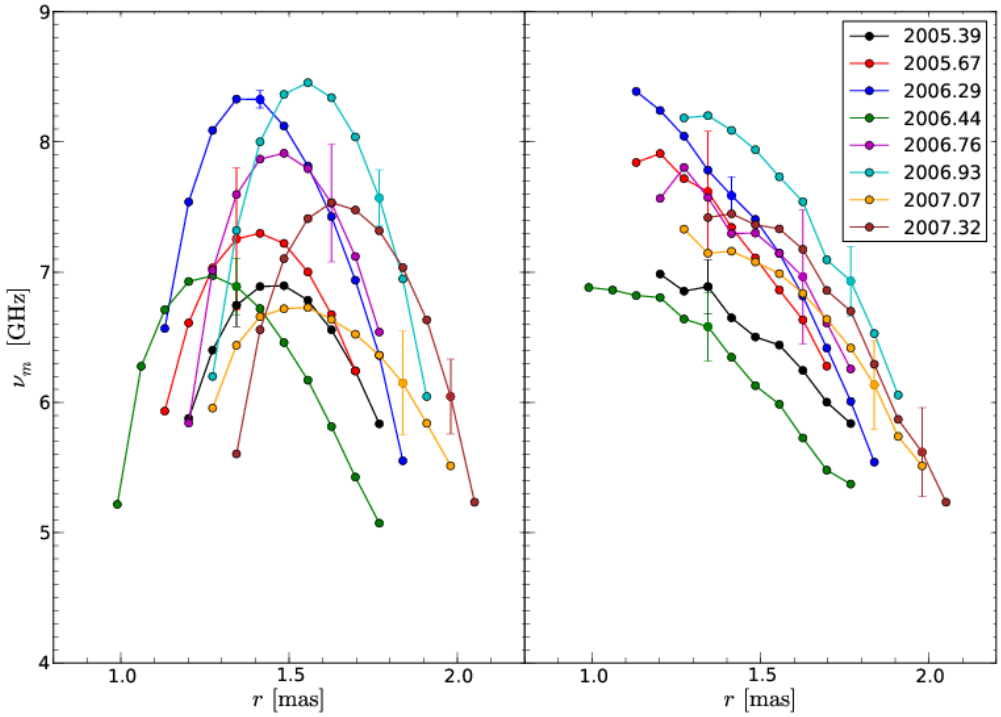

Figure 5.13: Evolution of the turnover frequency, ν_m, for region D (1 mas $< r <$ 4 mas) along the jet axis, where we used a beam size of 1.33×0.52 mas with a P.A. of $-9°$. For reasons of readability we plot only one representative uncertainty for each epoch. Left: along the jet ridge line. Right: average values transversal to the jet ridge line.

From the results of region D we can see significant changes in the turnover frequency and turnover flux density with time and position. Figure 5.16 shows the variation of the turnover values in the turnover frequency - turnover flux density ($\nu_m - S_m$) plane for a fixed position at $r = 1.5$ mas. The kinematic analysis of CTA 102 revealed a traveling component, labeled as D2, within this region and a possible standing component at $r =$ 1.5 mas (see region D in Sect. 4.2.5). The evolution in the $\nu_m - S_m$ plane shows an increase in both ν_m and S_m between 2005.3 and 2006.3 followed by an increase in 2006.44. For $t >$ 2006.44, the turnover flux density is smaller than in 2005.3 and the turnover frequency varies slightly.

The kinematical results (see Sect. 4.2) and the present spectral study point towards a situation in which component D2 crosses region D during the time span of our observations, possibly interacting with a standing emission region at $r \simeq 1.5$ mas. Following the

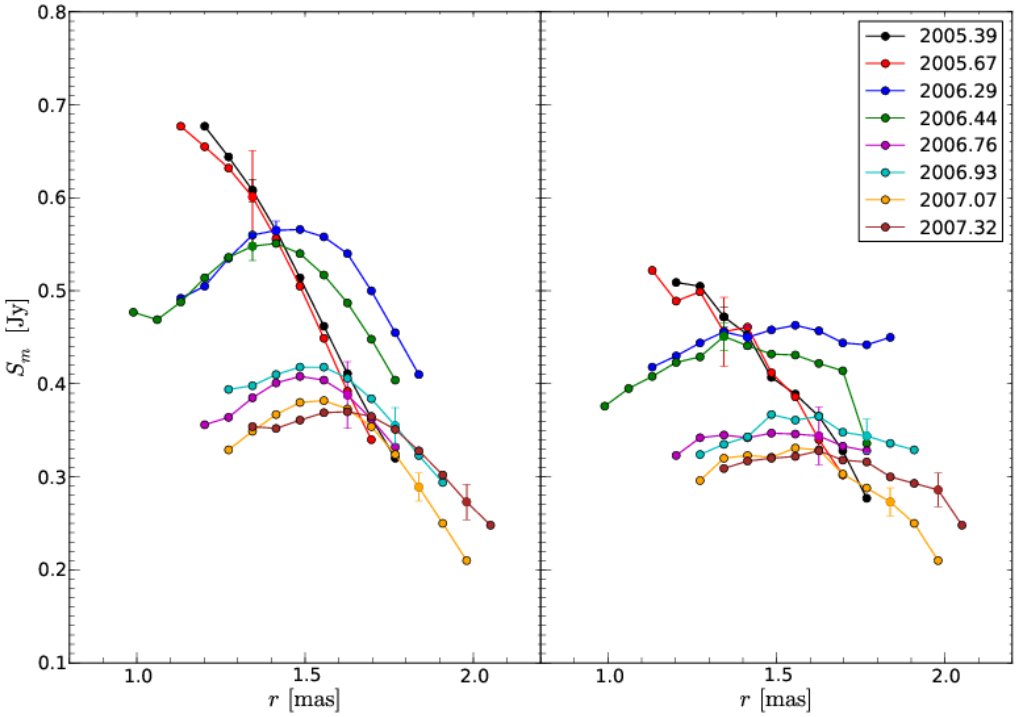

Figure 5.14: Same as Fig. 5.13 for the turnover flux density, S_m.

classical shock-in-jet model, we would expect a continuous decrease in turnover flux density and turnover frequency, since at this position, $r = 1.5$ mas (de-projected 86 pc), the main energy loss mechanism should be adiabatic expansion losses. However, we detect an increase in S_m at this position, which could be due to an re-accleration of relativistic electrons or an increase in the particle density (see Chapter 3). From the spectral analysis of region C we know that the turnover flux density and turnover frequency are monotonically decreasing (see Fig. 5.12). Therefore, the increase in the $\nu_m - S_m$ plane requires a region of locally increased density and/or magnetic field. Such a local increase in the physical parameters could be created by a recollimation shock. The results of the kinematic analysis in region D (see Sect. 4.2.5) and the study of the transversal jet width (Section 5.3) support this assumption.

5.4.3 Region B (4 mas $< r <$ 10 mas)

This region is characterized by three nearly stationary components (see Sect. 4.2.4) and by a plateau in the jet width (see section 5.3). Figure 5.17 shows the value of the spectral index along the jet. This region could be best studied by using a frequency range from 5 GHz to 15 GHz, a beam size of 2.32×0.97 mas, a P.A of $-7°$, and a pixel size of 0.10 mas. The spectral index at $r \sim 2.0$ mas is between $-0.8 < \alpha < -0.6$, which is consistent with the continuation of the observed evolution in region D (see fig. 5.15). For $r > 2.0$ mas an increase in the spectral index can be observed, followed by a plateau of nearly constant value at $r = 4.0$ mas (left panel in fig. 5.17). For larger distances, the

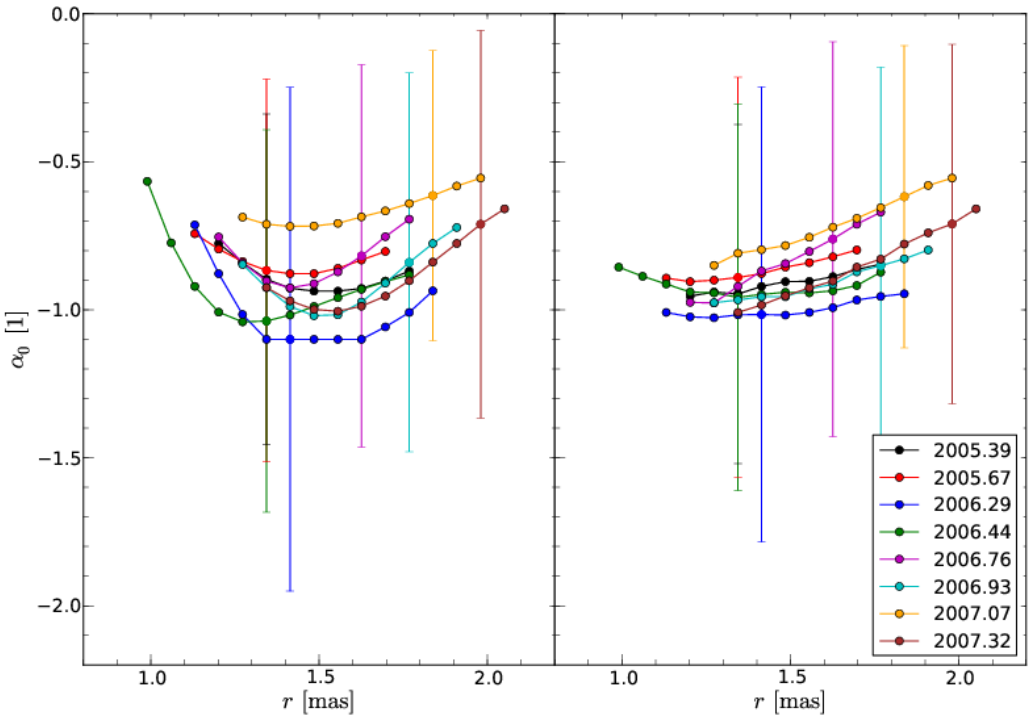

Figure 5.15: Same as Fig. 5.13 for the optically thin spectral index, α_0.

spectral index decreases with distance until $r \sim 7.0$ mas. Farther downstream there is an additional rise of the spectral index, although less pronounced than the one at $r = 4$ mas.

5.4.4 Region A ($8\,\text{mas} < r < 20\,\text{mas}$)

This region can be divided into two sub-regions, the inner, A2 ($8\,\text{mas} < r < 14\,\text{mas}$), and the outer, A1 ($14\,\text{mas} < r < 20\,\text{mas}$). For region A2 we used the VLBI images at 5 GHz, 8 GHz, and 15 GHz and a beam of 3.65×1.52 mas, a P. A. of $-8°$, and a pixel size of 0.15 mas. In contrast to region B, the spectral index decreases from $\alpha \sim -1.0$ to $\alpha \sim -1.2$ without major variations, best visible in the transversally averaged values (see fig. 5.18). The increase of the averaged values for the May 2005 observations (2005.39) is due to a region of high spectral indices at the edges of the jet (see Fig. C.6 in Appendix C).

In the case of A1, since the short uv-radii contribute to the outermost region of CTA 102 ($r > 14$ mas), we used only the 5 GHz and 8 GHz VLBI maps. The spectral index was, in contrast to the other regions, computed using Eq. 5.6 and not by fitting $S_\nu = \text{const}\,\nu^\alpha$. For the calculation of the spectral index we use the same beam as for region A2. Figure **??** shows the spectral index for region A1. In this region, the spectral index is roughly constant around $\alpha \sim 1.2$. The steep spectral index for the September 2005 and October 2006 observations could be due to antenna or weather problems (e.g., rain), which mainly affects the low frequencies and especially the outer structure of the source (see Fig. C.7 in Appendix C)

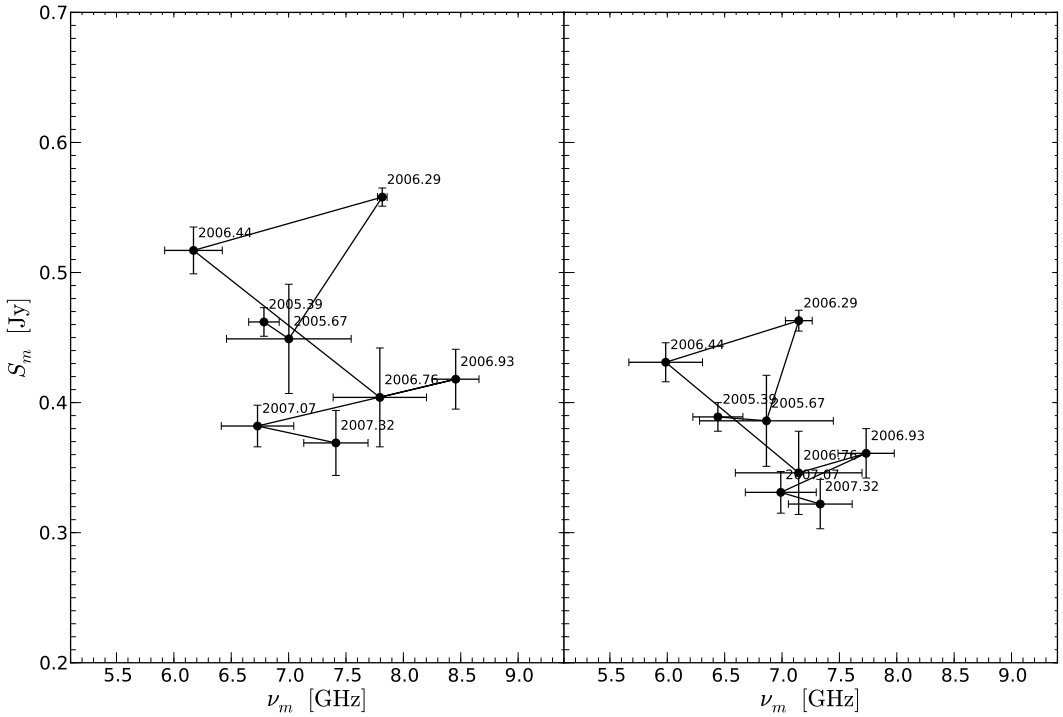

Figure 5.16: Turnover frequency–turnover flux density plane for region D at a fixed position of $r = 1.5$ mas, where the numbers represent the temporal evolution. Left: axial values Right: transversal averaged values (for more details see text).

5.5 Spatial and temporal evolution of physical parameters

5.5.1 Position of the jet nozzle

Only for the May 2005 observations of CTA 102 and for region C could we derive the turnover frequency, ν_m, and the turnover flux density, S_m. The spectral turnover values allow us to compute the magnetic field and the normalization coefficient of the relativistic electron distribution using equations 2.34 and 2.35, respectively. Furthermore, we could provide some estimates on the number density of the relativistic particles and on the magnetization, σ, of the plasma using the first order model presented in Sect. 2.2.1 and the jet width (see Sect. 5.3).

In this section we use the opacity corrected core position, i.e., radial origin corresponds to the location where $\tau = 1$ for $\nu \to \infty$ using the results of the core-shift analysis (see Table 5.2 in Sect. 5.2). In Table 5.8 we present the offset corrections for all epochs.

5.5.2 Core region in May 2005

For the calculation of the magnetic field intensity and the normalization coefficient of the relativistic electron distribution we need to know the evolution of the jet width and

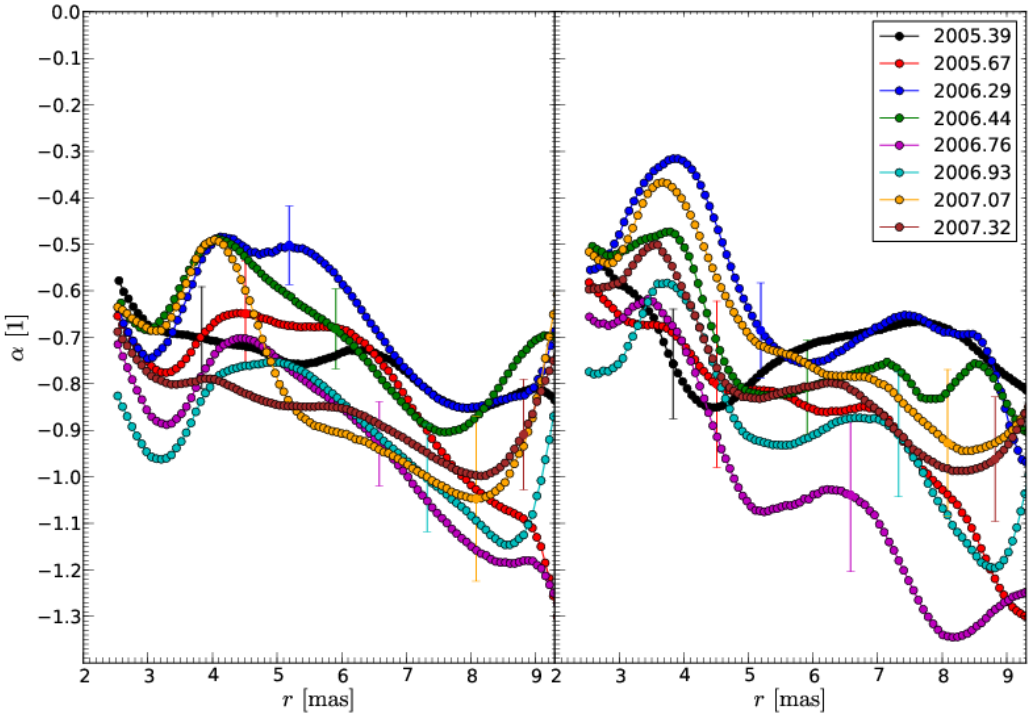

Figure 5.17: Evolution of the spectral index, α ($S_\nu \propto \nu^\alpha$) for region B (4 mas $< r <$ 10 mas) along the jet ridge line. For reasons of readability only one error bar per epoch is shown. Left: values along the jet ridge line. Right: average values transversal to the jet ridge line.

Table 5.8: Results of the core-shift analysis.

Epoch	$\Delta r_{\rm nozzle}$ [mas]
2005-05-19	0.02± 0.01
2005-09-01	0.03±0.08
2006-04-14	0.03±0.02
2006-06-08	0.04±0.03
2006-10-02	0.01±0.01
2006-12-02	0.05±0.03
2007-01-26	0.04±0.04
2007-04-26	0.01±0.01

an estimate for the Doppler factor along the jet. Since the turnover values for region C were obtained using the average beam size of the 22 GHz VLBI maps (see Sect. 5.4.1), we used the jet width calculated for this frequency (see Sect. 5.3). Based on the flux density evolution of the component labeled as C2 we calculated a variability Doppler factor $\delta_{\rm var} = 17 \pm 3$. A parameter space study based on the gradients in the brightness temperature, T_b, revealed that the Doppler factor increases within region C (see Sect. 5.4.1). Accordingly with the numbers obtains in Sect. 5.4.1, we adopted an exponent of

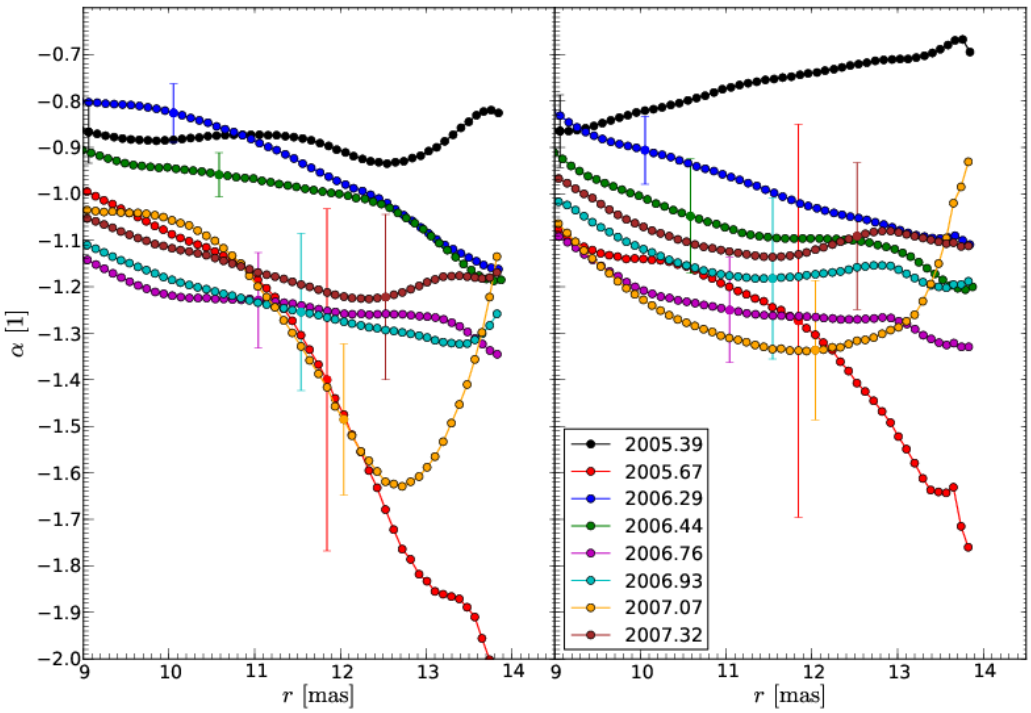

Figure 5.18: Evolution of the spectral index, α ($S_\nu \propto \nu^\alpha$) for region A2 (8 mas $< r <$ 14 mas) along the jet ridge line. For reasons of readability only one error bar per epoch is shown. Left: values along the jet ridge line. Right: average values transversal to the jet ridge line.

$d = -0.6$ ($\delta = R^{-d}$) and an upper value of $\delta = 17$ for the following analysis.

The magnetic field computed from the aforementioned parameters is presented in the upper panel of figure 5.20. The magnetic field intensity decreases from 60 mG at $r = 0.1$ mas to 10 mG at $r = 0.45$ mas. The influence of the spectral aging, i.e., the decrease of α_0, is visible in the continuos steepening of the magnetic field intensity. The results of an approximation of the evolution with a power law ($B \propto r^{b'}$) gives an exponent $b' = -0.3 \pm 0.1$ for the whole range (0.02 mas $< r <$ 0.45 mas, dashed red line in the upper panel of fig. 5.20). The flat spectral index for $r < 0.1$ mas could be due to convolution effects. Therefore, we additionally fitted the evolution of the magnetic field intensity for $r > 0.1$ mas and obtained an exponent of $b' = 0.7 \pm 0.1$ (solid red line in the upper panel of Fig. 5.20). Similar values for the magnetic field intensity, B, were obtained using the core-shift (see sect. 2.46). Since both methods are independent, the result of the magnetic field can be regarded as meaningful estimate.

The normalization coefficient of the relativistic electron distribution spans from 5.0 erg$^{-2\alpha_0}$cm^{-3} to 10^{-4} erg$^{-2\alpha_0}$cm^{-3}. We used a power law ($K \propto r^{k'}$) to fit the evolution of K with distance along the jet and obtained $k' = -3.6 \pm 0.3$ for the entire region (dashed red line in the lower panel of Fig. 5.20). As in the case of the magnetic field, the values for K steepen for $r > 0.1$ mas. A power law fit for this region results in $k' = -4.6 \pm 0.2$ (solid red line

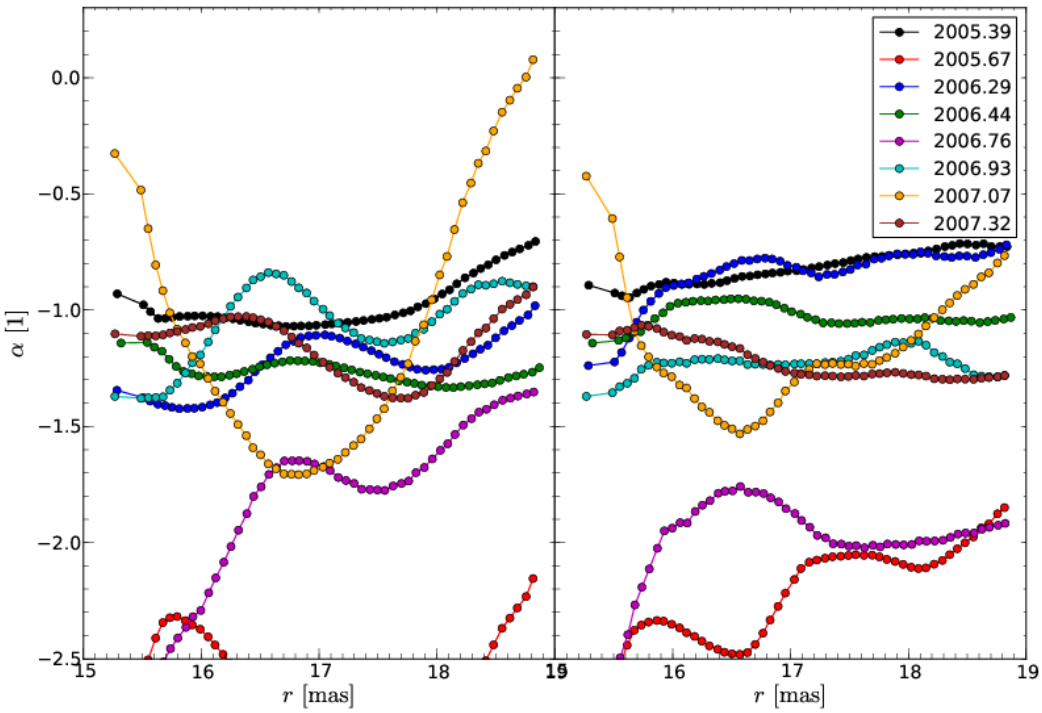

Figure 5.19: Evolution of the spectral index, α ($S_\nu \propto \nu^\alpha$) for region A1 (14 mas $< r <$ 20 mas) along the jet ridge line. Left: values along the jet ridge line. Right: average values transversal to the jet ridge line.

in the lower panel of Fig. 5.20). The values of the normalization coefficient can not be directly compared due to the varying spectral index along the jet (see bottom panel in figure 5.11 and Eq. 2.35).

The slopes obtained from the variation of the magnetic field, B, and the normalization coefficient, K, (see fig. 5.20) correspond to the evolution along the jet and include the influence of the jet geometry (e.g., the magnetic field along the jet is given by $B \propto r^{\epsilon b}$). We thus have to take into account the evolution of the jet radius in order to derive the geometry of the magnetic field. The evolution of the transversal jet size with distance in region C can be fitted with an exponent $\epsilon = 0.8 \pm 0.1$ ($R \propto r^\epsilon$). This results in $b = -0.4 \pm 0.1$ for the overall region and to $b = -0.9 \pm 0.2$ for $r > 0.1$ mas. For the evolution of the normalization coefficient K we computed an exponent of $k = -4.5 \pm 0.7$ for 0.02 mas $< r <$ 0.45 mas and $k = -5.7 \pm 0.8$ for $r > 0.1$ mas.

Assuming adiabatic expansion losses as the main energy loss mechanism, and following Marscher & Gear (1985); Lobanov & Zensus (1999), the slope in the $\nu_m - S_m$ plane is given by:

$$\eta_{\mathrm{adi}} = -\frac{2s + 13 - 5k - b(2s + 3) - d(3s + 7)}{2(k - 1) + (b + d)(s + 2)}, \tag{5.8}$$

with b the exponent for the evolution of the magnetic field intensity ($B \propto R^{-b}$), k the exponent for the evolution of the normalization coefficient of the relativistic electron distribution ($K \propto R^{-k}$), d the exponent for the evolution of the Doppler factor ($\delta \propto R^{-d}$),

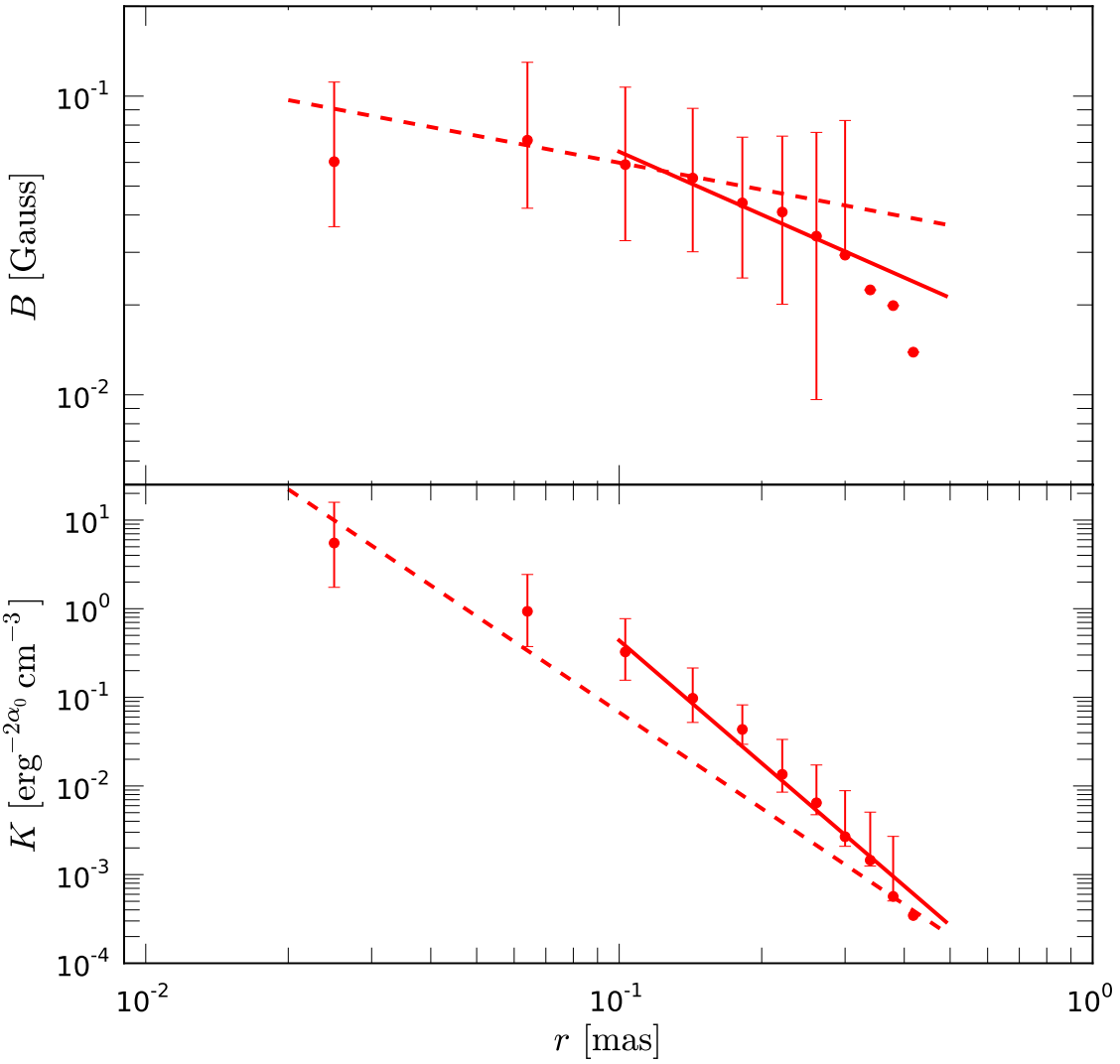

Figure 5.20: Evolution of the magnetic field B (top panel) and the normalization coefficient, K (bottom panel) for the May 2005 observation. The solid red and black lines correspond to a power law fits for the entire region and for $r > 0.1$ mas, respectively (see text for details).

and s the spectral slope ($N = K\gamma^{-s}$). A power law fit to the variation of the turnover flux density with respect to the turnover frequency provides an exponent $\eta = 0.8 \pm 0.1$ (see Fig. 5.12). Together with estimates on b, k and d, we obtained the average spectral slope $\langle s \rangle = 2.3 \pm 0.6$, by solving Eq. 5.8 for s. This value for the spectral slope is, within the uncertainties, in agreement with the results of the parameter space study based on the observed brightness temperature gradients for the adopted value of $d = -0.6$ (see panel 2 in Fig 4.16).

5.5.3 Region D

For the calculation of the magnetic field and the normalization coefficient for region D we used the jet width obtained from the stacked 15 GHz VLBI maps (see Fig. 5.9 in section 5.3). The jet expands until $r \sim 1.5$ mas and collimates between 1.5 mas $< r <$ 2.4 mas. Power law fits applied to the expansion and collimation regions give $\epsilon = 0.8 \pm 0.1$ and $\epsilon = -0.5 \pm 0.1$ (where ϵ is the jet opening index, $R \propto r^{\epsilon}$). The kinematic analysis of region D shows a decreasing trend for the Doppler factor, which is based only on two data points, due to the lack of traveling components within this region. Because of this, we used for the calculation of the magnetic field and the normalization coefficient the average of $\langle\delta\rangle = 7$.

The upper panels in Fig. 5.21 show the spatial and temporal evolution of the axial (left panel) and transversally averaged (right panel) magnetic field intensity. The axial magnetic field varies between 6 mG and 0.5 mG and the transversal averaged magnetic field spans from 10 mG to 0.5 mG. Like the turnover frequency for region D, the magnetic field intensity on-axis shows a parabola shaped distribution (there is a rise and a decrease within the region) whereas the transversally averaged magnetic field decreases with distance. However, both show an increase between 2005.39 and 2006.29, which could be due to the passage of a traveling feature through this region (see component D2 in Sect. 4.2.5).

The evolution of the normalization coefficient, K, with distance to the core is presented in the lower panels of figure 5.21. The left panel shows the on-axis values and the right panel shows the transversally averaged ones. In both cases, K decreases in the region 1.0 mas $< r <$ 1.5 mas and increases farther downstream. The variation in K is larger for the axial values (from 5×10^{-5} erg$^{2\alpha_0}$cm^{-3} to 10^{-11} erg$^{2\alpha_0}$cm^{-3}) than for the transversally averaged values (between 10^{-11} erg$^{2\alpha_0}$cm^{-3} and 10^{-7} erg$^{2\alpha_0}$cm^{-3}). The values for K depend on the optically thin spectral index and cannot therefore be directly compared. In contrast to the magnetic field intensity, the shape of the distribution is comparable for both values, and the increase in K could reflect a reaccleration of relativistic particles.

Due to the large scatter and uncertainties in B and K we use in the following the time averaged value at each position. The evolution of these time-averaged values with distance could be approximated by a power law and the results for the exponents are presented in figure 5.22 and table 5.9.

Table 5.9: Results of the power law approximations for B and K in region D

	$r < 1.4$ mas ($\rho = 0.8 \pm 0.1$)			
	b′	k′	b	k
axial	1.4±0.2	–	1.8±0.3	—
trans.	2.5±0.7	-9.6 ± 3	3.1±1.0	-12 ± 4
	$r > 1.4$ mas ($\rho = -0.5 \pm 0.1$)			
	b′	k′	b	k
axial	-0.4 ± 0.3	9.6±3	0.8±0.6	-19 ± 7
trans.	-2.1 ± 0.3	10.2±3	4.2±1.8	-20 ± 8

For $r < 1.4$ mas, b' is for both, on-axis and transversally averaged values in figure 5.22, that expected for a poloidal field ($b' \sim 2$), within the uncertainties. However, there is a

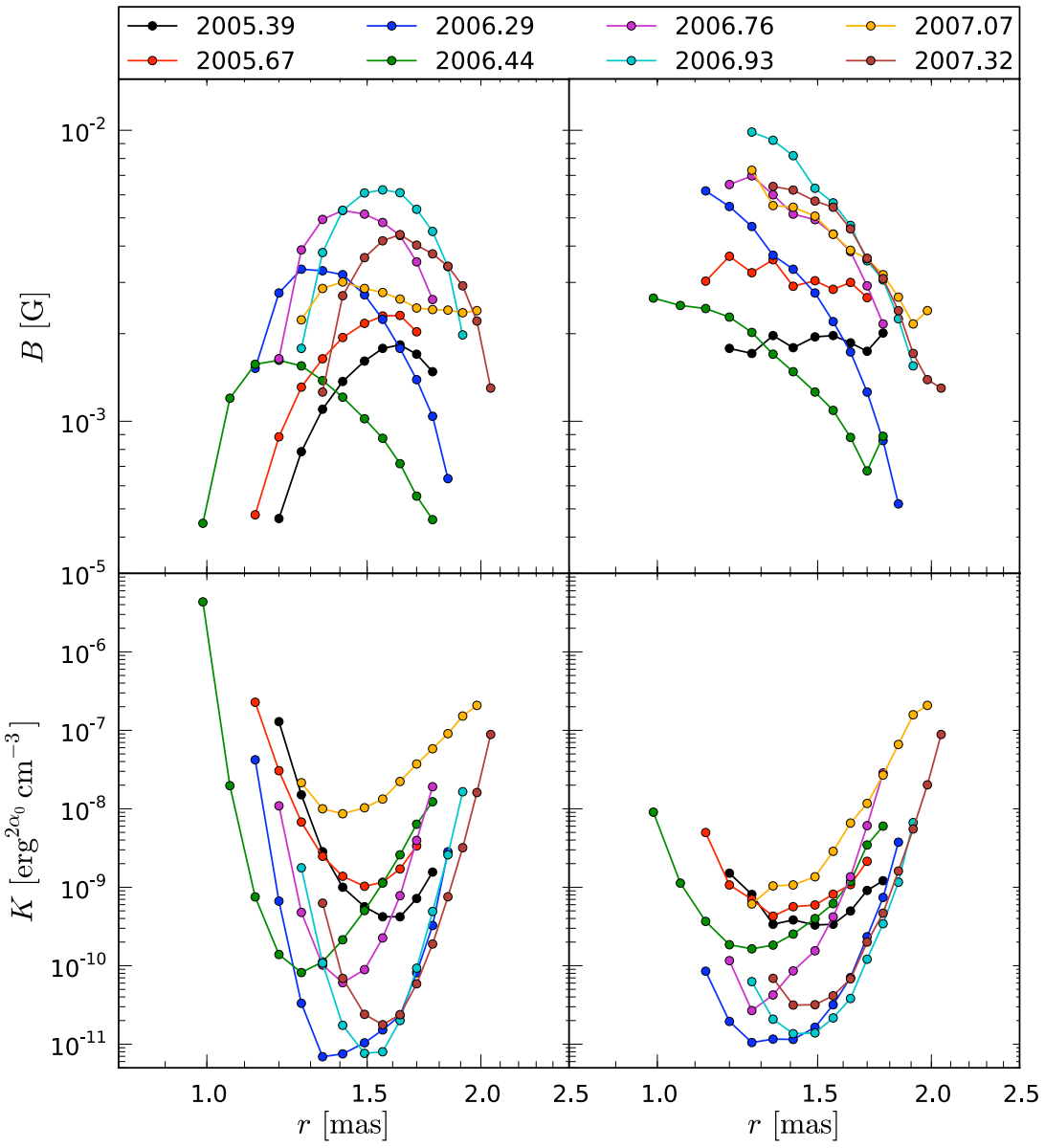

Figure 5.21: Evolution of the magnetic field B (top panel) and the normalization coefficient, K (bottom panel) for region D. The left hand side correspond to the axial values and the right hand side transversally averaged value along the jet.

significant difference between the value on-axis and the averaged one, indicating that the field is poloidal on average, but could have a toroidal component closer to the axis. The strong decrease in the value of K on-axis results in an exponent $k' \sim 30$ (not given in the table), which reflects the huge scatter in the temporal evolution of K (see Fig. 5.21). For the transversally averaged normalization coefficient, K, we obtained an exponent of $k = -12 \pm 4$.

For $r > 1.4$ mas (within region D), the difference in the exponent between the on-axis

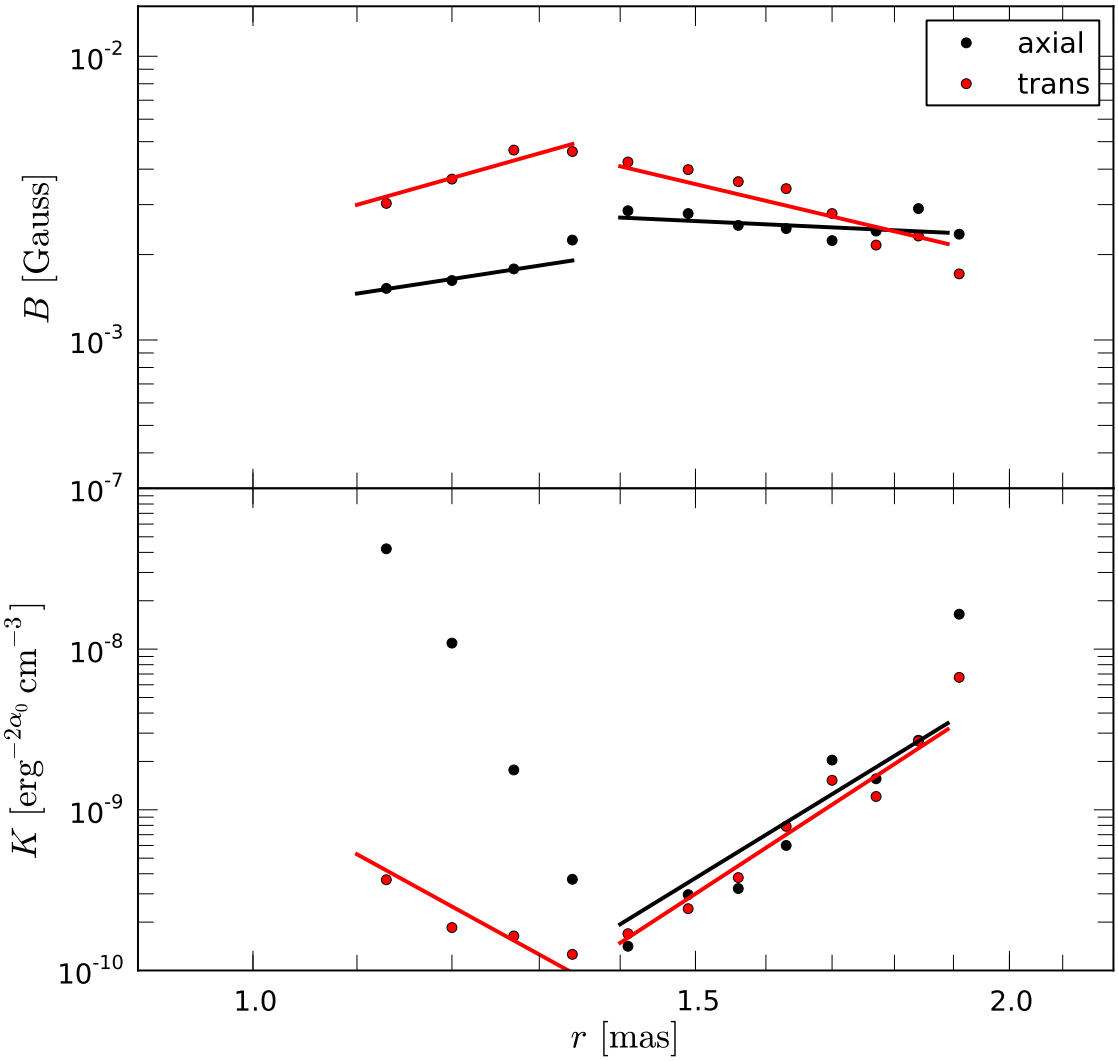

Figure 5.22: Evolution of the time averaged magnetic field B (top panel) and the normalization coefficient, K (bottom panel) for region D. The black points and lines correspond to averaged axial values and the red points an lines to the transversally averaged values along the jet.

values and the transversally averaged ones is larger. On-axis, the exponent indicates that the magnetic field is not organized in poloidal geometry, whereas the transversally averaged value of the field would keep the poloidal structure from the previous region. For both the on-axis and the transversally averaged normalization coefficients the exponent is $k \sim 20$. The unclear geometry of the magnetic field close to the jet axis in region D, together with the kinematic analysis for this region, could be interpreted in terms of an additional shock-shock interaction, as already suggested in Chapter 4. Such an interaction could lead to strong variations in magnetic field intensity and orientation. In particular, an increase in the transversal component (radial) is expected at the shock. Numerical simula-

tions show that, at the position of recollimation shocks, there is an adiabatic compression that causes a (symmetric) bump in the spectral index (Mimica et al. 2009).

Particle density, $N_{\rm tot}$ and relativistic energy density, U_e

We used the model presented in Sect. 2.2.1 together with the magnetic field, B, and the normalization coefficient, K, we could compute estimates for the evolution of the total particle density, $N_{\rm tot}$, and the relativistic energy density, $U_{\rm re}$ for regions C and D. The values of $N_{\rm tot}$ and $U_{\rm re}$ in region D were obtained from the average magnetic field and normalization coefficient (see Fig. 5.22). Figure 5.23 presents the results of our calculations taking radiative and adiabatic losses, and only adiabatic losses into account. The panels show the evolution of the total particle density, $N_{\rm tot}$ (panel i), the relativistic energy density, $U_{\rm re}$ (panel ii), the magnetization $\sigma = U_{\rm B}/U_{\rm re}$ (panel iii) and the electron Lorentz factor (panel iv). The circle and diamond markers in panel iv correspond to the upper and lower electron Lorentz factors. Since our model for the evolution of the electron Lorentz factor does not take into account traveling shock waves, the average values of B and K in region D reflect a calculated steady state. However, the possible passage of a traveling component through this region was reported in Chapter 4, so this may be the reason for differences between the model and the observed behavior.

The total particle density for region C ($r < 1$ mas) takes values between (200–15) cm^{-3} if we consider only adiabatic losses and in the range of (100–10) cm^{-3} if we additionally take radiative, here synchrotron losses, into account (panel i in Fig. 5.23). Farther downstream in region D (1 mas $< r <$ 4 mas) the particle density drops to roughly 1 cm^{-3} and increases at $r \sim 1.5$ mas to 5 cm^{-3} (location of a possible standing shock). The values for both models lead to similar values since the $N_{\rm tot} \propto \gamma_{\rm min}^{1-s}$ (see equation 2.36) and the evolution of the lower electron Lorentz factor is not affected by radiative losses (see panel iv).

The influence of radiative losses is clearly visible in the evolution of the relativistic energy density, $U_{\rm re}$, for region C (panel ii in Fig. 5.23). The energy density takes values in the range of $(5 \times 10^{-1}$–$5 \times 10^{-3})$ erg cm^{-3} if only adiabatic losses are considered and from (10^{-2}-10^{-3}) erg cm^{-3} if both, synchrotron and adiabatic losses are included. Since the spectral slope for region C is $s < 2$, the relativistic energy density is mainly proportional to $\gamma_{\rm max}$ (see Eq. 2.37). As shown in Sect. 2.2.1, radiative losses strongly affect the variation of $\gamma_{\rm max}$. The difference between the two models nearly disappears in region D, where we obtain values between 10^{-4} erg cm^{-3} and 10^{-5} erg cm^{-3}. The dependence of $U_{\rm re}$ changes from $U_{\rm re} \propto \gamma_{\rm max}^{2-s}$ to $U_{\rm re} \propto \gamma_{\rm min}^{2-s}$ since $s > 2$ within region D (see equation 2.37). As in the case of $N_{\rm total}$, the relativistic energy density increases by a factor 6 at $r \sim 1.5$ mas.

For both models, the jet is particle dominated ($\sigma < 1$) for $r > 0.1$ mas (see panel iv in Fig. 5.23). However, the mentioned differences in $U_{\rm re}$ lead to a difference of a factor 50 in the value of σ between the two models. The magnetization increases from a calculated value around $\sigma \sim 0.01$ in region C to $\sigma \sim 0.1$ in region D (see the third panel in Fig. 5.23) due to the increase of the magnetic field close to the location where we think that a standing shock is located, and drops to $\sigma \sim 0.01$ at $r = 1.5$ mas due to the increase of the particle density (first panel in Fig. 5.23) and the related rise of the relativistic energy

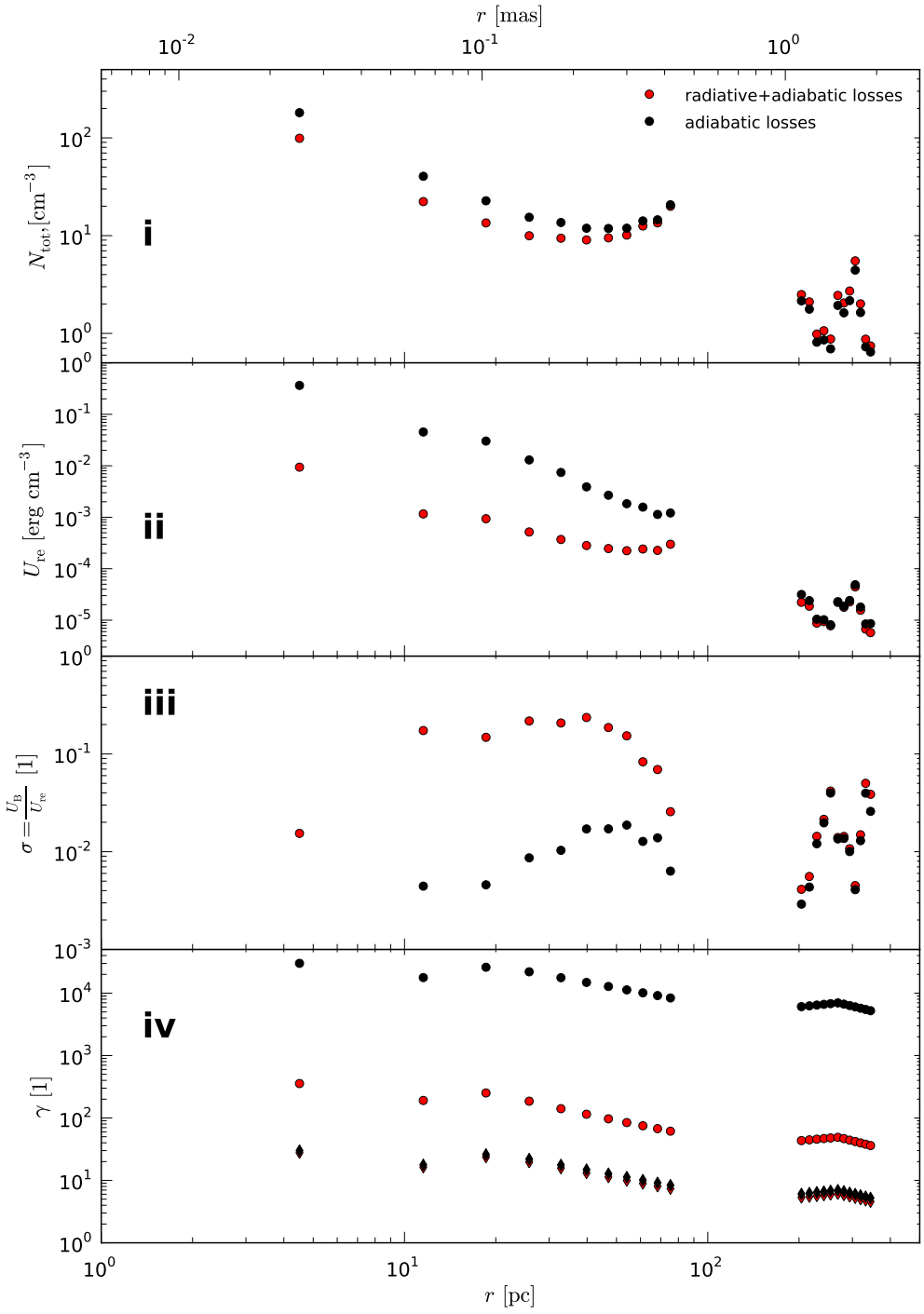

Figure 5.23: Evolution of the source intrinsic parameters taking radiative and adiabatic losses into account (red points) and only adiabatic losses (black points). The differet panels show the variation of the total particle density, $N_{\rm tot}$ (panel i), the relativistic energy density, $U_{\rm re}$ (panel ii), the magnetization $\sigma = U_{\rm B}/U_{\rm re}$ (panel iii) and the electron Lorentz factor (panel iv). The circle and diamond marker in panel D correspond to the upper and lower electron Lorentz factors. For more details see text.

density (second panel in Fig. 5.23).

5.6 Discussion

5.6.1 Region C (core)

Region C covers the first milliarcsecond of the radio-jet. The component ejected after the 2006 flare (C2) evolves during the time spanned by the observations (2005-2007) within this region. This component has a velocity of 0.25 ± 0.04 mas/yr, which translates into an apparent velocity of $13 \pm 2\,c$. In two years the component propagated within the first 0.5 mas. Unfortunately, we do not have enough resolution to identify C2 with accuracy in the spectral index maps of the region (Fig. 5.10 and Fig. C.1).

However, following the temporal evolution of the spectral index distributions (both the axial and the transversally averaged values, see Fig. 5.10), we observe that the first significative increase (beyond errors) of the spectral index in the region occurs at $\sim$ 2006.4 (blue dots). At this time, C2 should be crossing the region around 0.1 mas from the position of the 43 GHz core (0 mas in the plot, see Fig. A.14), which is the expected location of a stationary feature from our results in Chapters 3 and 4.

Chapter 3 we deduced that the flare started around 2005.6 from the spectral evolution of the source as derived from the single-dish data. This evolution was interpreted in terms of the shock-in-jet model (Marscher & Gear 1985). The ν_m, S_m plot after this flare revealed a Compton stage, which lasted until 2005.8, followed by an adiabatic stage. However, in the period 2006.0–2006.3, there was a reversal of the expected evolution, with an increase in the peak flux (S_m), while the peak frequency (ν_m) stayed basically constant. Finally, after 2006.3 the component returned to the expected spectral evolution dominated by adiabatic losses. This second and unexpected peak in S_m could be understood as due to injection of relativistic particles into the system, or to the existing particles going through a compression (Mimica et al. 2009). It was discussed in terms of the interaction of the component ejected after the flare with a standing shock close to the core region. We initially interpreted this stage as a new Compton stage due to its similar behavior in the ν_m, S_m plot. However, it could well be explained as a break within the adiabatic stage. This possibility is being tested using numerical simulations (see Chapter 6).

The observed increase of the spectral index in region C (Fig. 5.10) from the two epochs of 2005 (red and black dots) to that in 2006.4 (blue dots) fits well into the description given in the previous paragraph. After the passage of C2 through the innermost region, it should arrive to the expansion region between $\simeq$ 0.1 mas and $\simeq$ 1 mas (see Fig. 5.9). Then, the observed decrease in the spectral index can also been understood within the evolution of C2 inside the core. The rises of the spectral index in 2006.9 (light green in Fig. 5.10) and 2007.07 (yellow) are compatible with no changes within errors. However, the increase in 2007.4 (brown dots in Fig. 5.10) is clearly beyond errors and very similar to that in 2006.4. Although there is no evidence for a component crossing the core or the 0.1 mas standing feature at this epoch, component C3 is identified between 0 and 0.1 mas from the 43 GHz core position (see Fig. 4.11). Therefore this new increase could be related with the ejection of a new component.

The observed decrease of the spectral index with distance at each epoch can be easily understood in terms of synchrotron and adiabatic cooling times, which are larger in the case of higher frequencies (see, e.g., Blandford & Konigl 1979), so a steepening of the spectral distribution with distance is expected. In summary, the spectral evolution of region C until 2007 is consistent with the propagation of a shock produced by the perturbation ejected in the 2006 radio-flare.

5.6.2 Region D

Figures 5.15, 5.14, and 5.13 show the spectral index, peak flux and peak frequency of the spectral distribution of the jet along region D for the different epochs. The whole picture fits well with the passage of component D2 through the region, as shown by both the axial and averaged values of S_m. The peak in emission propagates from $r \simeq 1$ mas to $r \simeq 1.5$ mas in two years, which is in agreement with the velocity of the component D2 (0.16 ± 0.01 mas/yr, see Table 4.3).

There is discrepancy between the axial and averaged profile shapes of α_0 and ν_m in the 1.0–1.5 mas interval, which could be attached to edge effects (i.e., at the edges of the studied region) in the axial values produced by the alignment procedure. The result is compatible with a smooth decrease of the peak frequency with distance in the region. The large errors in the derivation of the spectral index make it difficult to make any statement regarding its evolution in space and time within the region, but the result seems to indicate that it does not undergo strong changes.

Figure 5.9 indicates that the jet is recollimating between 1 mas and 2 mas and this is confirmed in Fig. 4.8, which shows the continuous presence of a component at $\simeq$1.5 mas from the core, first identified as D1 and later as D2 in this figure. This was also reported by Jorstad et al. (2005b). The interaction between D2 and this standing feature could be responsible for the bump in emission at epochs 2005.39 to 2006.44 seen in the S_m plot (black, red, dark blue, and dark green points) and for the spectral index being possibly constant or slightly increasing within the region. A reconfinement region should generate a compression of the jet particles and generate a symmetric bump in the spectral index profile along the jet (Mimica et al. 2009).

5.6.3 Regions B and A2

The spectral index profile within region B (see Fig. 5.17) shows a clear indication for one or two bumps at 4-5 mas. The fairly symmetric shape of the bumps is an indication of a compression of the particles (Mimica et al. 2009). This could be also the case between 1.5 and 2.5 mas (region B, see below and Fig. 5.17), but we do not have data to probe this hypotheses. In addition, the kinematics of the source between 4 and 5 mas indicate that the components are stationary. Finally, the jet width goes through a plateau between $r \simeq 4$ mas and $r \simeq 8$ mas. These facts favor the standing shock scenario. From the data, it is difficult to say whether the whole region includes several of such shocks (as indicated by the fitted components), or whether it is a single, long reconfinement region similar to that observed in numerical simulations (Perucho & Martí 2007). In this respect, the maximum of emission in the radio maps corresponds to component B2 (see Fig. 4.2),

which is at $r \simeq 6$ mas from the core, but the first bump in the spectral index is observed around $r \simeq 4$ mas.

Regarding region A2, figure 5.18 shows the profile of the spectral index at the different epochs. A new plateau in the jet width, starting around 10 mas (see Fig. 5.9), could have an influence on the little change observed across this region at most epochs. However, within errors, the result is compatible with a smooth decrease of the spectral index with distance, as elected from adiabatic losses (see, e.g., Mimica et al. 2009).

5.7 Summary

In this Chapter we studied in detail the radio spectral variations in the jet of CTA 102 during the 2006 major flare. The core-shift analysis revealed that, on average, the observed VLBI core position behaves like $r \propto \nu^{-1}$. We calculated the magnetic field at the core to be $B_{\rm core} \sim 100\,{\rm mG}$ and the particle density $N_{\rm core} \sim 40\,{\rm cm}^{-3}$.
The spectral analysis of the core region showed a significant increase in the spectral index, α, during the period of the flare with a steepening of α for $r > 0.1$ mas. The increase of the spectral index is in agreement with the possible interaction of a traveling component C2 and a standing shock at this position. The location coincides with the first detection of the jet expansion. Within this region, adiabatic losses are dominant and the evolution go the magnetic field intensity indicates a toroidal geometry, with values of (9–50) mG.
Farther downstream, we found evidence for the possible crossing of the feature D2 through another possible standing feature at r≃1.5 mas. The analysis of the transversal structure showed evidence for recollimation of the jet. The spectral evolution of this region revealed an increase in the turnover frequency and turnover flux density during the period of the interaction between the components. The evolution of the magnetic field intensity in this region is compatible with a mixture of toroidal and poloidal structure between 10 mG and 1 mG.
Between r=3 mas and r=8 mas there are additional regions of recollimation, as shown by the jet width and the spectral index, which further support our hypothesis of an over-pressured jet.

Summarizing the results of Chapter 3 - 5, we conclude that the jet of CTA 102 cannot be simply described by an over-pressured or a helical jet, since we found evidence for both during our analysis. The morphology of VLBI images and the jet ridge line shows a clear helical pattern. The kinematic analysis reveals several standing components and the jet width exhibits regions with jet collimation, both being indications of an over-pressured jet. The symmetric variations around the locations of this stationary components is an additional proof for the existence of recollimation shocks in CTA 102. All these facts lead to the conclusion that the jet of CTA 102 is best described by helical patterns or flow motion developing within an over-pressured jet. Whether the observed helical structure corresponds to a pattern, as reported in Perucho et al. (2012), or the flow follows this helical path should be studied in detail in future.

Due to the limited resolution and frequency range, we could not derive the spectral evolution of the VLBA core and for jet features farther downstream ($r > 1$ mas). Moreover, the interaction between a traveling shock-wave and a re-collimation shock is a highly

non-linear process which requires a more detailed investigation. Such a study is only possible by performing numerical simulations and the full radiative transfer calculations including a self-similar treatment of the relativistic electron distribution (Mimica et al. 2009). In the next Chapter we study shock-shock-interaction in parsec-scale jets using relativistic hydrodynamic simulations.

6 eRHD Simulations

In the previous Chapters we have analysed the observations of the blazar CTA 102 and obtained physical parameters such as the bulk Lorentz factor and the intensity of the magnetic field. Based on the observations, we suggested the interaction between a travelling shock and a recollimation shock as physical process behind the 2006 flare in CTA 102. However, observationally there are two limitations which do not allow us to further investigations i) the angular resolution and ii) the sparse time sampling of the observations.
In the recent years, the advance in the available computational power made it possible to simulate relativistic flows and to calculate the non-thermal emission connected to the relativistic electrons imbedded in the flow. In this Chapter we use state-of-the art relativistic hydrodynamic (RHD) simulations to test our hypothesis of a shock-shock interaction in an over-pressured jet. We investigate three key questions: i) the formation and properties of recollimation shocks, ii) the interaction between travelling shock waves and recollimation shocks, and iii) the application to the blazar CTA 102 including the calculation of the non-thermal emission taking into account radiative (synchrotron) and adiabatic energy losses.

6.1 Setup of the simulations

We performed several 2D simulations of supersonic hydrodynamical jets ($M > 1$) using the finite-difference code *Ratpenat* (for more details see Perucho et al. 2010, and references therein). The simulations were performed on up to 64 processors at the local cluster at the Max-Planck-Institute for Radio Astronomy (MPIfR) and at *Tirant*, the Valencian Node of the Spanish Supercomputing Network (RES).

In this Chapter, the subscript j corresponds to quantities in the jet and a to the ones in the ambient medium. If not explicitly mentioned, we use units of the code, which are given in terms of the jet radii, R_j, the rest-mass density of the ambient medium at the jet nozzle, ρ_a, and the speed of light, c. Following this convention the pressure is given in terms of $\rho_a c^2$, the time in units of R_j/c, the rest-mass density in the jet, ρ_j, in units of the ambient rest-mass density, and the velocity of the fluid, v_j, in units of c. We use an ideal equation of state $p_j = (\hat{\gamma} - 1)\varepsilon\rho_j$, with adiabatic index, $\hat{\gamma}$, and specific internal energy, ε. Besides these quantities there are additional parameters defining the geometry and the thermodynamics of the simulated flows such as the pressure ratio between the jet and the ambient medium, $d_k = p_j/p_a$, and the Mach number, $M = v_j/c_s$, where c_s is the sound speed. All input parameters for the simulations are summarised in Table 6.1.

We use cylindrical, axisymmetric coordinates and define the z-axis in the direction of the jet propagation and the x-axis perpendicular to the z-axis. Depending on our needs,

Table 6.1: Parameters used in the simulation of relativistic jets

Parameter	Symbol	Units
speed of light	c	1
density in the ambient medium	ρ_a	1
jet radii	R_j	1
time in the lab frame	t	R_j/c
density in the jet	ρ_j	ρ_a
velocity in the jet	v_j	c
pressure in the jet	p_j	$\rho_a c^2$
Mach number in the jet*	$M = v_j/c_s$	c
adiabatic index of the jet	$\hat{\gamma}$	1
pressure ratio	$d_k = p_j/p_a$	1
specific internal energy	$\epsilon = c_s^2/[\hat{\gamma}(\hat{\gamma} - 1 - c_s^2)]$	c^2

* we use a Newtonian (classical) definition of the Mach number

the numerical grid expands transversally between $10\,R_j$ and $100\,R_j$ and axially between $200\,R_j$ and $2000\,R_j$. The numerical resolution spans from 4 cells per jet radii up to 64 cells per jet radii, depending on the simulation. The basic setup of our simulations for over-pressured jets is sketched in Fig. 3.12.

6.2 On the formation of recollimation shocks

Recollimation shocks are a common feature in non-pressure matched flows and are characterised by a local maximum in pressure and density. If a non-pressure matched flow emerges from a nozzle, the flow will expand until the pressure in the jet matches that in the ambient medium. This state is first reached at the jet boundary, i.e., the contact surface between jet and ambient medium, and leads to the formation of an inward travelling wave. Due to the finite speed of the waves, the inner layers of the jet will continue expanding while the outer ones are already collimating. This expansion of the inner layers will stop as soon as the wave crosses them. As a result, the recollimation shock occurs at different locations, depending on the radial coordinate of the stream line. In Figure 6.1, we illustrate this behaviour for the evolution of the pressure cuts along the jet taken at different radial positions. In this work we use the minimum of the pressure in the transversally averaged (mean) parameters as representative of the location of the recollimation shock, $z_{\rm rc}$. We measure the relative increase in the mean rest-mass density, $\rho_{\rm jump}$, as an additional parameter of the recollimation shock, defined as:

$$\rho_{\rm jump} = \frac{\rho_2 - \rho_1}{\rho_1}, \tag{6.1}$$

where the subscript 1 corresponds to the pre-shock region and 2 to the post-shock region. Additionally, we compute the relative increase in the bulk Lorentz factor, $\Gamma_{\rm jump}$, and the jet opening angle, φ, between the jet nozzle and the first recollimation shock. We define

$\Gamma_{\rm jump}$ by:

$$\Gamma_{\rm jump} = \frac{\Gamma_{\rm rc} - \Gamma_0}{\Gamma_0}, \tag{6.2}$$

with $\Gamma_{\rm rc}$ the bulk Lorentz factor at the location of the recollimation shock and Γ_0 the bulk Lorentz factor at the jet nozzle.

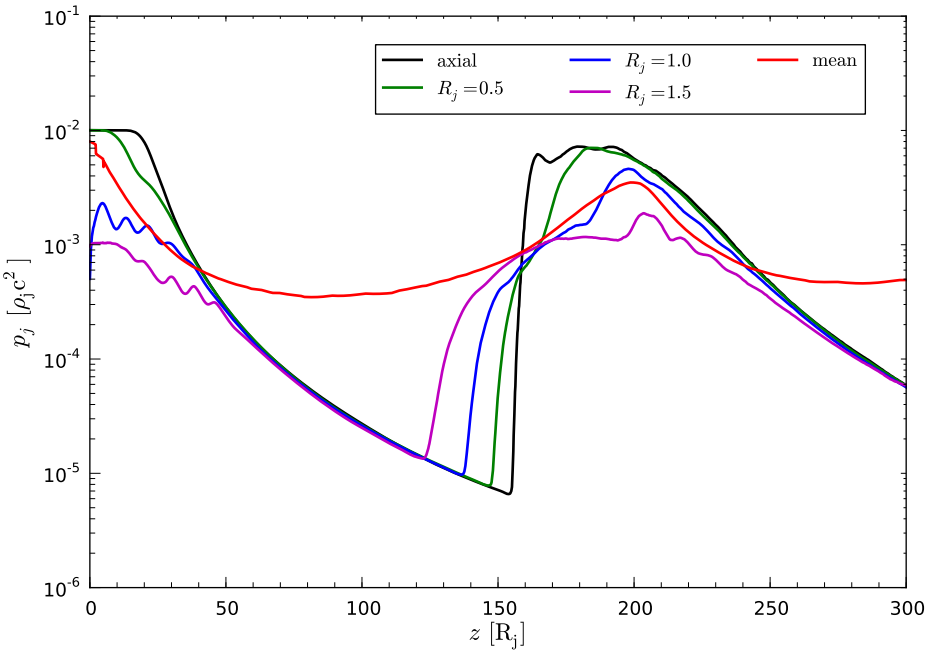

Figure 6.1: Pressure profiles taken at different radial positions. Notice the shift in the location of the local pressure minimum with radial position from the jet axis. The red line corresponds to the mean values.

6.2.1 Recollimation shocks in a homogeneous ambient medium

For our study of the formation of the first recollimation shock, we used a wide range of initial values and assumed that the flow is embedded in a homogeneous ambient medium. A direct consequence of the homogeneous ambient medium is that the secondary recollimation shocks are equidistantly located, with similar values for their shock-defined parameters, such as $\rho_{\rm jump}$. We used a numerical grid of $20R_j \times 600R_j$ and a resolution of 8 cells per jet radii. Our parameter space for this study is presented in Table 6.2.

In Figure 6.2 we show the influence of the over-pressure, d_k, on the formation of the recollimation shocks while keeping the other jet parameters fixed. There are three clearly visible effects i) the location of the recollimation shock shifts to larger distances from the nozzle with increasing d_k, ii) the opening angle of the jet is increasing with d_k, and iii) the rest-mass density falls to smaller values close to the shock for larger d_k values.

Table 6.2: Parameters space for the simulation of recollimation shocks in a homogeneous ambient medium

parameter	values
ρ_j	0.02, 0.04, 0.1
Γ_j	2, 4, 6, 8, 10
d_k	3, 6, 9, 12
M	1.5, 3, 6, 12
$\hat{\gamma}$	13/9, 4/3

The results of our analysis for jets ($\hat{\gamma} = 13/9$) with a fixed Mach number of $M = 3$ is presented in Fig. 6.3. The panels show the dependence of the location of the first recollimation shock, $z_{\rm rc}$ (panel A), the relative increase in the rest-mass density, $\rho_{\rm jump}$, (panel B), the relative increase bulk Lorentz factor, $\Gamma_{\rm jump}$ (panel C), and the jet opening angle, φ (panel D), on the initial Bulk Lorentz factor, Γ. The different line styles correspond to different initial rest-mass densities at the jet nozzle. The solid lines correspond to $\rho_j = 0.02$, the dashed lines to $\rho_j = 0.04$, and the dotted lines to $\rho_j = 0.1$.
The location of the first recollimation shock, $z_{\rm rc}$, is shifted farther away from the jet nozzle with increasing d_k and Γ. Given the same d_k, larger rest-mass densities lead to the formation of the recollimation shock at shorter distances from the nozzle. This effect is best visible for large values of Γ (see panel A in Fig. 6.3). In panel B we show the variation of $\rho_{\rm jump}$ with d_k and Γ. The larger the over-pressure, the larger is the increase in the rest-mass density. Besides this main dependence there is a decreasing trend in $\rho_{\rm jump}$ for larger Γ.
The acceleration of the flow between the jet nozzle and the first recollimation shock with initial bulk Lorentz factor is plotted in panel C. For $\Gamma < 6$, the acceleration of flow increases with Γ. For larger values of Γ the acceleration of the flow reaches a limit around $\Gamma_{\rm jump} \sim 0.3$. This behaviour is nearly independent of the initial rest-mass density at the jet nozzle (see scatter in the values for a given d_k).
The initial opening angle between the jet nozzle and the first recollimation shock, φ, decreases like $1/\Gamma$ (see panel D). For a fixed initial bulk Lorentz factor the opening angle increases with d_k, and the maximum opening angle is reached for $d_k = 6$ within our parameter space.

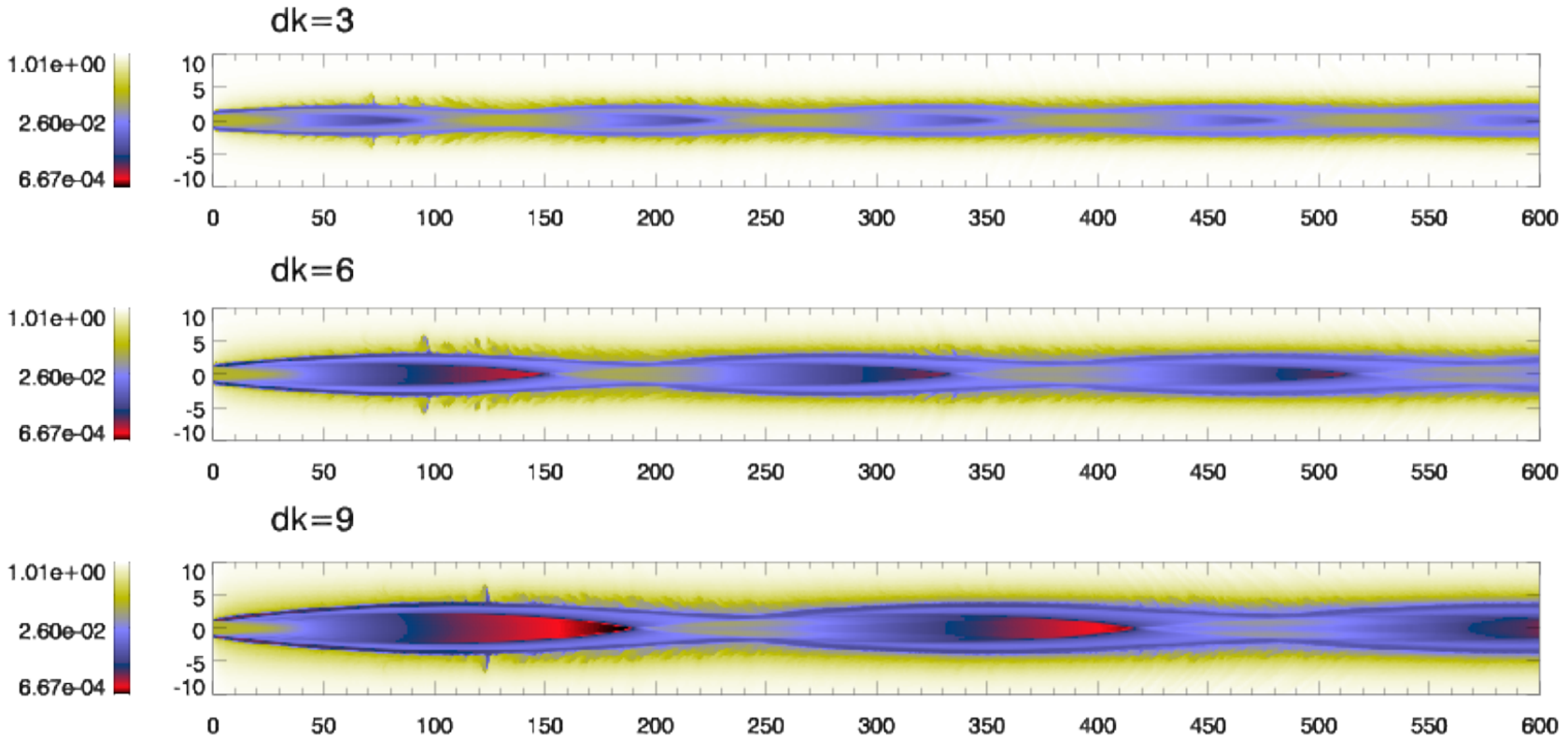

Figure 6.2: 2D distribution of the logarithm of the rest mass density for three different over-pressures $d_k = 3$ (top panel), $d_k = 6$ (middle panel), and $d_k = 9$ (bottom panel). For all three simulations we use a bulk Lorentz factor $\Gamma = 10$, an initial rest-mass density, $\rho_j = 0.1$, a Mach number, $M = 3$, and an adiabatic index, $\hat{\gamma} = 13/9$, which corresponds to fluid which consists of sub-relativistic protons and ultra-relativistic electrons. For details see text.

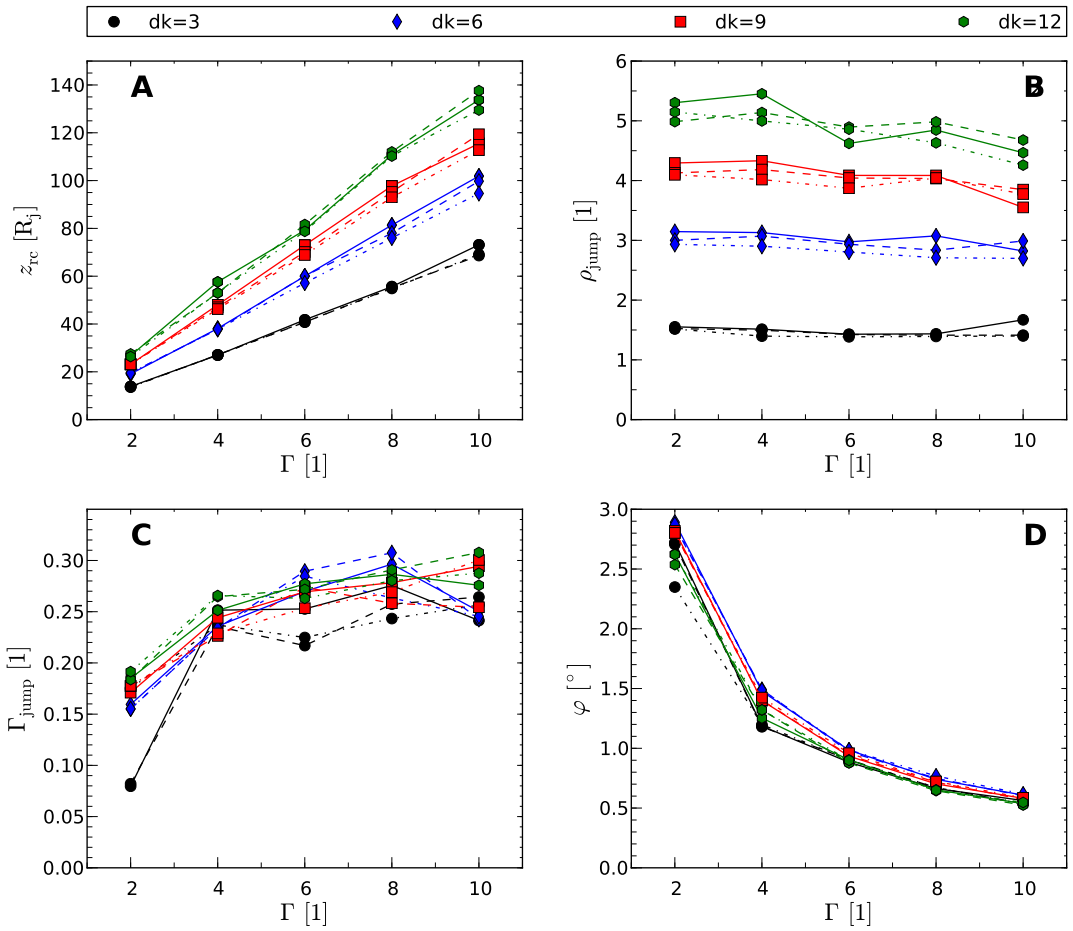

Figure 6.3: The influence of the bulk Lorentz factor, Γ, the density, ρ, and the over-pressure, d_k on the characteristic parameters of a recollimation shock. The panels show the variation of the location of the first recollimation shock, z_{rc}, (panel A), the relative increase in the rest-mass density, ρ_{jump}, (panel B), the relative increase bulk Lorentz factor, Γ_{jump} (panel C), and the jet opening angle, φ (panel D). The different symbols indicate different over-pressure, d_k, and the different line styles correspond to different initial rest-mass density values at the jet nozzle. For details see text.

Another important characteristic parameter within our analysis on the formation of the recollimation shocks is the specific internal energy of the jet, ε, defined as:

$$\varepsilon = \frac{c_s^2}{\hat{\gamma}\,(\hat{\gamma} - 1 - c_s^2)}. \tag{6.3}$$

Based on the value of ε, jets are divided into hot ($\varepsilon > c^2$) and cold jets ($\varepsilon < c^2$). For an ideal gas of adiabatic index $\hat{\gamma} = 13/9$ a sound speed of $c_s \geqslant 0.52$ is required to setup a hot jet, and for $\gamma = 4/3$, a sound speed $c_s \geqslant 0.44$.
We analysed the influence of the specific internal energy in terms of the Mach number[1]

[1] In the RHD code, the sound speed is set in terms of the Mach number and the fluid velocity

$M = v_b/c_s$ using $\hat{\gamma} = 13/9$ with a fixed fluid velocity $v_b = 0.995$ ($\Gamma = 10$), over-pressure $d_k = 3$ and initial rest-mass density of $\rho_j = 0.02$.

In Figure 6.4 we present the 2D distribution of the rest-mass density for three different initial Mach numbers $M = 1.5$ ($\varepsilon = 34$) (top panel), $M = 6$ ($\varepsilon = 0.05$) (middle panel), and $M = 12$ ($\varepsilon = 0.01$) (bottom panel). The inspection of the plots shows that the position of the recollimation shocks is shifted farther downstream with increasing Mach number and the increase in $\rho_{\rm jump}$ becomes smaller with growing Mach number.

A more detailed view on the properties of the recollimation shock is provided in Fig. 6.5. The first recollimation shock is formed at larger distances from the nozzle with increasing Mach number (panel A in Fig. 6.5) while the relative density increase drops with growing Mach number (panel B in Fig. 6.5). The acceleration of the fluid seen in panel C in Fig. 6.5 is a a typical behaviour of hot relativistic jets: For smaller Mach numbers (hot jets) the fluid accelerates faster than for larger values of M (cold(er) jets). The jet opening angle φ decreases with M and follows $\varphi \propto 1/M$.

Additionally, we investigated the influence of the jet composition either $\hat{\gamma} = 13/9$ or $\hat{\gamma} = 4/3$ plasma on the formation of the recollimation shocks. Our results showed that there is no significant difference in the shock properties studied. In general the recollimation shocks for $\hat{\gamma} = 13/9$ are formed at larger distances (roughly 7% larger) as compared to $\hat{\gamma} = 4/3$ jets.

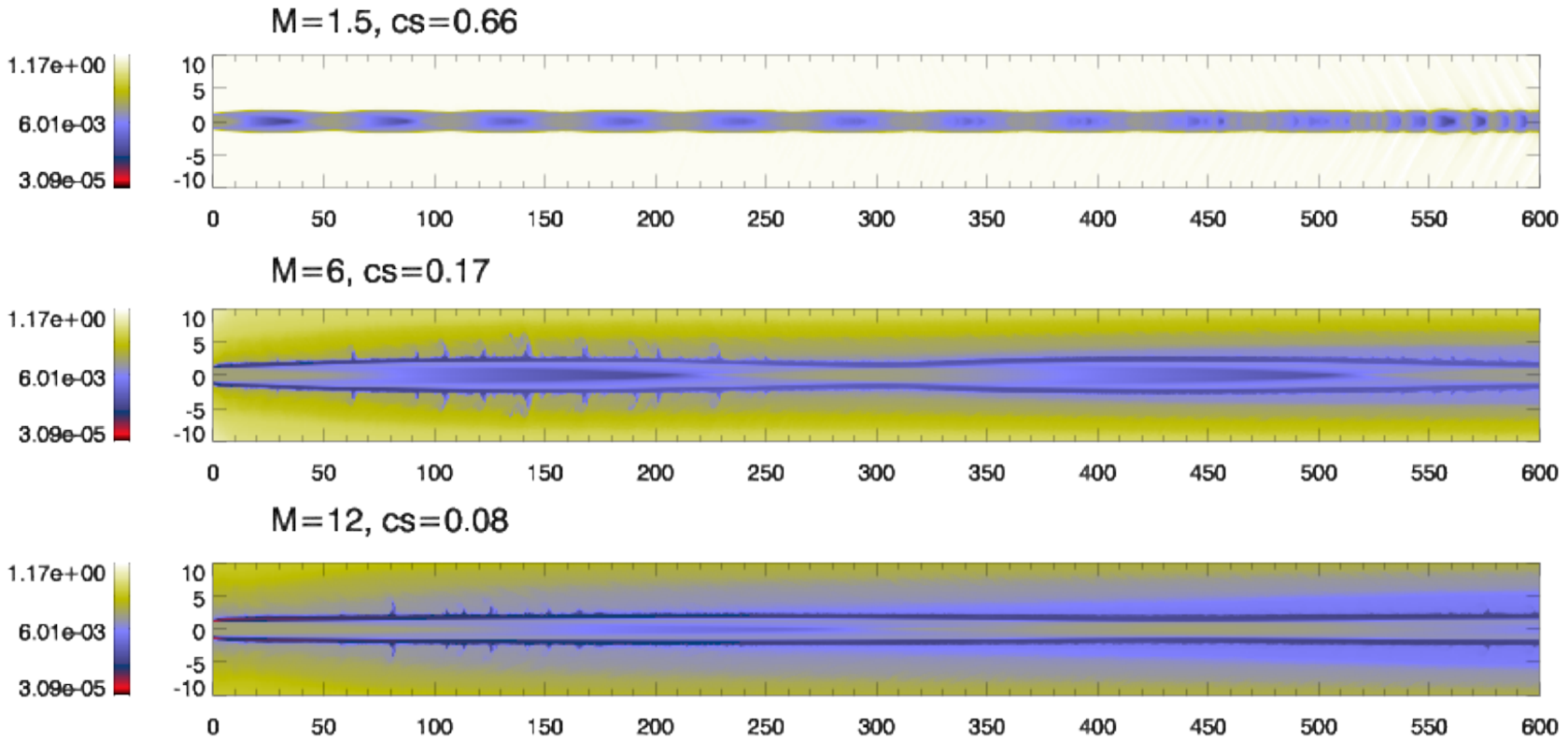

Figure 6.4: 2D distribution of the logarithm of the rest mass density for three different Mach numbers $M = 1.5$ (top panel), $M = 6$ (middle panel), and $M = 12$ (bottom panel). For all three simulations we use a bulk Lorentz factor $\Gamma = 10$, an initial rest-mass density $\rho_j = 0.02$, pressure ratio $d_k = 3$, and an adiabatic index, $\hat{\gamma} = 13/9$ which corresponds to fluid which consists of sub-relativistic protons and ultra-relativistic electrons.

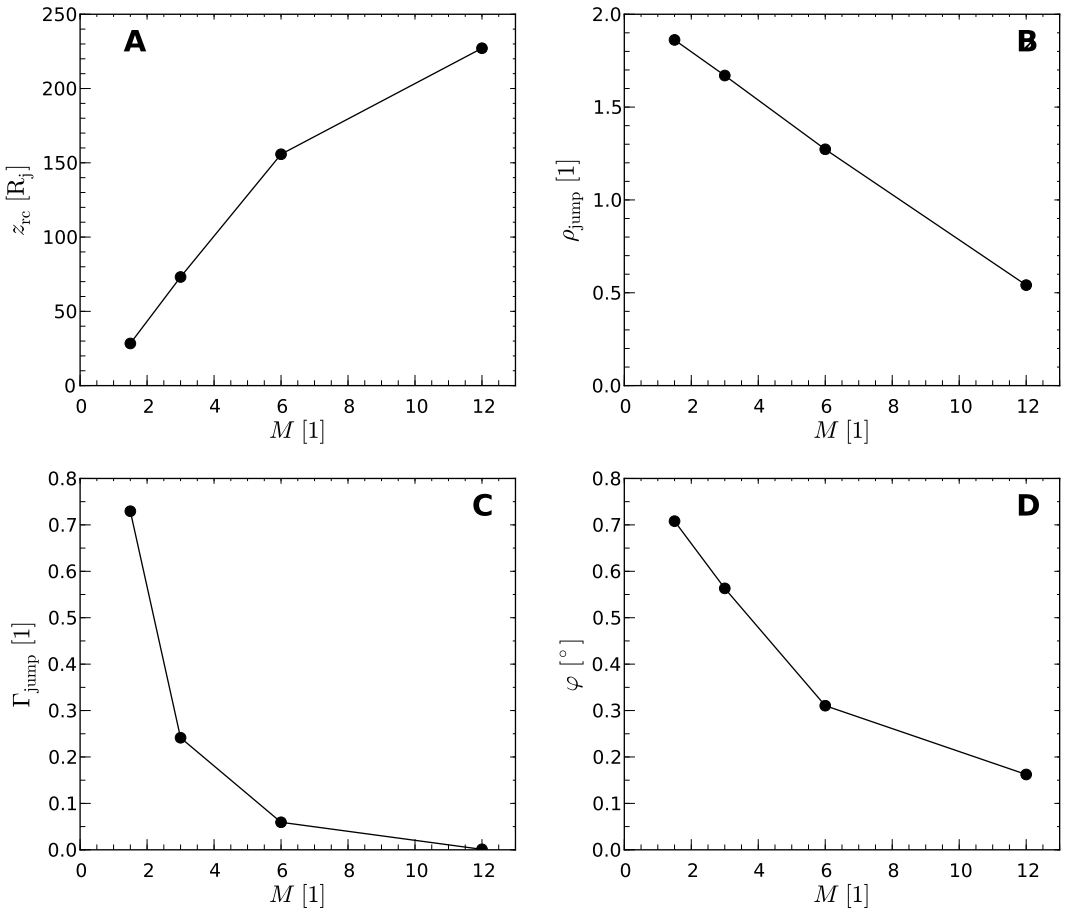

Figure 6.5: The influence of the Mach number, M, on the characteristic parameters of a recollimation shock. The panels show the variation of the location of the first recollimation shock, $z_{\rm rc}$, (panel A), the increase in density, $\rho_{\rm jump}$, (panel B), the increase in the bulk Lorentz factor, $\Gamma_{\rm jump}$ and the jet opening angle, φ with increasing Mach number, M. For all simulations we used a fixed over-pressure, $d_k = 3$, fluid velocity, $v_b = 0.995$, rest-mass density, $\rho = 0.02$, and adiabatic index, $\hat{\gamma} = 13/9$.

6.2.2 Recollimation shocks in a decreasing pressure ambient medium

The simulations performed with the setup presented in Sect. 6.2.1 we assumed a homogeneous ambient medium. Since AGN jets are embedded in their host galaxies the pressure in the ambient decreases with distance. We modelled this decrease in the pressure and the density in the ambient medium using the pressure profile presented in (Gomez et al. 1997):

$$p_a(z) = \frac{p_j}{d_k}\left[1 + \left(\frac{z}{z_c}\right)^n\right]^{\frac{m}{n}}, \tag{6.4}$$

where z_c can be considered as the "scale height" (core size in a King-like profile) and the exponents n and m control the steepening of the ambient pressure. In addition to the over-pressured jets ($d_k \neq 1$), we generated pressure matched, (i.e., conical) jets. To cover several recollimation shocks within our numerical grid we used an axial length of $2000\,R_j$ and a transversal grid of $100\,R_j$. Due to the increase of the numerical grid we reduced the numerical resolution from 8 cells per jet radii to 4 cells. This setup allowed us to keep the required computational time within acceptable boundaries[2]. In Table 6.3 we show the different parameters used for the simulations and Fig. 6.6 illustrates the pressure (top panel) and rest-mass density (right panel) evolution with distance in the ambient medium for two of the used profiles.

Table 6.3: Parameters used for the simulation of recollimation shocks in a decreasing pressure ambient medium

parameter	values
ρ_j	0.02
Γ_j	10
d_k	1, 3
M	3
$\hat{\gamma}$	13/9
z_c	100
n	2
m	1, 2

Figure 6.7 shows the 2D distribution of the logarithm of the rest-mass density for a pressure-matched, $d_k = 1$, (top panel) and two over-pressured jets, here $d_k = 3$, embedded in a decreasing pressure ambient medium with different gradients ($m = 1$, $n = 2$ top and middle panel, and $m = 2$, $n = 2$ bottom panel). For both cases, the gradient in the density and the pressure of the ambient medium leads to an opening of the jet (see jet radii at $z = 0\,\mathrm{R_j}$ and at $z = 2000\,\mathrm{R_j}$). The opening of the flow generates a conical jet for $d_k = 1$ and a spine-sheath structure for $d_k = 3$. In contrast to the featureless sheath, the spine consists of a series of recollimation shocks. The distances between the recollimation shocks increases with steeper gradients in the density and pressure of ambient medium (see Fig. 6.7).

The properties of the recollimation shocks properties are presented in Fig. 6.8. The position of the recollimation shocks and their transversal size with distance along the jet is plotted in panel A. For both ambient medium profiles the separation between the recollimation shocks and their transversal size grow with distance along the jet. The steeper the gradient in the ambient medium, the larger is the distance between the recollimation shocks and their transversal size. The larger the gradient in the density and in the pressure of the ambient medium the smaller the increase in the rest-mass density at the recollimation shock (see red and black points in panel B of Fig. 6.8). Additionally to these individual values of the recollimation shocks, we extracted the overall opening angle, φ, and the total acceleration along the jet. We computed these values between $z = 0\,\mathrm{R_j}$ (jet nozzle) and $z = 2000\,\mathrm{R_j}$ (edge of the numerical grid) and present the results in Table 6.4.

[2]We obtained a steady state jet after one week using 16 processors

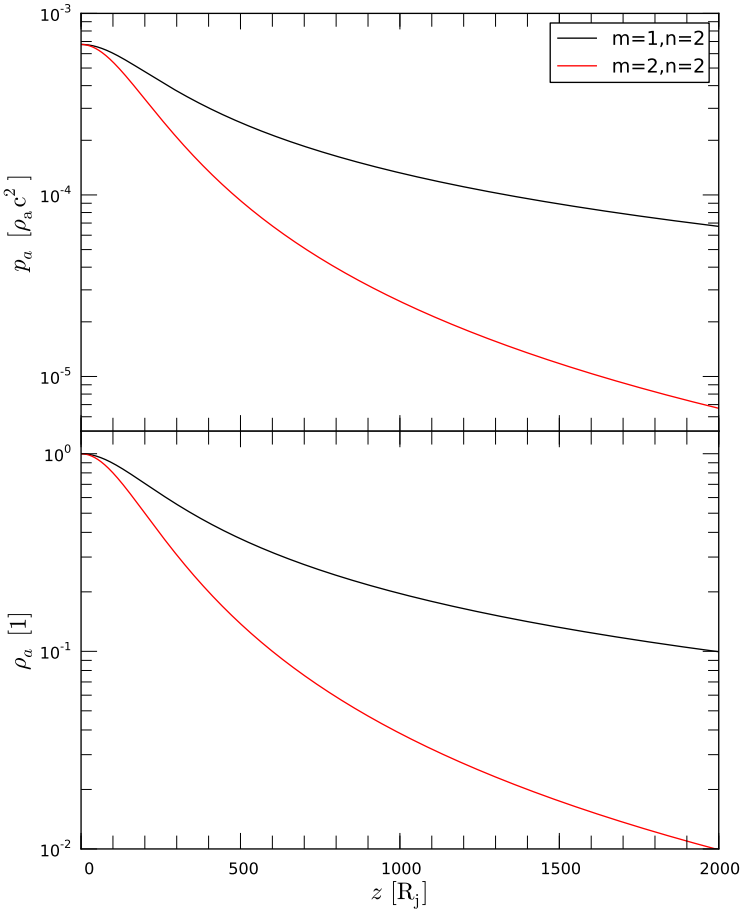

Figure 6.6: Initial profiles of the ambient pressure, p_a, (top panel) and rest mass density, ρ_a, (bottom panel) used in the simulations.

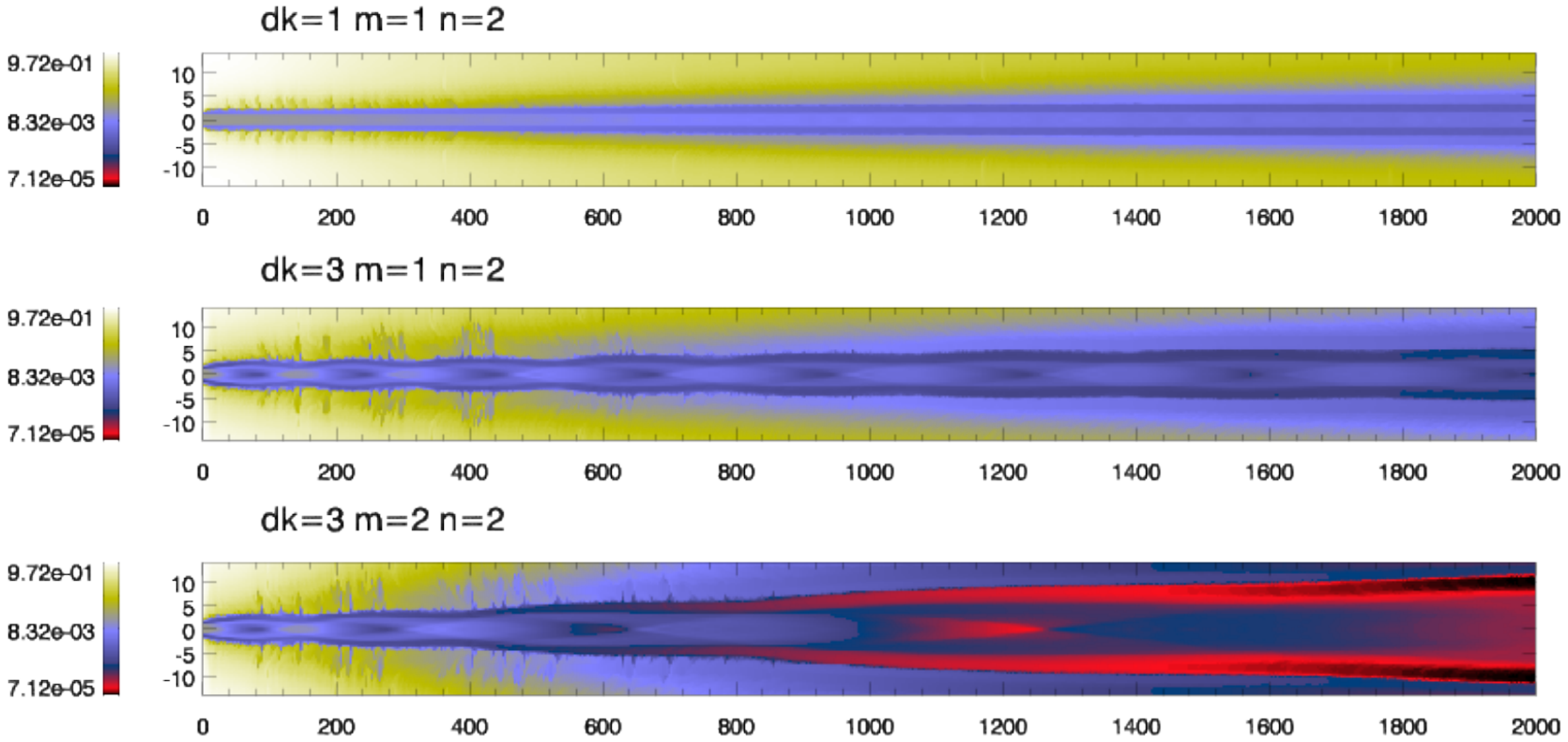

Figure 6.7: 2D distribution of the logarithm of the rest mass density for different ambient medium configurations. The panels show a conical jet ($d_k = 1$) and two over-pressured jets (here, $d_k = 3$) in an ambient medium with decreasing density. For all three simulations we use a bulk Lorentz factor $\Gamma = 10$, an initial rest-mass density $\rho_j = 0.02$, a Mach number $M = 3$, an adiabatic index, $\hat{\gamma} = 13/9$, and a scale height $z_c = 100\,\mathrm{R_j}$.

Table 6.4: Total jet opening, φ, and acceleration factor, $\Gamma_{\rm jump}$

	$m = 1, n = 2$		$m = 2, n = 2$
parameter	$d_k = 1$	$d_k = 3$	$d_k = 3$
$\varphi\,[^\circ]$	0.04	0.08	0.21
$\Gamma_{\rm jump}$	0.12	0.17	0.24

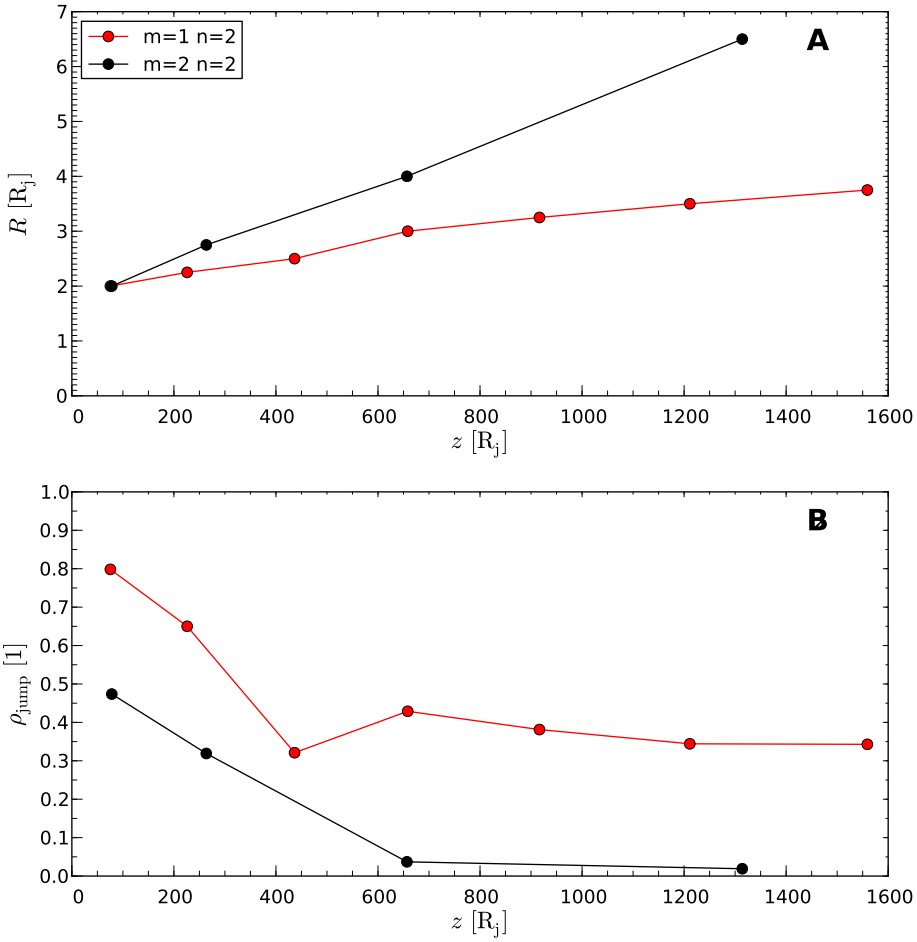

Figure 6.8: The influence of a decreasing density ambient medium on the characteristic parameters of the recollimation shocks. The panels show the location of the recollimation shocks and their transversal size along the jet (panel A) and the increase in the rest-mass density at the recollimation shock (panel B). We used a bulk Lorentz factor $\Gamma = 10$, an initial rest-mass density $\rho_j = 0.02$, Mach number $M = 3$, an adiabatic index, $\hat{\gamma} = 13/9$, and a scale height $z_c = 100\,\mathrm{R_j}$.

6.3 Recollimation shock – travelling shock interaction

For the study of the interaction between a recollimation shock and a travelling shock wave, we used a numerical resolution of 64 cells per jet radii and a numerical grid of $(10 \times 200)\, R_j$, which translates into a numerical box of (640×12800) cells. For this study we simulated a jet with initial rest-mass density $\rho_j = 0.02\rho_a$, Mach number $M = 3$, over-pressure $d_k = 3$, adiabatic index $\hat{\gamma} = 13/9$ and bulk Lorentz factor $\Gamma = 10$ ($v_j = 0.995\,\mathrm{c}$), embedded in a homogenous ambient medium. The travelling shock waves were generated by the temporal injection of a pressure and density perturbation at the jet nozzle. Table 6.5 summarises the different perturbations used in the simulations.

Table 6.5: Parameter for the injected perturbations

Model	$t_p\,[R_j/c]$	v_p [c]	$\rho_p\,[\rho_a]$	$p_p\,[\rho_a c^2]$
RTS1	0.1	0.995	0.04	0.004
RTS2	0.1	0.995	0.08	0.008
RTS3	0.1	0.995	0.12	0.012
RTS4	0.5	0.995	0.04	0.004
RTS5	0.5	0.995	0.08	0.008

In Figure 6.9 we show three snapshots from the *RTS5* simulation of the interaction between a travelling shock and a recollimation shock. (see Table 6.5 for shock parameters). The perturbation is located at $z \sim 20\,\mathrm{R_j}$ (top panel), at $z \sim 60\,\mathrm{R_j}$ (middle panel), and at $z \sim 80\,\mathrm{R_j}$ and leads to an increase in the rest-mass density.

The propagation and interaction of a travelling shock within an over-pressured jet can be best analysed using space-time plots. The space-time plot for the *RTS5* simulation is presented in Fig. 6.10. The x-axis corresponds to the distance along the jet z, the y-axis indicates the time, $t = R_j/c$ (increasing from top to bottom), and the colormap corresponds to the rest-mass density normalised to the steady-state rest-mass in the jet at the jet nozzle. The plot shows three regions of enhanced rest-mass density, where the first $(0 < z < 5)\,\mathrm{R_j}$ corresponds to the jet nozzle, the second $(65 < z < 95)\,\mathrm{R_j}$ to the first recollimation shock, and the third $(150 < z < 185)\,\mathrm{R_j}$ to the second recollimation shock. The distribution of the rest-mass density along the jet for the steady state is given for $t = 0\,R_j/c$. At $t = 1\,R_j/c$ we injected a perturbation with 4 times the initial pressure and rest-mass density values at the jet nozzle, during $\Delta t = 0.5\,R_j/c$ which led to the formation of a shock wave. The increase of the rest-mass density during the propagation of this shock wave is presented by the line of enhanced rest-mass density values. While the shock moves through the jet, the enhancement of rest-mass density decreases with distance along the jet and the shock expands (see $z < 50\,\mathrm{R_j}$). At $z = 65\,\mathrm{R_j}$, the travelling shock encounters the position of the first recollimation shock and there is a strong jump in the rest-mass density, resulting in values comparable to those at the jet nozzle. After the shock wave crosses the recollimation shock the rest-mass density decreases again and shock continues expanding until it reaches the second recollimation shock, where we observe again an increase in the rest-mass density.

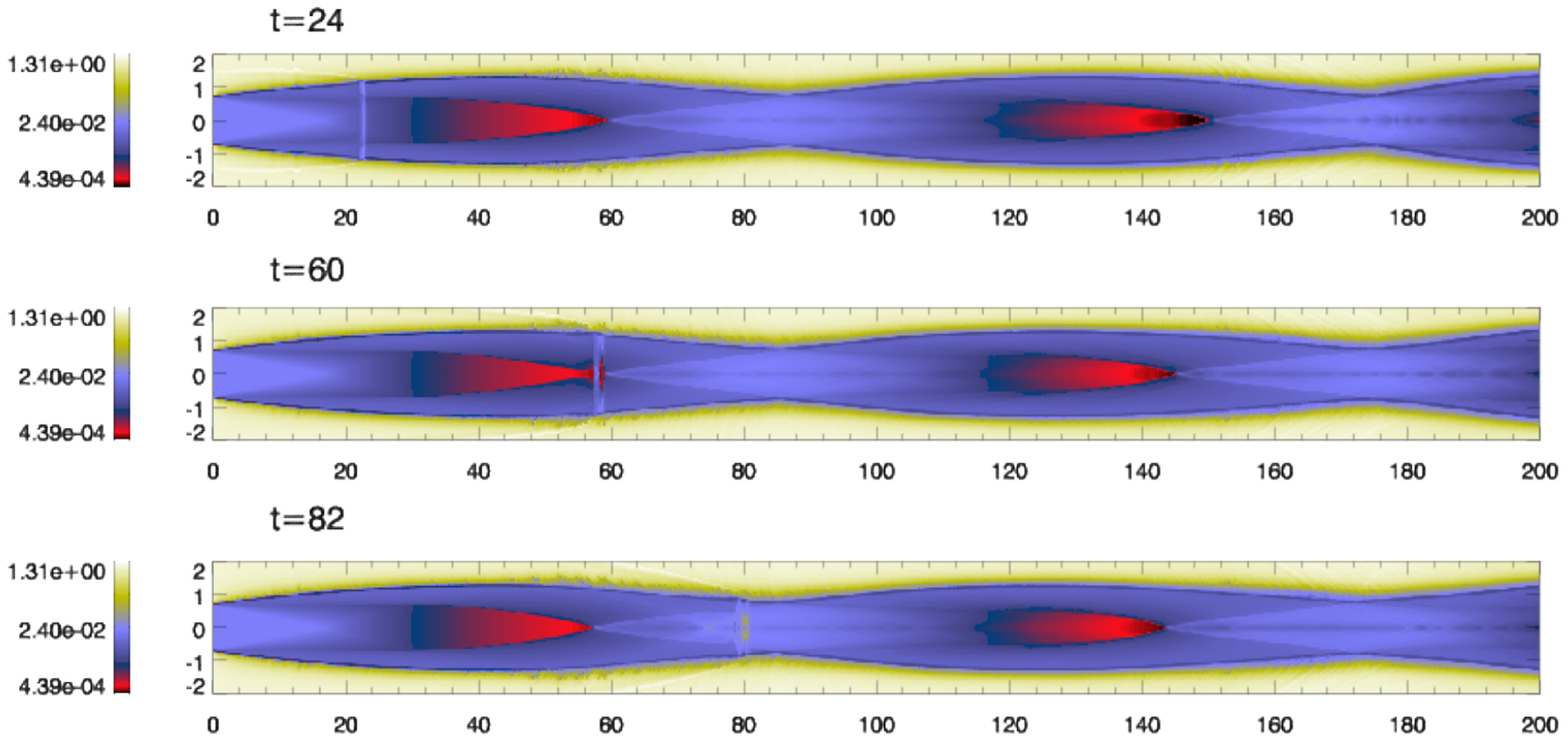

Figure 6.9: Snapshots for 2D distribution of the logarithm of the rest-mass density during the *RTS5* recollimation shock travelling shock interaction. The time of the snapshot is plotted in the left top corner of each panel in units of R_j/c. The initial parameters are: A rest-mass density $\rho_j = 0.02\rho_a$, Mach number $M = 3$, over-pressure $d_k = 3$, adiabatic index $\hat{\gamma} = 13/9$, and bulk Lorentz factor $\Gamma = 10$ ($v_j = 0.995\,\mathrm{c}$). For the parameters of the perturbation see Table 6.5.

A more detailed picture of the shock-shock interaction is given by the bottom panels in Fig. 6.10. The left panel shows the interaction with the first recollimation shock and the right panel with the second one. A travelling shock wave can be divided into four basic waves, i) forward shock, ii) the contact discontinuity, iii) the rarefaction wave, and iv) the reverse shock. Due to our high resolution we are able to partially resolve this structure of the travelling shock wave in our simulations. The rarefaction travelling behind the front shock leads to a decrease in the rest-mass density, best visible at $z = 70\,\mathrm{R_j}$ for $t = 73\,\mathrm{R_j/c}$ (upper left corner of the left bottom panel). A certain time after the shock-shock interaction, $\Delta t = 6\,R_j/c$, the initial rest-mass density value recovers, and it could be interpreted as the dragging of the recollimation shock by the moving one (Gomez et al. 1997). The splitting of the shock into forward and reverse shocks leads to stratification of the rest-mass density jump within the shock, i.e., there is a stronger increase in rest-mass density at the shock front and a less pronounced one for the reverse shock (see for example $t = 85\,R_j/c$ between $(81\,\mathrm{R_j} < z < 85)\,\mathrm{R_j}$). The expansion of the travelling shock wave and the influence of the forward and reverse shock on the rest-mass density is clearly visible during the interaction with the second recollimation shock (see right bottom panel). The separation between forward and reverse shock grows and their discrepancy in the amplification in the rest-mass density rises (see colour code at e.g., $t = 170\,R_j/c$). Furthermore, the crossing of the recollimation shock could also lead to the formation of secondary waves, the so-called trailing shocks (see, e.g., Agudo et al. 2001). The extended strips at the edges of the second recollimation shock could be an indication for the formation of such features.

The analysis of the other perturbations listed in Table 6.5 showed that weak perturbations like *RTS1* did not significantly increase the pressure and rest-mass density during the crossing of the recollimations shocks. The comparison between the simulation *RTS3* and *RTS4* revealed that the duration of the perturbation is more important than its deviation from the initial jet parameters at the nozzle for the increase of the pressure and rest-mass density at the recollimation shock. For a more detailed study of this highly non-linear process of shock-shock interaction, even higher numerical resolution and a larger parameter space are needed. From our simulations of travelling shock wave recollimation shock interaction we obtained that the rest-mass density can increase by a factor 1.5 -5.5 depending on the underlying steady-state flow and the properties of the travelling shock wave.

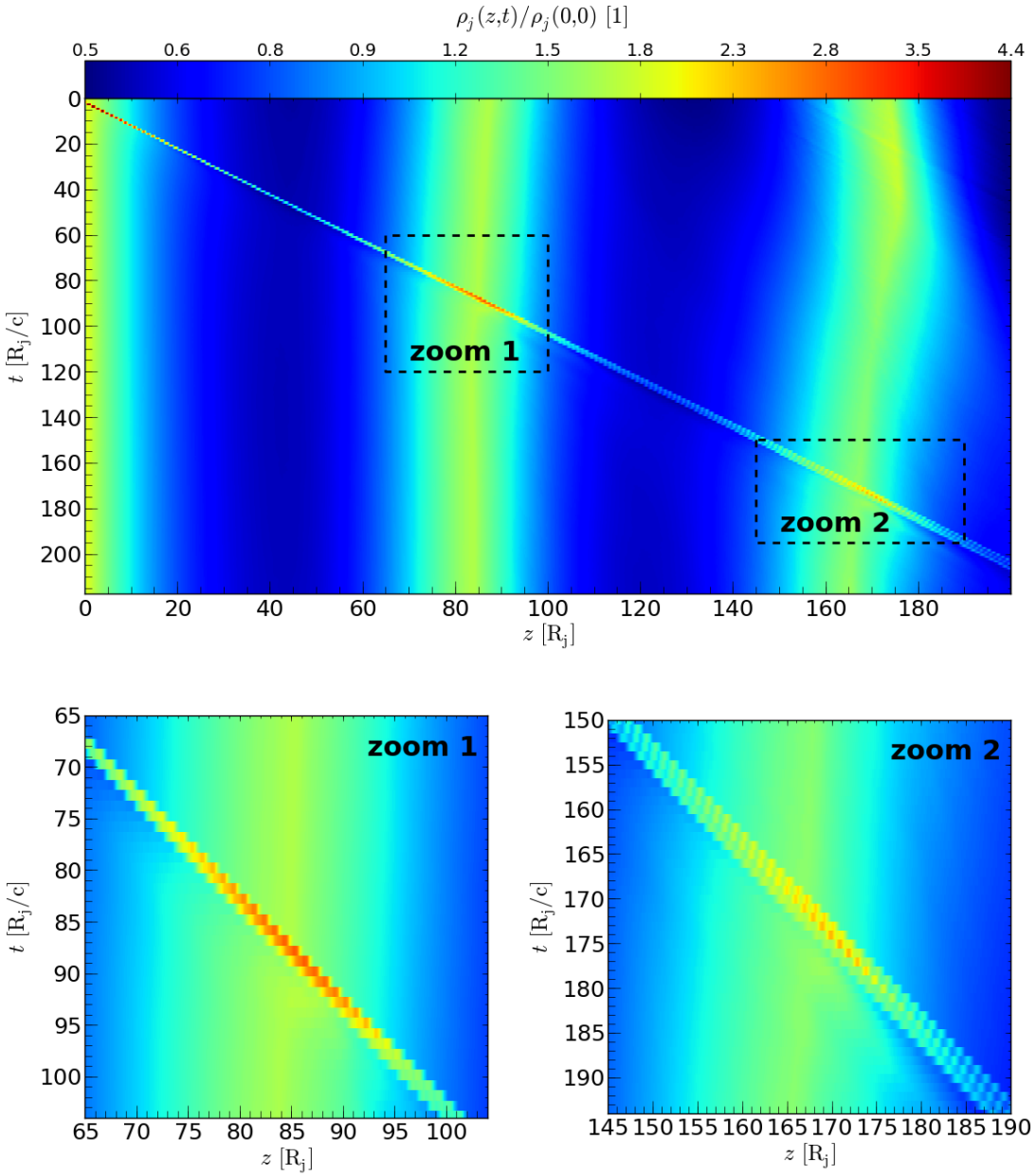

Figure 6.10: Space-time plots for the interaction between a travelling shock wave and a recollimation shocks for simulation *RTS5* (see Table 6.5 for initial parameters.) The panels show the logarithm of the normalised rest-mass density during the propagation of the shock wave (line of increased rest-mass density values). The overall evolution of the shock wave is presented in the top panel and the two bottom panels show a zoom into the interaction of the travelling shock wave with the first and the second recollimation shock, respectively.

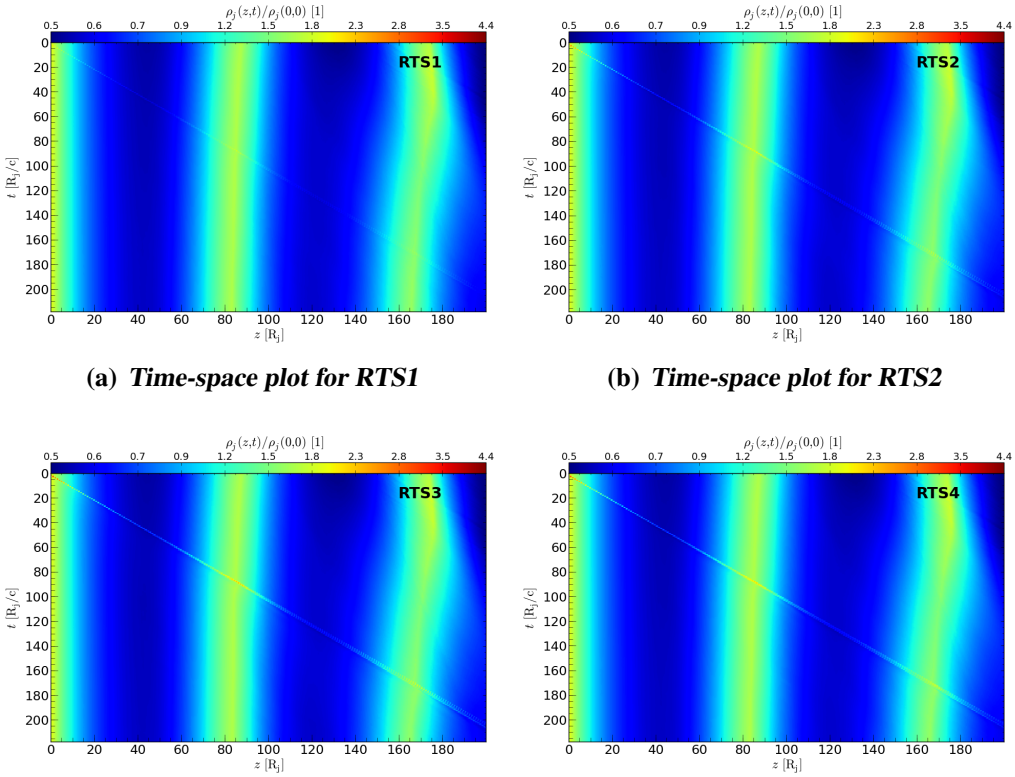

(a) ***Time-space plot for RTS1*** **(b)** ***Time-space plot for RTS2***

(c) ***Time-space plot for RTS3*** **(d)** ***Time-space plot for RTS4***

Figure 6.11: Time-space plots for different perturbations listed in Table 6.5. The colour scale is set to the one in Fig. 6.10 to allow the direct comparison between them.

6.4 Application to the blazar CTA 102

6.4.1 RHD Simulations

Based on the observations of CTA 102, we suggested that the jet in CTA 102 can be partially described as an over-pressured jet (see Chapter 3, 4, and 5). In this Section we used the parameters extracted from the VLBI observations (Chapter 4 and 5) as initial conditions for our simulations. We also took the classification of CTA 102 as an FRI type of radio galaxy into account to put a constraint on the total kinetic power of $L_{\rm kin} \sim 10^{43} - 10^{44}$ erg/s, which can be approximated for $\Gamma \gg 1$ by:

$$L_{\rm kin} \sim \rho_j \Gamma^2 \pi R_{j,0}^2 \left(1 - \Gamma^{-2}\right)^{1/2} c^3. \tag{6.5}$$

The jet radius at the jet nozzle can be computed from:

$$R_{j,0} \sim \frac{z_{\rm rc}}{3.3 \Gamma d_k}, \tag{6.6}$$

where $z_{\rm rc}$ is the position of the recollimation shock. We assumed that the position of the first collimation shock is at $z_{\rm rc} = 18$ pc and a bulk Lorentz factor of $\Gamma = 12$ (see Chapter 4). Additionally we used an over-pressure of $d_k = 3$ (Jorstad et al. 2005b) and estimated

the rest-mass density at the jet nozzle, $\rho_j = 3.4 \times 10^{-26}\,\mathrm{g/cm^3}$, by solving Eq. 6.5 for ρ_j. The simulated jets were embedded into a decreasing density ambient medium with $z_c = 100\,R_j$, $m = 1$, and $n = 2$ (see Eq. 6.4) or in a homogenous ambient medium as in the case of the CTA1 simulation. We used a numerical grid of $10\,R_j \times 700\,R_j$ with a numerical resolution of 8 cells per jet radii and initial parameters of the jet as listed in Table 6.6. In this Section we use cgs units, except for the distances, which are presented in parsec.

Table 6.6: Initial parameters for the simulations of the blazar CTA 102.

Model	$R_{j,0}$ [pc]	d_k [1]	Γ [1]	ρ_j [g/cm^3]	M [1]	$\hat{\gamma}$ [1]	m [1]	n [1]	z_c [pc]
CTA1[a]	0.15	3	12	$3.4 \cdot 10^{-26}$	3.0	13/9	0	0	0
CTA2[b]	0.15	3	12	$3.4 \cdot 10^{-26}$	3.0	13/9	1	2	15
CTA3[b]	0.15	3	12	$3.4 \cdot 10^{-26}$	1.6	13/9	1	2	15
CTA4[a]	0.15	1	12	$3.4 \cdot 10^{-26}$	3.0	13/9	1	2	15

[a] additionally with reduced grid $10\,R_j \times 300\,R_j$ and 32 cells per jet radii
[b] additionally with extended grid $30\,R_j \times 2000\,R_j$ and 4 cells per jet radii

In Fig. 6.12 we show the 2D distribution of the logarithm of the rest-mass density for the simulations *CTA1* (top panel), *CTA2* (middle panel), and *CTA4* (bottom panel). In contrast to the over-pressured models ($d_k = 3$), *CTA1* and *CTA2*, no recollimation shocks are generated in a pressure-matched jet (see bottom panel). The decreasing density in the ambient medium leads to a conical jet with smoothly decreasing the rest-mass density along the jet.

Since it is not possible to extract the Mach number observationally, we used two different settings for our simulations, $M = 1.6$ and $M = 3.0$. This choice of the Mach number directly affects the specific internal energy of the jet, ε, which is calculated from the Mach number together with the fluid velocity, v_j, and the adiabatic index, $\hat{\gamma}$. In our case $M = 1.6$ generates a hot jet ($\varepsilon > c^2$) and $M = 3$ a colder one ($\varepsilon < c^2$). This variation in the specific internal energy leads to differences in the characteristic values of the jet, illustrated in Fig. 6.13. The panels show the evolution of the mean rest-mass density, ρ_j, (top) and the mean bulk Lorentz factor, Γ, (bottom) along the jet for the simulations *CTA2* and *CTA3*.

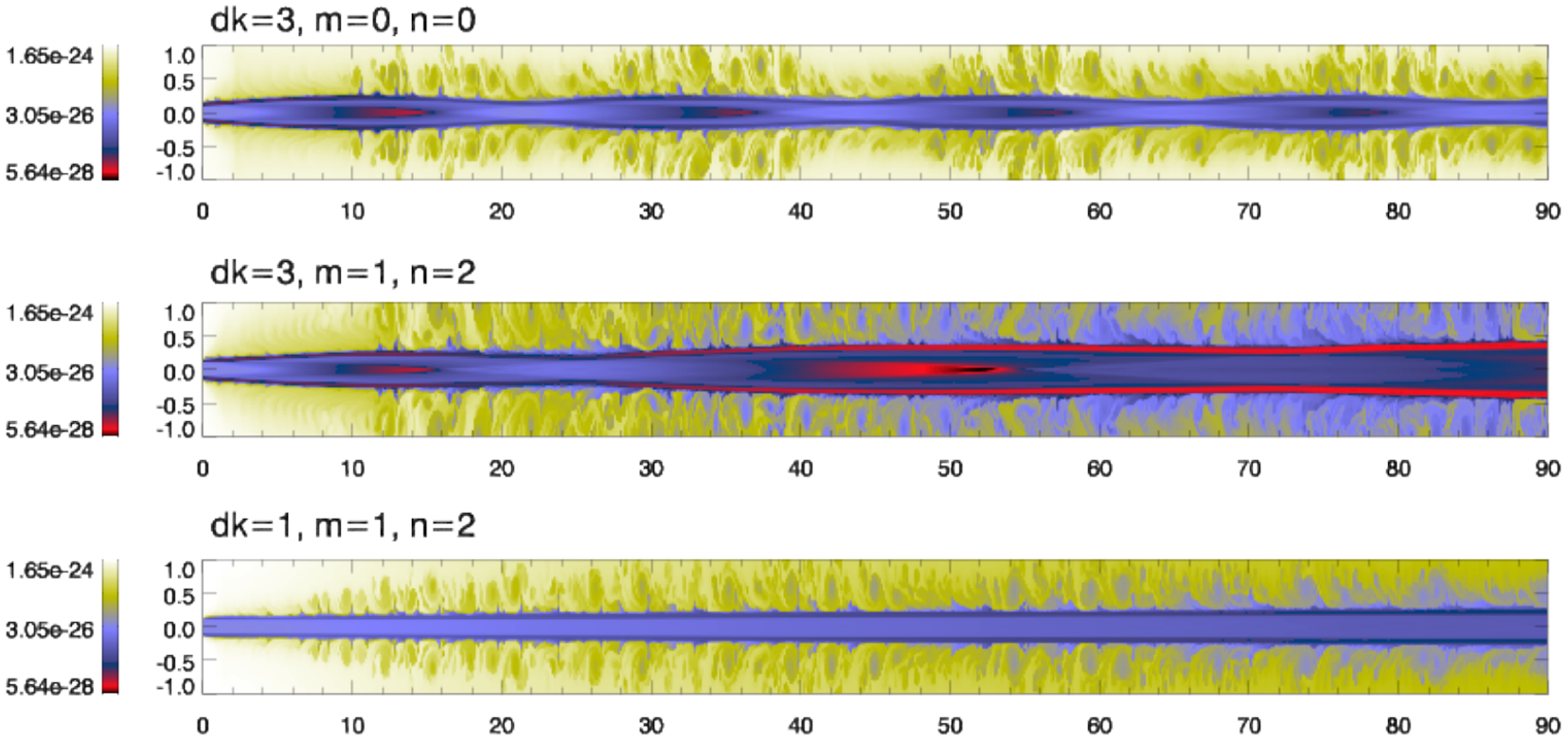

Figure 6.12: The logarithm of the 2D distribution of the rest mass density for simulation of CTA 102. The panels show a over-pressured jet ($d_k = 1$) in a homogeneous ambient medium (top panel), over-pressured jet ($d_k = 3$) in a decreasing density ambient medium (middle panel), and a pressure-matched jet ($d_k = 1$) in a decreasing density ambient medium (bottom panel). For all three simulations we use a bulk Lorentz factor $\Gamma = 12$, an initial rest-mass density $\rho_j = 3.4 \cdot 10^{-26}\mathrm{g/cm^3}$, a Mach number $M = 3$, an adiabatic index, $\hat{\gamma} = 13/9$. For the simulations embedded in a decreasing density ambient medium we used a scale height $z_c = 15\,\mathrm{pc}$, and exponents $m = 1$ and $n = 2$ defining the profile.

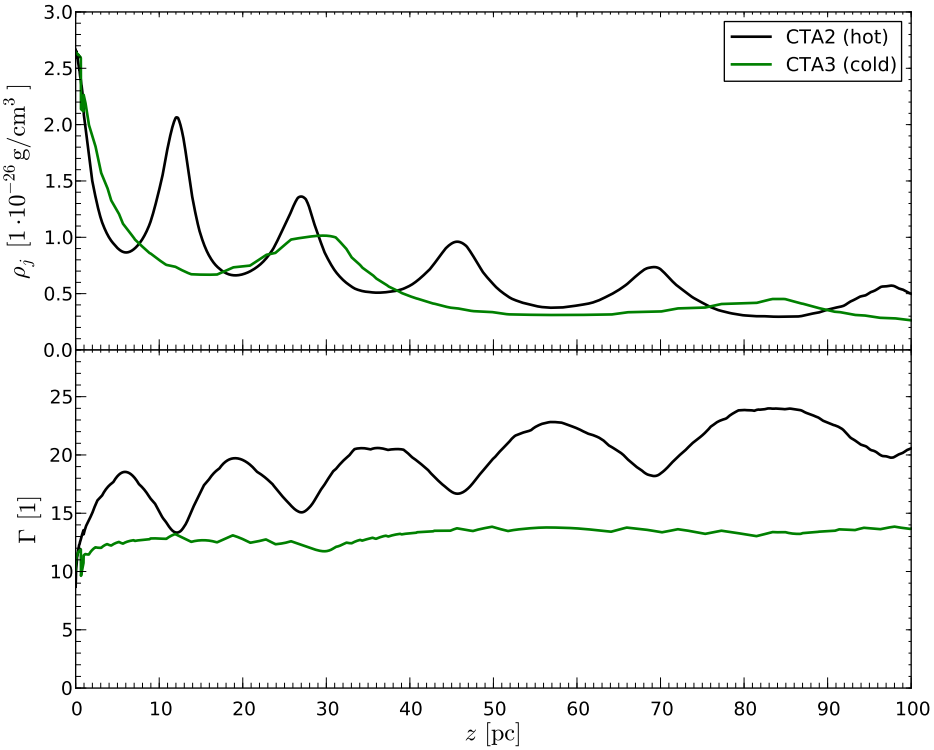

Figure 6.13: Evolution of the rest-mass density (top panel) and the bulk Lorentz factor (bottom panel) along the jet for a cold (black line) and a colder (green line) for the simulations *CTA2* (cold jet) and *CTA3* (hot jet), showing the difference in the number of formed recollimation shocks (bumps in the rest-mass density) and in the variation of the bulk Lorentz factor. See Table 6.6 for the initial values at the jet nozzle and the ambient medium

For the study of interaction between a travelling shock and a recollimation shock we injected several perturbations at the jet nozzle once a steady state was obtained and traced their evolution along the jet. In Table 6.7 we present the parameters for the injected perturbations. Since we were mainly interested in the interaction between the first recollimation shock and the travelling shock, we performed simulations with an increased numerical resolution of 32 cells per jet radii. Since such high-resolution simulations required a lot of computational time, we reduced the grid to (1.5×45) pc ($(10 \times 300)\,\mathrm{R_j}$) and assumed a homogeneous ambient medium.

Table 6.7: Parameter for the injected perturbations, see Table 6.6 for steady-state jets.

Model	t_p [days]	Γ_p [1]	ρ_p [g/cm^3]	p_p [dyne/cm^2]
P1	54	12	$6.8 \cdot 10^{-26}$	$6.3 \cdot 10^{-6}$
P2	54	12	$1.3 \cdot 10^{-25}$	$1.3 \cdot 10^{-5}$
P3	54	12	$2.0 \cdot 10^{-25}$	$1.9 \cdot 10^{-5}$
P4	54	12	$2.7 \cdot 10^{-25}$	$2.5 \cdot 10^{-5}$
P5	144	12	$2.7 \cdot 10^{-25}$	$2.5 \cdot 10^{-5}$

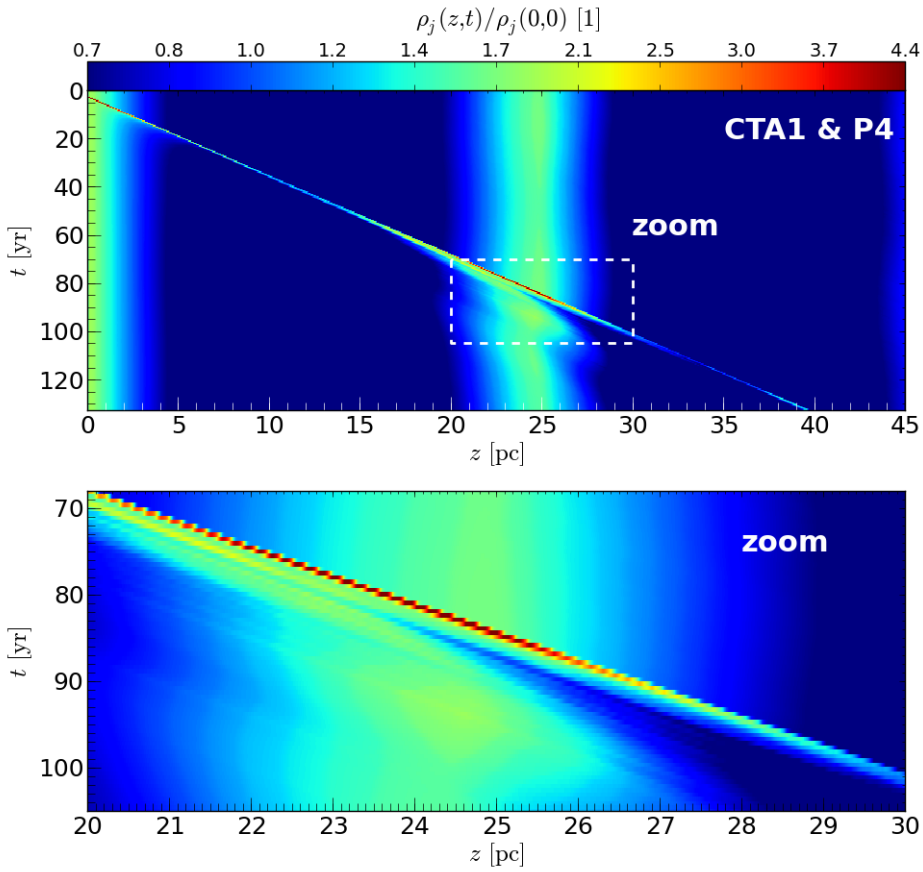

Figure 6.14: Space-time plots for the interaction between a travelling shock wave *P4* and a recollimation shock for simulation *CTA1* (see Table 6.7 and 6.6 for initial parameters.) The panels show the logarithm of the normalised rest-mass density during the propagation of the shock wave (line of increased rest-mass density values). The overall evolution of the shock wave is presented in the top panel and the bottom panels show a zoom into the interaction of the travelling shock wave with the recollimation shock.

In Fig. 6.15 we present three snapshots of the shock-shock interaction for the *P4* simulation. The panels show the logarithm of the 2D distribution of the rest-mass density for three different times indicated in the top left corner of each plot. The shock front is located at $z = 6\,\mathrm{pc}$, $z = 19\,\mathrm{pc}$ and at $z = 33\,\mathrm{pc}$. Notice the increase in the rest-mass density at the shock front. The temporal evolution and the increase in the rest-mass density are plotted in Fig. 6.14. During the interaction between the travelling shock and the recollimation shock, the rest-mass density increases ($(20 < z < 30)\,\mathrm{pc}$). The main perturbation drags the recollimation shock farther downstream and the rarefraction travelling behind the forward shock leads to a drop in the rest-mass density (see bottom panel in Fig. 6.14 during $85\,\mathrm{yr} < t < 95\,\mathrm{yr}$). After $t \sim 20\,\mathrm{yr}$ the recollimation shock is re-established at its initial position. Additionally, the main perturbation generates several trailing features travelling behind the main perturbation (see bottom panel in Fig. 6.14).

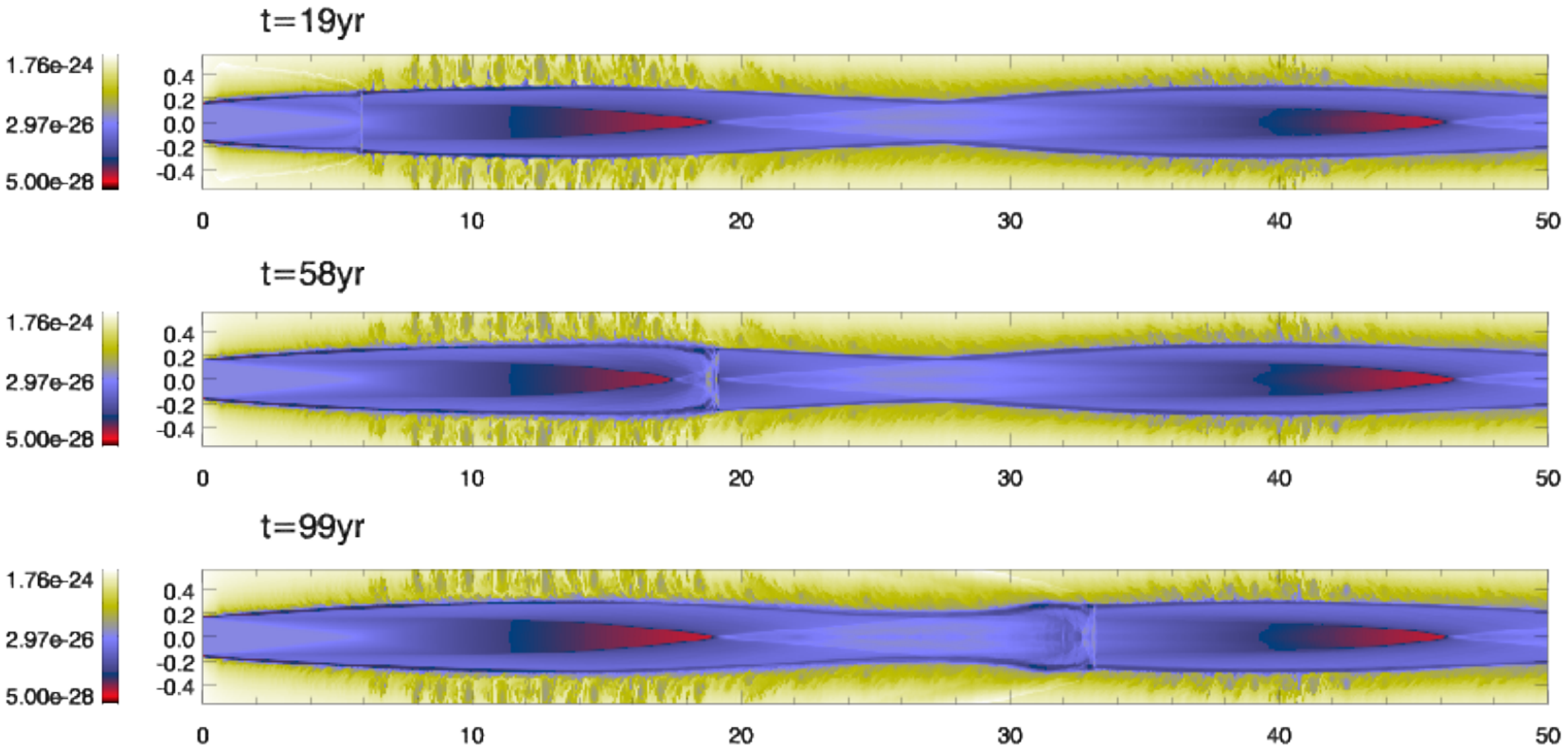

Figure 6.15: Snapshots of the travelling shock wave recollimation shock interaction. The panels show the logarithm of the 2D distribution of the rest mass density for three different times indicated in the top left corner of each panel and the travelling shock is located at $z = 6\,\mathrm{pc}$ (top panel), at $z = 19\,\mathrm{pc}$ (middle panel), and at $z = 33\,\mathrm{pc}$ (bottom panel). The steady-state corresponds to the *CTA1* simulation (see Table 6.6) and the parameters of the travelling shock wave corresponds are the ones of *P4* (see Table 6.7).

6.4.2 Non-thermal emission

To better compare our RHD simulations with the observations we compute the non-thermal emission. In this work we take only synchrotron radiation into account and assume that the non-thermal particles are embedded in the flow of the thermal particles. There are two main ingredients for the generation of synchrotron radiation: the magnetic field and the non-thermal population of particles. We follow the approach presented in Gomez et al. (1997) and Mimica et al. (2009) for the construction of the non-thermal particle population and their spatial and temporal evolution.

We assume that the magnetic field is a fraction ϵ_b of the equipartition magnetic field:

$$B = \left(\epsilon_b \frac{8\pi p_j}{\hat{\gamma} - 1} \right)^{1/2}, \tag{6.7}$$

where p_j is the thermal pressure in the jet, and $\hat{\gamma}$ the adiabatic index. A direct consequence of Eq. 6.7 is that the evolution of the magnetic field follows the variation in the thermal pressure.

The construction of the non-thermal particle distribution and its evolution requires a more detailed treatment than the magnetic field. We use a power-law distribution for the non-thermal particles with an electron Lorentz factor interval $\gamma_{\min}$ and $\gamma_{\max}$:

$$N(\gamma) = n_0(\gamma_{\min}) \left(\frac{\gamma}{\gamma_{\min}} \right)^{-p} \quad \gamma_{\min} < \gamma < \gamma_{\max}. \tag{6.8}$$

Estimates for the upper electron Lorentz factor can be computed assuming a balance between the synchrotron cooling timescale and the gyration time scale (Boettcher & Dermer 2010):

$$\gamma_{\max} = \left(\frac{9 m_e^2 c^4}{8\pi e^3 \epsilon_a B} \right)^{1/2}, \tag{6.9}$$

with m_e being the electron mass, e the elementary charge, and ϵ_a the acceleration factor which relates the number of gyrations of an electron in a magnetic field required to loose its energy through synchrotron radiation. If the relativistic particles are a fraction ϵ_e of the thermal population an estimation for the lower boundary of the relativistic electron distribution, $\gamma_{\min}$ is given by (see, e.g., Böttcher & Dermer 2010; Mimica et al. 2010):

$$\gamma_{\min} = \begin{cases} \frac{p_j}{\rho_j} \frac{m_p}{m_e c^2} \frac{(p-2)}{(p-1)(\hat{\gamma}-1)} \frac{\epsilon_e}{\zeta} & \text{if } p > 2 \\ \left(\frac{p_j}{\rho_j} \frac{m_p}{m_e c^2} \frac{(2-p)}{(p-1)(\hat{\gamma}-1)} \frac{\epsilon_e}{\zeta} \gamma_{\max}^{p-2} \right)^{1/(p-1)} & \text{if } 1 < p < 2 \\ \frac{p_j}{\rho_j} \frac{\epsilon_e}{\zeta} \frac{m_p}{m_e c^2 (\hat{\gamma}-1)} / \ln\left(\frac{\gamma_{\max}}{\gamma_{\min}} \right) & \text{if } p = 2 \end{cases}, \tag{6.10}$$

with thermal pressure, p_j, proton mass, m_p, and $\zeta = m_p/m_e$ for an electron-proton jet and $\zeta = 1$ for an electron-positron jet. The last expression for $\gamma_{\min}$ in Eq. 6.10 has to be solved numerically by a Newton-Raphson algorithm. Finally, the normalisation coefficient $n_0(\gamma_{\min})$ can be calculated form the total number of relativistic particles and the boundaries of the relativistic electron distribution (see, e.g., Böttcher & Dermer 2010; Mimica et al. 2010):

$$n_0(\gamma_{\min}) = \frac{\epsilon_e p_j (p-2)}{(\hat{\gamma}-1)\gamma_{\min}^2 m_e c^2} \left[1 - \left(\frac{\gamma_{\max}}{\gamma_{\min}} \right)^{2-p} \right]^{-1} \tag{6.11}$$

The equations presented above can be used to compute the synchrotron emission for a fixed position and time. However, we are interested in the evolution of the non-thermal emission of jet and therefore we have to evolve the magnetic field, the electron Lorentz factors and the normalisation coefficient of the relativistic electron distribution in space and time. There are two different techniques for the evolution of the non-thermal electron distribution: The adiabatic (see e.g., Gomez et al. 1997) and the spectral evolution method (Mimica et al. 2009)

The adiabatic approach

In this method the lower electron Lorentz factor is computed from the thermal pressure and the rest-mass density at the jet nozzle using Eq. 6.10. In addition, a fixed ratio between the upper and lower electron Lorentz factor, $C_\gamma = \gamma_{\rm max}/\gamma_{\rm min}$ is assumed. Thus, the evolution of $\gamma_{\rm min,max}$ and $n_0\,(\gamma_{\rm min})$ can be calculated along the jet. Once the value of C_γ is set, it is preserved throughout the entire jet. Therefore, the variation in $\gamma_{\rm min}$ depends only on the evolution of p_j and ρ_j.

The spectral evolution (SPEV) approach

Mimica et al. (2009) presented a more detailed method for the calculation of the temporal and spatial variation in the parameters determining the non-thermal emission, taking both, adiabatic and radiative losses into account. The time dependence of the electron Lorentz factor is expressed in the following differential equation (see also section 2.2.1):

$$\frac{d\gamma}{d\sigma} = k_a\gamma - k_s\gamma^2, \tag{6.12}$$

where $d\sigma$ is the length interval in the source frame, k_a is the adiabatic, and k_s is the synchrotron loss term:

$$k_a = \frac{1}{3}\frac{dln\rho_j}{d\sigma} \tag{6.13}$$

$$k_s = \frac{2}{3}\frac{e^4}{8\pi m_e^3 c^5}B^2. \tag{6.14}$$

The authors assume that within a small proper time interval, $d\tau$, the adiabatic and radiative losses are constant and Eq. 6.12 can be solved in analytically(see Eq. 28 in Mimica et al. 2009):

$$\gamma(\sigma) = \gamma_0\frac{k_a e^{k_a\Delta\sigma}}{k_a + \gamma_0 k_s\left(e^{k_a\Delta\sigma} - 1\right)}, \tag{6.15}$$

where $\Delta\sigma = \sigma - \sigma_0$ is a length interval and the subscript 0 indicates values at the location σ_0. Once the evolution of the electron Lorentz factor is given, the calculation of the normalisation coefficient follows (see Eq. 29 in Mimica et al. 2009):

$$n_0(\gamma(\sigma)) = n_0\left(\gamma_0\right)\left[e^{k_a\Delta_\sigma}\left(1 + \gamma_0\frac{k_s}{k_a}\left(e^{k_a\Delta\sigma} - 1\right)\right)\right]^2 \tag{6.16}$$

Calculation of the synchrotron spectrum

The exact[3] emission, ϵ_ν, and the absorption coefficient, κ_ν can be written in the most general form as:

$$\epsilon_\nu = \frac{\sqrt{3}e^3 B \sin\theta}{4\pi m_e c^2} n_0(\gamma_{\min})\gamma_{\min} H\left(\frac{\nu}{\nu_0\gamma_{\min}^2}, p, \eta\right) \tag{6.17}$$

$$\kappa_\nu = \frac{\sqrt{3}e^3 B \sin\theta}{4\pi m_e^2 c^2} n_0(\gamma_{\min})\frac{p+2}{\nu^2} H\left(\frac{\nu}{\nu_0\gamma_{\min}^2}, p+1, \eta\right), \tag{6.18}$$

where we define $\eta = \gamma_{\max}/\gamma_{\min}$, and the characteristic frequency, $\nu_0 = 3eB\sin\theta/(4\pi m_e c)$. The function H is given by:

$$H(x,p,\eta) = \frac{1}{2}x^{(1-p)/2}\int_{x/\eta^2}^{x} d\xi \xi^{(p-3)/2} F(\xi), \tag{6.19}$$

where $F(\xi)$ depends on orientation of the magnetic field:

$$F(\xi) = x\int_x^\infty d\xi K_{5/3}(\xi) \quad \text{ordered magnetic field} \tag{6.20}$$

$$R(\xi) = \frac{1}{2}\int_0^\pi d\alpha \sin^2\alpha F\left(\frac{x}{\sin\alpha}\right) \quad \text{random magnetic field,} \tag{6.21}$$

where $K_{5/3}$ is the modified Bessel function of order 5/3. The functions $F(\xi)$ and $R(\xi)$ are tabulated (see e.g., Crusius & Schlickeiser 1986). To speed up the numerical integration of $H(x,p,\eta)$ we used the numerical approximations presented in Joshi & Böttcher (2011)

$$F(x) = 1.800151957 x^{0.304526404} e^{-x} \tag{6.22}$$

$$R(x) = 1.4980728 x^{1/3} \quad \text{for } x < 0.01 \tag{6.23}$$

$$R(x) = 1.08895 x^{0.20949} e^{-x} - 2.35861\cdot 10^{-3} x^{-0.79051} e^{-x} \quad \text{for } x > 0.01 \tag{6.24}$$

Figure 6.16 shows that the tabulated and the approximated values are in good agreement.

The observed flux density is calculated by integrating the specific intensity, I_ν, across the jet cross section and correcting for the cosmological distance. In our case we consider cylindrical slices with radii R and width Δx.

$$S_\nu = \frac{1+z}{D_l^2}\Delta x \int_0^R dy \frac{\epsilon'_\nu}{\kappa'_\nu}\left(1 - e^{-\kappa'_\nu 2\sqrt{R^2-y^2}}\right), \tag{6.25}$$

where z is the red-shift, D_l is the luminosity distance, and the prime quantities correspond to the values transformed into the observers frame using:

$$\epsilon'_{\nu'} = \delta^2 \epsilon_{(\nu'(1+z)/\delta)} \tag{6.26}$$

$$\kappa'_{\nu'} = \delta^{-1} \kappa_{(\nu'(1+z)/\delta)}. \tag{6.27}$$

In the reconstruction of the non-thermal particle distribution we introduce several parameters which are not directly measurable from the observations of jets. Therefore, we have to investigate their influence on the calculated emission which will help us to better model the observed properties of jets.

[3] In Chapter 2 we used an approximation of the emission and absorption coefficients assuming $\gamma_{\min} = 1$ and $\gamma_{\max} = \infty$

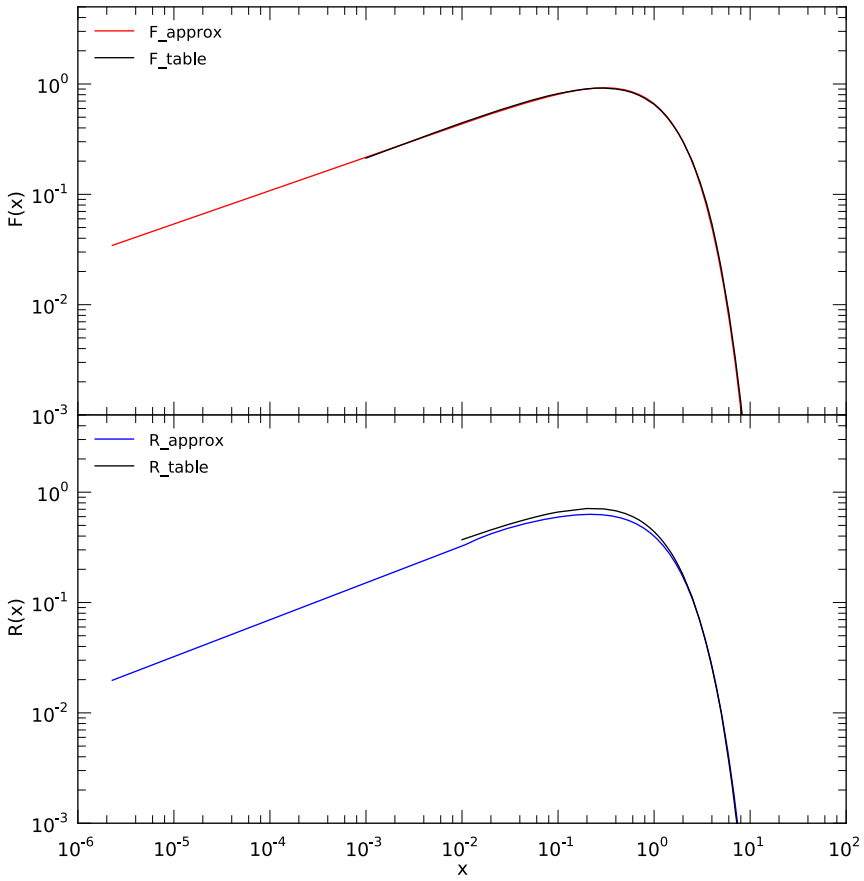

Figure 6.16: Tabulated (black lines) and approximated values for $F(x)$ (top panel) and $R(x)$ bottom panel. The approximations are calculated using Eq. 6.24. For both functions the approximated values are in good agreement with the tabulated ones (black line).

6.4.3 The influence of the cooling mechanism on the non-thermal emission

The influence of the assumed cooling mechanism is shown by the evolution of the upper and lower electron Lorentz factors. In Fig. 6.17 we show for the same initial RHD simulation, *CTA2* (see Table 6.6 for initial hydro-dynamic parameters), the evolution of the magnetic field (top panel), the electron Lorentz factor (middle panel, where the solid line corresponds to $\gamma_{\rm max}$ and the dashed line to $\gamma_{\rm min}$), and the normalisation coefficient of the relativistic electron distribution, $n_0\,(\gamma_{\rm min})$.

We used for the calculations of the non-thermal emission $\epsilon_b = 0.03$, $\epsilon_e = 0.01$, $\epsilon_a = 1 \cdot 10^6$ and a spectral slope of $p = 2.2$. The influence of the cooling mechanism is best visible in the evolution of the electron Lorenz factors (middle panel). If considering only adiabatic losses, the ratio between $\gamma_{\rm max}$ and $\gamma_{\rm min}$ is fixed, here $C_\gamma = 10^3$ (solid black line in the middle panel of Fig. 6.17). On the other hand, radiative losses lead to a strong decrease in $\gamma_{\rm max}$ within the first 10 pc, and the ratio between $\gamma_{\rm max}$ and $\gamma_{\rm min}$ varies with distance along the jet (solid blue line in the middle panel of Fig. 6.17). The radiative losses are the dominant loss mechanism within the first 10 pc, and less important farther downstream,

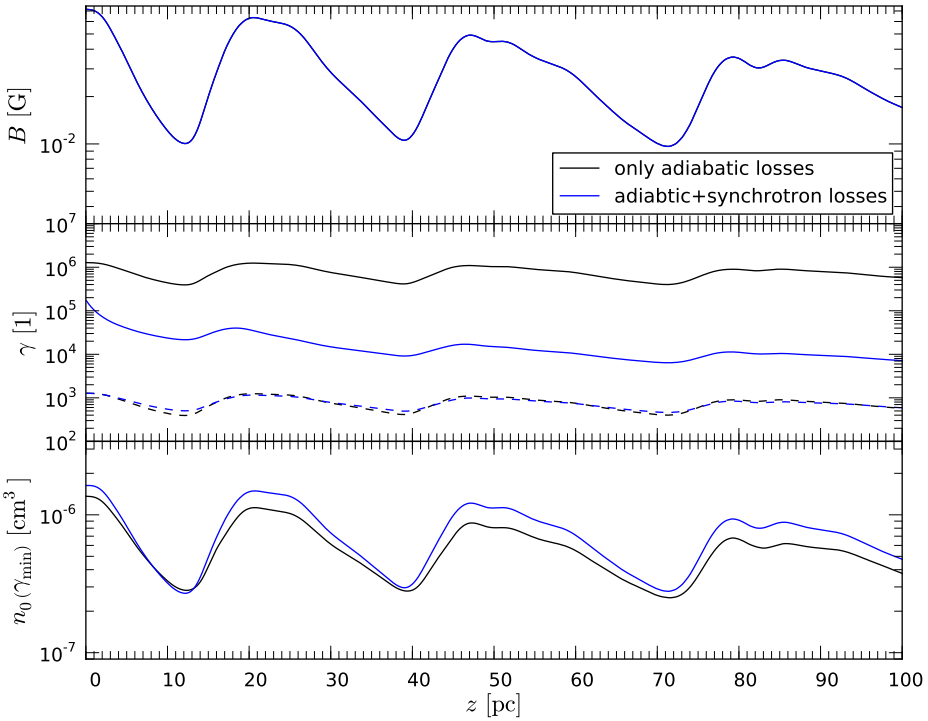

Figure 6.17: Evolution of the non-thermal parameters computed from the *CTA2* simulation (see Table 6.6 for initial hydro-dynamic parameters) assuming only adiabatic losses (black lines) and adiabatic and synchrotron losses (blue lines). The panels show the evolution of the magnetic field (top panel), the electron Lorentz factor (middle panel) and the normalisation coefficient of the relativistic electron distribution (bottom panel). The influence of the synchrotron cooling is best visible in the evolution of the upper electron Lorentz factor (solid lines in middle panel).

where the slopes of the evolution of $\gamma_{\rm max}$ between the two models are comparable. The radiative losses mainly affect the upper electron Lorentz factor, as shown in the evolution of $\gamma_{\rm min}$ (dashed lines in the middle panel of Fig. 6.17). In the single-dish spectrum, the difference between the adiabatic model and the one including the radiative losses is visible in the high frequency part $\nu > 10^{12}$ Hz (see Fig. 6.18). The larger values for $\gamma_{\rm max}$ for the model assuming only adiabatic losses leads to larger flux densities including the radiative losses as well. Besides the difference in the flux density, there are clear changes in the high frequency cut-off in the spectrum. For the model including the radiative losses the high frequency cut-off is at $\nu \sim 10^{14}$ Hz, where as adiabatic model shows a cut-off around $\nu \sim 10^{16}$ Hz. The low frequency cut-off is, in both cases around $\nu \sim 5 \cdot 10^{5}$ Hz.

6.4.4 The influence of ϵ_b, ϵ_e, and, ϵ_a on the non-thermal emission

Besides the two different cooling models (only adiabatic losses or adiabatic and synchrotron losses) there are three additional parameters which determine the shape of the non-thermal spectrum.

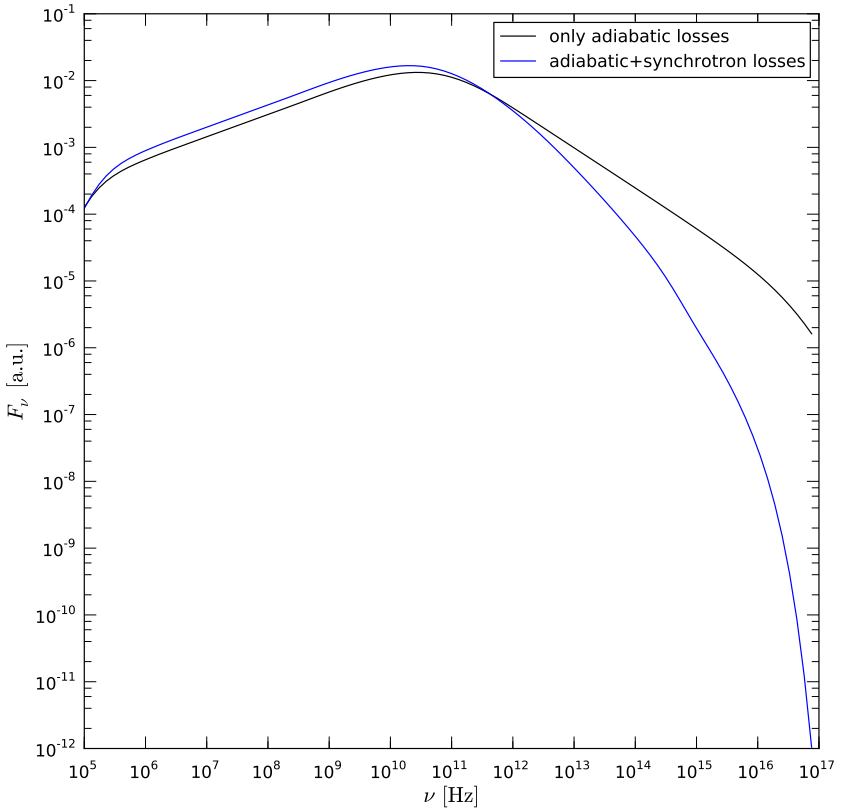

Figure 6.18: Single-dish spectrum calculated at a viewing angle of $\vartheta = 90°$ and a redshift of $z = 1.037$ for an adiabatic model and for a model taking adiabatic and synchrotron losses into account. The underlying hydro-dynamic model is *CTA2* (see Table 6.6) and for the generation of the non-thermal particle distribution we $\epsilon_b = 0.3$, $\epsilon_e = 0.01$, and $\epsilon_a = 10^6$.

The larger the ratio between the non-thermal and thermal particles, ϵ_e, the higher is the turnover frequency and there is a small increase in the turnover flux density. This behaviour is shown in the top panel of Fig. 6.19, where we kept the other parameters $\epsilon_b = 0.1$, and $\epsilon_a = 10^6$ constant, took both, radiative and adiabatic losses into account and used the *CTA2* simulation as underlying RHD model (see Table 6.6 for initial parameters).

The middle panel of Fig. 6.19 shows the influence of the fraction of the equipartition magnetic field on the non-thermal emission, ϵ_b. The increase in ϵ_b leads to a rise in the turnover flux density while keeping the shape of the spectrum un-changed. With larger magnetic field values (larger values of ϵ_b).

The impact of the acceleration factor, ϵ_a, on the non-thermal emission is plotted in the bottom panel of Fig. 6.19. This parameters leads to a variation in the high-frequency cut-off. The larger ϵ_a the smaller is the high frequency cut-off and the steeper is the spectrum.

In sum a larger ϵ_e increases the turnover frequency, an increase in ϵ_b results in a growth of the turnover flux density, and the high-frequency shape of the spectrum is determined by ϵ_a.

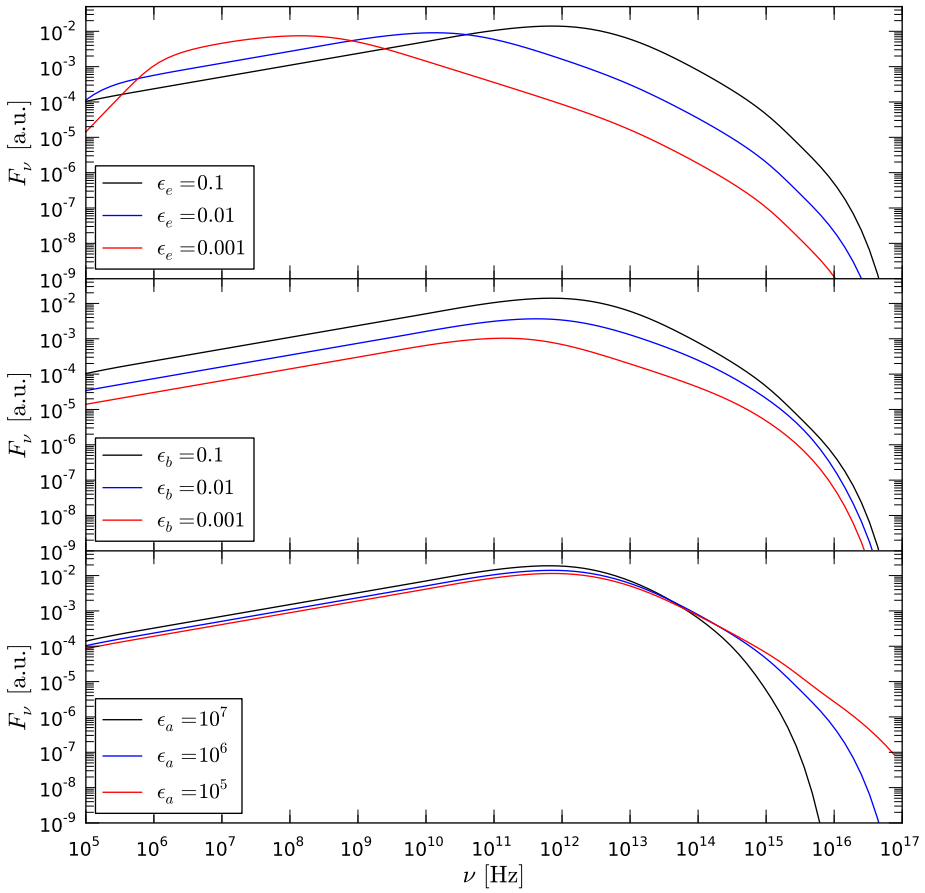

Figure 6.19: The influence of the parameters, ϵ_e (top panel), ϵ_b (middle panel), and ϵ_a (bottom panel) on the shape of the single-dish spectrum (see text for more details).

6.4.5 Single-dish spectra and radio maps for CTA 102

Based on the values obtained from the observations of CTA 102 (see Chapter 3 and 5) and on the study of the influence of the emission parameters on spectral turnover (see Sect. 6.4.4), we selected a set of parameter which provided the best possible agreement with the observations. In Table 6.8 we present the parameters used the calculation of the non-thermal emission. In our calculations we took adiabatic and synchrotron cooling into account. In Fig. 6.20 we present the evolution of the magnetic field (top panel), the electron Lorentz factor (middle panel) and the normalisation coefficient (bottom panel) with distance for the simulations *CTA2* (cold jet) and *CTA3* (hot jet).

For both jets, we obtained comparable results with our set of selected parameters (ϵ_b, ϵ_e, and ϵ_a). However, there are clear differences between the cold and the hot jet. At the recollimation shock there is a local maximum in the pressure and the rest-mass density, which translates into an increase of B, $\gamma_{\mathrm{min/max}}$, and $n_0\,(\gamma_{\mathrm{min}})$. Since in a hot jet there are more recollimation shocks than in a cold one (see Sect. 6.2.1) the variation in the non-thermal parameters is larger (see Fig. 6.20). The larger variation, especially in γ_{max},

Table 6.8: Selected parameter for the calculation of the non-thermal emission

parameter	cold jet	hot jet
ϵ_b	0.3	0.02
ϵ_e	$5 \cdot 10^{-3}$	$5 \cdot 10^{-4}$
ϵ_a	$1 \cdot 10^{6}$	$1 \cdot 10^{6}$
p	2.2	2.2

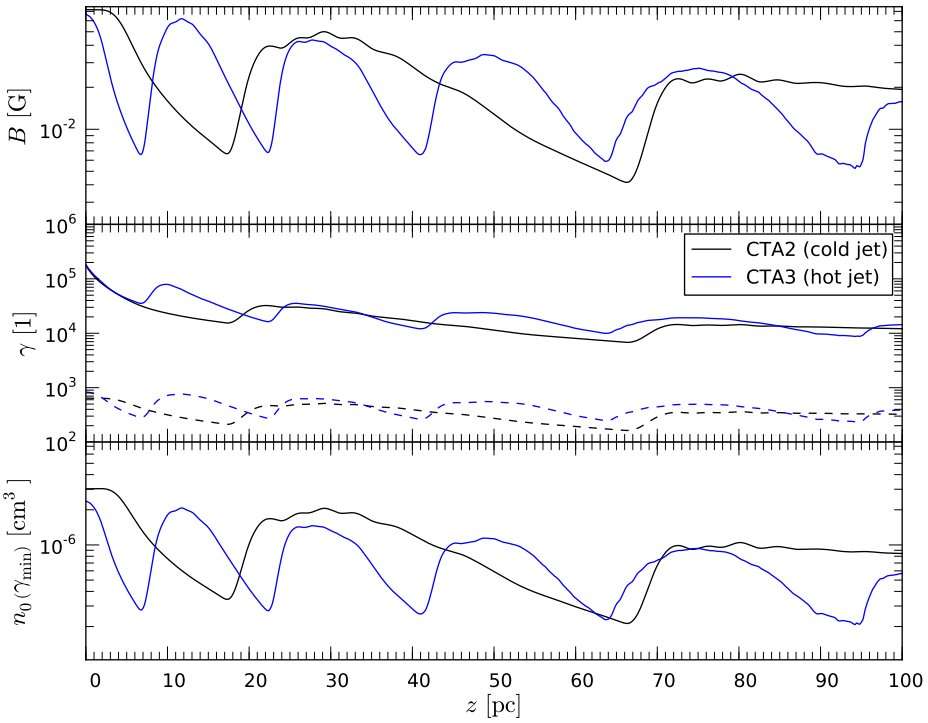

Figure 6.20: Variation of the magnetic field (top panel), the electron Lorentz factor (middle panel), and normalisation coefficient of the non-thermal particle distribution (bottom panel) for a cold (black line) and a hot jet (blue line) with distance. See Table 6.8 for the used emission parameters

leads to increased single-dish flux densities throughout the entire synchrotron spectrum (see Fig. 6.21).

Since the recollimation shocks were not directly visible in the single-dish spectra we calculated synthetic radio maps at several frequencies and convolved them with typical image parameters taken from the VLBA observations of CTA 102 (see Table 5.1). In Fig. 6.22 we present synthetic radio maps from 5 GHz - 86 GHz computed from *CTA2* (cold jet, left column) and from *CTA3* (hot jet, right column) seen under a viewing angle of 90° at $z = 1.037$. For the better comparison the radio maps were normalised to their peak flux density. The location of the recollimation shocks are clearly visible as regions of increase flux density. In the case of the cold jet (left) we observed three and for the hot one (right) five regions of enhanced emission. The location of the first peak in the flux

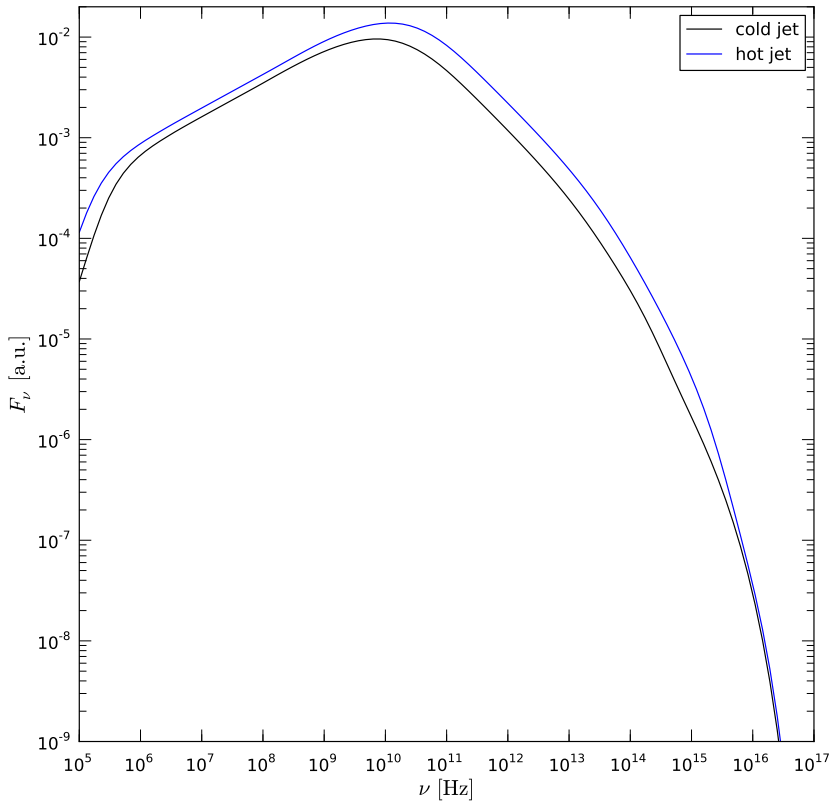

Figure 6.21: Single-dish spectrum calculated at a viewing angle of $\vartheta = 90°$ and a redshift of $z = 1.037$ for a cold jet (black line) and a hot jet (blue line). The underlying hydro-dynamic models are *CTA2* (cold jet) and *CTA3* (hot jet) (see Table 6.6) and for the calculation of the synchrotron spectrum we used the parameters given in Table 6.8.

density is shifted towards smaller distances with increasing frequency in case of the cold jet and appears stationary in the case of the hot jet. This effect can be explained by the first peak being equal to the $\tau = 1$-surface (cold jet) or a physical feature, here the first recollimation shock (hot jet), respectively. As soon as the emission from the recollimation shock becomes optically thin, its position is frequency independent (here $\nu \sim 15\,\mathrm{GHz}$). The variation this position with frequency as measured from the jet nozzle for both jet models is plotted in Fig. 6.23. The black points correspond to the cold jet (*CTA2*) and the red points to the hot jet (*CTA3*). The lines represent a relation of the position-shift with frequency $\Delta r \propto \nu^{-1/k_r}$ as derived from synchrotron-self absorption (see Chapter 2). The value for $k_r \neq 1$ is due to i) the jets are not in equipartition (here $\epsilon_b = 0.3$), and ii) the jets are not of conical geometry.

The effect of the energy losses (adiabatic and radiative) is visible in the shortening of the jet. Farther downstream, the non-thermal particles have already cooled (smaller electron Lorentz factors, see also middle panel in Fig. 6.20) and can no longer produce high-frequency synchrotron emission.

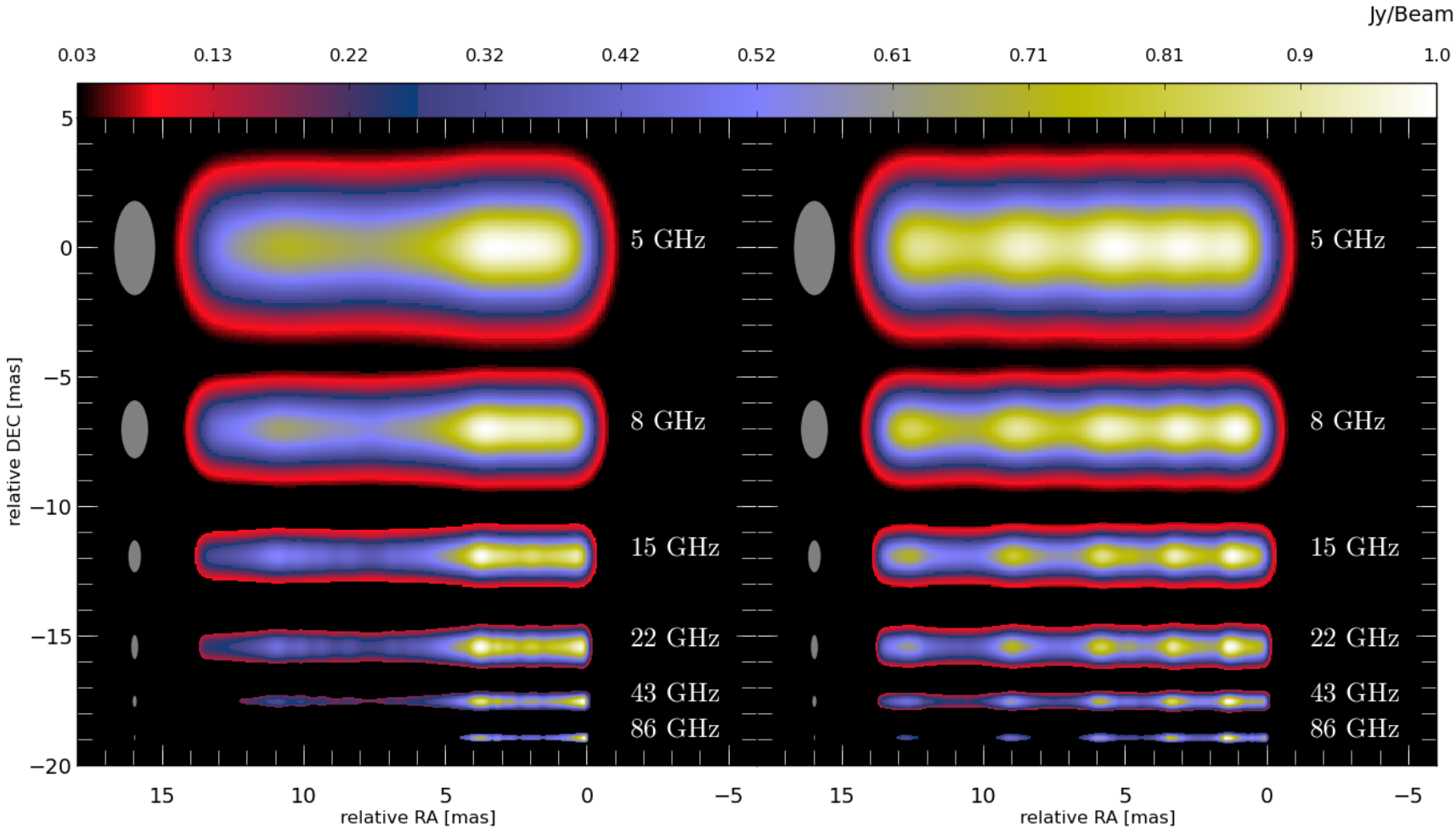

Figure 6.22: Synthetic radio maps normalised to their peak flux density for a cold jet (*CTA2*, left column) and a hot jet (*CTA3*, right column) at different frequencies (5 -86) GHz. The used beam size is plotted next to each radio map (see text for details).

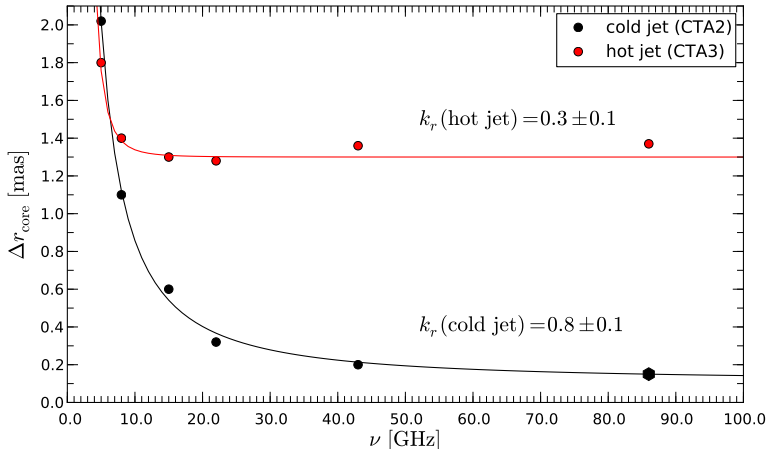

Figure 6.23: Variation of the position of the first bright emission region with frequency for a cold jet (black) and a hot jet (red). The lines correspond to power law fits $\Delta r \propto \nu^{-1/k_r}$ and the value for k_r is presented in the plot. For more details see text

6.4.6 Emission calculation for shock–shock interaction

We used the high-resolution simulations presented in Table 6.7 to compute single-dish spectra and synthetic radio maps for the travelling shock-recollimation shock interaction. We used 30% of the equipartition magnetic field ($\epsilon_b = 0.3$), and assumed that 0.5% of the thermal particle population follow a power-law distribution with spectral index $p = 2.2$ ($\epsilon_e = 0.005$). For the calculation of the single-dish spectrum we used a frequency range from 10^5 Hz to 10^{17} Hz on a logarithmic grid with 1000 points and we selected a time step of 0.5 year (measured in the source frame) which guarantees a dense time coverage of the interaction (see, e.g., Mimica et al. 2009).

The injection of the perturbation leads to a jump in pressure and rest-mass density and corresponds to an increase in both, the electron Lorentz factor ($\gamma_{\rm min}$, $\gamma_{\rm max}$), and the number of relativistic particles ($n_0\,(\gamma_{\rm min})$). Due to the expansion of the jet, the pressure and the rest-mass density decrease with distance from the jet nozzle. However, there is a strong increase in the pressure and the rest-mass density at the location of the recollimation shock which effects also the non-thermal parameters. In Fig. 6.24 we present the evolution of the rest-mass density (top panel), the electron Lorentz factor (middle panel), and the normalisation coefficient of the non-thermal particle distribution (bottom panel) for four different times. The increase in the thermal and non-thermal parameters during the propagation of the shock wave is clearly visible. Notice the strong increase in the rest-mass density and in the normalisation coefficient at the location of the recollimation shock in both cases, the quiescent state (black line, t=0 yr) and during the interaction with the travelling shock (green line, t=81 yr).

We computed the single-dish synchrotron spectrum and subtracted the quiescent state to trace the changes in the turnover frequency, ν_m, and the turnover flux density, S_m, during the propagation of the travelling shock through the over-pressured jet. We show the evolution of ν_m (top panel) and S_m (bottom panel) for the flaring spectrum in Fig. 6.25.

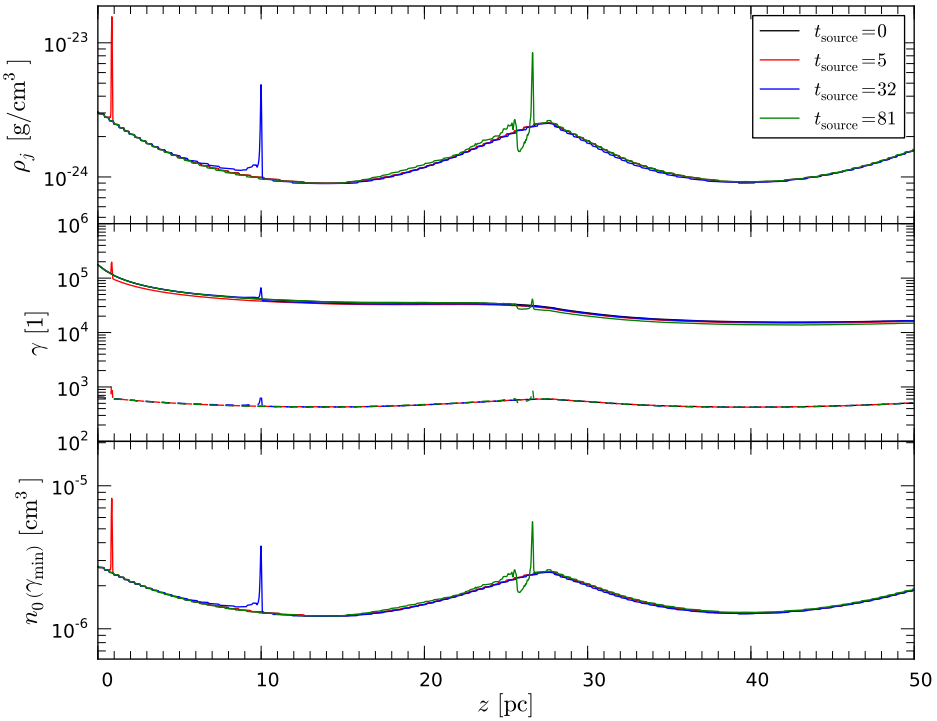

Figure 6.24: Variation of the rest-mass density (top panel), the electron Lorentz factor (middle panel), and normalisation coefficient of the non-thermal particle distribution (bottom panel) during the propagation of a relativistic shock for four different times for the jet simulation *CTA1* and perturbation *P4* (see Table 6.6 and 6.7).

The injection of the perturbation leads to an increase in the turnover frequency and the turnover flux density (0 yr $< t <$ 15 yr). While the shock travels through an environment with decreasing pressure and rest-mass density, the turnover frequency and the turnover flux density decrease (15 yr $< t <$ 50 yr). As soon as the travelling shock encounters the recollimation shock, there is an additional increase in ν_m and S_m (50 yr $< t <$ 80 yr). The third peak in the turnover frequency could be due to the formation of trailing features (secondary shock waves created in the wake of the main perturbation). For $t >$ 90 yr both parameters decrease. Notice that we used a homogeneous ambient medium, which led to similar pressure and rest-mass density at the jet nozzle and the recollimation shock. These circumstances create similar values for ν_m and S_m at the jet nozzle and the recollimation shock.

In addition to the single-dish spectra for the shock-shock interaction we produced synthetic radio maps for several frequencies. In Fig. 6.26 we present six snapshots for the travelling shock-recollimation shock interaction using the jet simulation *CTA1* and perturbation *P4* (see Tables 6.6 and 6.7). The left column shows synthetic radio maps at 15 GHz normalised to the peak flux density and the right column shows the spectral index maps between 43 GHz and 15 GHz. The maps were computed at a redshift of $z = 1.037$, seen under a viewing angle of 90°, and we used a convolving beam of (1.3 × 0.5) mas. The time in the source frame is plotted in the centre for each snapshot. The travelling

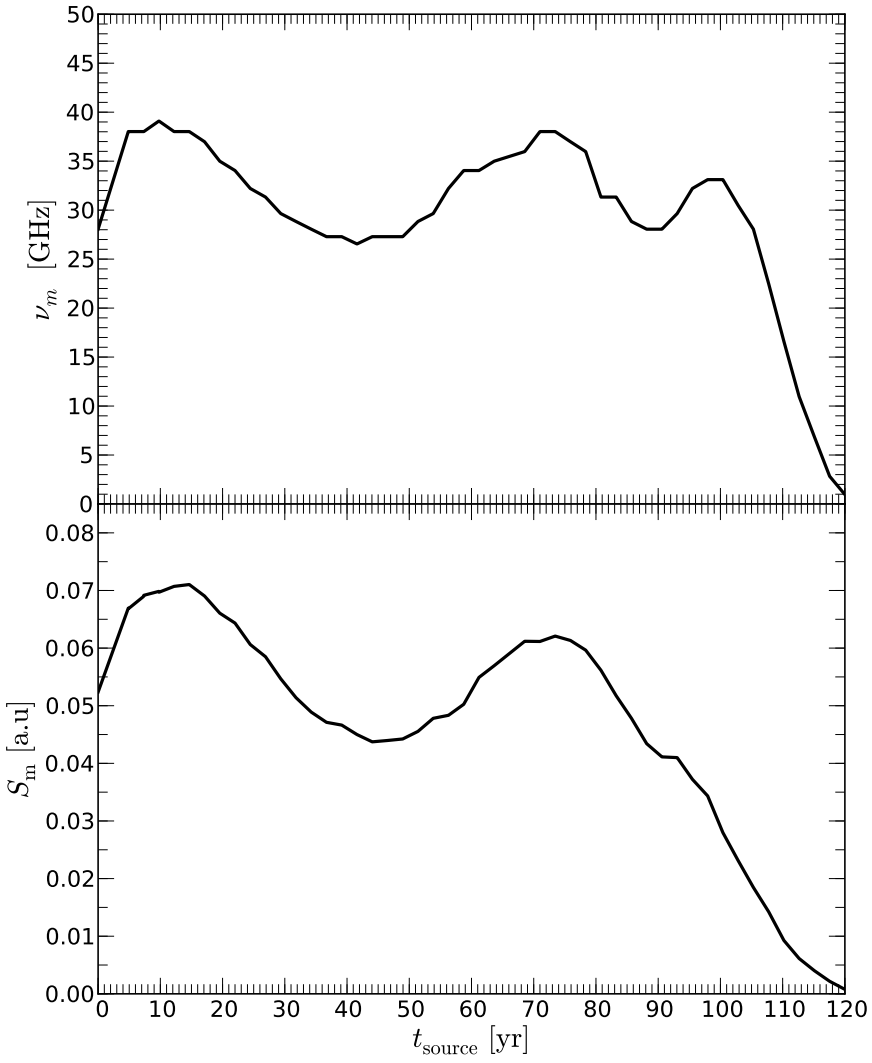

Figure 6.25: Evolution of the turnover frequency, ν_m, (top panel) and the turnover flux density, S_m, (bottom panel) of the flaring spectrum during the propagation of relativistic shock through an over-pressure jet for the jet simulation *CTA1* and perturbation *P4* (see Table 6.6 and 6.7).

shock leads to an increase in the core flux density and the spectral index (see t=15 yr), and the propagation of the shock is clearly visible as a separated component of increased flux density (left column) and as a region of increased (flattened) spectral index (right column). The interaction of the travelling shock with the recollimation shock leads to an apparent inward dragging of the recollimation shock and a splitting into two separate components (t=86 yr). After the travelling shock has passed through the recollimation shock, its initial position is re-established (t=130 yr).

The temporal evolution of the separation of the detectable components at 15 GHz from the jet nozzle (here $z = 0$) is presented in Fig. 6.27. The black points corresponds to the

first component ($r \sim 0.3$ mas), the blue one to the recollimation shock ($r \sim 3.2$ mas), and the red one to the travelling shock. Due to the limited resolution, the travelling shock is not directly visible after its injection. However its presence is detectable by the downstream dragging of the first component (20 yr $< t <$ 40 yr) and becomes detectable for 40 yr $< t <$ 60 yr. The interaction with the recollimation shock leads to an apparent inward dragging of the recollimation shock (80 yr $< t <$ 110 yr) and its initial position is re-established after the travelling shocks passes the recollimation shock ($t >$110 yr).

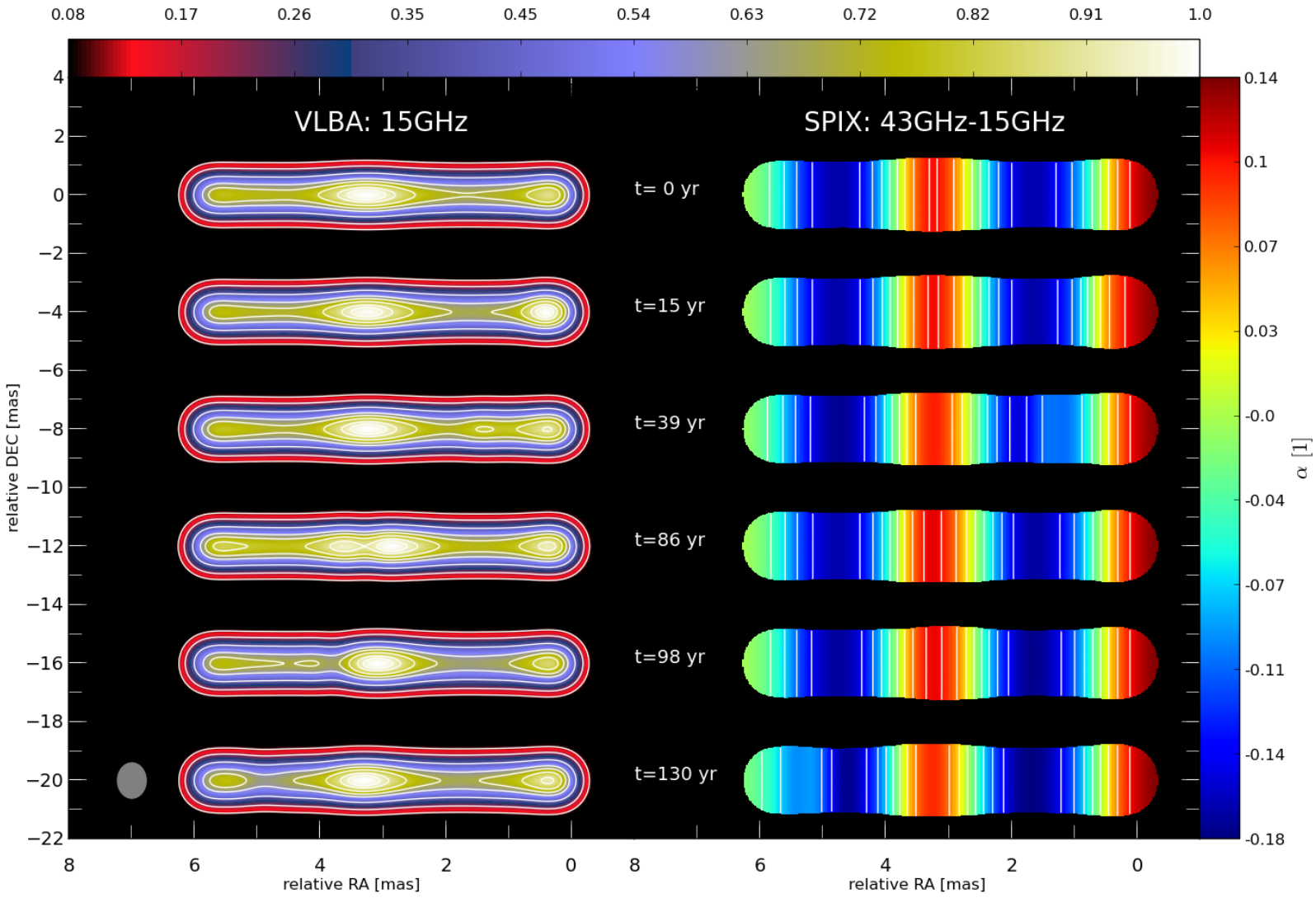

Figure 6.26: Synthetic 15 GHz radio maps (left column) and spectral index maps between 43 GHz and 15 GHz for several snapshots during the travelling shock recollimation shock interaction seen under a viewing angle of 90°. We used a redshift of $z = 1.037$ and the maps are convolved with a beam of (1.3×0.5) mas. For more details see text.

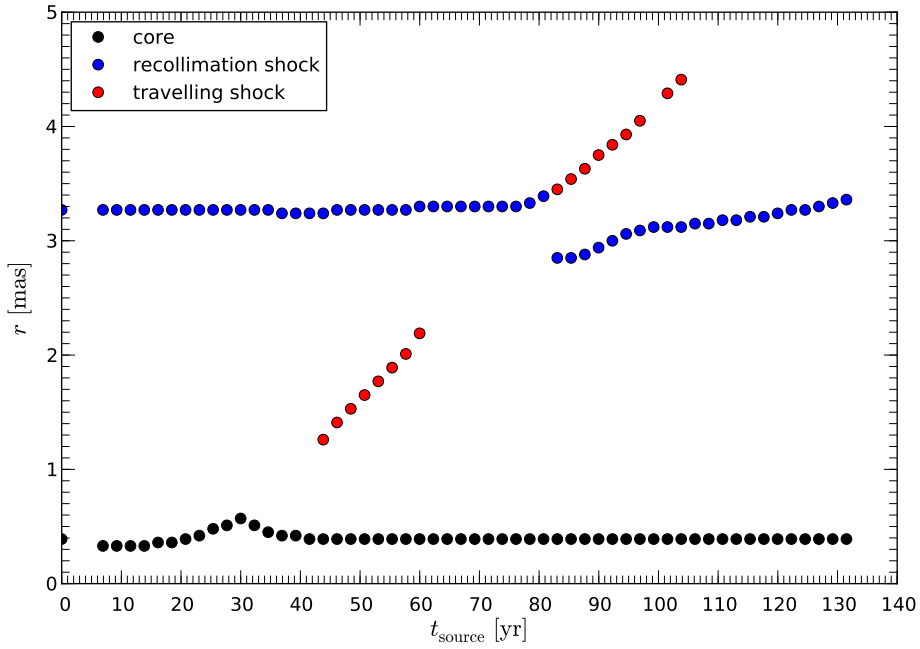

Figure 6.27: Temporal evolution of the separation of the detectable components at 15 GHz from the jet nozzle. The black points corresponds to the core, the blue ones to the recollimation shock and the red ones to the travelling shock. The abscissa axis corresponds to the time in the source frame.

6.5 Comparison with observations

The calculated evolution of the turnover frequency and the turnover flux density (see Fig. 6.25) are in good agreement with the observed spectral evolution (see Fig. 3.5). Since we assumed a homogenous ambient medium the evolution of the turnover flux density is flatter than in the observations. However, the increase in both, turnover flux density and turnover frequency during the interaction between the travelling shock and the recollimation shock is clearly visible.

From the synthetic radio maps we extracted the detectable motion of components and showed that there is an apparent inward dragging of the recollimation shock. The complex interaction between the travelling and the recollimation shock together with the limited resolution of the observations can easily lead to the misidentification of VLBI components. In Fig. 6.27 we show the trajectory of the travelling shock wave and it reproduces nicely the observed trajectories of the VLBI features (see Fig. 4.8).

The observed continuous decrease of the core-shift with frequency together with results from the synthetic multi-frequency maps favour that the observed VLBI core corresponds to the $\tau = 1$-surface. We obtained from both, the observations and the simulations an exponent $k_r = 0.8$ (see Fig. 6.23 and Table 5.2). The variation in the spectral in-

dex obtained from the simulations can partially account for the observed variations in the spectral index (see Figs. 6.26 and C.1).

6.6 Summary

In this Chapter we used state-of the art RHD simulations to investigate the formation of recollimation shocks and their interaction with travelling shocks in extragalactic relativistic flows. We performed a large parameter space study to analyse the dependence of the shock properties from the initial conditions at the jet nozzle and from the conditions in the ambient medium.

Our study of the interaction between travelling shocks and recollimation shocks revealed that there is a strong increase in pressure and rest-mass density during the interaction. Moreover, strong travelling shocks can drag the recollimation shock downstream and trigger the formation of trailing shocks.

We used the source intrinsic parameters obtained from the observations of the blazar CTA 102 and performed several source-tailored high-resolution simulations. For the calculation of the non-thermal emission we followed the SPEV approach (Mimica et al. 2009) and took both, adiabatic and synchrotron losses into account. To compare our simulations with the observations, we computed the single-dish spectrum and its variation during the propagation of relativistic shock. For the comparison with high-resolution radio maps, synthetic multi-frequency radio maps were conducted. We used these maps to derive the observed radio component kinematics and the spatial and temporal evolution of the spectral index.

7 The jet in CTA 102. A global perspective

7.1 Observations

From the accumulated evidences in this work, we can discuss the general nature of the jet in CTA 102. First of all, the jet shows kinks and helical structures with different wavelengths showing up at different observing frequencies (see also Perucho et al. 2012). The regions in the stacked image (0–1 mas, 1–2 mas, 5–8 mas, and >10 mas) coincide with the transversal displacement of the ridge line in East–West direction at 15 GHz, which is a central frequency to the whole analysis. The latter is the main reason why the jet viewing angle at this frequency plays a crucial role in selecting regions for our analysis.

Following the results in Chapter 4, the jet flow should be accelerating in order to explain the observed increase in the Doppler factor at the core region (0.1 to 1 mas, see Fig. 4.13). Moreover, acceleration of the flow is also expected in a hot flow after compression in a standing shock, as it has been claimed to be the case at 0.1 mas.

Farther downstream, the changes in the brightness temperature along the jet include discontinuous jumps at $r \simeq 1-2$ mas and $r \simeq 4-5$ mas (see Fig. 4.15), which cannot be accounted for in terms of a continuous change in the viewing angle. At the same positions (1-2 mas and 4 mas), the jet-width profile flattens (see Fig. 5.9) and the spectral index shows 'bumps' in some cases (e.g., $r \simeq 4-5$ mas, Fig. 5.17). Both facts point to the presence of recollimation shocks. Therefore, the jet morphology at, e.g., 15 GHz, indicates that helical motion is responsible for the highest relative flux in regions D, B, and A2. However, the spectral properties and, to some extent also the kinematics, favor the over-pressured jet scenario and the existence of recollimation regions at $r \simeq 0.1$ mas (de-projected 16 pc from the core), at $r \simeq 1-2$ mas (de-projected 160-320 pc from the core), at $r \simeq 5$ mas (de-projected 800 pc from the core), and possibly at $r \simeq 10$ mas (de-projected 1600 pc from the core). The increasing distance between the positions of the subsequent shock candidates suggest that the jet propagates in a decreasing density ambient medium. However, it is difficult to know whether, for instance, there is only one or more standing shocks in region B (components B1, B2 and B3 at $4\,\mathrm{mas} \leq r \leq 8$ mas, see Figs. 4.6 and 4.7). The lack of correspondence of the plateaus in the jet radius (including stationary components and bumps in the spectral index profiles) with the boosted regions of the jet can be taken as an evidence of their independent nature.

Interestingly, the width of the jet at 2 GHz increases in region D whereas it seems to remain constant at higher frequencies. Only at $r \simeq 10$ mas the jet-width at 2 GHz

becomes flatter. This result should be understood in terms of transversal jet structure and different internal and external dynamics in the jet, which can be compared to simulations or theoretical models of over-pressured jets (Begelman et al. 1984; Perucho & Martí 2007; Nalewajko 2012). At the largest scales, the 2 GHz jet-width is $\simeq$ 6 mas ($\simeq$ 50 pc), whereas at 5 GHz the jet-width is $\simeq$ 3.5 mas ($\simeq$ 30 pc), which can give an idea of the width of the shear/mixing layer surrounding the jet (see, e.g., Perucho & Martí 2007; Wang et al. 2011). A deeper study of the ridge-line and jet transversal structure will be presented elsewhere.

7.2 Simulations

We used RHD simulations to test your hypothesis of shock-shock interaction as the physical mechanism behind the 2006 radio flare in CTA 102. We used the obtained initial parameters of the source as input values for our simulations and computed the non-thermal emission using the SPEV approach (Mimica et al. 2009).

The synthetic single-dish spectra and radio maps could reproduce some of the observed properties of CTA 102, such as the double hump in the turnover frequency and in the turnover flux density. In addition, the synthetic radio maps allowed us to re-construct the trajectory of the detectable components, which showed some characteristics of the observed VLBI trajectories. Based on these results, we can confirm independently our initial hypothesis of shock-shock interaction in the jet of CTA 102.

However, for a more detailed modelling of the source, 3D relativistic magneto-hydrodynamic (RMHD) simulations are needed, which would allow us to lower some of our assumptions and to test different physical processes (Leismann et al. 2005). By using 3D simulations we can test non-axisymmetric effects such as the interaction between helical modes and pinching modes (Perucho et al. 2010). Together with a more advanced 2D or 3D ray-tracing technique which includes time-delay effects more realistic emission calculations can be obtained (Aloy et al. 2003).

In the future we plan to address those topics, starting with the improvement of our emission code.

A Model fit results

Here we show results of the circular Gaussian modeling for the individual frequencies (5 GHz – 43 GHz) during our multi-frequency campaign (May 2005 until April 2007). For each frequency we present contour plots of the source including position of the fitted circular Gaussian components and its structural evolution during our observations. Furthermore, we show the temporal evolution of the component parameters, e.g., position, flux density and size, and the results of a polynomial fit to the cross-identified features are summarize in Tables A.1 - A.5 . The component parameters for all frequencies and epochs can be found at the end of the Appendix in Tables A.6 and A.7.

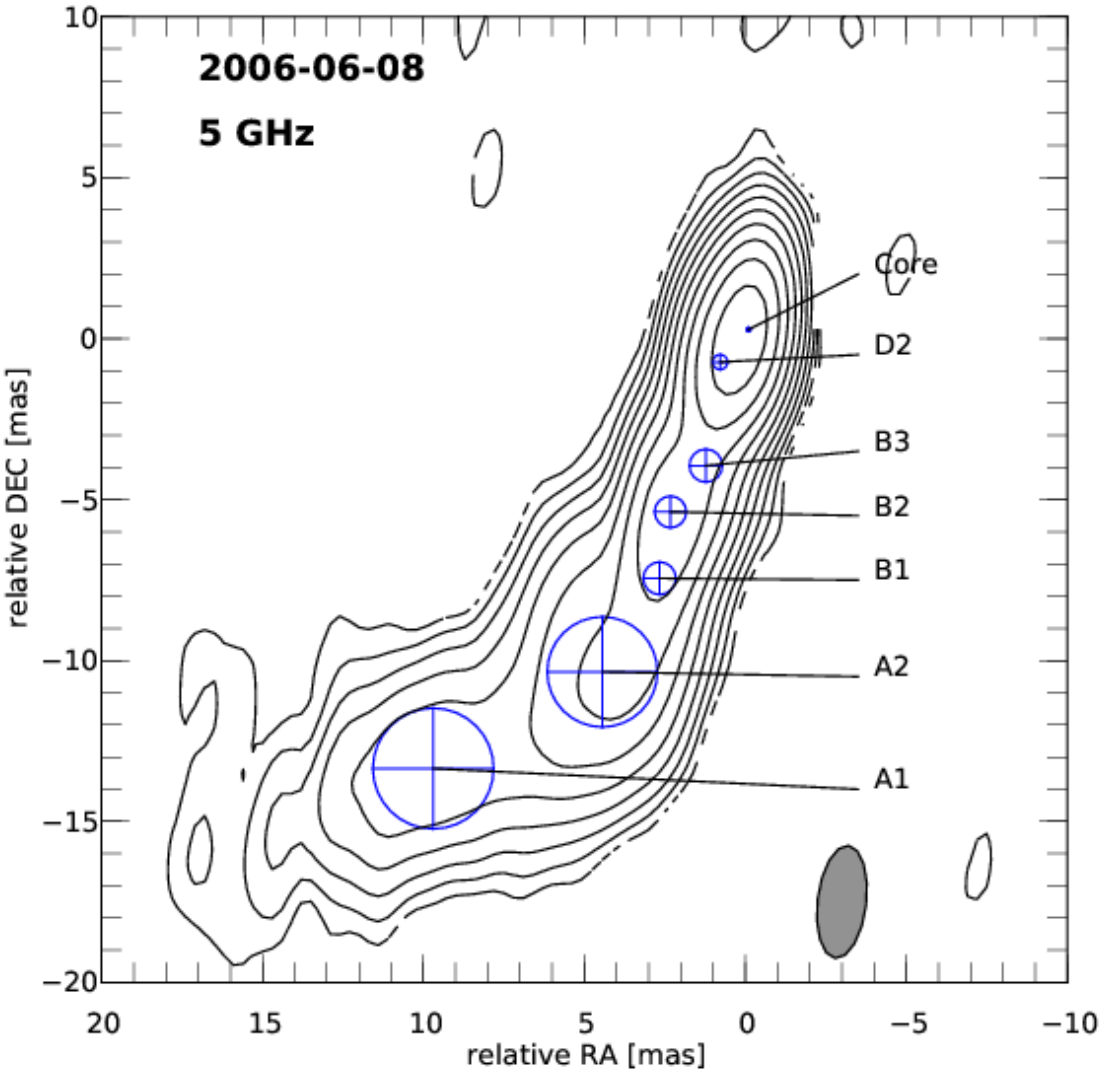

Figure A.1: 5 GHz uniformly weighted VLBA CLEAN image of CTA 102 observed on 8th of June 2006 with overlaid fitted circular Gaussian components. The map peak flux density was 2.0 Jy/beam, where the convolving beam was 3.5×1.5 mas at P.A. -5.3. he lowest contour is plotted at $10\times$ the off-source rms and increases in steps of 2.

Table A.1: Results of the kinematic analysis for the fitted components at 5 GHz

Comp	μ [mas/yr]	β_{app} [c]	δ_{min} [1]	ϑ_{max} [°]	Γ_{min} [1]	t_{ej} [yr]	$< r >$ [mas]	t_{min} [yr]	t_{max} [yr]	acceleration	classification
A1	0.2±0.1	8±4	8	7	8	−−	16.9±0.2	2005.39	2007.32	no	non-radial outward
A2	0.20±0.05	11±2	11	5	11	1947±15	11.6±0.2	2005.39	2007.32	no	radial outward
B1	0.07±0.07	4±4	4	16	4	−−	8±0.3	2005.39	2007.32	no	non-radial outward
B2	0.05±0.04	2±2	2	21	2	−−	6.2±0.1	2005.39	2007.32	no	non-radial outward
B3	0.07±0.06	4±3	4	14	4	−−	4.3±0.1	2005.39	2007.32	no	non-radial outward
D2	0.14±0.01	8±1	8	8	8	1997.3±0.7	1.3±0.1	2005.39	2007.32	no	radial outward

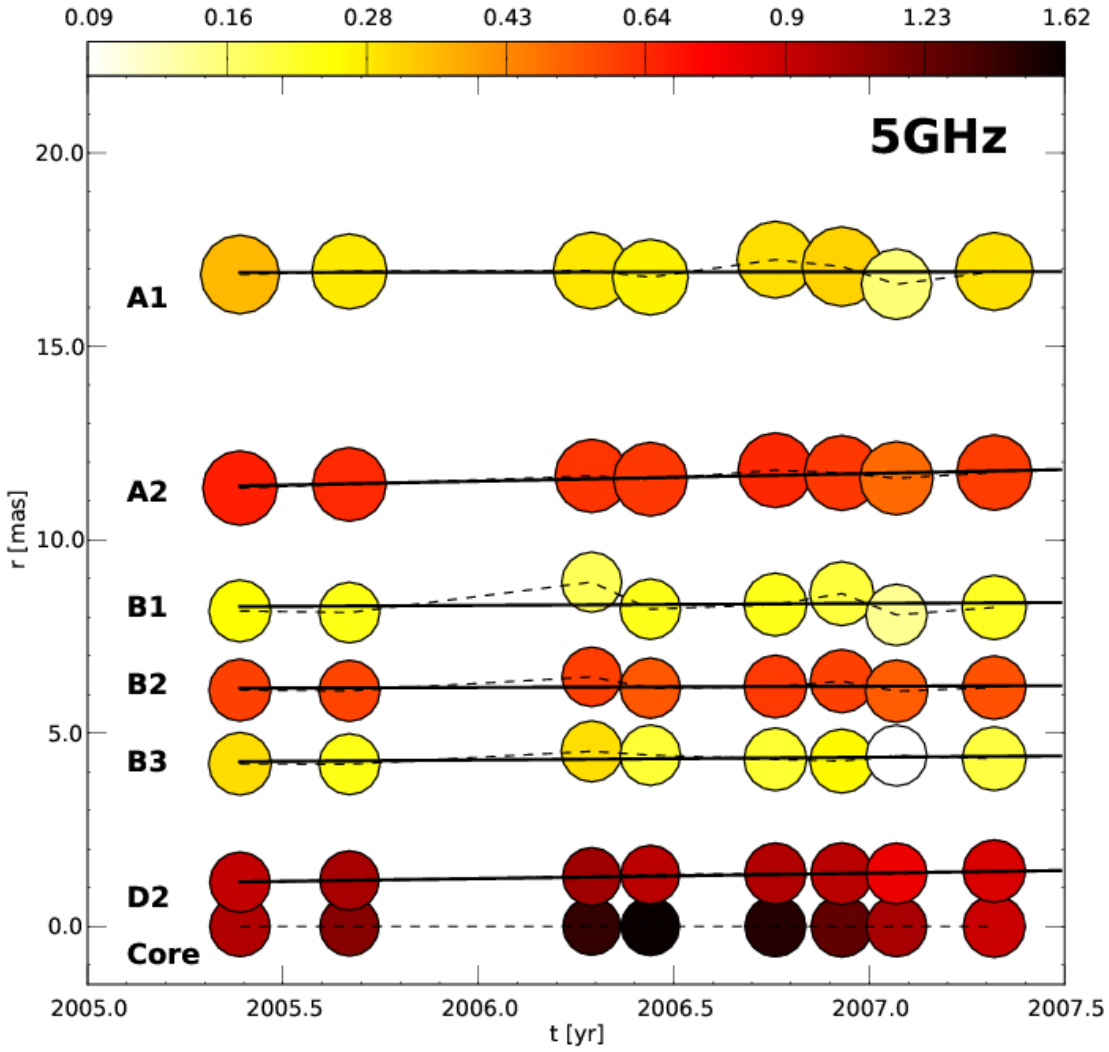

Figure A.2: Temporal evolution of the separation from the core for the 5 GHz components. The color scale corresponds to the flux density and the size of the circles to the relative size (FWHM) of the components. The solid black lines correspond to a linear fits of the component trajectory.

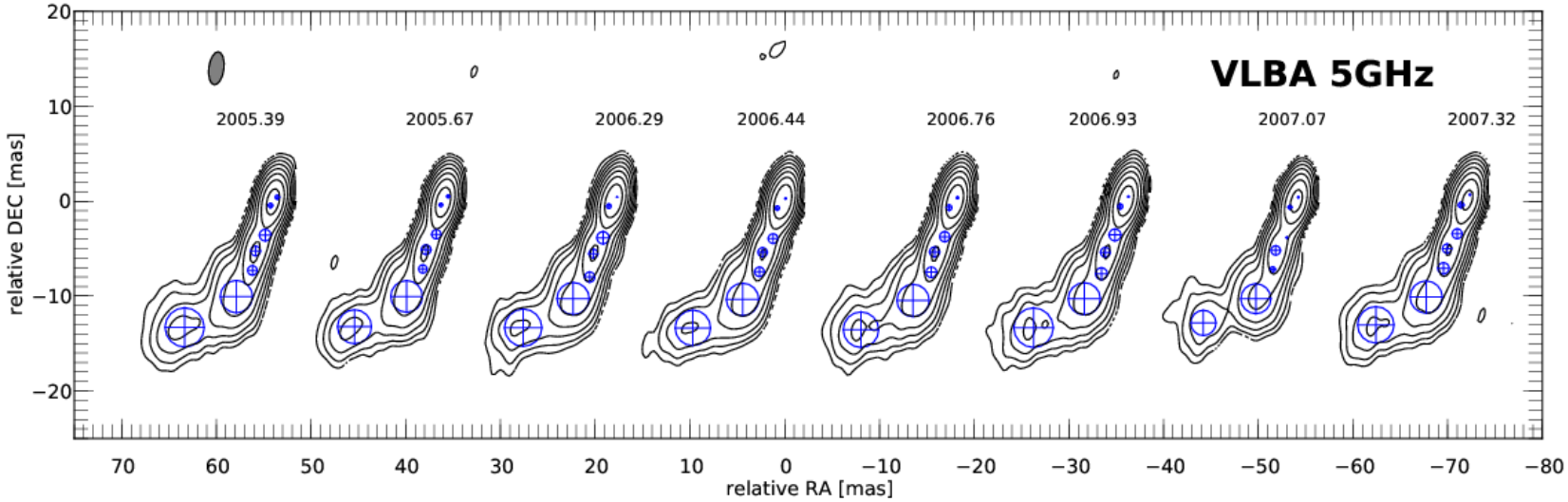

Figure A.3: 5 GHz uniform weighted VLBA images of CTA 102 with fitted circular Gaussian components. For the better comparison all maps are convolved with a common beam of 3.5 × 1.6 mas at P.A. −7.4 and the epoch of the observations is indicated above each contour map. The lowest contour levels is plotted 10× of the maximum off-source rms and increases in steps of 2.

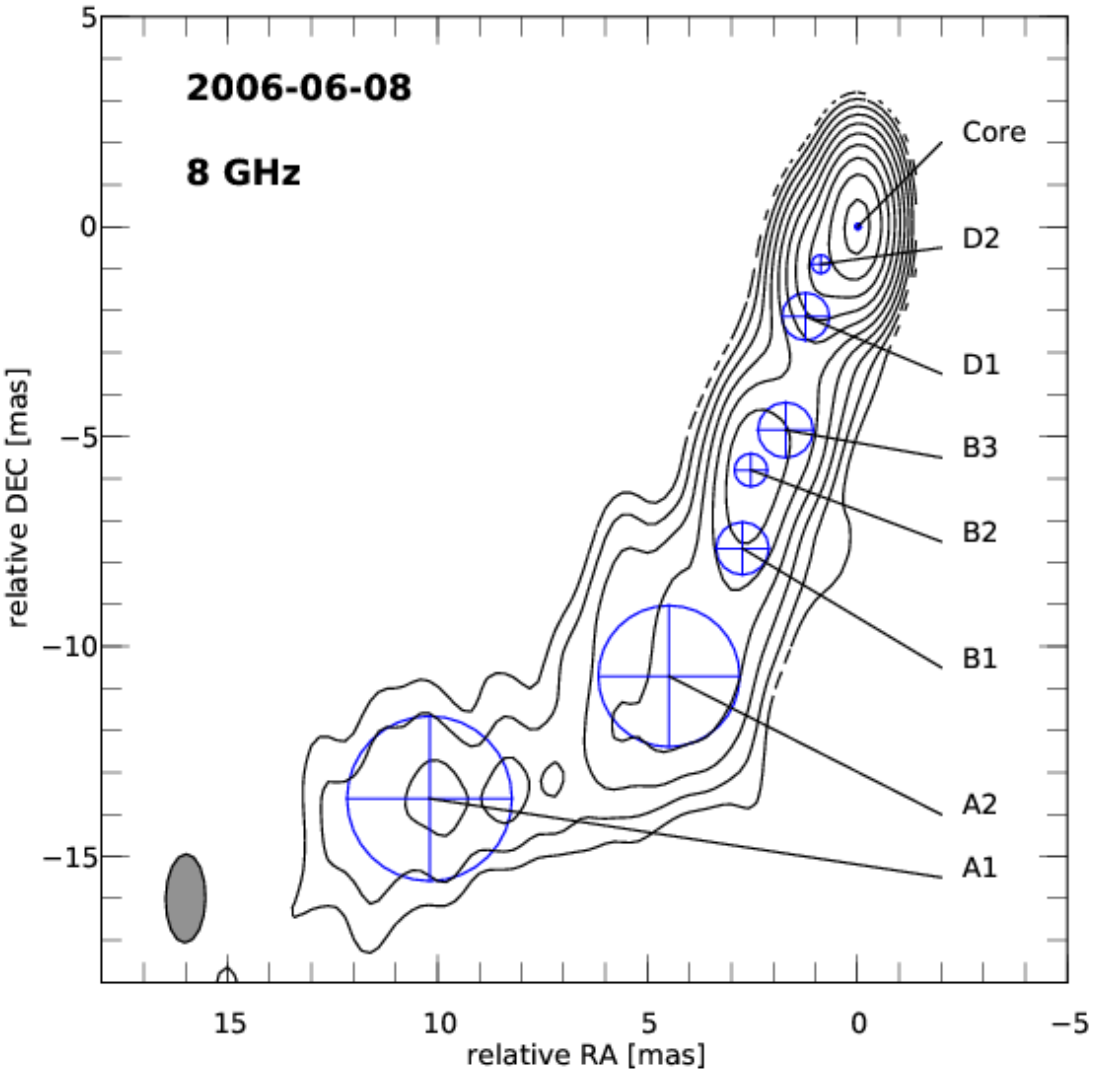

Figure A.4: 8 GHz uniformly weighted VLBA CLEAN image of CTA 102 observed on 8th of June 2006 with overlaid fitted circular Gaussian components. The map peak flux density was 2.8 Jy/beam, where the convolving beam was 2.1×0.9 mas at P.A. -0.9. he lowest contour is plotted at 10× the off-source rms and increases in steps of 2.

Table A.2: Results of the kinematic analysis for the fitted components at 8 GHz

Comp	μ [mas/yr]	β_{app} [c]	δ_{min} [1]	ϑ_{max} [°]	Γ_{min} [1]	t_{ej} [yr]	$< r >$ [mas]	t_{min} [yr]	t_{max} [yr]	acceleration	classification
A1	0.30±0.20	15±8	15	4	15	−−	17.2±0.3	2005.39	2007.32	no	non-radial outward
A2	0.10±0.06	6±3	6	10	6	−−	11.5±0.1	2005.39	2007.32	no	radial outward
B1	0.08±0.08	4±4	4	13	4	−−	7.9±0.1	2005.39	2007.32	no	radial inward
B2	0.04±0.03	2±2	2	26	2	−−	6.2±0.1	2005.39	2007.32	no	radial inward
B3	0.14±0.07	7±4	7	8	7	1970±20	5.0±0.2	2005.39	2007.32	no	radial outward
D1	0.8±0.1	43±7	43	1	43	−−	2.4±0.5	2005.39	2007.32	no	non-radial outward
D2	0.30±0.02	16±1	16	4	16	2002.3±0.2	1.2±0.2	2005.39	2007.32	no	radial outward

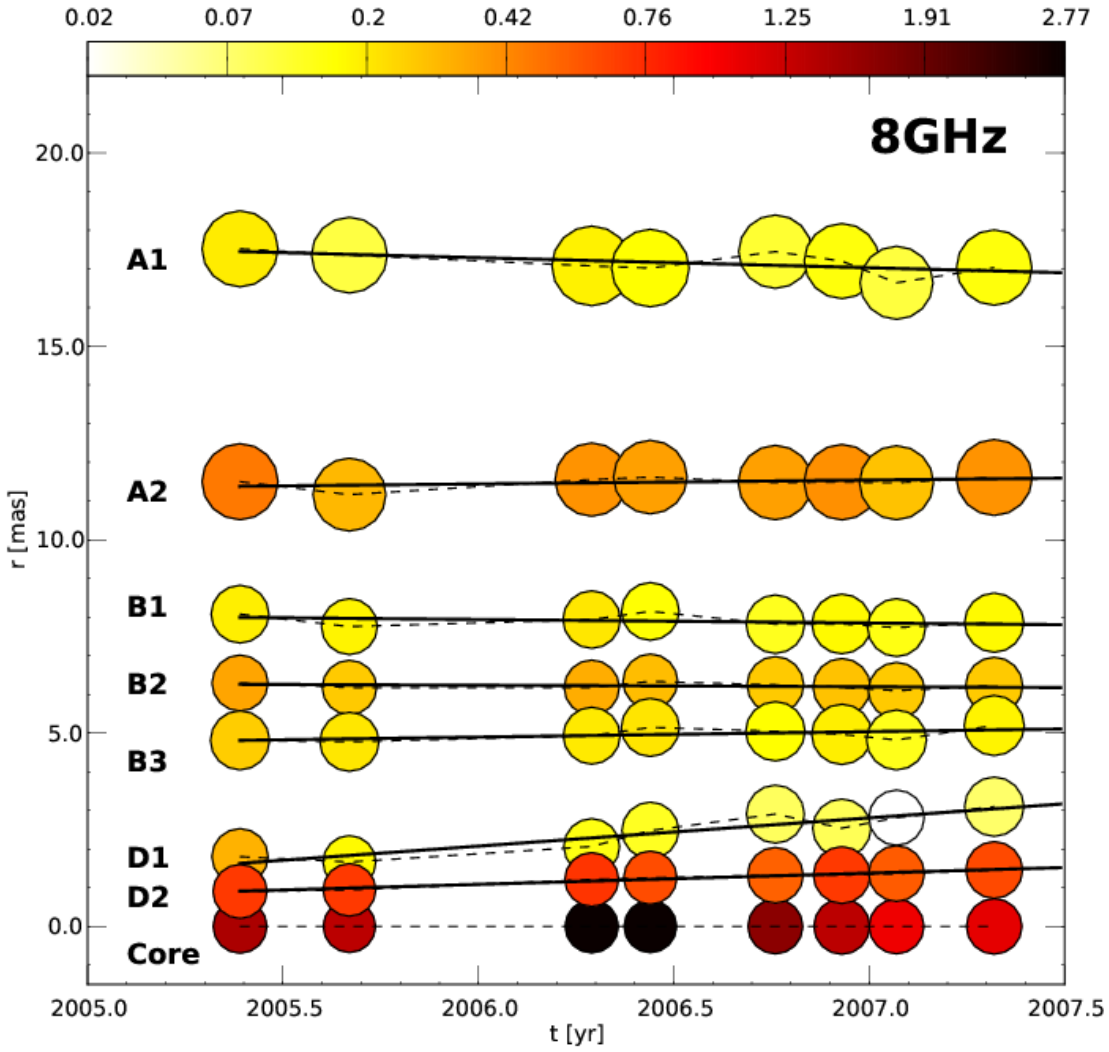

Figure A.5: Temporal evolution of the separation from the core for the 8 GHz modeled features. The color scale corresponds to the flux density and the size of the circles to the relative size (FWHM) of the components. The solid black lines correspond to a linear fit of the component trajectory.

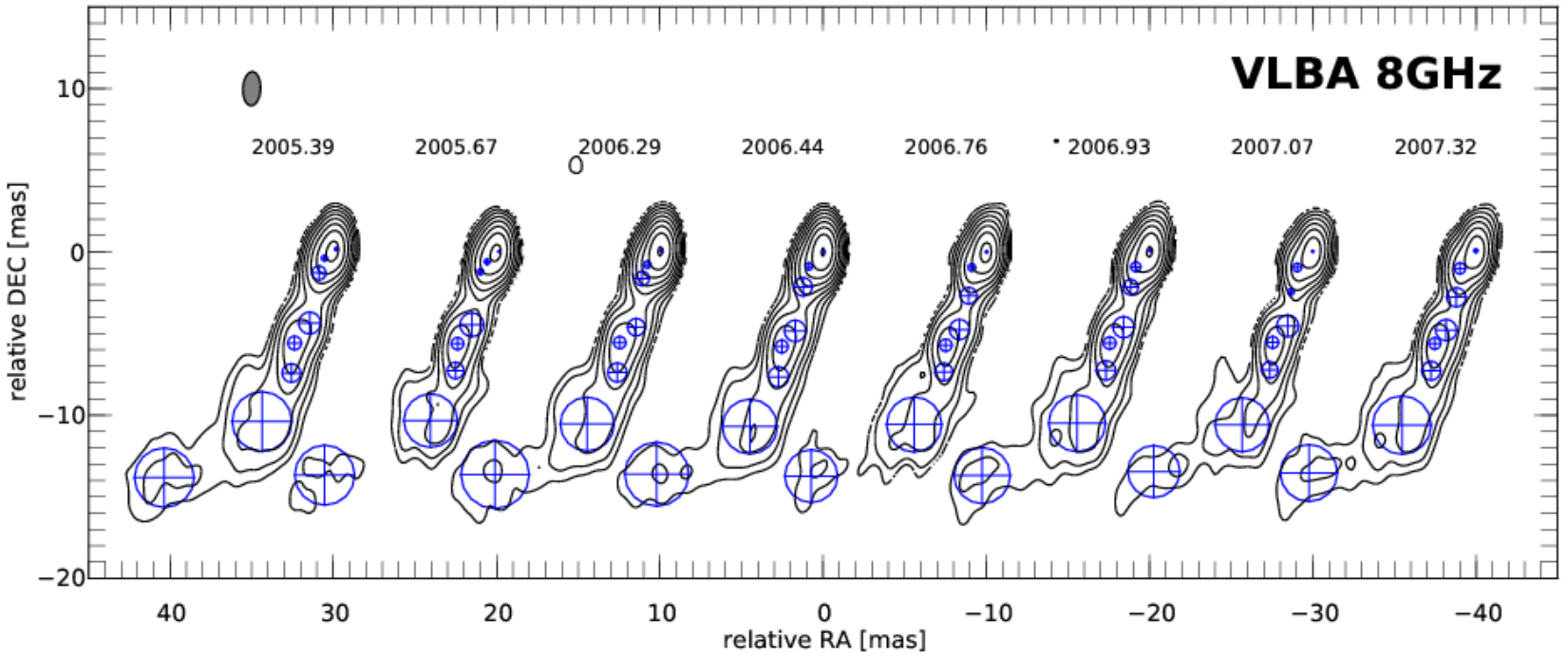

Figure A.6: 8 GHz uniform weighted VLBA images of CTA 102 with fitted circular Gaussian components. For the better comparison all maps are convolved with a common beam of 2.1 × 1.1 mas at P.A. −2.6 and the epoch of the observations is indicated above each contour map. The lowest contour levels is plotted 10× of the maximum off-source rms and increases in steps of 2.

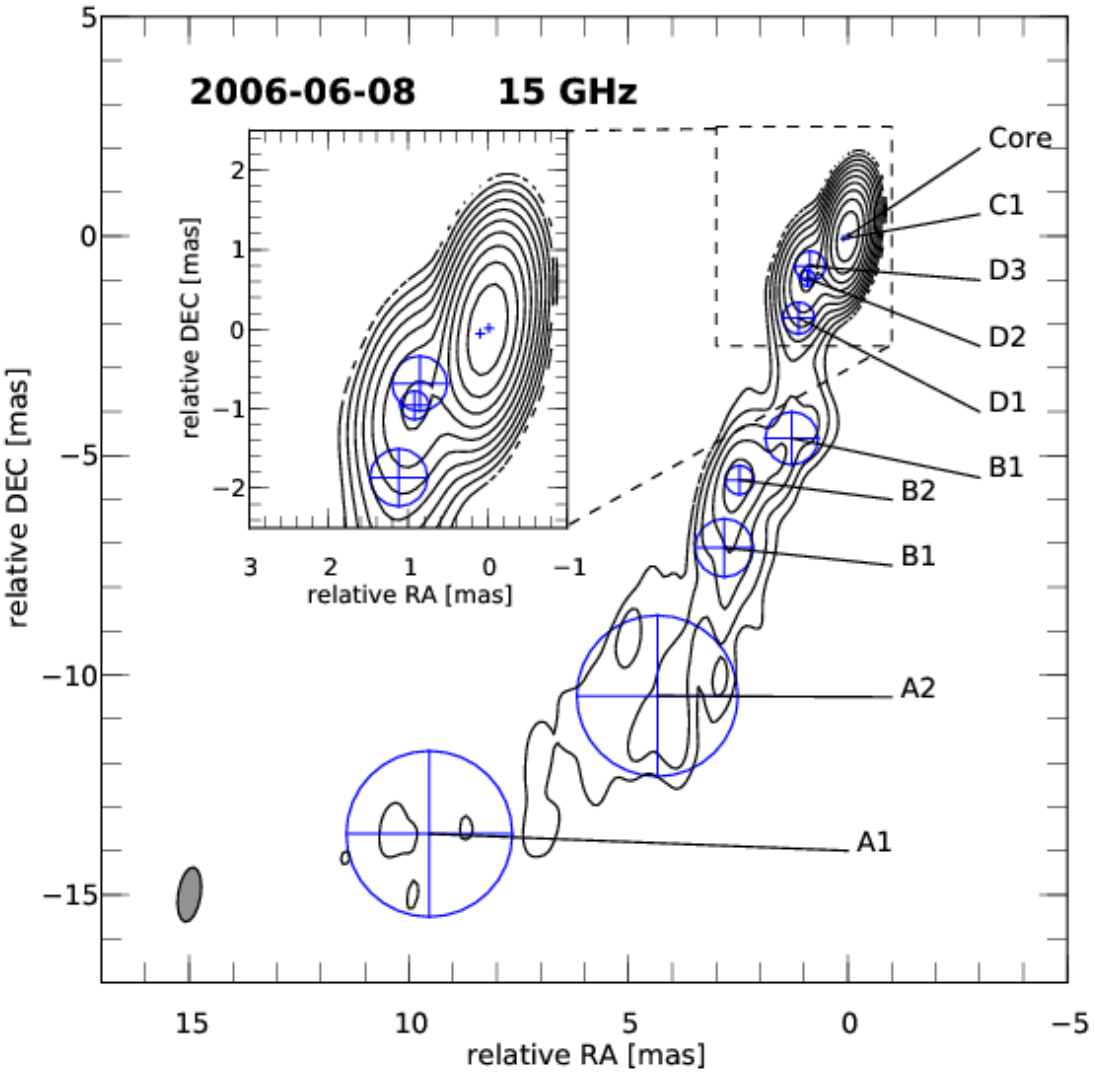

Figure A.7: 15 GHz uniformly weighted VLBA CLEAN image of CTA 102 observed on 8th of June 2006 with overlaid fitted circular Gaussian components. The map peak flux density was 4.13 Jy/beam, where the convolving beam was 1.3×0.5 mas at P.A. -6.2. he lowest contour is plotted at 10× the off-source rms and increases in steps of 2.

Table A.3: Results of the kinematic analysis for the fitted components at 15 GHz

Comp	μ [mas/yr]	β_{app} [c]	δ_{min} [1]	ϑ_{max} [°]	Γ_{min} [1]	t_{ej} [yr]	$< r >$ [mas]	t_{min} [yr]	t_{max} [yr]	acceleration	classification
A1	0.20±0.03	9±2	9	6	9	−−	17.0±0.5	1996.8	2010.8	no	no-radial inward
A2	0.20±0.01	9±1	9	7	9	1945±6	11.2±0.2	1996.8	2010.8	no	radial outward
B1	0.02±0.01	1.0±0.5	1	–	–	−−	7.6±0.3	1995.6	2010.8	yes	no-radial outward
B2	0.01±0.01	0.6±0.5	1	–	–	−−	6.2±0.1	1996.8	2010.8	no	radial inward
B3	0.03±0.01	1.4±0.3	2	–	–	−−	5.1±0.2	1995.9	2010.8	no	non-radial outward
D1	0.10±0.02	6±2	6	10	6	−−	2.1±0.4	1995.9	2007.6	no	non-radial outward
D2	0.20±0.01	8±1	8	7	7	1997.1±0.4	1.6±0.4	2000.0	2011.0	yes	radial outward
D3	0.37±0.02	20±1	20	3	20	−−	1.1±0.4	2004.3	2007.6	no	non-radial outward

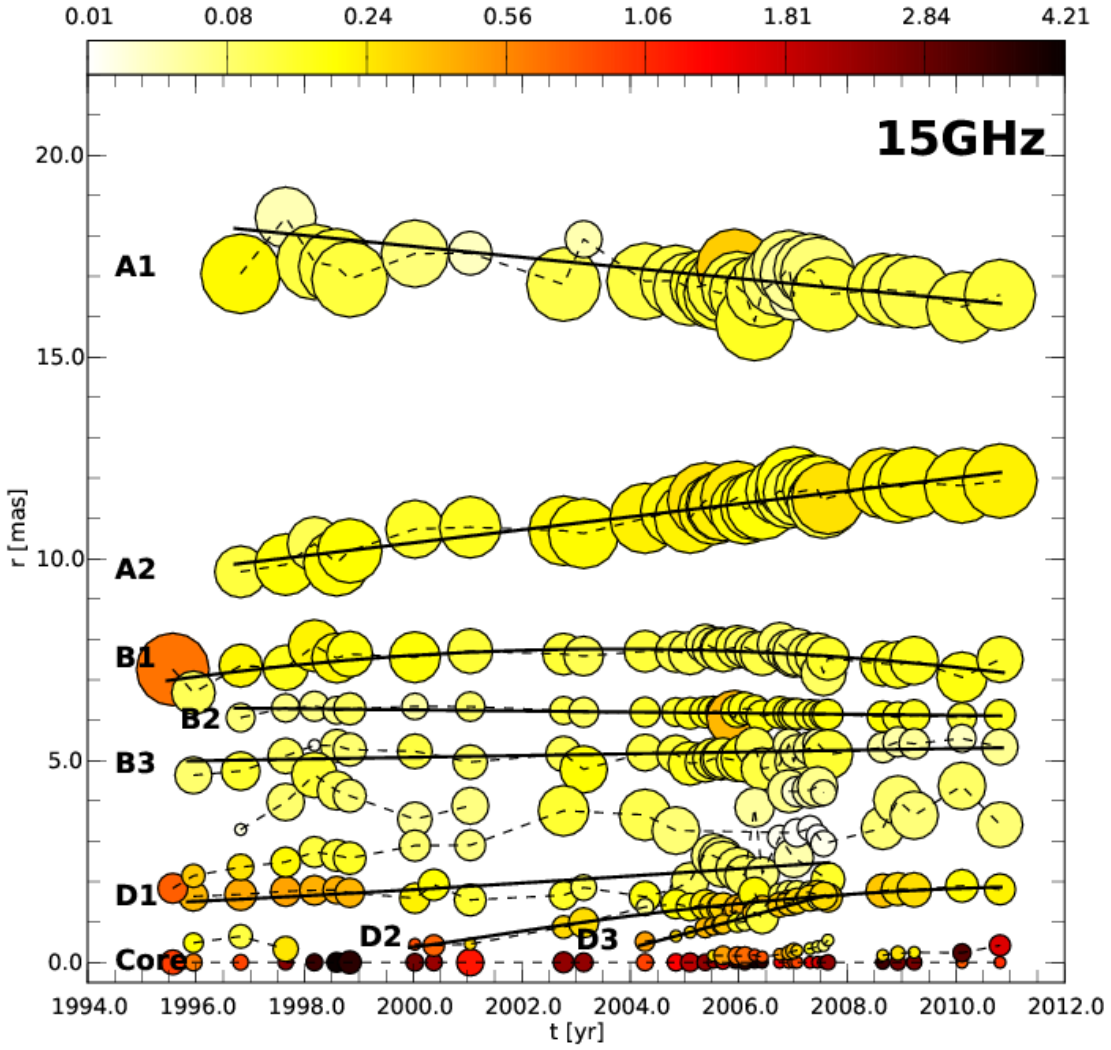

Figure A.8: Temporal evolution of the separation from the core for the 15 GHz components from Lister et al. (2009a) and combined with our 15 GHz data. The color scale corresponds to the flux density and the size of the circles to the relative size (FWHM) of the components. The solid black lines correspond to a polynomial fit of the component trajectory.

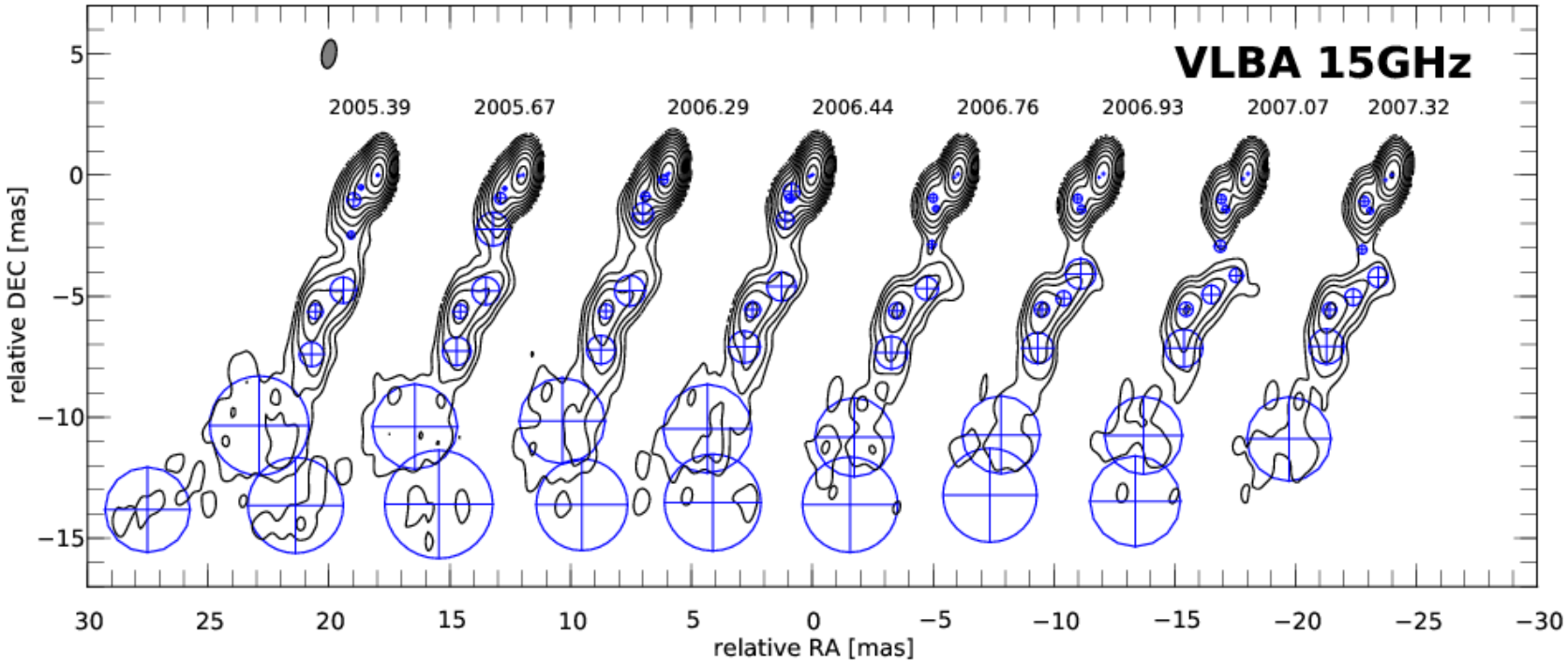

Figure A.9: 15 GHz uniform weighted VLBA images of CTA 102 with fitted circular Gaussian components from our multi-frequency VLBI observations. For the better comparison all maps are convolved with a common beam of 1.2×0.6 mas at P.A. -9.9 and the epoch of the observations is indicated above each contour map. The lowest contour levels is plotted $10\times$ of the maximum off-source rms and increases in steps of 2.Notice that the outermost component (A1) for each epoch is plotted almost overlapping with the jet of the earlier epoch (to its left) in this representation.

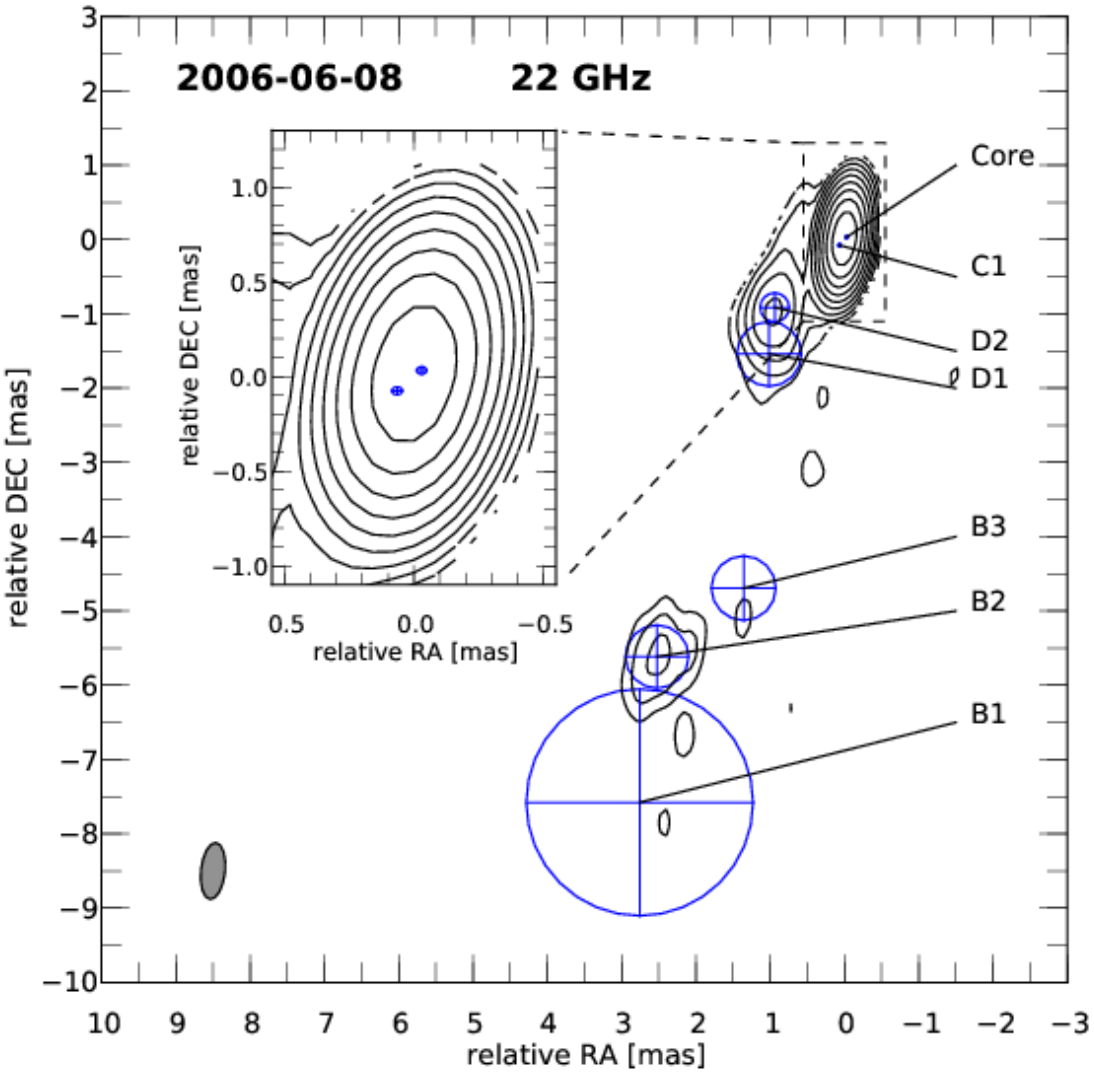

Figure A.10: 22 GHz uniformly weighted VLBA CLEAN image of CTA 102 with overlaid fitted circular Gaussian components observed 8th of June 2006. The map peak flux density was 3.8 Jy/beam, where the convolving beam was 0.76×0.33 mas at P.A. -6.2. he lowest contour is plotted at $10\times$ the off-source rms and increases in steps of 2.

Table A.4: Results of the kinematic analysis for the fitted components at 22 GHz

Comp	μ [mas/yr]	β_{app} [c]	δ_{min} [1]	ϑ_{max} [°]	Γ_{min} [1]	t_{ej} [yr]	$< r >$ [mas]	t_{min} [yr]	t_{max} [yr]	acceleration	classification
B1	0.06±0.11	3±6	–	–	–	−−	8.1±0.2	2005.39	2007.32	no	non-radial outward
B2	0.03±0.02	2±1	2	32	2	−−	6.2±0.1	2005.39	2007.32	no	radial inward
B3	0.1±0.1	7±7	7	8	7	−−	4.9±0.2	2005.39	2007.32	no	non-radial outward
D1	0.6±0.1	31±6	31	2,	31	−−	1.9±0.2	2005.39	2006.76	no	non-radial outward
D2	0.30±0.03	17±2	17	3	17	−−	1.4±0.2	2005.39	2007.32	no	non-radial outward
C1	0.10±0.03	5	5	12	5	2004.4±0.5	0.2±0.1	2005.39	2007.32	no	radial outward

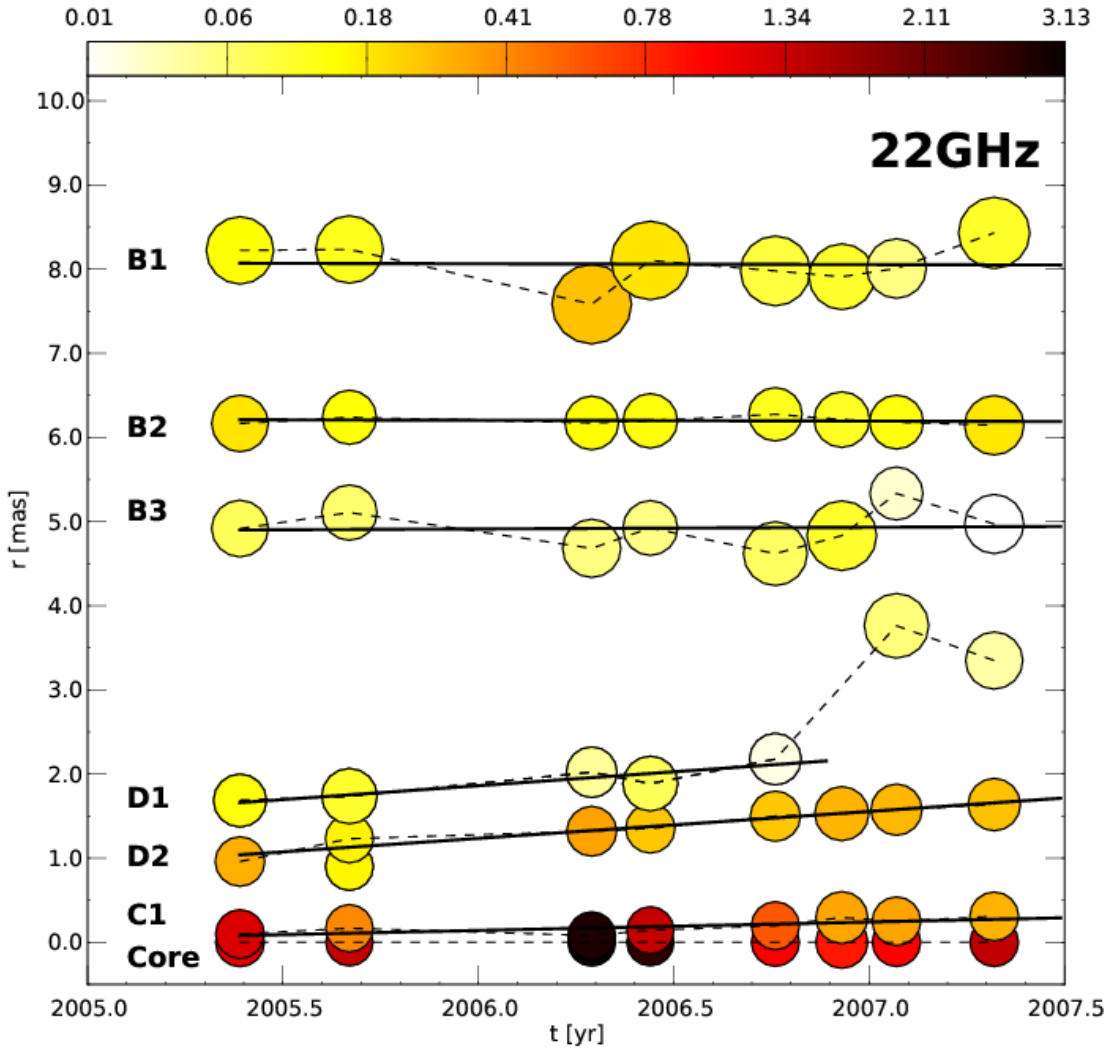

Figure A.11: Temporal evolution of the separation from the core for the 22 GHz components. The color scale corresponds to the flux density and the size of the circles to the relative size (FWHM) of the components. The solid black lines correspond to a linear fit of the component trajectory.

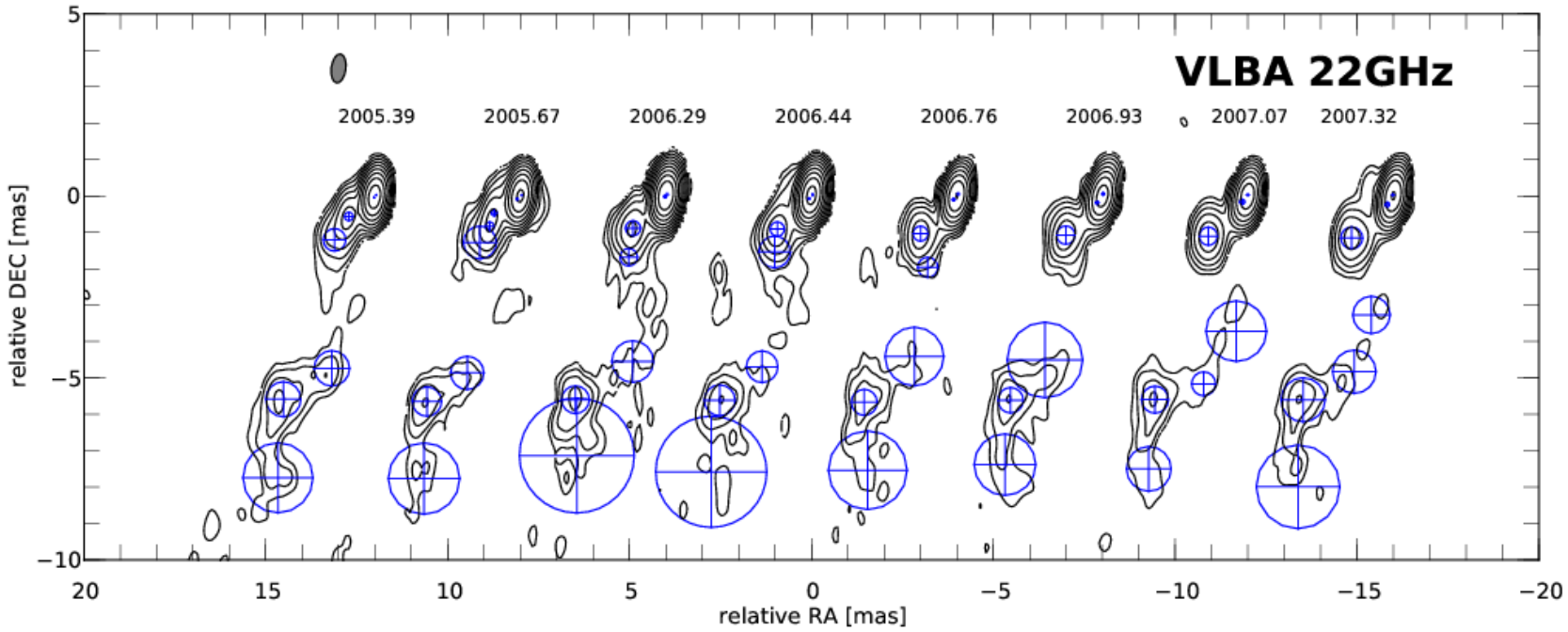

Figure A.12: 22 GHz uniform weighted VLBA images of CTA 102 with fitted circular Gaussian components. For the better comparison all maps are convolved with a common beam of 0.8×0.4 mas at P.A. -7.6 and the epoch of the observations is indicated above each contour map. The lowest contour levels is plotted $10\times$ of the maximum off-source rms and increases in steps of 2.

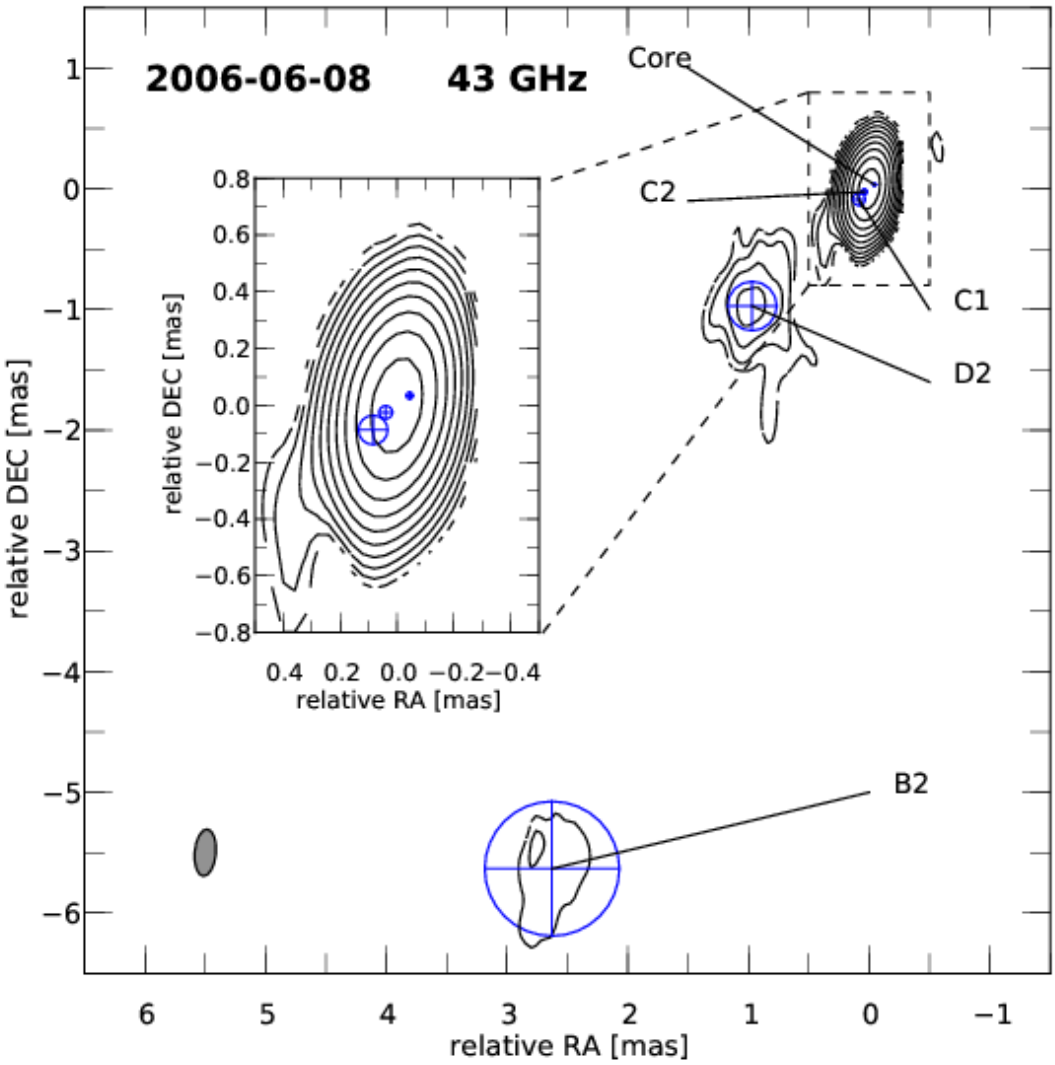

Figure A.13: 43 GHz uniformly weighted VLBA image of CTA 102 with overlaid fitted circular Gaussian components observed 8th of June 2006. The map peak flux density was 3.61 Jy/beam, where the convolving beam was 0.39×0.19 mas at P.A. -5.0. The lowest contour is plotted at $5\times$ the off-source rms and increases in steps of 2.

Table A.5: Results of the kinematic analysis for the fitted components at 43 GHz

Comp	μ [mas/yr]	β_{app} [c]	δ_{min} [1]	ϑ_{max} [°]	Γ_{min} [1]	t_{ej} [yr]	$< r >$ [mas]	t_{min} [yr]	t_{max} [yr]	acceleration	classification
C1	0.20±0.10	12±3	12	5	12	2005.1±0.2	0.2±0.1	2005.4	2006.8	no	radial outward
C2	0.25±0.04	13±2	13	4	13	2005.9±0.2	0.4±0.2	2006.3	2008.0	no	radial outward
C3	0.07±0.01	4±1	4	15	4	−−	0.2±0.1	2007.5	2009.7	yes	radial/non-radial outward
C4	0.17±0.01	9±1	9	6	9	−−	0.2±0.1	2008.2	2011.0	yes	non-radial outward

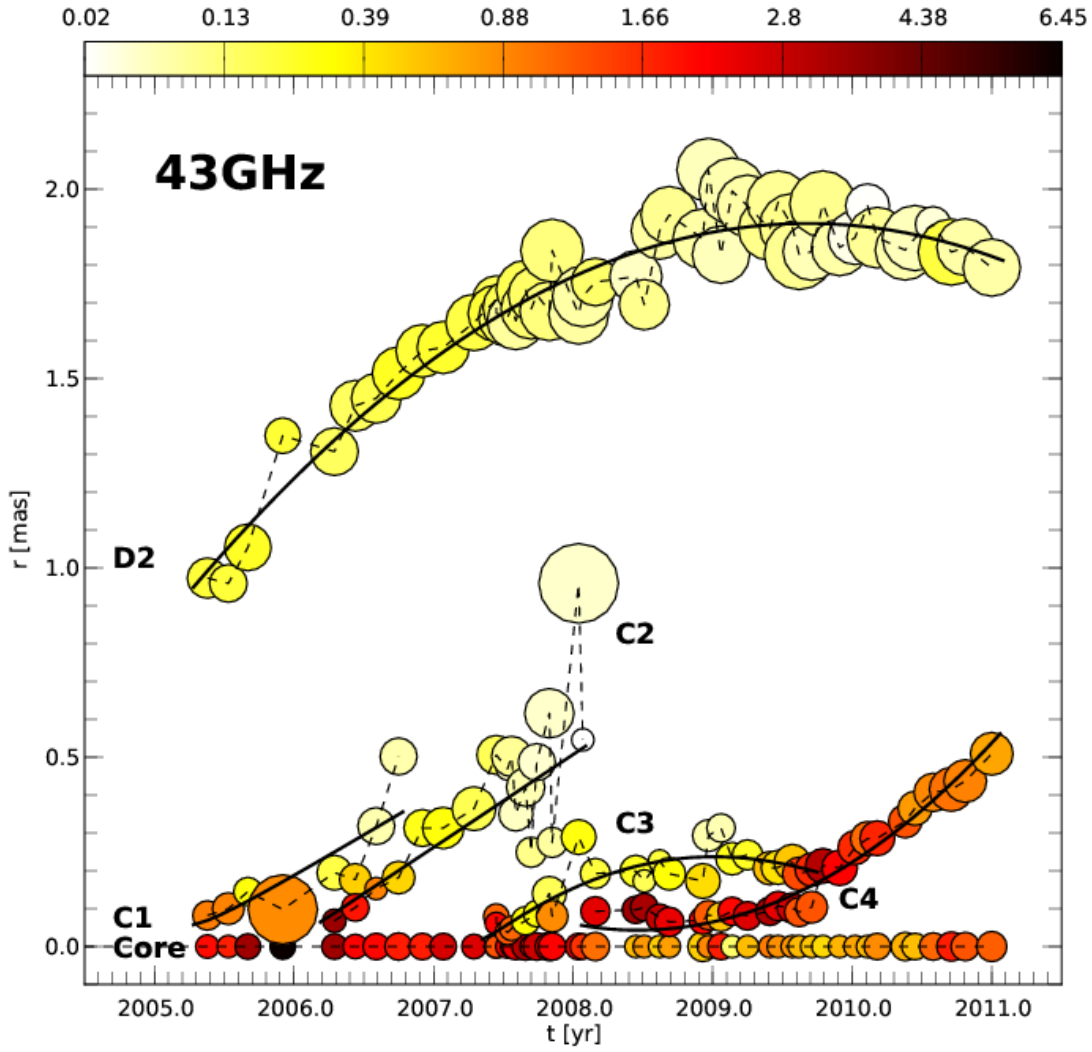

Figure A.14: Temporal evolution of the separation from the core for the 43 GHz components. The color scale corresponds to the flux density and the size of the circles to the relative size (FWHM) of the components. The solid black lines correspond to a polynomial fit of the component trajectory.

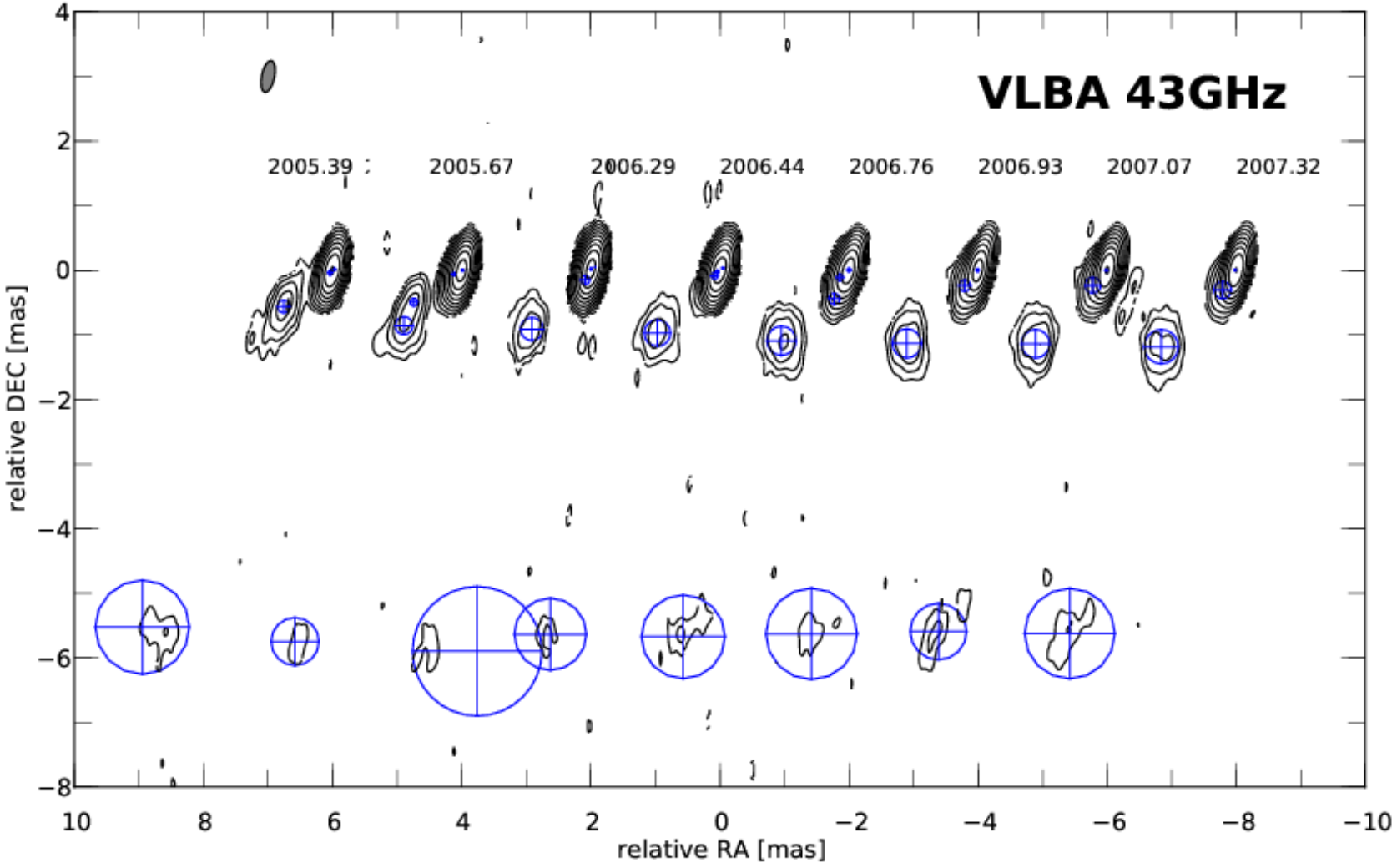

Figure A.15: 43 GHz uniform weighted VLBA images of CTA 102 with fitted circular Gaussian components from our multi-frequency VLBI observations. For the better comparison all maps are convolved with a common beam of 0.5×0.2 mas at P.A. -11.9 and the epoch of the observations is indicated above each contour map. The lowest contour levels is plotted $10\times$ of the maximum off-source rms and increases in steps of 2.

Table A.6: Fitted components for multi-frequency VLBI observations

2005-05-19					2005-09-01					2006-04-14					2006-06-08				
ID	S [Jy]	R [mas]	ϑ °	FWHM [mas]	ID	S [Jy]	R [mas]	ϑ °	FWHM [mas]	ID	S [Jy]	R [mas]	ϑ °	FWHM [mas]	ID	S [Jy]	R [mas]	ϑ °	FWHM [mas]
ν = 5 GHz																			
core	0.98	0.00	0.00	0.45	core	1.12	0.00	0.00	0.33	core	1.45	0.00	0.00	0.07	core	1.62	0.00	0.00	0.14
D2	0.92	1.14	−50.18	0.48	D2	1.02	1.19	−49.08	0.38	D2	1.04	1.29	−47.82	0.49	D2	0.94	1.34	−48.87	0.46
B3	0.30	4.21	−72.20	1.22	B3	0.23	4.19	−72.57	0.98	B3	0.29	4.53	−70.87	1.30	B3	0.21	4.43	−72.62	1.03
B2	0.58	6.11	−67.85	1.03	B2	0.58	6.09	−67.39	1.03	B2	0.59	6.45	−67.22	0.95	B2	0.54	6.16	−66.83	0.98
B1	0.25	8.16	−71.13	1.00	B1	0.23	8.12	−70.67	0.88	B1	0.18	8.90	−71.08	1.08	B1	0.23	8.20	−70.34	1.01
A2	0.67	11.34	−67.56	3.41	A2	0.64	11.43	−67.38	3.35	A2	0.61	11.65	−66.53	3.41	A2	0.61	11.56	−66.88	3.42
A1	0.35	16.86	−54.49	4.14	A1	0.28	16.93	−54.24	3.59	A1	0.28	16.96	−54.24	3.94	A1	0.26	16.79	−54.31	3.75
ν = 8 GHz																			
core	1.44	0.00	0.00	0.18	core	1.33	0.00	0.00	0.08	core	2.76	0.00	0.00	0.13	core	2.77	0.00	0.00	0.14
D2	0.69	0.90	−37.79	0.34	D2	0.70	0.94	−41.33	0.34	D2	0.72	1.21	−45.04	0.44	D2	0.63	1.26	−45.33	0.44
D1	0.31	1.80	−54.26	0.87	D1	0.18	1.67	−47.67	0.38	D1	0.15	2.06	−55.53	0.89	D1	0.13	2.48	−59.85	1.13
B3	0.26	4.81	−70.38	1.35	B3	0.21	4.77	−69.82	1.46	B3	0.20	4.93	−71.93	1.08	B3	0.21	5.14	−70.42	1.32
B2	0.35	6.29	−66.17	0.84	B2	0.26	6.18	−65.87	0.75	B2	0.33	6.17	−65.74	0.75	B2	0.29	6.33	−66.27	0.79
B1	0.19	8.07	−70.21	1.14	B1	0.18	7.75	−70.06	1.02	B1	0.20	7.93	−70.17	1.17	B1	0.16	8.14	−70.26	1.26
A2	0.47	11.50	−66.76	3.67	A2	0.30	11.16	−68.04	3.29	A2	0.40	11.55	−66.91	3.30	A2	0.36	11.62	−67.20	3.37
A1	0.20	17.52	−53.09	3.65	A1	0.11	17.36	−52.10	3.68	A1	0.19	17.08	−53.42	4.19	A1	0.17	17.02	−53.17	3.93
ν = 15 GHz																			
core	2.35	0.00	0.00	0.10	core	1.77	0.00	0.00	0.00	core	4.07	0.00	0.00	0.00	core	3.62	0.00	0.00	0.00
C1	–	–	–	–	C1	0.23	0.17	−9.95	0.00	C1	0.91	0.18	−38.88	0.00	C1	0.82	0.13	−31.94	0.00
D3	0.39	0.86	−35.85	0.20	D3	0.34	0.93	−36.36	0.15	D3	0.20	1.71	−53.60	0.66	D3	0.13	1.12	−38.58	0.70
D2	0.24	1.43	−45.52	0.57	D2	0.30	1.34	−45.86	0.48	D2	0.36	1.24	−42.07	0.34	D2	0.34	1.35	−45.97	0.36
D1	0.04	2.71	−65.94	0.31	D1	0.08	2.55	−61.06	1.39	D1	0.05	3.84	−75.49	1.04	D1	0.07	2.19	−58.83	0.73
B3	0.14	4.96	−73.25	1.09	B3	0.15	5.03	−72.20	1.16	B3	0.11	5.34	−71.22	1.01	B3	0.12	4.79	−74.38	1.21
B2	0.18	6.19	−65.40	0.62	B2	0.19	6.21	−65.31	0.59	B2	0.18	6.25	−65.27	0.58	B2	0.18	6.10	−65.98	0.66
B1	0.10	7.89	−69.68	1.02	B1	0.11	7.77	−69.37	1.19	B1	0.11	7.71	−69.12	1.11	B1	0.12	7.65	−68.30	1.33
A2	0.26	11.45	−64.62	4.10	A2	0.22	11.31	−66.72	3.53	A2	0.23	11.32	−66.79	3.39	A2	0.19	11.36	−67.45	3.67
A1	0.15	16.79	−55.41	3.52	A1	0.15	16.57	−55.40	3.96	A1	0.15	15.87	−55.25	4.38	A1	0.14	16.64	−54.99	3.78
ν = 22 GHz																			
core	1.16	0.00	0.00	0.01	core	1.37	0.00	0.00	0.01	core	3.13	0.00	0.00	0.01	core	2.72	0.00	0.00	0.04
–	–	–	–	–	–	0.16	0.90	−32.83	0.16	–	–	–	–	–	–	–	–	–	–
C1	1.22	0.10	−48.10	0.01	C1	0.42	0.17	−40.03	0.05	C1	2.86	0.08	−41.50	0.07	C1	1.38	0.14	−48.53	0.04
D2	0.30	0.96	−38.01	0.23	D1	0.10	1.74	−48.44	0.91	D2	0.34	1.32	−44.48	0.41	D1	0.07	1.89	−56.45	0.87
D1	0.13	1.69	−47.03	0.62	D2	0.16	1.23	−44.15	0.24	D1	0.04	2.02	−58.35	0.48	D2	0.25	1.35	−44.31	0.39
B3	0.07	4.92	−75.59	0.97	B3	0.06	5.11	−72.90	0.91	B3	0.05	4.68	−78.27	1.15	B3	0.04	4.92	−73.65	0.87
B2	0.19	6.17	−65.50	0.97	B2	0.14	6.24	−65.27	0.81	B2	0.14	6.17	−65.86	0.76	B2	0.13	6.20	−65.68	0.85
B1	0.14	8.22	−70.81	1.93	B1	0.11	8.23	−70.93	1.96	B1	0.26	7.58	−70.87	3.16	B1	0.19	8.10	−69.90	3.05
ν = 43 GHz																			
core	1.84	0.00	0.00	0.03	core	3.45	0.00	0.00	0.03	core	3.48	0.00	0.00	0.03	core	2.14	0.00	0.00	0.02
C2	–	–	–	–	C2	–	–	–	–	C2	3.48	0.07	154.45	0.01	C2	1.88	0.10	−35.12	0.05
C1	0.19	0.97	−36.19	0.20	C1	0.29	0.14	−22.02	0.06	C1	0.19	0.20	−61.77	0.14	C1	0.50	0.18	−43.26	0.10
D2	0.93	0.08	−38.94	0.07	D2	0.24	1.05	−39.11	0.33	D2	0.15	1.31	−45.41	0.35	D2	0.15	1.43	−44.77	0.41
B2	0.16	6.29	−61.75	1.46	B2	0.05	6.25	−65.31	0.48	B2	0.07	6.18	−73.39	2.00	B2	0.10	6.26	−64.76	1.12

Table A.7: Fitted components for multi-frequency VLBI observations

2006-10-02					2006-12-04					2007-01-26					2007-04-26				
ID	S [Jy]	R [mas]	ϑ °	FWHM [mas]	ID	S [Jy]	R [mas]	ϑ °	FWHM [mas]	ID	S [Jy]	R [mas]	ϑ °	FWHM [mas]	ID	S [Jy]	R [mas]	ϑ °	FWHM [mas]
ν = 5 GHz																			
core	1.50	0.00	0.00	0.24	core	1.26	0.00	0.00	0.14	core	1.02	0.00	0.00	0.14	core	0.90	0.00	0.00	0.12
D2	0.98	1.36	−49.67	0.59	D2	0.96	1.36	−49.23	0.57	D2	0.80	1.37	−49.75	0.40	D2	0.86	1.43	−49.51	0.59
B3	0.21	4.32	−71.81	1.08	B3	0.26	4.27	−70.51	1.25	B3	0.09	4.42	−74.15	0.16	B3	0.20	4.34	−71.89	1.04
B2	0.60	6.20	−67.09	1.06	B2	0.59	6.34	−67.42	1.03	B2	0.53	6.08	−66.88	0.99	B2	0.55	6.17	−67.06	0.97
B1	0.23	8.32	−70.65	1.12	B1	0.20	8.61	−70.59	1.25	B1	0.14	8.05	−70.38	0.56	B1	0.22	8.25	−70.21	1.19
A2	0.65	11.80	−66.58	3.42	A2	0.61	11.73	−66.53	3.40	A2	0.50	11.59	−67.22	3.17	A2	0.59	11.73	−66.81	3.41
A1	0.29	17.24	−53.77	3.75	A1	0.31	17.06	−54.01	4.17	A1	0.16	16.61	−52.84	2.66	A1	0.29	16.93	−54.07	3.85
ν = 8 GHz																			
core	1.64	0.00	0.00	0.12	core	1.33	0.00	0.00	0.13	core	1.03	0.00	0.00	0.10	core	1.10	0.00	0.00	0.22
D2	0.55	1.32	−46.27	0.46	D2	0.69	1.33	−48.44	0.60	D2	0.56	1.37	−46.55	0.51	D2	0.63	1.46	−48.33	0.68
D1	0.09	2.90	−67.69	1.03	D1	0.09	2.54	−61.80	0.95	D1	0.02	2.81	−61.84	0.39	D1	0.08	3.10	−67.31	1.18
B3	0.17	5.04	−70.73	1.24	B3	0.19	4.97	−70.86	1.30	B3	0.14	4.82	−71.45	1.34	B3	0.18	5.19	−69.53	1.31
B2	0.27	6.24	−66.34	0.76	B2	0.28	6.18	−66.32	0.77	B2	0.26	6.09	−66.29	0.73	B2	0.26	6.22	−66.16	0.71
B1	0.14	7.82	−70.36	1.09	B1	0.18	7.82	−69.69	1.19	B1	0.15	7.73	−70.10	1.01	B1	0.17	7.85	−69.60	1.16
A2	0.36	11.48	−67.25	3.38	A2	0.40	11.49	−67.06	3.49	A2	0.28	11.47	−67.87	3.32	A2	0.39	11.61	−67.06	3.59
A1	0.12	17.45	−51.98	3.24	A1	0.16	17.20	−53.25	3.44	A1	0.11	16.64	−54.20	3.20	A1	0.16	17.04	−53.11	3.50
ν = 15 GHz																			
core	1.53	0.00	0.00	0.00	core	0.92	0.00	0.00	0.00	core	0.89	0.00	0.00	0.00	core	1.47	0.00	0.00	0.00
C1	0.47	0.20	−39.77	0.00	C1	0.41	0.24	−40.72	0.05	C1	0.30	0.29	−46.86	0.00	–	0.15	0.34	−39.12	0.00
D3	0.10	1.69	−57.23	0.25	D3	0.09	1.72	−58.46	0.34	D3	0.09	1.73	−57.88	0.31	D3	0.09	1.73	−58.79	0.27
D2	0.32	1.43	−43.67	0.35	D2	0.32	1.48	−44.16	0.37	D2	0.28	1.52	−43.66	0.38	D2	0.28	1.59	−43.70	0.41
D1	0.02	3.10	−69.54	0.33	A13	0.06	4.24	−77.13	1.26	D1	0.01	3.21	−69.00	0.49	D1	0.01	3.32	−68.39	0.37
D0	–	–	–	–	D0	–	–	–	–	D0	0.03	4.23	−83.43	0.58	D0	0.04	4.27	−82.33	0.84
B3	0.10	4.89	−74.66	0.95	B3	0.06	5.40	−72.27	0.63	B3	0.07	5.22	−73.09	0.77	B3	0.07	5.30	−72.40	0.70
B2	0.18	6.19	−65.74	0.66	B2	0.16	6.16	−65.58	0.62	B2	0.15	6.16	−65.38	0.59	B2	0.16	6.13	−65.20	0.58
B1	0.09	7.87	−69.50	1.36	B1	0.10	7.70	−69.33	1.29	B1	0.09	7.68	−69.79	1.57	B1	0.11	7.59	−69.15	1.47
A2	0.16	11.68	−68.43	3.26	A2	0.15	11.59	−68.56	3.23	A2	0.14	11.65	−68.18	3.22	A2	0.16	11.71	−68.65	3.48
A1	0.09	16.94	−53.17	4.00	A1	0.08	17.22	−52.51	3.94	A1	0.05	17.04	−51.19	3.88	A1	0.07	17.16	−51.76	3.75
ν = 22 GHz																			
core	1.04	0.00	0.00	0.00	core	0.88	0.00	0.00	0.07	core	1.02	0.00	0.00	0.00	core	1.40	0.00	0.00	0.00
C1	0.59	0.20	−50.59	0.07	C1	0.33	0.29	−55.68	0.09	C1	0.34	0.25	−50.84	0.14	C1	0.29	0.31	−59.64	0.13
D2	0.24	1.50	−46.43	0.41	D2	0.29	1.53	−47.75	0.51	D2	0.28	1.58	−46.27	0.50	D2	0.26	1.64	−46.29	0.60
D1	0.01	2.18	−67.46	0.55	D1	–	–	–	–	D1	0.05	3.76	−85.10	1.67	D1	0.03	3.35	−79.88	1.02
B3	0.06	4.62	−74.93	1.61	B3	0.10	4.83	−70.66	2.08	B3	0.02	5.33	−76.78	0.66	B3	0.01	4.97	−77.68	1.19
B2	0.11	6.28	−65.71	0.71	B2	0.11	6.21	−65.83	0.70	B2	0.13	6.18	−65.58	0.74	B2	0.18	6.14	−66.33	1.21
B1	0.09	7.98	−71.86	2.16	B1	0.10	7.91	−70.04	1.69	B1	0.05	8.01	−70.10	1.23	B1	0.10	8.43	−72.00	2.30
ν = 43 GHz																			
core	1.83	0.00	0.00	0.05	core	1.77	0.00	0.00	0.04	core	2.64	0.00	0.00	0.04	core	2.54	0.00	0.00	0.02
C2	0.48	0.18	−39.01	0.11	C2	0.30	0.31	−50.25	0.18	C2	0.29	0.31	−47.75	0.24	C2	0.18	0.36	−57.45	0.27
C1	0.07	0.50	−62.96	0.17	C1	–	–	–	–	C1	–	–	–	–	C1	–	–	–	–
D2	0.25	1.51	−46.27	0.45	D2	0.20	1.57	−46.01	0.45	D2	0.23	1.58	−46.00	0.44	D2	0.18	1.65	−45.94	0.53
B2	0.15	6.23	−65.64	1.29	B2	0.14	6.19	−65.43	1.41	B2	0.13	6.17	−65.05	0.87	B2	0.16	6.18	−65.49	1.40

B The influence of the uv-range on the spectral parameters

We performed several tests to investigate the influence of the non-identical uv-range on the spectral indices derived from images at several different wavelengths and therefore with different projected baselines in wavelength units. For extracting the spectral parameters we use both, a power law fit $S_\nu \propto \nu^{+\alpha}$ and the approximation of the synchrotron-self-absorped spectrum (see Eq. 2.27). The image parameters, i.e., convolving beam size and pixel size, used for the analysis are presented in Table. B.1.

Table B.1: Summary of image parameters used for the spectral analysis

region	r [mas]	ν [GHz]	beam [mas]	ps [mas]	uv-range Mλ
C	0–1	15–43	0.95×0.33,−13°	0.03	27–450
C[a]	0–1	8–86	0.95×0.33,−13°	0.03	66–250
D[b]	1–4	5–22	1.33×0.52,−9°	0.04	14–144
B	4–8	5–15	2.32×0.97,−7°	0.10	9–144
A2	8–14	5–15	3.65×1.52,−8°	0.15	9–144
A1[c]	14–20	5–8	3.65×1.52,−8°	0.15	9–144
B+A[d]	4–20	5–43	3.65×1.52,−8°	0.10	27–144

[a] used to extract turnover values for 2005.39
[b] used to extract turnover values
[c] no fitting, spectral index computed between two frequencies
[d] test of influence of frequency range on α

In Fig. B.1 we show the 2D distribution of the spectral index, α, for region C using a frequency range from 15 GHz to 43 GHz. The left panel shows the distribution for a non-identical uv-range and the middle panel the distribution for a limited uv-range, here from 27 Mλ to 450 Mλ. The difference in α between the two maps shows that the central region is only marginally affected by the used uv-range ($\Delta(\alpha) < 10^{-3}$) and the differences increase with distance from the center. The largest discrepancy is found at the edges of the distribution where $\Delta(\alpha) > 0.1$.

For the May 2005 observations of CTA 102 we could derive the spectral turnover, i.e, ν_m and S_m, using a frequency range from 8 GHz to 86 GHz The uv-range is set at (66 – 250) Mλ and the difference in the spectral values as compared to the unlimited uv-

range is shown in Fig. B.2 -B.4. The large frequency range and the short uv-range lead to strong variation of the spectral parameters at the edges of the distribution upto 70% for α, 60% for ν_m and 30% for S_m. Despite these large discrepancies at the edges, the values along the jet axis show variations up to 10%.

As mentioned in Sect. 5.4.2 for region D, the turnover frequency lies within our frequency range and we can derive the turnover frequency, ν_m, the turnover flux density, S_m and the optically thin spectral index, α_0. For the analysis we used a beam size of (1.33×0.52) mas at a P.A. of $-9°$ and a frequency range from 5 GHz to 22 GHz. We limited the uv-range to 14 Mλ to 144 Mλ and compared the results of the spectral analysis to the outcome of the un-limited uv-range (see Fig. B.5 -B.7). In general there is the trend that the discrepancies between the two methods are largest at the edges of the distribution. However, in contrast to the distribution of α there are also regions in the center of the distribution which show large differences.

The difference between turnover flux density derived by using limited and full uv-range are at most 10% and a similar value is obtained for the optically thin spectral index. For the turnover flux density, the differences are much larger and can reach at the edges of the distribution 50%. Furthermore, the limiting the uv-range affects less the distribution of the turnover flux density and more the turnover frequency and optically thin spectral index.

For region B (4 mas $< r <$ 8 mas) we use a frequency range form 5 GHz to 15 GHz and the different in the uv-ranges lead only to small variations in the spectral index. As for region C, the largest differences in α can be found at the edges of the distribution. It is worth to mention, that even those differences are less than 10% (see Fig. B.8).

Besides the influence of the uv-range, we tested the impact of the frequency range on the spectral parameters obtained. Therefore, we enlarged for region B and region A the frequency range from 5 GHz to 43 GHz and the result for the spectral index is presented in Fig. B.9. The difference in α increased by a factor of 3 as compared to values calculated using a frequency range from 5 GHz to 15 GHz (see Fig. B.8) and regions of increased residuals extend into the central distribution of α.

The results of these test can be summarized as follows:
i) if the frequency range is not larger than a factor 4, the difference in the uv-radii influences mainly the edges of the distribution.
ii) for the calculation of the turnover values the uv-range affects the overall distribution of the spectral parameters. Therefore, the uv-range should be in general limited to the short uv-radii of the largest frequency and long uv-radii of the smallest frequency involved in the spectral analysis.

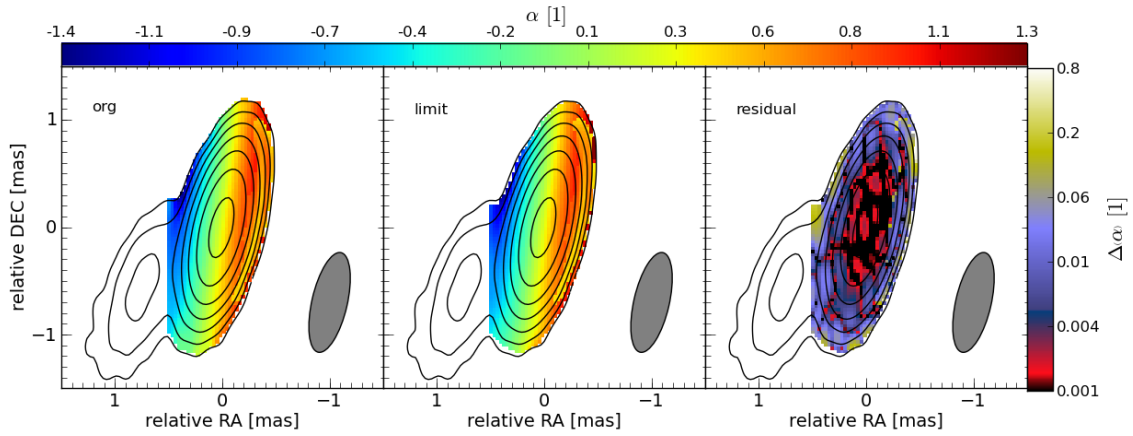

Figure B.1: Influence of the uv-range on the 2D distribution of the spectral index, α ($S_\nu \propto \nu^\alpha$) for region C ($r < 1$ mas) using a beam size of 0.95×0.33 mas with a P.A. of $-13°$ and a pixel size of 0.03 mas. The left panel shows the spectral index for a un-limited uv-range, the middle panel for limited uv-range and the right panel the residuals between them. The contours correspond to the 43 GHz VLBI observations, where the lowest contour is plotted at 10× the rms value and further contours increase by factors of 2.

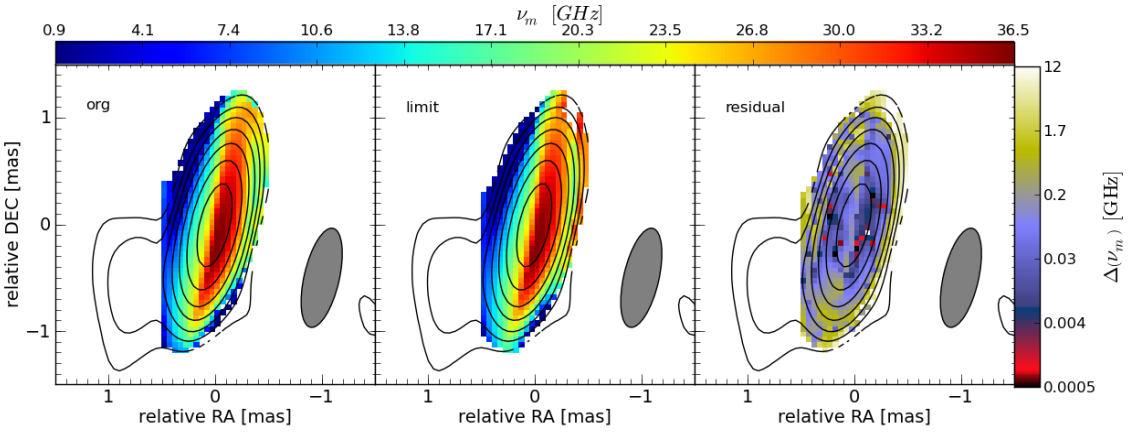

Figure B.2: Influence of the uv-range on the 2D distribution of the turnover frequency, ν_m for region C ($r < 1$ mas) using a beam size of 0.95×0.33 mas with a P.A. of $-13°$ and a pixel size of 0.03 mas. The left panel shows the turnover frequency for a un-limited uv-range, the middle panel for limited uv-range and the right panel the residuals between them. The contours correspond to the 86 GHz VLBI observations, where the lowest contour is plotted at 10× the rms value and further contours increase by factors of 2.

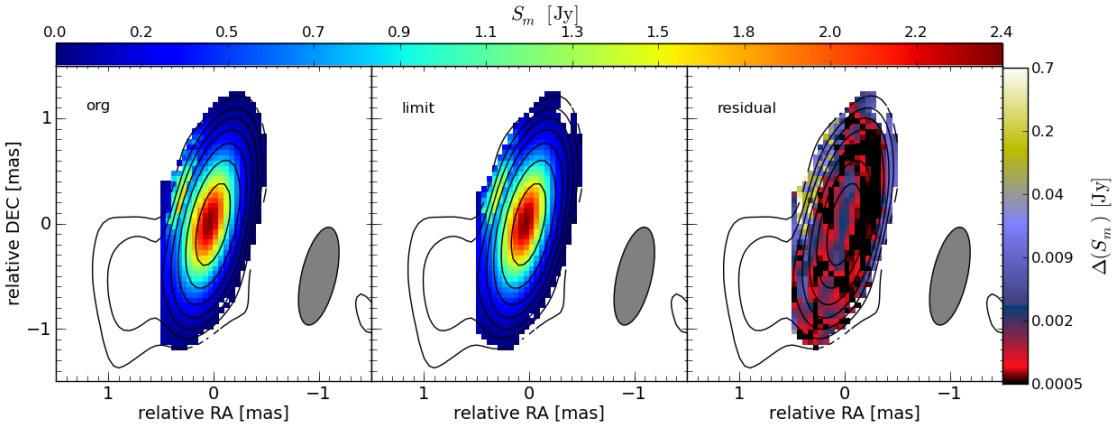

Figure B.3: Same as Fig. B.2 for the turnover flux density, S_m.

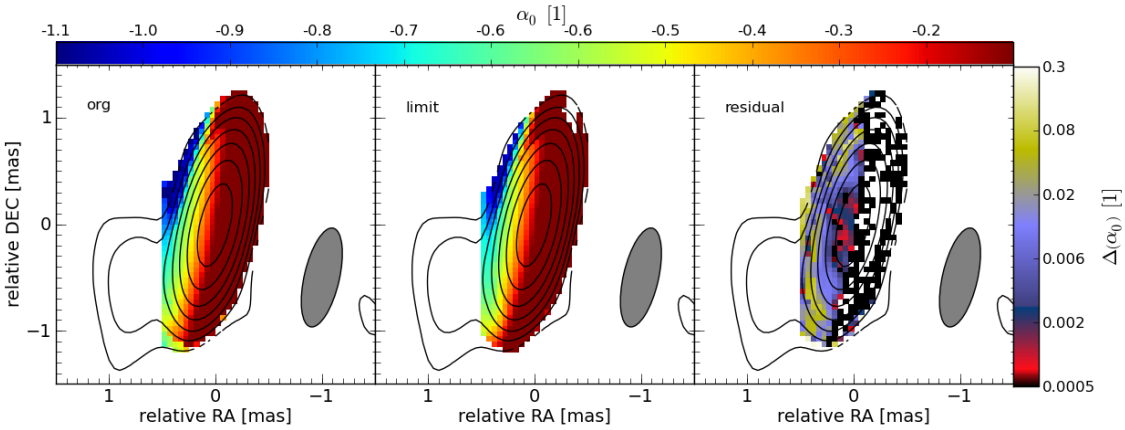

Figure B.4: Same as Fig. B.2 for the optically thin spectral index, α_0

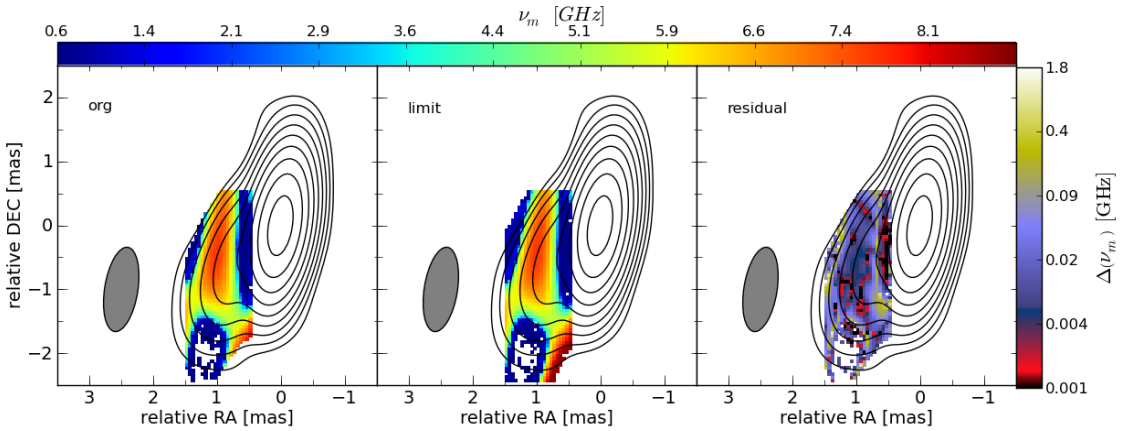

Figure B.5: Influence of the uv-range on the 2D distribution of the turnover frequency, ν_m for region D (1 mas $< r <$ 4 mas) using a beam size of 1.33×0.52 mas with a P.A. of $-7°$ and a pixel size of 0.04 mas. The left panel shows the turnover frequency for a unlimited uv-range, the middle panel for limited uv-range and the right panel the residuals between them. The contours correspond to the 43 GHz VLBI observations, where the lowest contour is plotted at 10× the rms value and further contours increase by factors of 2.

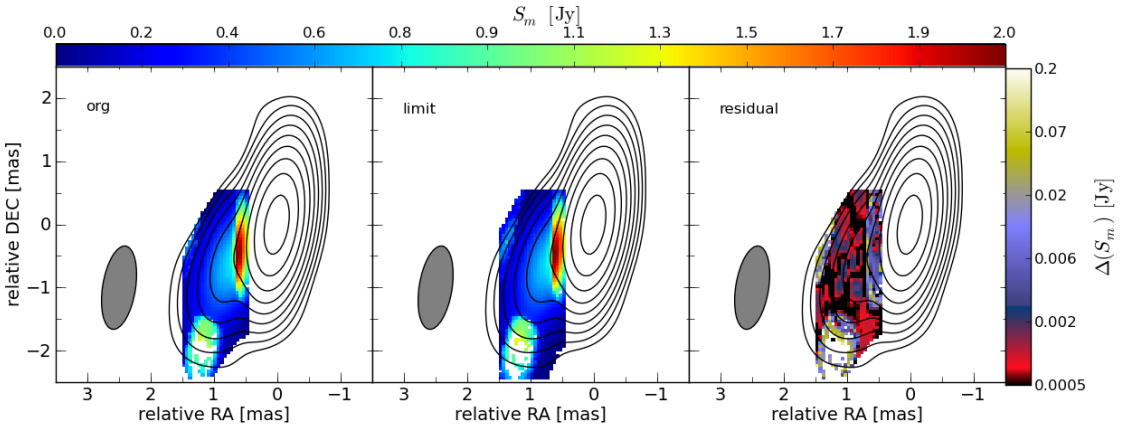

Figure B.6: Same as Fig. B.5 for the turnover flux density, S_m.

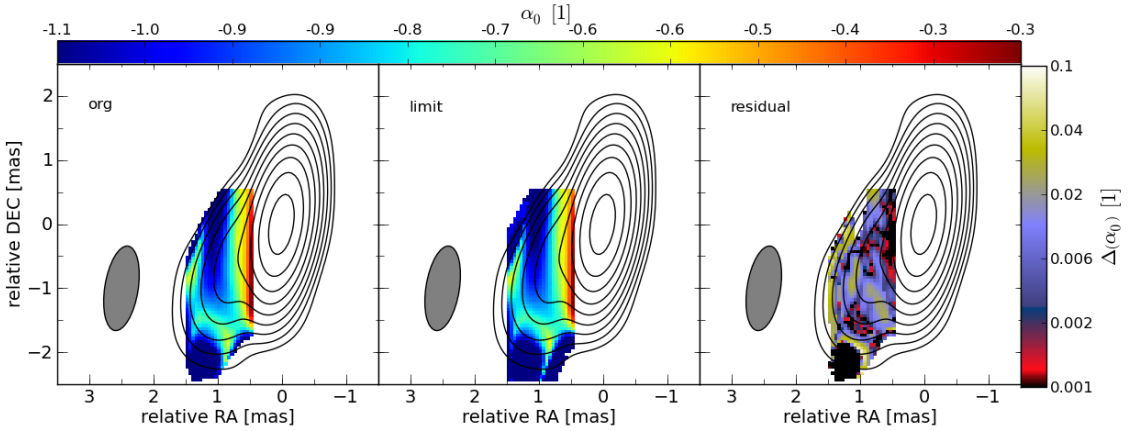

Figure B.7: Same as Fig. B.7 for the optically thin spectral index, α_0.

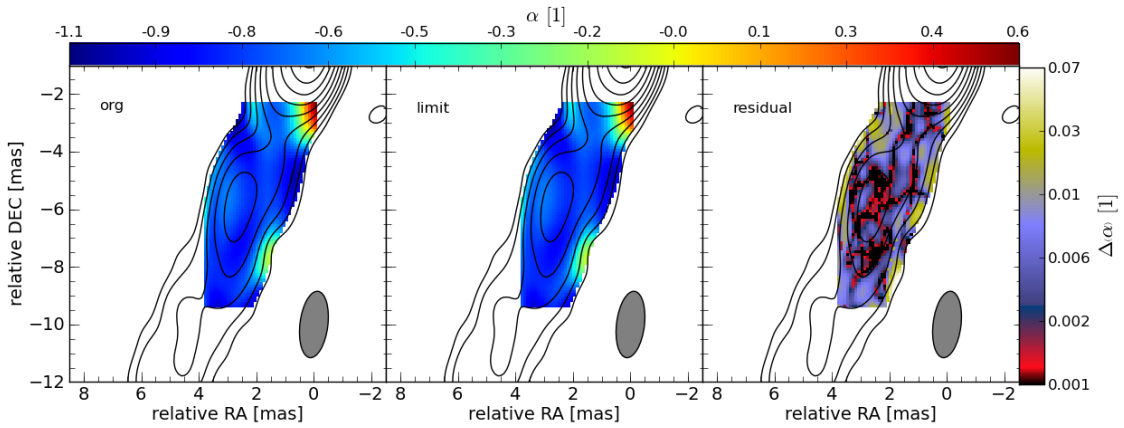

Figure B.8: Influence of the uv-range on the 2D distribution of the spectral index, α ($S_\nu \propto \nu^\alpha$) for region B (4 mas $< r <$ 8 mas) using a beam size of 2.32 × 0.97 mas with a P.A. of −7° and a pixel size of 0.10 mas. The left panel shows the spectral index for a unlimited uv-range, the middle panel for limited uv-range and the right panel the residuals between them. The contours correspond to the 15 GHz VLBI observations, where the lowest contour is plotted at 10× the rms value and further contours increase by factors of 2.

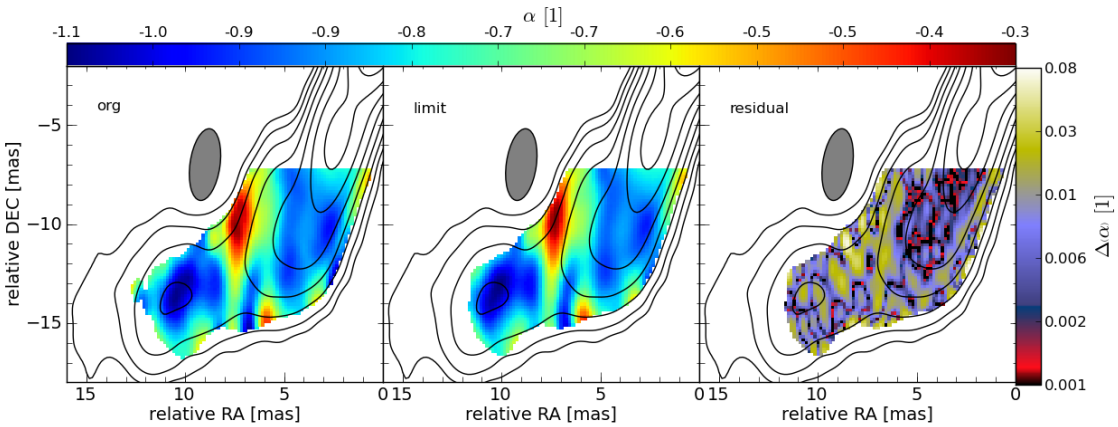

Figure B.9: Influence of the uv-range on the 2D distribution of the spectral index, α ($S_\nu \propto \nu^\alpha$) for region A and region B (4 mas $< r <$ 21 mas) using a beam size of 3.65×1.52 mas with a P.A. of $-8°$ and a pixel size of 0.10 mas. The left panel shows the spectral index for a un-limited uv-range, the middle panel for limited uv-range and the right panel the residuals between them. The contours correspond to the 8 GHz VLBI observations, where the lowest contour is plotted at 10× the rms value and further contours increase by factors of 2.

C Spectral parameter maps

Here we present the 2D distribution of the spectral index, α ($S_\nu \propto \nu^\alpha$) or the turnover values (ν_m, S_m and α_0) for regions C, D, B, and A. In Table B.1 we summarize the used image parameters for the spectral analysis.

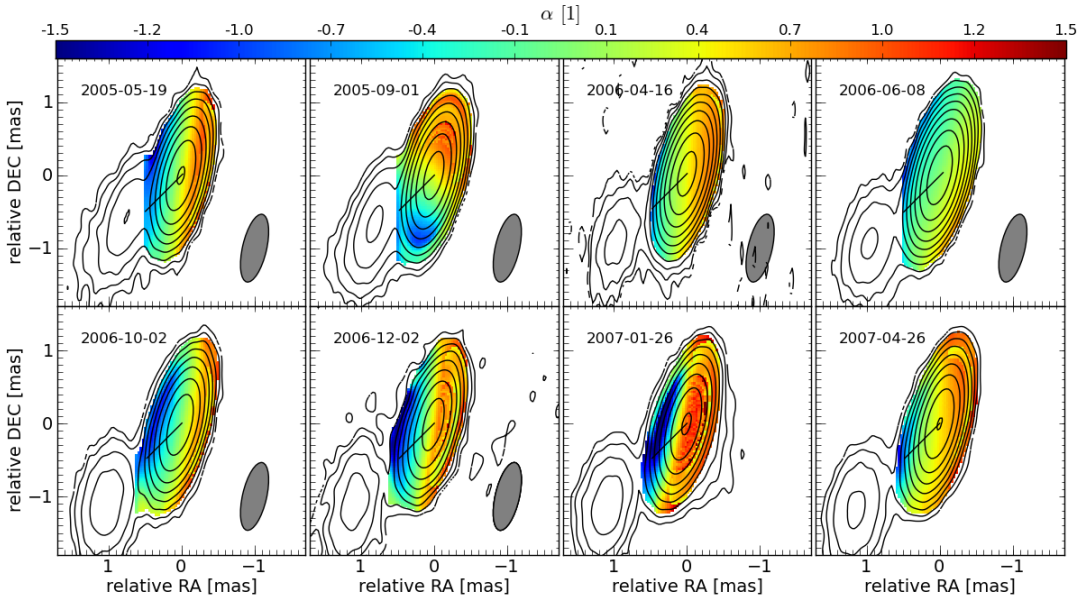

Figure C.1: 2D distribution of the spectral index, α ($S_\nu \propto \nu^\alpha$) for region C ($r < 1$ mas) using a beam size of 0.95×0.33 mas with a P.A. of $-13°$ and a pixel size of 0.03 mas. The color map in each panel shows for a given epoch (indicated in the top right corner) the distribution of α and the contours correspond to the 43 GHz VLBI observations, where the lowest contour is plotted at 10× the rms value and further contours increase by factors of 2.

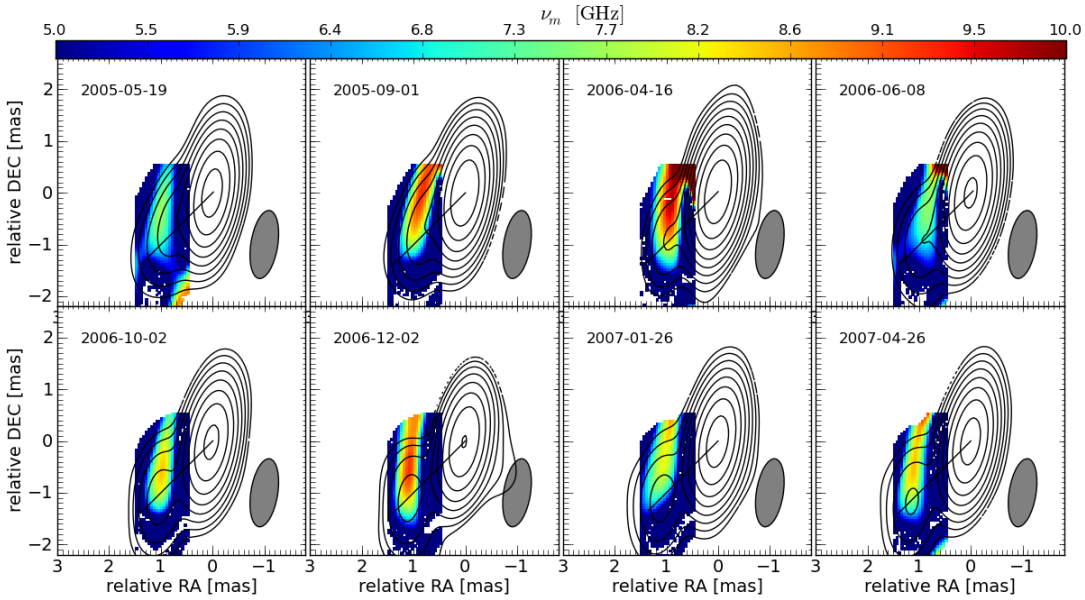

Figure C.2: 2D distribution of the turnover frequency, ν_m for region D (1 mas $< r <$ 4 mas) using a beam size of 1.33×0.52 mas with a P.A. of $-7°$ and a pixel size of 0.04 mas. The color map in each panel shows for a given epoch (indicated in the top right corner) the distribution of ν_m and the contours correspond to the 43 GHz VLBI observations, where the lowest contour is plotted at 5× the rms value and further contours increase by factors of 2.

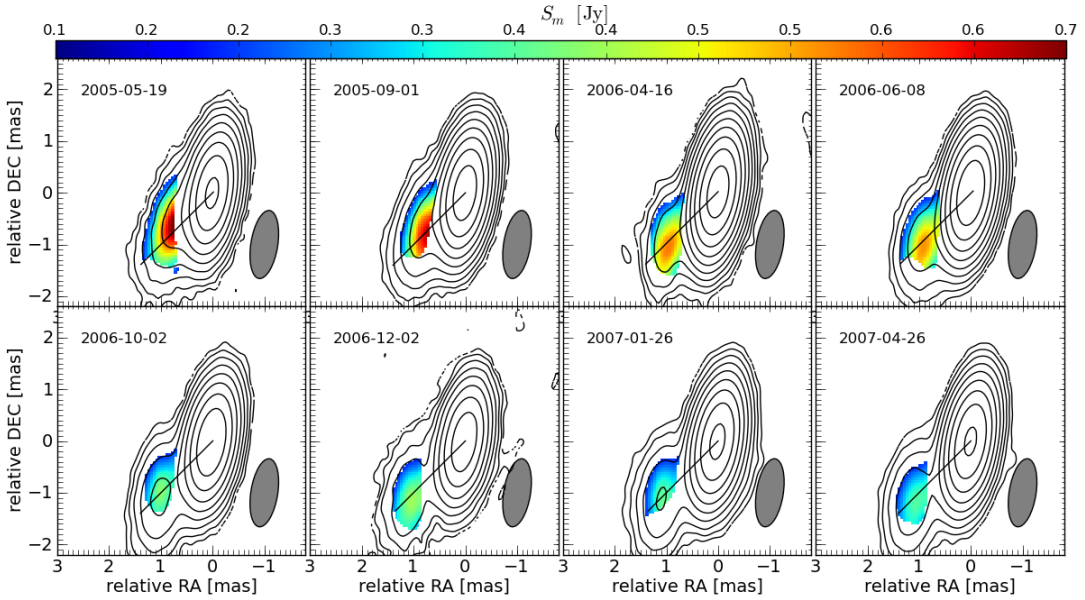

Figure C.3: Same as Fig. C.2 for the turnover flux density, S_m.

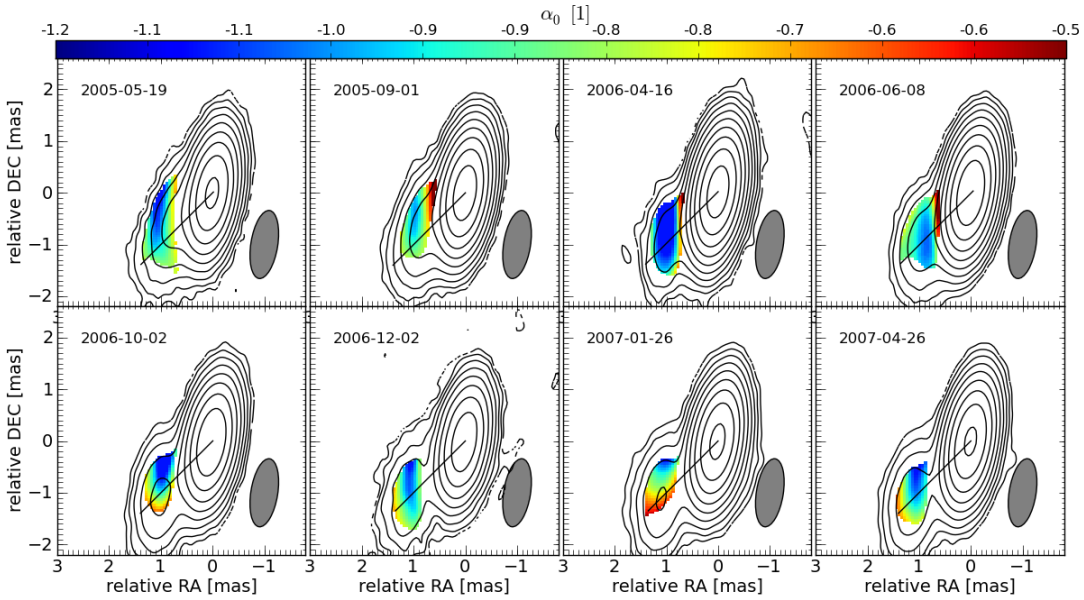

Figure C.4: Same as Fig. C.2 for the optically thin spectral index, α_0.

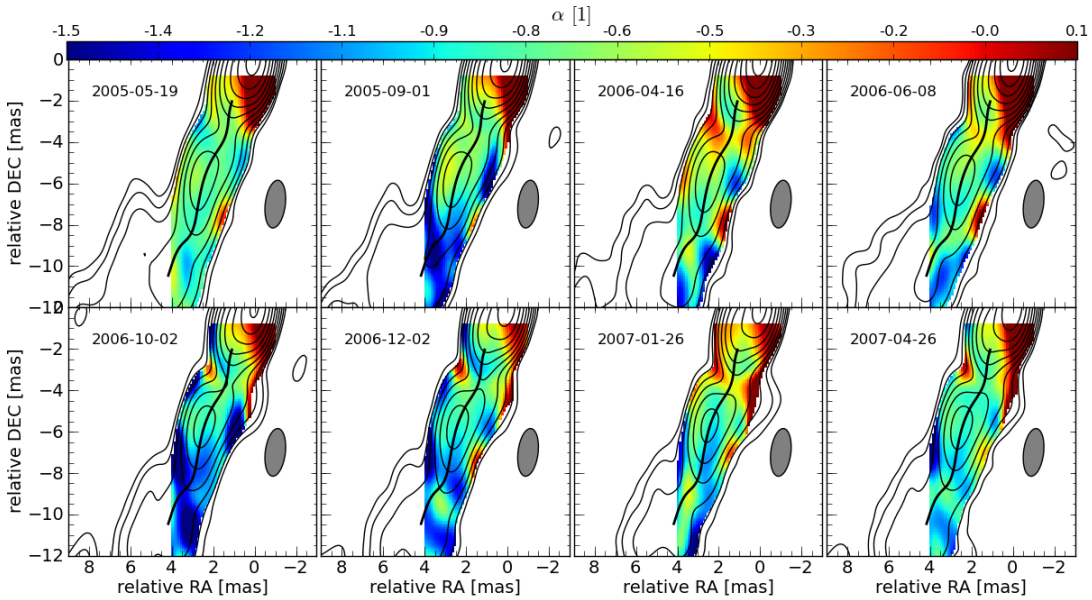

Figure C.5: 2D distribution of the spectral index, α ($S_\nu \propto \nu^\alpha$) for region B (4 mas $< r <$ 8 mas) using a beam size of 2.32×0.07 mas with a P.A. of $-7°$ and a pixel size of 0.1 mas. The color map in each panel shows for a given epoch (indicated in the top right corner) the distribution of α and the contours correspond to the 15 GHz VLBI observations, where the lowest contour is plotted at 5× the rms value and further contours increase by factors of 2.

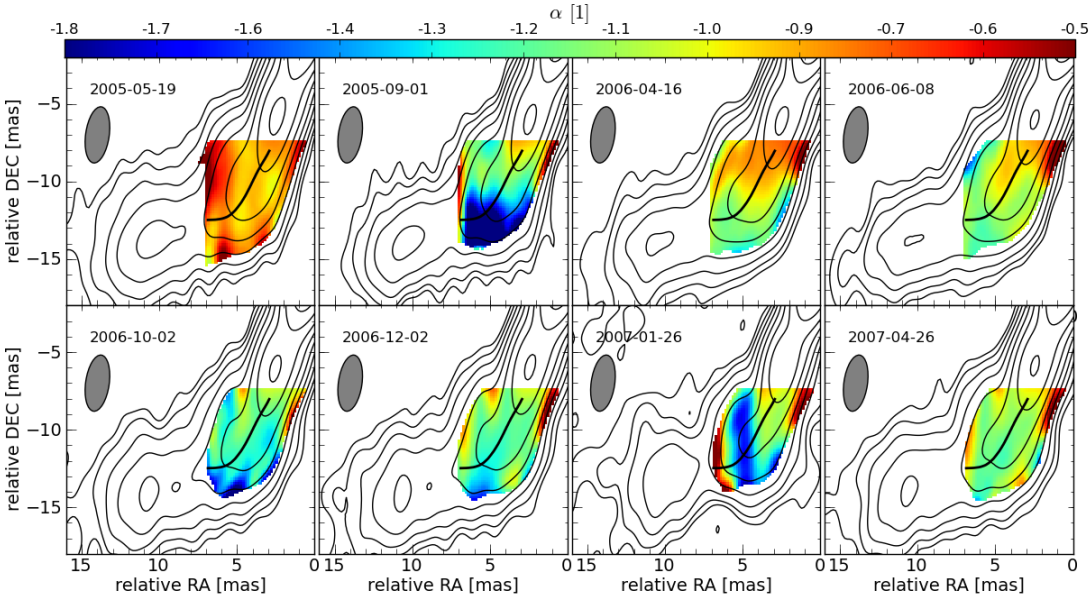

Figure C.6: 2D distribution of the spectral index, α ($S_\nu \propto \nu^\alpha$) for region A2 (8 mas $< r <$ 14 mas) using a beam size of 3.65 × 1.52 mas with a P.A. of −8° and a pixel size of 0.15 mas. The color map in each panel shows for a given epoch (indicated in the top right corner) the distribution of α and the contours correspond to the 15 GHz VLBI observations, where the lowest contour is plotted at 10× the rms value and further contours increase by factors of 2.

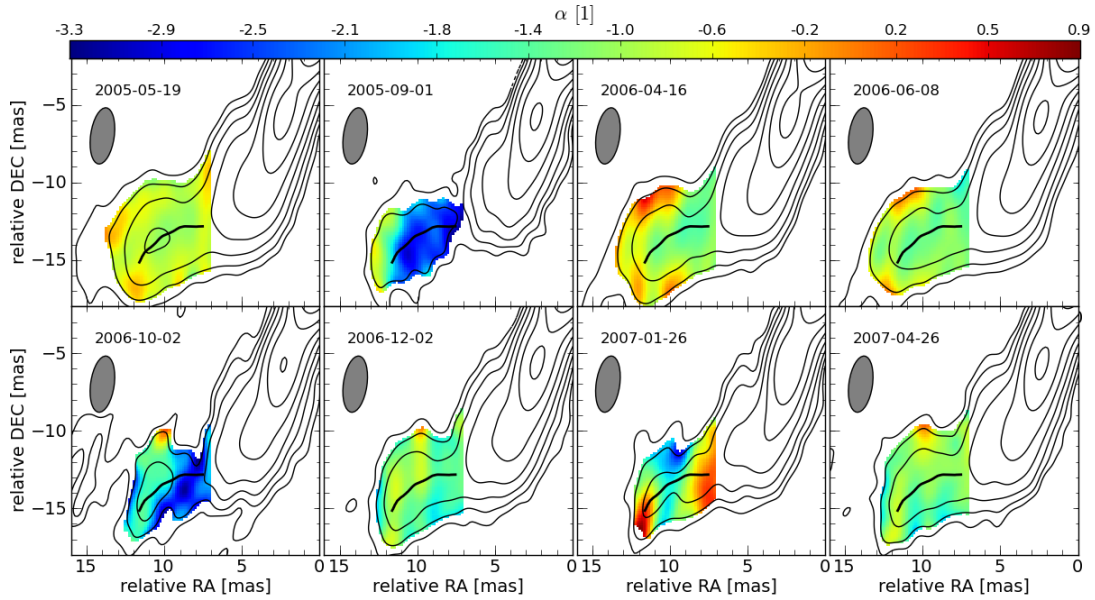

Figure C.7: 2D distribution of the spectral index, α ($S_\nu \propto \nu^\alpha$) for region A1 (14 mas $< r <$ 19 mas) using a beam size of 3.65 × 1.52 mas with a P.A. of −8° and a pixel size of 0.15 mas. The color map in each panel shows for a given epoch (indicated in the top right corner) the distribution of α and the contours correspond to the 8 GHz VLBI observations, where the lowest contour is plotted at 10× the rms value and further contours increase by factors of 2.

D Error estimates for the spectral parameters

The estimate of the uncertainties of parameters determined from extremely non-linear equations is a difficult task, and it is also the case in a space parameter with very different ranges of input parameters, as it is for the determination of spectral parameters from multi-wavelength VLBI images. We address this problem of estimating the uncertainties in α_0, α, S_m, ν_m, B, and K from Eq. 2.34 - 2.35 by using the flux density uncertainties on the individual pixels used in each of the combined images, and the uncertainties caused by the image alignment. This is performed by using the Monte Carlo technique.

We assume that the uncertainties on the obtained image shift are of the order of the used pixel size (see Sect. 5.1.1). Based on this assumption, and assuming additionally a normal distribution for the scatter of the image shifts, we compute 10^4 random image shifts and perform for each shift value a spectral analysis (see Sect. 5.1.2). Figure D.1 shows the distribution of the image shifts using 1000 random shifts for the May 2005 observations relative to the 86 GHz image. The different colors correspond to the absolute shifts between the reference VLBI map (here 86 GHz) and the other VLBI maps included in the spectral analysis. The initial shift positions for each frequency are indicated by the hexagon symbol.

The uncertainties on the spectral parameters for each pixel are calculated from the obtained distribution. Since the equation of the synchrotron spectrum and the spectral slope are highly non linear (Eq. 2.27), the spectral parameters are log-normal distributed. Therefore, the 1σ interval is asymmetric around the mean value.

The distributions calculated from the random shifts for one selected position are presented in Fig. D.2 and show the clearly the log-normal distribution of the spectral parameters.

Once the variation in the spectral parameters is obtained, we use these results for the calculation of the uncertainties of the magnetic field, B, and the normalization coefficient of the relativistic electron distribution, K. Again, we use a Monte Carlo approach and select 10^4 random values from the log-normal distribution of the spectral parameters and compute the scatter in B and K using Eq. 2.34 and Eq. 2.35 and the estimates of the jet width, R, and the Doppler factor, δ presented in Sect. 5.5. The dependence of the magnetic field and the normalization coefficient on the spectral parameters is highly non-linear which results in strongly skewed distributions. In Fig D.3 we present the distributions of the spectral parameters, the magnetic field and the normalization coefficient.

The uncertainties on the spectral index, α, ($S_\nu \propto \nu^\alpha$) in the different regions are calculated in a similar way.

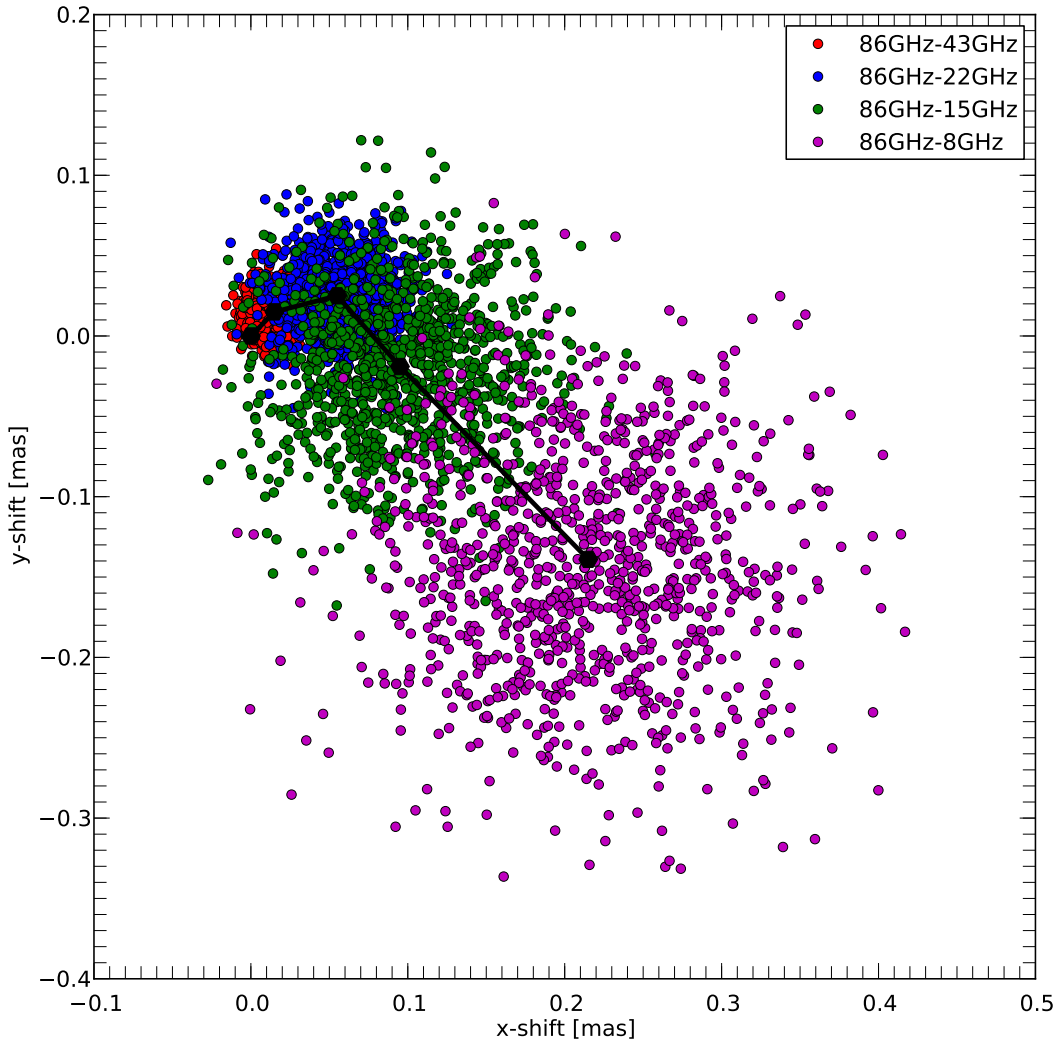

Figure D.1: Calculated random shifts obtained from a normal distribution using the initial shift value as mean and the uncertainty as standard derivation. Different colors correspond to different frequency pairs (see plot legend) and black hexagons indicate the initial shift position. See text for more details.

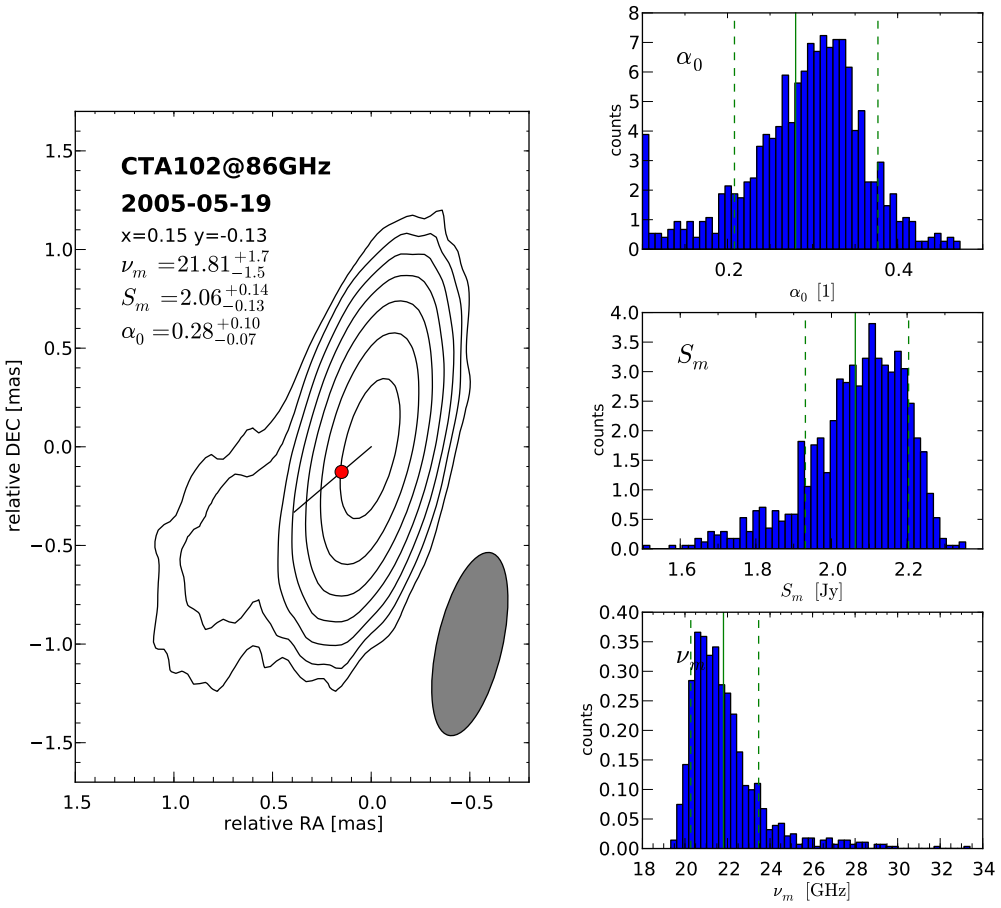

Figure D.2: Result of the Monte Carlo Simulation for the May 2005 observations at the position $x = 0.15$ mas, $y = -0.13$ mas. The left panel shows the 86 GHz contours where the lowest contour is plotted at 5× the rms value and increase by factors of 2. The solid black line correspond to the jet axis and the red point indicates the selected position. The right panels show from top to bottom the distribution of the optical thin spectral index, α_0, the turnover flux density, S_m, and the turnover frequency, ν_m. The solid green lines indicates the mean of the distribution and the dashed green lines the 1σ confidence interval. The values for the spectral values are plotted in the upper left corner of the contour plot. Notice the asymmetric error bars and tailed distribution of the spectral parameters.

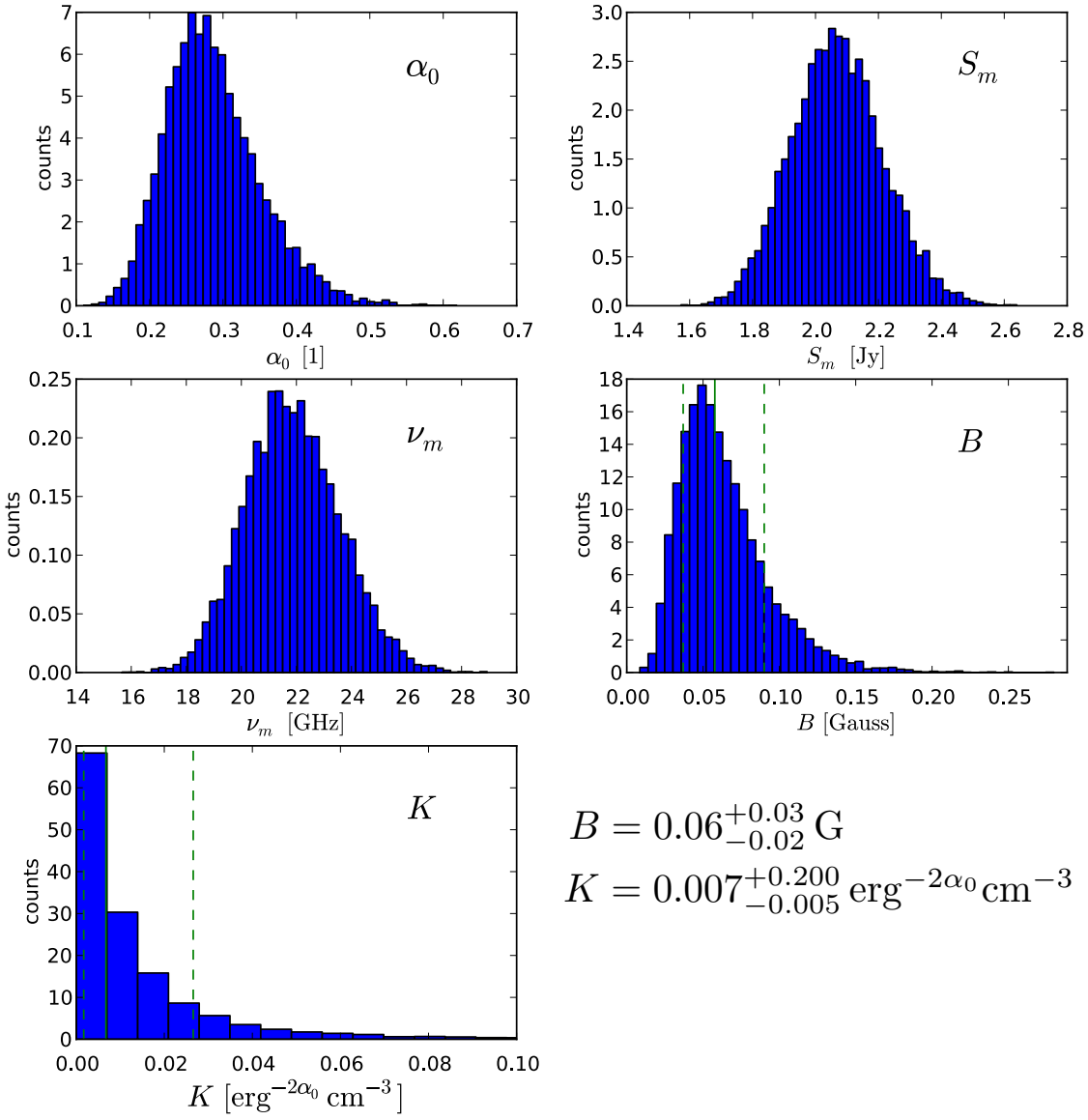

Figure D.3: Result of the Monte Carlo Simulation to study the dispersion of magnetic field, B, (panel 4) and the normalization coefficient, K (panel 5). The other panels show the distribution of the spectral parameters which are used for the calculation of B and K. The solid green lines indicates the mean of the distribution and the dashed green lines the 1σ confidence interval. The values obtained for B and K are plotted in lower right corner. Notice the asymmetric error bars and tailed distribution for all parameters.

Bibliography

Abdo, A. A., Ackermann, M., Ajello, M., et al. 2009, ApJS, 183, 46

Agudo, I., Gómez, J.-L., Martí, J.-M., et al. 2001, Astrophys. J., 549, L183

Aller, H. D., Aller, M. F., & Hodge, P. E. 1981, Astron. J., 86, 325

Aloy, M.-Á., Martí, J.-M., Gómez, J.-L., et al. 2003, Astrophys. J., 585, L109

Altschuler, D. R., Gurvits, L. I., Alef, W., et al. 1995, A&AS, 114, 197

Antonucci, R. 1993, Ann. Rev. Astron. Astrophys., 31, 473

Bååth, L. B. 1988, The Impact of VLBI on Astrophysics and Geophysics; Proceedings of the 129th IAU Symposium, 129, 117

Begelman, M. C., Blandford, R. D., & Rees, M. J. 1984, Reviews of Modern Physics, 56, 255

Björnsson, C.-I. & Aslaksen, T. 2000, Astrophys. J., 533, 787

Blandford, R. D. & Konigl, A. 1979, Astrophys. J., 232, 34

Blandford, R. D. & Payne, D. G. 1982, MNRAS, 199, 883

Blandford, R. D. & Znajek, R. L. 1977, MNRAS, 179, 433

Boettcher, M. & Dermer, C. D. 2010, American Astronomical Society, 11, 706

Boettcher, M., Harris, D. E., & Krawczynski, H. 2012, Relativistic Jets from Active Galactic Nuclei, Wiley & Sons

Böttcher, M. & Dermer, C. D. 2010, Astrophys. J., 711, 445

Burke, B. F. & Graham-Smith, F. 2009, An Introduction to Radio Astronomy, Cambridge University Press

Chang, C.-S. 2010, PhD thesis, University of Cologne, Germany

Croke, S. M. & Gabuzda, D. C. 2008, MNRAS, 386, 619

Crusius, A. & Schlickeiser, R. 1986, A&A, 164, L16

Daly, R. A. & Marscher, A. P. 1988, Astrophys. J., 334, 539

Falle, S. A. E. G. 1991, MNRAS, 250, 581

Fanaroff, B. L. & Riley, J. M. 1974, MNRAS, 167, 31P

Fromm, C. M., Ros, E., Savolainen, T., et al. 2010, eprint arXiv, 1011, 4831

Fuhrmann, L., Zensus, J. A., Krichbaum, T. P., Angelakis, E., & Readhead, A. C. S. 2007, in American Institute of Physics Conference Series, Vol. 921, The First GLAST Symposium, 249–251

Georganopoulos, M. & Marscher, A. P. 1998, Astrophys. J., 506, 621

Gomez, J. L., Marti, J. M. A., Marscher, A. P., Ibanez, J. M. A., & Alberdi, A. 1997, Astrophys. J.Letters v.482, 482, L33

Hardee, P. 2008, Journal of Physics: Conference Series, 131, 2052

Hardee, P. E. 2000, Astrophys. J., 533, 176

Hardee, P. E., Bridle, A. H., & Zensus, J. A. 1996, Astronomical Society of the Pacific Conference Series, 100

Hardee, P. E. & Eilek, J. A. 2011, Astrophys. J., 735, 61

Hardee, P. E. & Hughes, P. A. 2003, Astrophys. J., 583, 116

Hardee, P. E., Walker, R. C., & Gómez, J. L. 2005, Astrophys. J., 620, 646

Harris, D. E. & Roberts, J. A. 1960, Publications of the Astronomical Society of the Pacific, 72, 237

Hewitt, A. & Burbidge, G. 1989, ApJS, 69, 1

Hirotani, K. 2005, Astrophys. J., 619, 73

Hovatta, T., Lister, M. L., Aller, M. F., et al. 2012, Astrophys. J., 144, 105

Hovatta, T., Valtaoja, E., Tornikoski, M., & Lähteenmäki, A. 2009, A&A, 494, 527

Jorstad, S., Marscher, A., Stevens, J., et al. 2005a, Future Directions in High Resolution Astronomy: The 10th Anniversary of the VLBA, 340, 183

Jorstad, S. G., Marscher, A. P., Lister, M. L., et al. 2005b, Astron. J., 130, 1418

Joshi, M. & Böttcher, M. 2011, Astrophys. J., 727, 21

Kadler, M., Ros, E., Lobanov, A. P., Falcke, H., & Zensus, J. A. 2004, A&A, 426, 481

Kardashev, N. S. 1964, Soviet Astronomy, 8, 217

Kellermann, K. I., Sramek, R., Schmidt, M., Shaffer, D. B., & Green, R. 1989, Astrophys. J., 98, 1195

Komissarov, S. S. & Falle, S. A. E. G. 1997, MNRAS, 288, 833

Konigl, A. 1981, Astrophys. J., 243, 700

Kovalev, Y. Y., Lobanov, A. P., Pushkarev, A. B., & Zensus, J. A. 2008, A&A, 483, 759

Krolik, J. H. 1999, Active galactic nuclei: from the central black hole to the galactic environment, Princeton University Press

Lampton, M., Margon, B., & Bowyer, S. 1976, Astrophys. J., 208, 177

Leismann, T., Antón, L., Aloy, M. A., et al. 2005, A&A, 436, 503

Lind, K. R. & Blandford, R. D. 1985, Astrophys. J., 295, 358

Lister, M. L., Aller, H. D., Aller, M. F., et al. 2009a, The Astron. J., 137, 3718

Lister, M. L., Cohen, M. H., Homan, D. C., et al. 2009b, The Astron. J., 138, 1874

Lister, M. L. & Homan, D. C. 2005, The Astron. J., 130, 1389

Lobanov, A. P. 1998, A&ASupplement, 132, 261

Lobanov, A. P. & Zensus, J. A. 1999, Astrophys. J., 521, 509

Marcaide, J. M. & Shapiro, I. I. 1983, Astron. J., 88, 1133

Marscher, A. P. 1980, Astrophys. J., 235, 386

Marscher, A. P. 1987, IN: Superluminal radio sources; Proceedings of the Workshop, 280

Marscher, A. P. 1990, Parsec-scale radio jets, 236

Marscher, A. P. 2006, Relativistic Jets: The Common Physics of AGN, 856, 1

Marscher, A. P. & Gear, W. K. 1985, Astrophys. J., 298, 114

Martí, J. M. & Müller, E. 1999, Living Reviews in Relativity, 2, 3

Martí, J. M. A., Mueller, E., Font, J. A., Ibáñez, J. M. A., & Marquina, A. 1997, Astrophys. J., 479, 151

Meier, D. L., Koide, S., & Uchida, Y. 2001, Science, 291, 84

Mimica, P., Aloy, M.-A., Agudo, I., et al. 2009, Astrophys. J., 696, 1142

Mimica, P., Giannios, D., & Aloy, M. A. 2010, MNRAS, 407, 2501

Nalewajko, K. 2012, MNRAS, 420, L48

Nalewajko, K. & Sikora, M. 2009, MNRAS, 392, 1205

Nolan, P. L., Bertsch, D. L., Fichtel, C. E., et al. 1993, Astrophys. J., 414, 82

O'Sullivan, S. P. & Gabuzda, D. C. 2009, MNRAS, 400, 26

Pacholczyk, A. G. 1970, Radio astrophysics. Nonthermal processes in galactic and extragalactic sources, W. H. Freeman & Company

Perucho, M. 2005, PhD thesis, Universitat de València, Spain

Perucho, M. 2012, International Journal of Modern Physics: Conference Series, 08, 241

Perucho, M., Agudo, I., Gómez, J. L., et al. 2008, A&A, 489, L29

Perucho, M., Hanasz, M., Martí, J. M., & Sol, H. 2004a, A&A, 427, 415

Perucho, M., Kovalev, Y. Y., Lobanov, A. P., Hardee, P. E., & Agudo, I. 2012, Astrophys. J., 749, 55

Perucho, M. & Martí, J. M. 2007, MNRAS, 382, 526

Perucho, M., Martí, J. M., Cela, J. M., et al. 2010, A&A, 519, 41

Perucho, M., Martí, J. M., & Hanasz, M. 2004b, A&A, 427, 431

Pica, A. J., Smith, A. G., Webb, J. R., et al. 1988, Astron. J., 96, 1215

Piner, B. G., Mahmud, M., Fey, A. L., & Gospodinova, K. 2007, The Astron. J., 133, 2357

Pushkarev, A. B., Hovatta, T., Kovalev, Y. Y., et al. 2012, A&A, 545, A113

Pushkarev, A. B., Hovatta, T., Kovalev, Y. Y., et al. 2012, eprint arXiv, 1207, 5457

Pushkarev, A. B., Kovalev, Y. Y., Lister, M. L., & Savolainen, T. 2009, A&A, 507, L33

Rees, M. J. 1967, MNRAS, 135, 345

Ros, E. 2005, Future Directions in High Resolution Astronomy: The 10th Anniversary of the VLBA, ASP Conference Series, 340, 482

Savolainen, T., Wiik, K., Valtaoja, E., Jorstad, S. G., & Marscher, A. P. 2002, A&A, 394, 851

Savolainen, T., Wiik, K., Valtaoja, E., & Tornikoski, M. 2008, Extragalactic Jets: Theory and Observation from Radio to Gamma Ray, ASP Conference Series, 386, 451

Schinzel, F. K., Lobanov, A. P., Taylor, G. B., et al. 2012, A&A, 537, 70

Schmidt, M. 1963, Nature, 197, 1040

Shepherd, M. C. 1997, Astronomical Data Analysis Software and Systems VI, 125, 77

Sholomitskii, G. B. 1965, Soviet Astronomy, 9, 516

Spencer, R. E., McDowell, J. C., Charlesworth, M., et al. 1989, MNRAS, 240, 657

Stevens, J. A., Litchfield, S. J., Robson, E. I., et al. 1996, Astrophys. J., 466, 158

Terasranta, H., Tornikoski, M., Valtaoja, E., et al. 1992, A&ASupplement Series (ISSN 0365-0138), 94, 121

Thompson, A. R., Moran, J. M., & Swenson, G. W. 2007, Interferometry and Synthesis in Radio Astronomy, John Wiley & Sons

Tornikoski, M., Terasranta, H., Balonek, T. J., & Beckerman, E. 1999, BL Lac Phenomenon Poster Session, 159, 307

Türler, M., Courvoisier, T. J.-L., & Paltani, S. 1999, A&A, 349, 45

Türler, M., Courvoisier, T. J.-L., & Paltani, S. 2000, A&A, 361, 850

Véron-Cetty, M.-P. & Véron, P. 2003, A&A, 412, 399

Wang, Y., Knigge, C., Croston, J. H., & Pavlovski, G. 2011, MNRAS, 418, 1138

Wehrle, A. E. & Cohen, M. 1989, Astrophys. J., 346, L69

Zensus, J. A., Ros, E., Kellermann, K. I., et al. 2002, The Astron. J., 124, 662

Acknowledgements

Zum Abschluss möchte ich mich bei allen bedanken, die mich während der Anfertigung meiner Arbeit unterstützt haben:

Ich danke Prof. Dr. Pavel Kroupa, Prof. Dr. Ian Brock und PD Dr.-Ing. Axel Nothnagel für Ihre Bereitschaft meine Arbeit zubegutachten, der Teilnahmen am Promotionskolloquium und der Disputation.

Mein besonderer Dank gilt Prof. Dr. J. Anton Zensus, der es mir ermöglichte meine Arbeit in seiner Gruppe am Max-Planck-Institut für Radioastronomie anzufertigen. In den letzten acht Jahren in seiner Gruppe konnte ich mich immer auf seine Unterstützung verlassen. Ich bin dankbar, für das Stipendium der Internationalen Max Planck Research School welches mir erlaubte meine Ergebnisse auf mehreren internationalen Konferenzen vorzustellen und am Synthesis Imaging Workshop in New Mexico teilzunehmen.

Ohne die Hilfe meiner Betreuer Prof. Dr. Eduardo Ros und Dr. Manel Perucho wäre es mir nicht möglich gewesen diese Arbeit anzufertigen. In den letzten Jahren standen sie mir in jeder erdenklichen Situation hilfreich zur Seite. Die Dankbarkeit, die ich gegenüber meinen Doktorvätern empfinde lässt sich schwer in Worte fassen. Besonders ihre Gastfreundschaft und Fürsorge wähnend meiner vielen Aufenthalte an der Universität Valencia werden mir immer in Erinnerung bleiben.

Herzlich bedanken möchte ich mich bei Dr. Tuomas Savolainen und Dr. Petar Mimica, die mich tatkräftig in der VLBI Datenauswertung und bei der Berechnung der Synchrotronstrahlung unterstützt und mit zahlreichen Diskussionen zum Gelingen der Arbeit beitrugen. Dr. Andrei P. Lobanov gilt mein Dank für zahlreiche Diskussionen und Anregungen über die Interpretation des Core-shifts in AGN Jets.

Ich danke Dr. Frank Schinzel für all die Diskussionen, die wir in den letzten Jahren geführt haben. Besonders unsere Reisen nach Argentinien und Griechenland werden mir unvergessen bleiben. Mit Dr. Mar Mezcua, Dr. Chin-Shin Chang und Jan Wagner habe ich die letzen zwei Jahre das Büro geteilt. Zusammen mit ihnen habe ich eine sehr schöne Zeit verbracht und zahlreiche Unterhaltung über Physik und die wichtigen Dinge im Leben geführt. Danke. Ein besonderer Dank gilt meinen Kollegen in der VLBI Gruppe und der Astronomie und Astrophysik Abteilung der Universität Valencia für die zahlreichen Anregungen und Diskussionen.

Meinen Eltern, Geschwistern und Doro möchte ich für ihre Unterstützung danken, auf die ich mich immer verlassen kann und ohne die diese Arbeit nicht entstanden wäre.